TUM School of Engineering and Design
Technische Universität München

Satellite Monitoring of River Discharge

Daniel Scherer

Vollständiger Abdruck der von der TUM School of Engineering and Design der Technischen Universität München zur Erlangung des akademischen Grades eines

Doktors der Ingenieurwissenschaften (Dr.-Ing.)

genehmigten Dissertation.

Vorsitz:

Prof. Dr. Katharina Anders

Prüfende der Dissertation:

1. Prof. Dr.-Ing. Florian Seitz
2. Prof. Dr.-Ing. Markus Disse
3. Prof. Tamlin M. Pavelsky, Ph.D.

Die Dissertation wurde am 15.04.2025 bei der Technischen Universität München eingereicht und durch die TUM School of Engineering and Design am 03.10.2025 angenommen.

Abstract

Measurements of river discharge are essential for effective flood protection, sustainable water management, and research aimed at understanding the drivers and impacts of climate change within the global hydrologic cycle. Despite their importance, the number of in-situ discharge gauges is declining and unevenly distributed, with significant gaps in remote basins or developing regions most vulnerable to water scarcity and extreme events that are intensified by climate change. Therefore, observations of *Water Surface Elevation* (WSE) or *Water Surface Area* (WSA) from radar altimeters and multispectral sensors onboard satellites, which have been available globally for more than three decades, are regularly used to extend the discharge time series of discontinued gauges via functional relationships. However, research on satellite monitoring of discharge in ungauged river basins is still limited.

This work exploits the large variety of WSE, WSA, and *Water Surface Slope* (WSS) measurements from multiple satellite missions to derive hydraulic parameters required for Manning's empirical flow law to calculate river discharge time series in ungauged basins. The thesis describes the fundamental framework and hydraulic parameters to estimate river discharge and discusses the applied approximations from a remote sensing perspective. The derived parameters are studied individually in a closed-loop test, and innovative methods are developed to improve the multi-mission satellite measurements in terms of accuracy and transferability. A global reach-scale WSS dataset is calculated from the precise and synchronous measurements of the lidar altimeter onboard ICESat-2. The WSE time series from radar altimeters are significantly improved by slope corrections for the ground track shift using this WSS dataset. Deep-learning water classification is applied to high-resolution satellite imagery to monitor the WSA of narrow rivers and capture small variations of the river extent. By combining WSE and WSA through a hypsometric curve, a large part of the river bathymetry can be constructed. The depth of the unknown, permanently submerged part of the bathymetry is estimated using an empirical width-to-depth function, and the shape of the submerged geometry is approximated by a parabola. The closed-loop test reveals that the unknown roughness, which is first obtained from literature decision guides, causes the largest errors. Therefore, a roughness optimization approach is developed, which uses flow law inversion based on the principle of mass conservation, following current research in the scope of the novel SWOT satellite. SWOT is the first mission to measure WSE, WSA, and WSS synchronously and will facilitate the hydraulic parameter estimation by overcoming challenges when combining the observations of multiple missions as in this work. However, the approach based on multi-mission data significantly extends the temporal coverage, which is required for climate studies, and ensures redundancy by complementing the SWOT measurements.

The optimization approach requires only minimal expert input and is independent of calibration against in-situ data. It is validated globally at 27 river sections with a median normalized root mean square error of 12%. Furthermore, the research focuses on quantifying the uncertainties of the satellite observables and transferring them to the estimated discharge to obtain a realistic uncertainty range, which is crucial for data assimilation into hydrological models. On average, the 90% uncertainty range includes 91% of the in-situ measurements. This research contributes to a more comprehensive understanding of global river discharge dynamics and provides valuable data for improved water resource management and climate change modeling in ungauged basins.

Zusammenfassung

Messungen der Abflussmenge von Flüssen sind entscheidend für wirksamen Hochwasserschutz, nachhaltiges Wassermanagement und liefern wichtige Erkenntnisse über Ursachen und Wirkungen des Klimawandels innerhalb des globalen Wasserkreislaufs. Jedoch ist die Anzahl von In-Situ-Abflussmessstationen trotz ihrer Bedeutung vor allem in abgelegenen Flussgebieten oder Entwicklungsregionen stark abnehmend. Dabei ist die Bevölkerung dort besonders von zunehmenden Extremereignissen durch den Klimawandel bedroht. Daher werden schon häufig Satellitenmessungen des *Wasserstandes* (WSE) und der *Wasserfläche* (WSA) genutzt, um die Abflusszeitreihen von ehemaligen Messstationen über funktionale Beziehungen zu verlängern. Diese Messungen von Radaraltimetern und Multispektralsensoren sind seit mehr als drei Jahrzehnten verfügbar. Die Forschung zur Abflussberechnung ohne vorherige In-Situ-Messungen und ausschließlich basierend auf Satellitenbeobachtungen ist jedoch noch begrenzt.

Diese Arbeit nutzt die große Vielfalt an Satellitenmessungen von WSE, WSA und Flussgefälle (WSS), um die hydraulischen Parameter abzuleiten, welche für die empirische Fließformel zur Abflussberechnung nach Manning notwendig sind. Die hydraulischen Parameter und notwendigen Näherungen werden aus der Fernerkundungsperspektive diskutiert. Die abgeleiteten Parameter werden durch die Ersetzung mit In-Situ-Messungen einzeln untersucht, und innovative Methoden werden entwickelt, um die Genauigkeit und Übertragbarkeit der Satellitenbeobachtungen zu verbessern. Die präzisen und synchronen Messungen des ICESat-2 Lidar-Altimeters werden genutzt, um einen globaler WSS-Datensatz zu berechnen. Basierend auf diesem WSS-Datensatz werden leichte Messverschiebungen der Radaraltimeter korrigiert und die Genauigkeit der WSE-Zeitreihen dadurch deutlich verbessert. Mittels Deep-Learning wird die WSA in hochauflösenden Satellitenbildern klassifiziert, wodurch auch kleine Veränderungen von schmalen Flüssen erfasst werden können. WSE und WSA werden durch eine hypsometrische Funktion kombiniert, um einen großen Teil der Bathymetrie zu konstruieren. Die unbekannte Tiefe unterhalb des minimalen WSE wird mit einem empirischen Breite-Tiefe-Verhältnis geschätzt und die Geometrie durch eine Parabel ergänzt. Die Untersuchungen zeigen, dass die manuelle Schätzung des unbekannten Rauheitsbeiwerts die größten Fehler verursacht. Deshalb wird ein Ansatz zur Optimierung des Rauheitsbeiwerts basierend auf der Massenerhaltung entwickelt. Dieser Ansatz folgt der aktuellen Forschung im Rahmen der neuartigen SWOT-Mission, welche als erste WSE, WSA und WSS gleichzeitig messen kann. Dadurch werden Herausforderungen bei der Kombinierung der Beobachtungen zu unterschiedlichen Messzeitpunkten, wie sie sich in dieser Arbeit stellen, überwunden. Jedoch kann der Ansatz basierend auf mehreren Missionen einen deutlich längeren Zeitraum abdecken, welcher besonders für Klimastudien wichtig ist, und bietet Redundanz für die SWOT-Messungen.

Der Optimierungsansatz erfordert nur minimalen Experteneingriff und keine Kalibrierung durch In-Situ-Messungen. Die globale Validierung an 27 Flussabschnitten ergibt einen mittleren Fehler von 12 %. Darüber hinaus konzentriert sich die Arbeit auf die Quantifizierung der Unsicherheiten der Satellitenbeobachtungen und deren Übertragung auf den geschätzten Abfluss, um einen realistischen Unsicherheitsbereich zu erhalten. Dieser ist für die Datenassimilation in hydrologische Modelle unerlässlich und umfasst im Durchschnitt 91 % der In-Situ-Messungen. Diese Arbeit trägt zu einem umfassenderen Verständnis der globalen Flussabflussdynamik bei und liefert wertvolle Daten für ein verbessertes Wassermanagement und die Modellierung des Klimawandels in Flussgebieten ohne In-Situ-Messungen.

Contents

1 Introduction

1.1 Background and Motivation

Rivers are lifelines for ecosystems, human welfare, food security, and industry (Wang & He, 2022). Access to freshwater is critical for prosperity and peace, and geopolitical conflicts can be caused by the unequal allocation of water resources that is intensified by climate change (UN, 2024). The number of violent conflicts triggered by the access to freshwater increased from 8 in 2010 to 85 in 2021 (Shumilova et al., 2023). As part of the global water cycle, river discharge directly responds to extreme drought and precipitation events, serving as a critical indicator that characterizes Earth's climate (Vicente-Serrano et al., 2014). With climate change, there is an increasing risk of ecological change to rivers (Thompson et al., 2021) and the future global streamflow declines could be more severe than previously estimated (Zhang et al., 2023). Additionally, varying freshwater fluxes impact ocean salinity and temperature, which lead to shifts in ocean circulation that drive climate change (IPCC, 2022). Consequently, it is important to monitor river discharge (Depetris, 2021), and the *Global Climate Observing System* (GCOS) lists river discharge as an *Essential Climate Variable* (ECV), expressing the requirement for a dense global network of streamflow gauging stations (GCOS, 2022).

Over 50% of the world's population live within a 3 km distance of freshwater with the highest population density along large rivers (Kummu et al., 2011). To protect these people from flood damage and ensure sustainable water supply, water management decisions rely on streamflow data (UN, 2024). However, in-situ gauges for measuring river discharge are distributed unevenly with a bias towards large, perennial, and regulated rivers within watersheds of large human impact. In contrast, limited data is available for less developed economies, which are most vulnerable to water scarcity, droughts, or flood events (Krabbenhoft et al., 2022; Wilby, 2019). This is reflected by the declining number of active stations in global discharge databases, such as the *Global Runoff Data Centre* (GRDC). Especially, up-to-date data is not available in developing countries (Hannah et al., 2011) such as large parts of Africa, which are at high risk of high and low flow extremes under any warming scenario (Thompson et al., 2021). Although Riggs et al. (2023) demonstrated that the GRDC only includes a fraction of discharge data compared to gathering them from individual sources, data availability in developing and vulnerable regions is still relatively small and decreasing when using data beyond the GRDC. Furthermore, daily discharge time series are missing 14% of data on average (Riggs et al., 2023).

Missing data and discontinued time series can be compensated by calibrating a functional relationship, often referred to as a rating curve, to the observed discharge and hydrogeodetic observations (e.g., Elmi et al., 2024; Paris et al., 2016; Pavelsky, 2014; Riggs et al., 2023; Tarpanelli et al., 2019). Hydrogeodesy, the science of monitoring terrestrial waters from space-based sensors, is an emerging field within Earth observation (Jaramillo et al., 2024). The two most commonly used hydrogeodetic observables are *Water Surface Elevation* (WSE) measured from satellite altimetry and *Water Surface Area* (WSA) or the related river width derived from remote sensing techniques such as multispectral or *Synthetic Aperture Radar* (SAR) satellite imagery sensors (Gleason & Durand, 2020). In contrast to in-situ gauges, space-based sensors provide continuous and coherent global coverage (Stammer & Cazenave, 2017). WSE time series from satellite altimetry are provided at so-called virtual stations by platforms such as the *Database for Hydrological Time Series of Inland Waters* (DAHITI, Schwatke et al., 2015) or Hydroweb (Cretaux et al., 2011; Normandin et al., 2018; Santos da Silva et al., 2010). Both databases cover more than 10,000 virtual stations globally. These virtual stations are located at the intersection of the satellite's ground track with an inland water

body because classical altimetry measurements work only in the nadir direction. Although developed for ocean applications, early altimetry satellites could already be used to opportunistically measure the WSE of wide rivers since the 1990s, and with improved sensors, a larger fraction of the World's rivers could be monitored since the launch of the Jason-2 mission in 2008 (Seyler et al., 2013). However, for the majority of rivers on Earth, space-based WSE measurements with sufficient accuracy have only been possible since the launch of Sentinel-3A in 2016. Using global covering satellite imagery, WSA rating curves can be used to estimate even longer discharge time series dating back to 1984, only limited by cloud coverage and the coarse ground sample distance of 30 m of early remote sensing sensors (Elmi et al., 2024). This resolution improved with the launch of Sentinel-2A (2015) to 10 m, but WSA variations of small rivers can only be observed since the PlanetScope constellation with a resolution of 3 m was reached in 2018. Given the recent advancements in sensor technology and data availability, the full potential of hydrogeodetic observations for comprehensive river monitoring is only beginning to be realized.

Although remote sensing observations and in-situ discharge measurements are not required to overlap for fitting a rating curve to the data (Tourian et al., 2013), the river must have been gauged for a certain period of time. However, many river basins have never been gauged, or the data is not publicly available for political reasons (Gleason & Durand, 2020). The estimation of river discharge independent of in-situ gauges would be beneficial to answer many of the "23 unsolved problems in hydrology" summarized by Blöschl et al. (2019), which can already be covered partially with various methods of hydrogeodesy (Jaramillo et al., 2024). The launch of the novel wide-swath *Surface Water and Ocean Topography* (SWOT) mission in 2022 and the first unconstrained (no calibration with gauges) SWOT discharge results (Andreadis et al., 2025) mark an important step towards addressing the "Holy Grail of scientific hydrology" (Beven, 2006), improving our ability to close the water balance at various spatial and temporal scales and advancing our understanding of hydrological processes. The SWOT mission is capable of measuring WSE, WSA, and *Water Surface Slope* (WSS) simultaneously with high spatial resolution. Several algorithms have been developed specifically for observations from the SWOT mission (Andreadis et al., 2025; Durand et al., 2016). While some of these methods utilize large-scale data assimilation with hydraulic models (Andreadis et al., 2020; Larnier et al., 2020; Larnier & Monnier, 2023; Oubanas et al., 2018), the approaches by Brinkerhoff et al. (2020) and Durand et al. (2014) solve the remaining unknown hydraulic parameters (riverbed roughness and submerged bathymetry cannot be measured from space) on reach scale based on the principle of mass conservation. The anticipated error range of SWOT discharge is below 30% (Durand et al., 2023), and the first results show the expected quality in discharge variations but with a higher bias than predicted (Andreadis et al., 2025).

Despite these promising results, the planned mission period of SWOT is only three years (2022-2025), and a follow-on mission is not expected to launch before 2032 (Vuilleumier & Egido, 2023). This makes it challenging to rely solely on SWOT data for climate studies, which require decades of data to accurately capture long-term trends and variability (Marchi et al., 2020). Furthermore, focusing on a single mission introduces a potential vulnerability, as the continuity of data depends on the lifespan of SWOT and possible successors. Therefore, it is crucial to investigate methods for estimating river discharge without in-situ calibration from pre-SWOT satellite data such as nadir altimetry and optical imagery. Such diversification of approaches would not only provide redundancy but also extend temporal coverage, complementing the revolutionary data delivered by the SWOT mission (Cerbelaud et al., 2025).

The potential for measuring river discharge from multi-mission satellite data was explored by Bjerklie et al. (2003), who developed multiple models for different combinations of hydrogeodetic observables such as WSE, WSA, and WSS. Bjerklie et al. (2018), Sichangi et al. (2018), and Zakharova et al. (2020) successfully combined WSE, WSA, and WSS observed from multiple satellite missions to derive discharge in local studies. However, the spatial applicability of these approaches is limited because they require, e.g., significant width variations detectable from moderate resolution (250 m) daily satellite imagery to derive the velocity via the time lag (Sichangi et al., 2018), or opportunistically located virtual stations enclosing the studied reach to derive WSS (Bjerklie et al., 2018). Furthermore, these approaches require extensive expert judgment, especially when choosing coefficients to parameterize the riverbed roughness.

In this thesis, WSE, WSA, and WSS from pre-SWOT multi-mission satellite data are used to estimate discharge similar to Bjerklie et al. (2018), Sichangi et al. (2018), and Zakharova et al. (2020). The individual observables are studied for possible improvements in accuracy and scalability using innovative sensors and techniques. Figure 1.1 shows an illustration of the multiple sensors employed. Additionally, the mass-conserved flow law inversion applied to SWOT data by Brinkerhoff et al. (2020) and Durand et al. (2014) is transferred to the pre-SWOT data to mitigate the required expert judgment in choosing the roughness coefficients. In this way, this thesis integrates long-term pre-SWOT observations with recent advances in remote sensing hydraulics, introducing a method for estimating long-term discharge time series in ungauged basins. The results contain realistic uncertainty quantification, ensuring their suitability for assimilation into hydrological models to enhance our understanding of climate change and develop strategies to adapt to its threatening consequences.

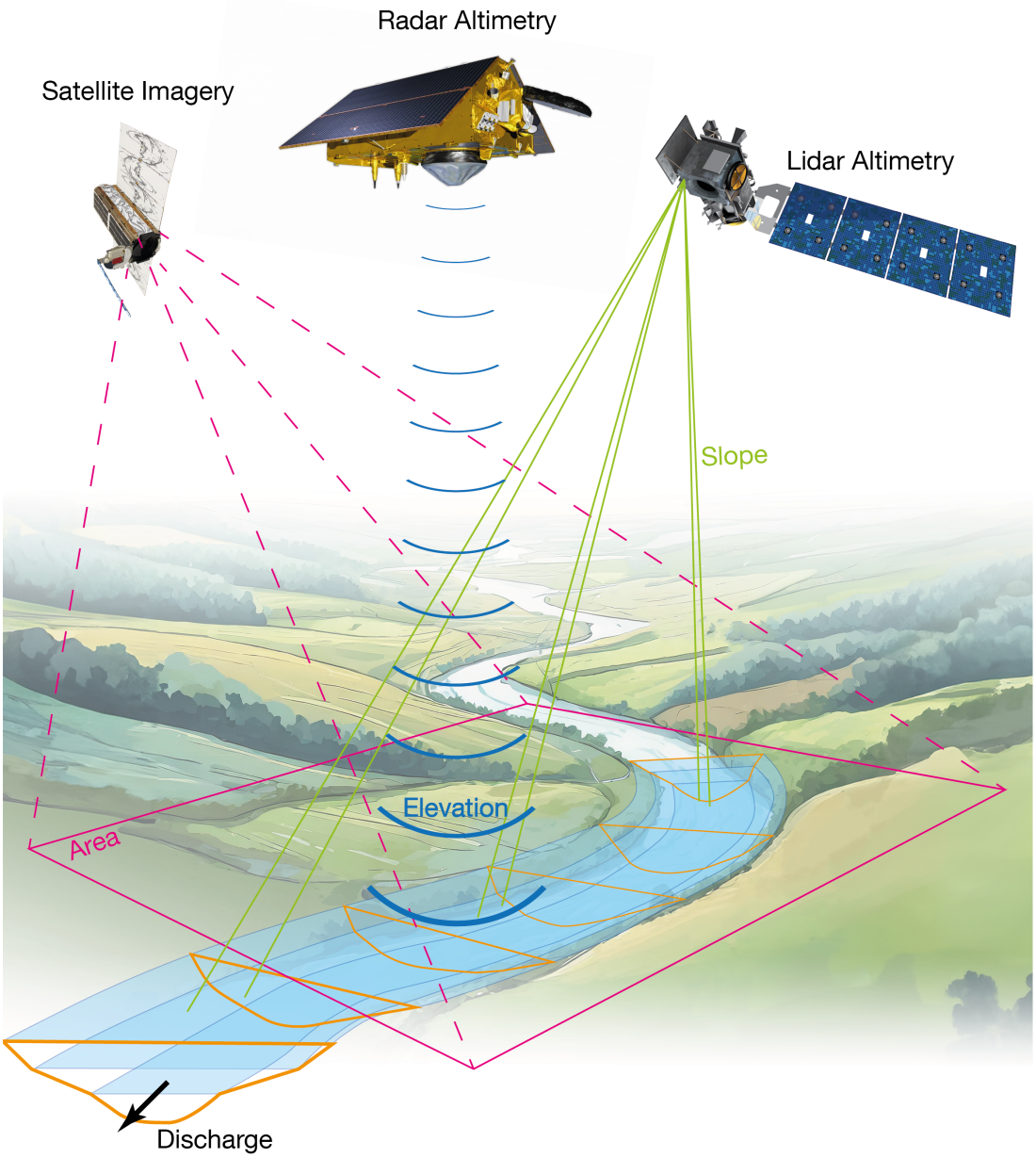

Figure 1.1 Satellite sensors and observables for the estimation of river discharge.

1.2 Objectives and Outline

As introduced in Section 1.1, hydrogeodetic observations have primarily been used to extend existing in-situ discharge time series in gauged basins. However, the field of deriving river discharge in ungauged basins without requiring calibration with in-situ measurements has not yet been well studied. There have been recent advances using the novel SWOT sensor, whose current temporal coverage is low and continuation is insecure, but there are only a few studies using long-term multi-mission satellite data. Therefore, this thesis aims to develop a method to derive river discharge in ungauged basins only using multi-mission hydrogeodetic observations without the need for calibration by in-situ data and with minimal expert decisions required. This thesis addresses the following three objectives to achieve this goal:

O1 Identify the potential and limitations of uncalibrated satellite monitoring of river discharge
A framework for the estimation of river discharge will be established, and methods to derive the required hydraulic parameters from multi-mission satellite observations without calibration by in-situ data will be assessed. This involves evaluating the sensitivity to the parameters and possible improvements in their observation or estimation. Furthermore, river conditions that are most favorable or limit the applicability of the developed methods will be identified.

O2 Investigate innovative techniques to improve the hydraulic parameter estimation
The observation or estimation of the hydraulic parameters will be improved not only in terms of errors but also regarding robustness, scalability, and transferability. Additionally, the need for expert adjustments and the risk of observer bias shall be minimized using unsupervised methods.

O3 Provide reliable uncertainty quantification
Uncertainties and error quantification are important for users when incorporating the data into broader hydrologic models. The discharge results shall include a confidence interval based on the uncertainties of the input observations and estimations.

These objectives are addressed by the following four publications, which are the main part of this thesis containing detailed discussions of the materials and methods and are included in the Appendix:

P1 Scherer, D., Schwatke, C., Dettmering, D., & Seitz, F. (2020). **Long-Term Discharge Estimation for the Lower Mississippi River Using Satellite Altimetry and Remote Sensing Images**. *Remote Sensing*, *12*, 2693. https://doi.org/10.3390/rs12172693

P2 Scherer, D., Schwatke, C., Dettmering, D., & Seitz, F. (2022). **ICESat-2 Based River Surface Slope and Its Impact on Water Level Time Series From Satellite Altimetry**. *Water Resources Research*, *58*, 1–25. https://doi.org/10.1029/2022WR032842

P3 Scherer, D., Schwatke, C., Dettmering, D., & Seitz, F. (2023). **ICESat-2 river surface slope (IRIS): A global reach-scale water surface slope dataset**. *Scientific Data*, *10*, 359. https://doi.org/10.1038/s41597-023-02215-x

P4 Scherer, D., Schwatke, C., Dettmering, D., & Seitz, F. (2024). **Monitoring river discharge from space: An optimization approach with uncertainty quantification for small ungauged rivers**. *Remote Sensing of Environment*, *315*, 114434. https://doi.org/10.1016/j.rse.2024.114434

P1 is dedicated to **O1**, establishing a fundamental framework for estimating discharge using satellite data. Exploiting the well-studied and data-rich Lower Mississippi Basin, **P1** contains a closed-loop test to study the sensitivity of the hydraulic parameters and limitations of the approach. Dedicated to **O2**, **P2** introduces an innovative approach for measuring WSS using lidar altimetry. The approach of **P2** is scaled to a global reach-scale dataset in **P3**. **P4** addresses all objectives by propagating the uncertainties of the input data to the discharge results (**O3**), introducing an optimization approach for unbiased estimation of the roughness parameter (**O2**), and transferring the improved methods of **P1** to smaller rivers of different flow regimes using high-resolution sensors (**O1**).

Figure 1.2 shows the general outline of the content of this thesis sorted by chapter and publication. Because the contents of the publications partially overlap or describe different methods to derive the same parameters to fulfill **O2**, this thesis starts with a general introduction to river hydraulics in Chapter 2, describing the applied hydraulic methods, required hydraulic parameters, and approximations from a remote sensing perspective. Then, Chapter 3 describes briefly the different sensors and methods used to derive the hydraulic parameters side-by-side structured by the observables WSE, WSS (including summaries of **P2** and **P3**), WSA, and their combination. Chapter 4 comprises **P1** and **P4**, which describe the initial discharge framework, closed-loop test, and the improved optimization approach with uncertainty quantification. An overall summary with conclusions on the research objectives is given in Chapter 5 followed by an outlook with recommendations for future work in Chapter 6.

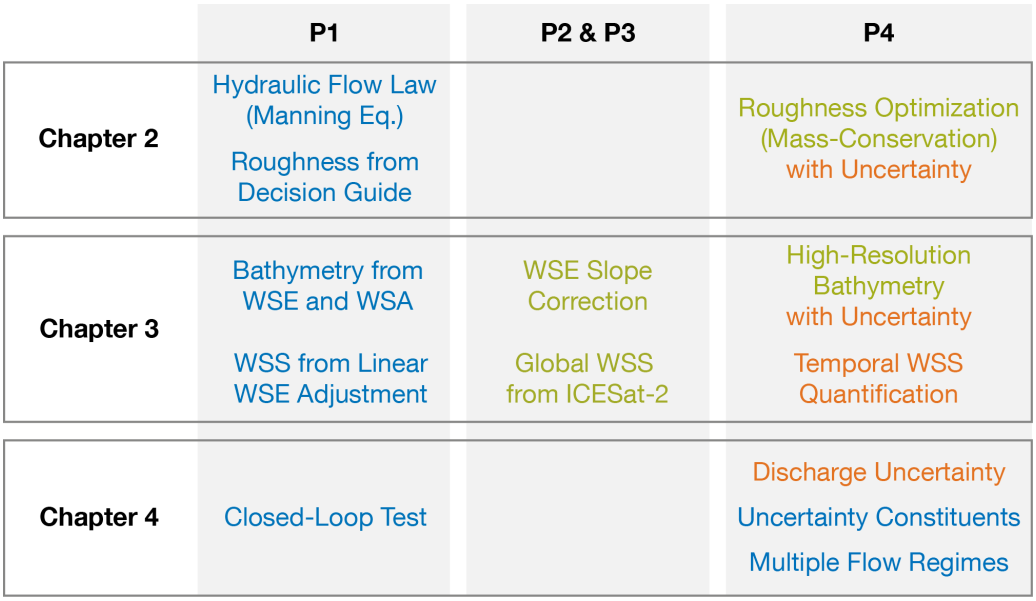

Figure 1.2 Thesis outline with key contents sorted by chapter and describing publication colored by objective (blue: O1, green: O2, orange: O3)

Additional contributions related to the objective and referenced in this thesis have been made in the following publications:

AP1 Schwatke, C., Scherer, D., & Dettmering, D. (2019). **Automated Extraction of Consistent Time-Variable Water Surfaces of Lakes and Reservoirs Based on Landsat and Sentinel-2**. *Remote Sensing*, *11*, 1010. https://doi.org/10.3390/rs11091010

AP2 Dettmering, D., Ellenbeck, L., Scherer, D., Schwatke, C., & Niemann, C. (2020). **Potential and limitations of satellite altimetry constellations for monitoring surface water storage changes—A case study in the Mississippi basin**. *Remote Sensing*, *12*. https://doi.org/10.3390/rs12203320

AP3 Schwatke, C., Halicki, M., & Scherer, D. (2024). **Generation of High-Resolution Water Surface Slopes From Multi-Mission Satellite Altimetry**. *Water Resources Research*, *60*. https://doi.org/10.1029/2023WR034907

AP1 describes an automated method for water classification in multispectral satellite images. This method is applied in **P1**. **AP2** discusses the potential of different satellite altimetry constellations to cover inland water bodies and addresses **O1**, as the coverage with space-based WSE measurements is one major limitation of the multi-mission approach described in this thesis. **AP3** describes a further alternative approach to obtain WSS from multi-mission altimetry, using the results of **P2** and **P3** for calibration and validation purposes.

2 River Hydraulics

This thesis combines space-based geodetic measurement techniques with fundamental hydraulic equations and principles to obtain river discharge. While the hydrogeodetic satellite sensors provide a variety of observables, not all required hydraulic parameters can be derived from space-based measurements. This chapter introduces the applied hydraulic concepts and the required parameters and links them to the satellite observables described in Chapter 3.

2.1 Fundamental Concepts in River Hydraulics

This thesis refers to river discharge as the open-channel flow of natural rivers with the water surface subject to atmospheric pressure (Chow, 1959). River discharge Q [m^3/s], the mass of water passing a location of measurement (x) along the river at a time step (t), cannot be measured directly but must be calculated from the flow velocity v [m/s] and the cross-sectional area A [m^2] (Julien, 2018).

$$Q(t,x) = v(t,x) \cdot A(t,x) \tag{2.1}$$

In-situ, hydroacoustic instruments like the *Acoustic Doppler Current Profiler* (ADCP) become increasingly common to measure v and A. ADCPs transmit sound signals from multiple transducers and receive reflections from suspended particles in the water. Because of the Doppler effect, the frequency of the received signals is shifted proportionally to v. Using range bins, a vertical velocity profile and the flow depth can be measured across the river (Rhoads, 2020; Turnipseed & Sauer, 2010). While measurements near the transducers, the riverbed, and in shallow waters are unreliable or impossible (Mueller et al., 2007), the majority of the cross-sectional geometry and area A can be obtained from ADCPs (Rhoads, 2020).

Without ADCPs, extensive measurements of v with rotating mechanical or electromagnetic current meters are required (Rhoads, 2020). The cross-sectional geometry and velocity distribution must be determined manually, e.g., using the mid-section method, which accounts for the velocity profile across the channel, by dividing the cross-section into n segments and measuring the depth-averaged velocity $\bar{v}_i$ and mean depth of each segment i. For natural channels, Turnipseed and Sauer (2010) recommend up to 30 segments depending on the river width, and the flow at the selected site should be steady and uniform. Based on the segment's mean depth and width, its cross-sectional area A_i is calculated to obtain the discharge within each segment, the sum of which is the total discharge at the cross-section (Rhoads, 2020):

$$Q(t,x) = \sum_{i=1}^{n} \bar{v}_i(t,x) \cdot A_i(t,x) \tag{2.2}$$

This segmentation into vertical sections is also employed in **P1** and **P4** to consider the different flow velocities across the channel.

Even though advanced sensors such as ADCPs are available and can now be attached to unmanned aerial systems for cost-effective surveys (Frias et al., 2025), discharge measurements still require considerable financial, temporal, and human resources. Therefore, the river discharge of a natural channel is typically not measured continuously. Instead, only a few samples are used to calibrate a stage-discharge model (rating curve) at different stages. Hysteresis effects, channel dynamics, and the sparse sampling of discharge extremes can cause significant uncertainties in these models (Le Coz et al., 2014). Therefore, errors w.r.t. the in-situ discharge must not necessarily indicate that the data, assumptions, and methods applied in this thesis are unsuitable for deriving river discharge.

2.1.1 Flow Types

Different types of flow can be classified in open-channel hydraulics based on spatial and temporal variations in discharge, velocity, and the cross-sectional area within the channel. The flow is steady if the discharge is constant over the time interval of observation and uniform if v and A do not change within the studied channel section. Based on these features, four classes can be defined (Rhoads, 2020):

Steady Uniform Flow occurs when the discharge is at a constant rate over time, and the cross-sectional area and velocity do not change along the channel. $\frac{\partial Q}{\partial t} = 0, \frac{\partial A}{\partial x} = 0, \frac{\partial v}{\partial x} = 0$

Steady Non-Uniform Flow refers to a constant rate of discharge through a channel of changing cross-sectional area and velocity in space. $\frac{\partial Q}{\partial t} = 0, \frac{\partial A}{\partial x} \neq 0, \frac{\partial v}{\partial x} \neq 0$

Unsteady Uniform Flow is an extremely rare state when v and A are constant along the channel, but the discharge changes over time. $\frac{\partial Q}{\partial t} \neq 0, \frac{\partial A}{\partial x} = 0, \frac{\partial v}{\partial x} = 0$

Unsteady Non-Uniform Flow can be observed when a flood wave of varying discharge passes a channel with spatiotemporally varying cross-sectional area and velocity. $\frac{\partial Q}{\partial t} \neq 0, \frac{\partial A}{\partial x} \neq 0, \frac{\partial v}{\partial x} \neq 0$

The flow can be further classified as laminar, turbulent, or transitional, depending on the Reynolds number, which considers water viscosity, velocity, and channel geometry. However, laminar flow occurs very rarely in open channels (Chow, 1959). Therefore, the flow of the natural channels studied in this thesis is always considered turbulent. Depending on the Froude number, which considers flow velocity, depth, and gravity, the flow can be classified into subcritical (calm, small v relative to depth with dominant gravitational forces), critical, and supercritical (rapid, large v relative to depth with dominant inertial forces) (Chow, 1959). In subcritical conditions, which are most common in natural rivers except for mountain rivers or flood events, waves caused by a downstream flow disturbance can propagate upstream because the wave velocity (celerity) exceeds the flow velocity (Rhoads, 2020). Subcritical flow is also affected further upstream by backwater effects from dams or natural barriers than supercritical flow (Chow, 1959).

2.1.2 Approximations

The flow complexity varies depending on the flow type. For steady uniform flow, the velocity in the downstream direction is predominant (one-dimensional flow), and the slope of the river bed is equal to the slope of the water surface. With increasing variations in v, A, and Q over t or x (i.e., in backwater affected, unsteady, or non-uniform flow), the complexity increases so that the velocity vector must also be considered laterally and vertically (two- and three-dimensional flow) (Rhoads, 2020). However, the steady non-uniform flow can be divided into

Steady Gradually Varied Flow with slight changes in area and velocity along the channel.
$\frac{\partial Q}{\partial t} = 0, \frac{\partial A}{\partial x} \approx 0, \frac{\partial v}{\partial x} \approx 0$

Steady Rapidly Varied Flow with rapid changes in area and velocity along the channel.
$\frac{\partial Q}{\partial t} = 0, \frac{\partial A}{\partial x} \neq 0, \frac{\partial v}{\partial x} \neq 0$

so that one-dimensional flow laws designed for steady uniform flow can be applied to steady gradually varied flow as the expected errors from this approximation are “small compared with those ordinarily incurred in the use of a uniform-flow formula and in the selection of the roughness coefficient” (Chow, 1959).

All natural rivers are unsteady and non-uniform to some degree. Their discharge varies over time depending on precipitation and melting with different frequencies and amplitudes depending, among others, on morphology, catchment area, land use, soil, or climate (Rhoads, 2020; Cerbelaud et al., 2024). The channel form can be highly variable, e.g., depending on sediment size, river bed material, or mean annual discharge. However, when the studied site is carefully selected so that the channel geometry on a reach scale does not change significantly, gradually varied flow can be approximated. Especially reaches upstream of abrupt changes of bed slope or channel geometry, waterfalls, rapids, confluences, or lakes can

be influenced by significant backwater effects that require more sophisticated flow models (Bauer-Gottwein et al., 2024; J. Liu et al., 2023) but can be avoided judging from satellite imagery and the river topology. Furthermore, with instantaneous observations of a long-term unsteady flow, it can be approximated to be quasi-steady (Battjes & Labeur, 2017).

In this thesis, daily discharge is calculated on a reach scale of ∼10 km based on instantaneous observations from satellite imagery of maximum 3 m resolution and satellite altimetry with decimeter uncertainties (see Chapter 3). These scales and uncertainties must be considered when deciding whether the approximation of steady uniform flow is suitable for the studied river sections. The expected error by applying a one-dimensional flow law to a section that is more complex on a smaller scale might still be low compared to the uncertainties propagated from the satellite observations.

2.2 Gauckler-Manning-Strickler Formula and Hydraulic Parameters

Various empirical equations have been developed to approximate the open-channel uniform flow velocity. Robert Manning calculated the flow velocity using seven established equations (by Du Buat, Eytelwein, Weisbach, St. Venant, Neville, Darcy and Bazin, and Ganguillet and Kutter) for different conditions and developed an empirical formula best fitting the mean results (Fischenich, 2000; Manning, 1891; Chow, 1959; Chaudhry, 2022):

$$v = k \cdot R^{\frac{2}{3}} \cdot I^{\frac{1}{2}} \quad \text{with} \quad R = A/P \tag{2.3}$$

where k [m$^{1/3}$/s] is the Strickler roughness coefficient, R [m] is the hydraulic radius calculated from the cross-sectional area A [m^2] and wetted perimeter P [m], and I [m/m] is the energy slope. The velocity vector of this formula is one-dimensional, so it requires the approximation of steady uniform flow as introduced in Section 2.1.2. The formula is also influenced by Gauckler (1868) and Strickler (1923), but for simplicity, it is called the Manning equation in this thesis. Applying the vertical segmentation of Equation 2.2, the Manning equation can be written as follows to account for the velocity profile across the river:

$$\bar{v_i}(t,x) = k_i(t,x) \cdot R_i(t,x)^{\frac{2}{3}} \cdot I(t,x)^{\frac{1}{2}} \quad \text{with} \quad R_i(t,x) = A_i(t,x)/P_i(t,x) \tag{2.4}$$

Figure 2.1 shows a schematic cross-section with the parameters required for applying the Manning equation per vertical segment. The following sections introduce the hydraulic parameters of the Manning equation in terms of their potential for observation using satellite-based sensors. The methods to derive the parameters from these sensors are discussed in more detail in Chapter 3 and the four publications.

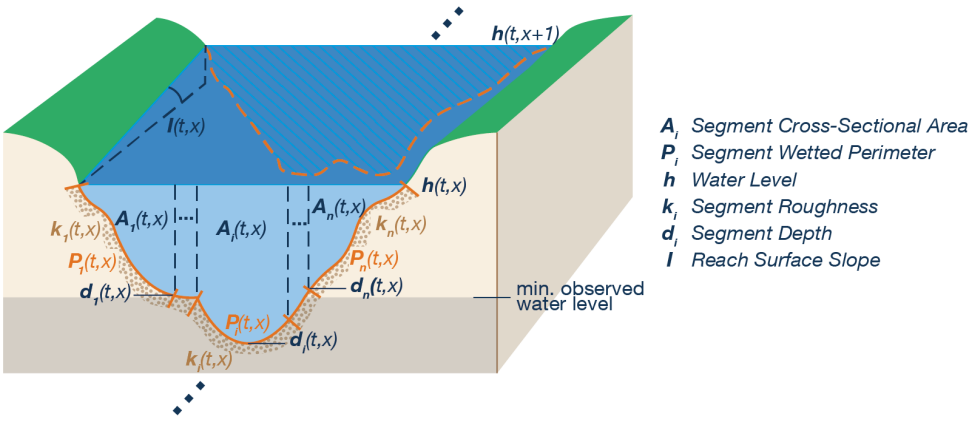

Figure 2.1 Schematic cross-sections with hydraulic parameters required for the Manning equation per vertical segment. The width of the segments is exaggerated in relation to the depth.

2.2.1 Slope

Equation 2.3 is valid for uniform flow where the energy slope I is parallel to the bed slope and WSS (Chow, 1959). In non-uniform flow, I can significantly deviate from the bed slope and WSS depending on, e.g., the flow regime or variations in the cross-sectional area. However, in rivers with gentle slopes and gradually varied flow, I can be approximated by WSS (Chow, 1959). WSS can either be obtained from radar (**P1**) or lidar (**P2**) altimetry (see Section 3.2). The spatial coverage of WSS derived from lidar altimetry is significantly higher compared to radar altimetry and is used to map reach-scale WSS globally in **P3**, addressing **O2** to improve the transferability. However, neither sensor can be used to globally observe the reach-scale temporal variability or the spatial variability of WSS within a reach, which can vary significantly, especially in backwater-affected reaches (Bauer-Gottwein et al., 2024). This is only possible with the novel wide-swath altimetry sensors such as SWOT, which combine high temporal resolution with large spatial coverage but have only been available since 2023. Therefore, the WSS is assumed to be constant in **P1** and **P4**. A closed-loop test in **P1** shows that using a time-variable slope yields the least significant error improvements among the hydraulic parameters in large alluvial rivers and that a high spatial resolution is more important. Nevertheless, the reach-scale WSS extremes can be estimated using lidar altimetry and are used in **P4** as uncertainty criteria to fulfill **O3**.

2.2.2 Roughness

The Strickler roughness coefficient k_{St} (for simplicity called k in this thesis) is the inverse of Manning's n parameter (Chaudhry, 2022) and is commonly used for SI units. The roughness coefficient is not physically based but comprises any resistance to the flow and is originally derived by Strickler (1923) through empirical studies. Within natural rivers, k typically ranges from 10 (high friction) to 50 (low friction) (Lecher et al., 2021). It cannot be measured but must be determined via flow-law inversion or estimated from literature values. Furthermore, k is not dimensionless and, therefore, depends on R and the flow depth (LUBW, 2002). In contrast, the dimensionless friction factor λ is used in the physically based Darcy-Weisbach equation (Julien, 2018; LUBW, 2002):

$$v = \frac{1}{\sqrt{\lambda}} \cdot \sqrt{8g} \cdot \sqrt{R \cdot I} \tag{2.5}$$

where g is the gravity of Earth [m/s^2]. Following Colebrook and White (1937), λ can be derived as a function of R, the Reynolds number (see Section 2.1.1), and the equivalent sand-grain roughness k_s [m] defined by Nikuradse (1932). However, in natural rivers without in-situ measurements, k_s can also only be estimated from empirical factors, and the calculation of λ requires a high computational effort (LUBW, 2002). Furthermore, in turbulent flow (high Reynolds number), λ can be approximated (DVWK, 1990) with

$$\frac{1}{\sqrt{\lambda}} = 2.33 \cdot (k_s/4R)^{-\frac{1}{6}} \tag{2.6}$$

which can be inserted into Equation 2.5 to get

$$\begin{aligned} v &= 2.33 \cdot (k_s/4R)^{-\frac{1}{6}} \cdot \sqrt{8g} \cdot \sqrt{R \cdot I} \\ &= 2.33 \cdot 4^{\frac{1}{6}} \cdot \sqrt{8g} \cdot k_s^{-\frac{1}{6}} \cdot R^{\frac{1}{6}} \cdot R^{\frac{1}{2}} \cdot I^{\frac{1}{2}} \end{aligned} \tag{2.7}$$

and after rearrangements (LUBW, 2002) results in the form of Equation 2.3 (Manning):

$$v = k \cdot R^{\frac{2}{3}} \cdot I^{\frac{1}{2}} \quad \text{with} \quad k = 5.87 \cdot \sqrt{2g} \cdot k_s^{-\frac{1}{6}} \tag{2.8}$$

where k is the Strickler roughness coefficient [m$^{1/3}$/s]. Therefore, when there is turbulent flow (as assumed in all cases studied in this thesis) and Equation 2.6 is valid, k can be approximated to be independent of R and related to the physical parameters k_s and g. Nevertheless, neither k nor k_s can be observed from satellite sensors.

However, the roughness coefficient can be estimated using adjustment factors such as the river bed material and grain size n_b (which poses similar challenges as estimating k_s), surface irregularities n_1, variations in channel shape and size n_2, obstruction n_3, the amount of submerged vegetation n_4, and the amount of meandering m (Chow, 1959). Arcement and Schneider (1989) provide a guide to select suitable factors so that the roughness coefficient can be calculated as follows:

$$k = \frac{1}{(n_b + n_1 + n_2 + n_3 + n_4)m} \tag{2.9}$$

This equation is used in **P1** to estimate k. Although the factors can be approximated from planform features visible in satellite imagery, such as the meandering pattern, sandbars, or type of meander cutoff (Rosgen, 1996; Schumm, 1977), the choice is highly subjective and prone to errors as the guide still leaves a wide range of possible values and the factors are not quantitative (Ye et al., 2018). Even in-situ, Chow (1959) describes the process of selecting a roughness value as "a matter of intangibles" and "it can be no more than a guess, and different individuals will obtain different results." The closed-loop test in **P1** confirmed that the roughness coefficient causes the most significant errors in discharge.

Addressing **O2**, an optimization approach is applied in **P4** to overcome the caveats of using Equation 2.9 and objectively estimate the roughness coefficient based on the principle of mass-conservation (see Section 2.3). Additionally, the roughness coefficient is varied depending on the river sinuosity s (which is similar to m in Equation 2.9) and the flow depth:

$$k_i(t,x) = \frac{k_B(x)}{d \cdot s(x)} \quad \text{with} \quad d = \begin{cases} (d_i(t,x)/d_0)^{-\epsilon} & \text{if } d_i(t,x) > d_0 \\ 1, & \text{otherwise} \end{cases} \tag{2.10}$$

where k_B is the optimized base roughness coefficient, $d_i(t)$ is the section's flow depth, d_0 is the minimum depth below which the roughness is assumed to be constant, and ϵ is a drag coefficient. This approach follows a method proposed by Jain et al. (2004), and the concept of a depth-dependent roughness coefficient within the context of satellite data has been successfully demonstrated by Bjerklie et al. (2018). Using Equation 2.10, the roughness not only varies over time but also across the vertical segments i. Strong roughness differences between adjacent segments can cause shear stress, which requires additional roughness consideration at the boundaries of the segments (LUBW, 2002). However, these are not implemented because of the expected measurement uncertainties and applied approximations (cf. Section 2.1.2).

2.2.3 Geometry

The shape of the cross-sectional geometry is required to derive the segment's cross-sectional area A_i and wetted perimeter P_i to get R_i in Equation 2.4. Additionally, it is required to get the depth of the segment d_i as part of the depth-dependent roughness estimation in Equation 2.10. The cross-section can be divided horizontally into two parts, above (observed) and below (unobserved) the minimum measured WSE as shown in Figure 2.1. In ephemeral rivers, the entire cross-section can be observed, while in large downstream main stems, the observable variations cover only a fraction of the entire cross-sectional geometry. A river bathymetry map showing the observable part of the geometry is constructed by combining WSE measurements from satellite altimetry with the WSA from satellite imagery. The observed cross-sectional geometry is sampled from the bathymetry map along the normal of the river centerline at the location of measurement x. An empirical width-to-depth relationship by Moody and Troutman (2002) is used to estimate the riverbed elevation. The unobserved part of the geometry is constructed by a parabola to the estimated riverbed elevation. This method is described in detail in Section 3.4. The approach was validated in **P1** and works best in straight and relatively wide river sections because the river erosion in curved or narrowing sections cannot be modeled. As the empirical width-to-depth relationship is only valid in meandering rivers, the approach cannot be applied to braided rivers. Based on the assumption of gradually varied flow, the river bed elevations of the cross-sections are further optimized in **P4** (see Section 3.4.1), to improve the estimation (**O2**) and address **O3** by quantifying the depth uncertainty.

2.3 Mass-Conservation

Instead of limiting the discharge estimation to a single cross-section, estimates from multiple locations can be integrated based on the principle of mass conservation to improve the hydraulic parameters and derive their uncertainties. In this thesis, the discharge of rivers wider than ∼50 m is estimated over ∼10 km long reaches within which the flow is assumed uniform (i.e., without significant tributaries or withdrawal) and steady (i.e., no changes in flow rate during the time of measurement) as discussed in Section 2.1. With the assumption of steady uniform flow, the discharge is continuous, i.e., constant along the reach as defined by Chow (1959):

$$Q(t) = v(t, x_1) \cdot A(t, x_1) = v(t, x_2) \cdot A(t, x_2) = \dots \tag{2.11}$$

which can be expressed using Equations 2.2, 2.4, and 2.10 as:

$$\begin{aligned} Q(t) &= \sum_{i=1}^{n} \frac{k_B(x_1)}{d \cdot s(x_1)} \cdot R_i(t, x_1)^{\frac{2}{3}} \cdot I(t, x_1)^{\frac{1}{2}} \cdot A_i(t, x_1) \\ &= \sum_{i=1}^{n} \frac{k_B(x_2)}{d \cdot s(x_2)} \cdot R_i(t, x_2)^{\frac{2}{3}} \cdot I(t, x_2)^{\frac{1}{2}} \cdot A_i(t, x_2) \\ &= \dots \\ \text{with } d &= \begin{cases} \left(\frac{d_i(t,x)}{d_0}\right)^{-\epsilon}, & \text{if } d_i(t, x) > d_0, \\ 1, & \text{otherwise.} \end{cases} \end{aligned} \tag{2.12}$$

The parameters d_i, s, R_i, I, and A_i can be observed using space-based sensors, although there are specific limitations for each parameter, as discussed in Section 2.2 and Chapter 3. According to the law of mass conservation in steady uniform flow, the values of the unknown parameters $k_B(x)$, ϵ, and d_0 must yield zero differences between the results at any location of measurement x. Due to the uncertainty in the observed parameters, the approximation of steady uniform flow, and Manning's simplified one-dimensional flow equation, the exact state of zero differences cannot be attained, but the differences must be minimal. In **P4**, this constraint is expressed as the following objective function:

$$\min_{\dot{\mathbf{k}}} \frac{max(k_B)}{min(k_B)} \sum_{a=1}^{m} \sum_{b=1, a \neq b}^{m} \left(\frac{1}{\bar{Q}(a)} \sqrt{\frac{1}{l} \sum_{t=1}^{l} (Q(t, a) - Q(t, b))^2} \right)^2 \tag{2.13}$$

where m is the number of cross-sections, l is the number of time steps in the WSE time series, and $\dot{\mathbf{k}}$ is the vector of unknowns $[k_B(a), \dots, k_B(m), d_0, \epsilon]$. The objective function is basically the *Normalized Root Mean Square Error* (NRMSE) sum between all cross-sections factored by the ratio between the maximum and minimum k_B as regularization to prevent unexpected high variations under the assumption of gradually varied flow. Still, there is the possibility of multiple solutions because the objective function has a high degree of freedom with multiple local minima, and the problem remains ill-posed. However, the expert user can usually identify the most likely solution and accordingly adjust the boundary values of the unknowns as discussed in **P4**. In this way, this approach for estimating the roughness coefficient is much more robust and objective than using literature decision guides.

As introduced in Section 2.1.2, the application of a one-dimensional flow law such as the Manning equation requires gradually varied flow, i.e., minimal differences in A, across the consecutive locations of measurements x. Therefore, before optimizing the roughness based on the principle of mass conservation with Equation 2.13, the unknown river bed elevations are first optimized in **P4** by reducing the differences of A at mean flow across the locations x to ensure the condition of gradually varied flow, as further described in Sections 3.4.1 and 3.4.2.

2.3.1 Optimization Algorithm

The central element of **P4** is the optimization of unknown parameters by minimizing the result of an objective function such as Equation 2.13 to obtain the optimal roughness coefficient or the optimal riverbed elevation (Equation 3.7). For this optimization, a parallel version (Gerber & Furrer, 2019; Gerber et al., 2023) of the *Limited-Memory BFGS Algorithm with Box Constraints* (L-BFGS-B, Byrd et al., 1996; D. C. Liu and Nocedal, 1989; C. Zhu et al., 1997) is used. The *Broyden–Fletcher–Goldfarb–Shanno Algorithm* (BFGS, Broyden, 1970; Fletcher, 1970; Goldfarb, 1970; Shanno, 1970) is a quasi-Newton method that, like Newton's method, considers gradient changes (curvature) of the objective function to find its minimum. By incorporating curvature information, Newton's method can utilize larger step sizes during each iteration compared to methods that consider only the gradient, which leads to faster convergence, particularly in ill-conditioned problems (Papageorgiou et al., 2012).

Newton's method requires the exact Hessian matrix, which is the second derivative of the multivariate objective function and thus represents its curvature. An analytical calculation of the exact Hessian matrix is not feasible for complex objective functions with sub-routines, and a numerical determination is computationally expensive because it requires matrix inversion (Papageorgiou et al., 2012). In contrast, quasi-Newton methods like BFGS approximate the Hessian matrix without matrix inversion and are particularly suitable for solving large optimization problems (Nocedal & Wright, 2006). For each iteration, BFGS uses a line search to adaptively choose the optimal step size that satisfies the Wolfe conditions (significant decrease of the objective value and a reduced curvature) (Nocedal & Wright, 2006). Then, the algorithm calculates the local gradient and uses the difference between successive gradients to update the approximated Hessian.

While BFGS stores all Hessian approximations, L-BFGS (D. C. Liu & Nocedal, 1989) keeps only the most recent updates to reduce memory usage and ensure scalability for large problems (Nocedal & Wright, 2006). Additionally, L-BFGS-B (Byrd et al., 1996; C. Zhu et al., 1997) provides the possibility of defining boundary conditions. The implementation by Gerber et al. (2023) reduces the computation time by parallelizing the evaluations required to calculate the local gradient. The L-BFGS-B algorithm approximates the Hessian for optimization efficiency, but a more accurate Hessian is calculated using finite differences after convergence (Nocedal & Wright, 2006). The inverse of this more accurate Hessian can be considered the covariance matrix (Niwa & Fujii, 2020) so that high curvature represents low variance values. To fulfill **O3**, the standard deviations which quantify the uncertainty of the optimal parameters are obtained from the squared diagonal of the covariance matrix.

3 Satellite Observables and Derivables

In this thesis, different hydrogeodetic sensors onboard a wide range of satellites commissioned by the *European Space Agency* (ESA), *National Aeronautics and Space Administration* (NASA), and commercial operators are used. Figure 3.1 shows a timeline of these satellite missions colored by similar orbit attributes and grouped by sensor type. The sensors can be categorized into satellite altimetry comprising radar and lidar altimeters and satellite imagery from multi-spectral sensors. The radar altimetry is used to observe WSE (Sec. 3.1), which is the fundamental driver of the discharge algorithm presented in this thesis. The WSS of the rivers is derived from lidar altimetry (Sec. 3.2) as an input for the Manning equation and to correct the radar WSE time series. The multi-spectral sensors are used to observe the WSA (Sec. 3.3) of the studied river sections, which is combined with the WSE to derive the river bathymetry (Sec. 3.4). Figure 3.1 does not represent an exclusive list of remote sensing techniques and missions applicable to hydrogeodesy and instead includes only the missions mentioned in this study. Other important missions are, e.g., the *Gravity Recovery and Climate Experiment* (GRACE) for monitoring terrestrial water storage, the *Moderate Resolution Imaging Spectroradiometer* (MODIS) for observing large-scale inundation or snow cover with high temporal resolution, or the *Shuttle Radar Topography Mission* (SRTM) used to derive vector representations of river networks.

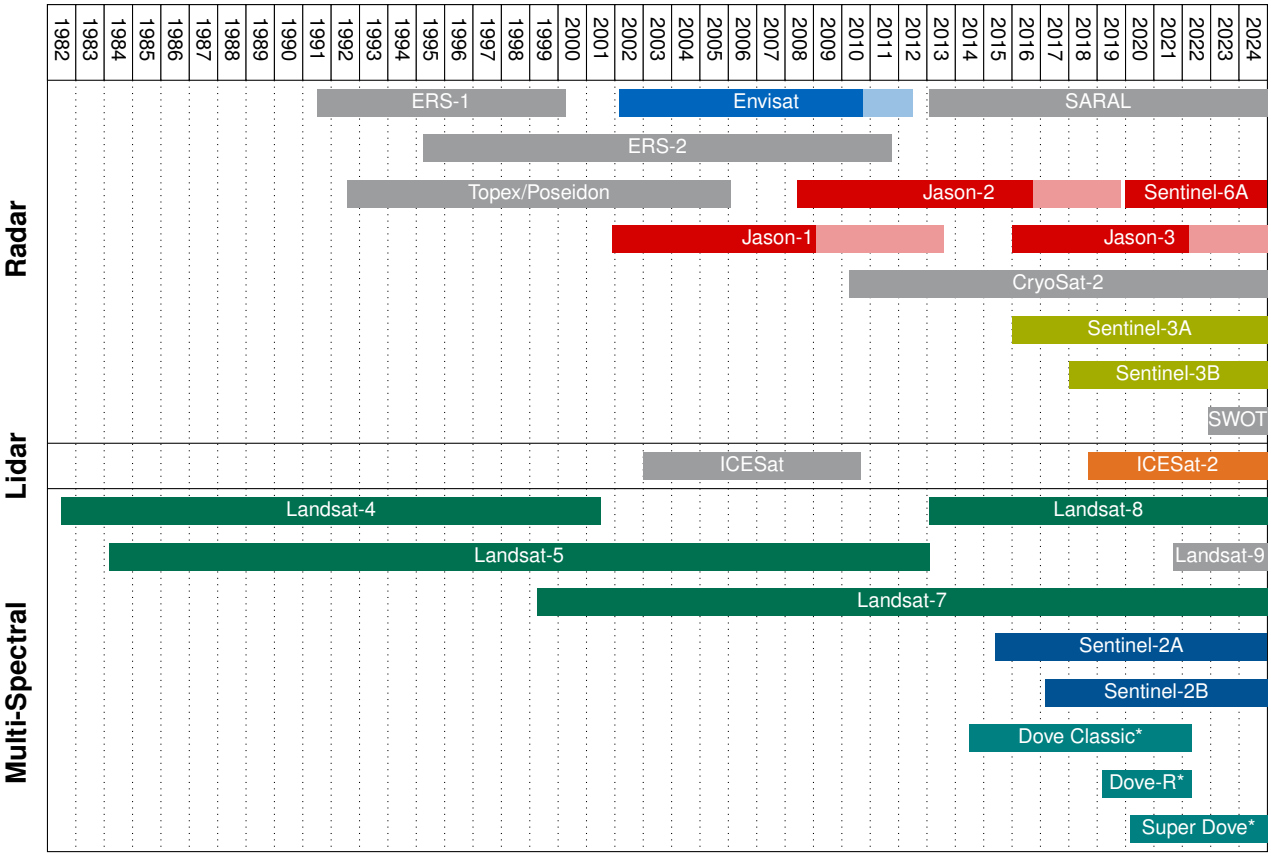

Figure 3.1 Timeline of satellite missions and constellations (*) grouped by sensor types and colored by similar orbit attributes. Gray missions are not used in this thesis. Light colors show extended phases on different orbits.

3.1 Water Surface Elevation

The WSE is observed by satellite altimetry, which utilizes active space-based geodetic sensors to measure the range between the spacecraft and Earth surface based on the signal propagation time from pulse emission to the reception of a reflection. The technique was initially developed in the 1970s with a focus on monitoring ocean dynamics and deriving information on Earth's gravity field, but the first observations contained considerable uncertainties due to large errors in the *Precise Orbit Determination* (POD) (Stammer & Cazenave, 2017). With improvements to the POD such as new reflectors for *Satellite Laser Ranging* (SLR) and *Doppler Orbitography and Radiopositioning Integrated by Satellite* (DORIS), the data quality of the Topex/Poseidon and *European Remote Sensing* (ERS-1) missions launched in the 1990s was sufficient to monitor large inland water bodies (Schwatke et al., 2015; Stammer & Cazenave, 2017). Advancing innovations in radar altimetry (see Section 3.1.1) and new techniques like lidar or wide-swath altimeters increase the capability of retrieving the WSE of inland waters such as rivers and the WSE time series can span over more than two decades by now. **P1** and **P4** use WSE time series from DAHITI as a primary input to obtain the river geometry and estimate river discharge. In DAHITI, repeated radar altimeter measurements at the intersection of the satellite's ground track and an inland water body are binned into a so-called *Virtual Station* (VS).

3.1.1 Radar Altimeters

Radar altimeters emit a radar signal and measure the range R between the satellite and Earth surface through waveform retracking of the received reflection (see Section 3.1.3) to calculate the surface height h (or WSE) (Rosmorduc et al., 2016):

$$h = H - (R + \Delta R) \tag{3.1}$$

where H is the POD-derived orbit height of the satellite above a reference ellipsoid and ΔR is the sum of corrections, which are described in Section 3.1.4. The two most common types of altimeters are the pulse-limited *Low Resolution Mode* (LRM) and the Delay-Doppler SAR sensors, which differ primarily in their signal footprint shape and size as shown in Figure 3.2. LRM altimeters have a large radial footprint with a diameter of up to 30 km (Cretaux et al., 2017), while SAR sensors can differentiate the received signal into strip-shaped footprints of a few hundred meters in the along-track direction using the Delay-Doppler technique (Rosmorduc et al., 2016).

Pulse-limited LRM altimeters are operated by the Jason-1/2/3 and Envisat missions. They transmit radar pulses for a duration of 105.6 µs (20 µs for Envisat) on a primary Ku-band frequency of 13.575 GHz at a repetition rate of 1.80 to 2.06 kHz depending on the mission. Between the transmitted pulses, the previous backscattered signal from the surface is received. Multiple received returns are accumulated onboard the satellite for an improved *Signal-to-Noise Ratio* (SNR) so that the resulting temporal resolution of the downlinked signals is approximately 20 Hz (eoPortal, 2024; Escudier et al., 2017).

SAR altimeters exploit the Doppler frequency change caused by the speed of the satellite (Escudier et al., 2017). Analogous to LRM altimeters, the SAR altimeters onboard the Sentinel-3A/B constellation use the primary Ku-band frequency of 13.575 GHz. However, the signal is emitted in bursts of 64 pulses with a significantly higher pulse repetition rate of 17.8 kHz compared to LRM altimeters. These bursts are required to ensure a constant phase of the transmitted pulses, which is critical to detecting the frequency changes in the unfocused Delay-Doppler SAR processing. Thereby, the footprint size is reduced to 330 m in the along-track direction, improving the SNR (Cretaux et al., 2017; ESA, 2023) and facilitating WSE and discharge measurements of small rivers in **P4**. Sentinel-6A is the follow-on of the Jason-3 mission and is supposed to continue the measurements in coherence. The satellite carries an LRM with similar characteristics as the Jason-1/2/3 missions and an additional SAR altimeter (Donlon et al., 2021).

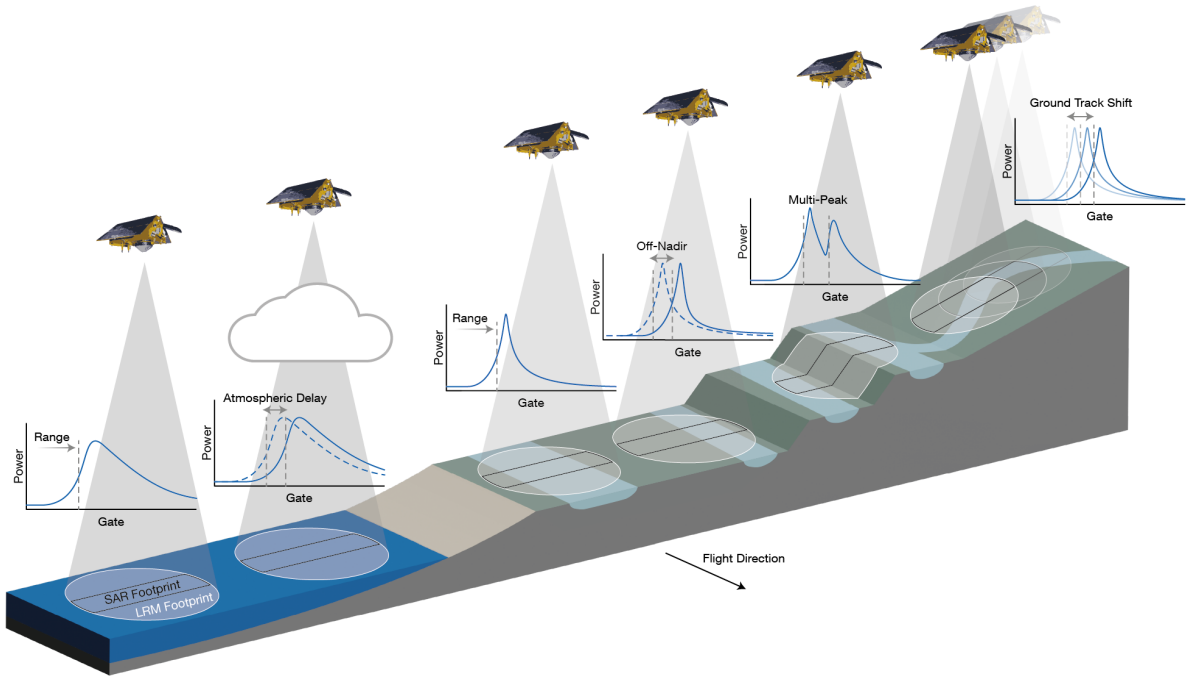

Figure 3.2 Received radar waveforms affected by different conditions requiring corrections.

3.1.2 Limitations by Orbit Configuration

Besides the sensor capabilities, the most significant factor limiting global inland water monitoring with satellite altimetry is the orbit configuration of the spacecraft and the resulting measurement geometry (Alsdorf et al., 2007). Classical altimeters measure only in the nadir direction and miss any water body that does not intersect the ground track of the satellite. The spatial pattern of the ground tracks is governed by the mission's repeat cycle, which ranges from 10 days (Jason-1/2/3) to 35 days (Envisat) and also limits the temporal resolution of the WSE time series. Shorter repetitions would be beneficial because any extreme flood or drought events in between the cycles cannot be captured (Cerbelaud et al., 2025), but the spatial coverage decreases. Long repeat cycles are required for a dense ground track pattern, but these missions cannot be used to obtain meaningful WSE time series. This limitation is quantified in **AP2** (Dettmering et al., 2020) with a case study for the Mississippi River basin. Four different satellite altimetry configurations are studied: Jason only (same as Topex/Poseidon and Sentinel-6), Sentinel-3 (A and B), the past configuration (Jason and Envisat), and the current configuration (Jason, Sentinel-3, CryoSat-2, and SARAL). The current configuration misses 67% of the lakes and reservoirs larger 1 km^2. The probability of rivers being intersected by nadir altimeters is higher because of their oblong geometry. Alsdorf et al. (2007) demonstrate that 19 to 44% of rivers are missed depending on the repeat cycle. However, the likelihood that a specific location of interest is missed or that the intersection situation is not suitable for monitoring the WSE is still very high. New wide-swath altimeters such as SWOT will be capable of filling this gap of observations.

3.1.3 Waveform Tracking and Retracking

The waveforms of the radar echoes describe the received power as a function of time binned into reception gates. The typical gate size of 3.125 ns is equivalent to a range of 0.47 m (ESA, 2023; Gommenginger et al., 2011). The onboard tracker adjusts the reception window of the altimeter to ensure the correct capture of the backscattered signal, and retracking algorithms are applied to the waveform to retrieve the range R. Echoes of the open ocean have a standard waveform with a sharp rise called the leading edge followed by a gentle decline called the trailing edge (Figure 3.2). The leading edge slope is influenced by the significant

wave height, and the amplitude of the leading edge depends on the sea surface roughness due to the wind speed. During retracking, this physically derived model can be fitted to the ocean waveforms, and the range to the water surface is represented by the gate of the half-power point of the leading edge (Brown, 1977). However, over heterogeneous surfaces such as coastal or continental areas, the waveforms do not follow this standard shape but are specular and contaminated by noise and secondary peaks in power from nearby off-nadir targets as shown in Figure 3.2. This is most notable with the large footprint diameter of LRM altimeters and can lead to significant errors in the onboard processing of the tracker unit and the range retracking (Cretaux et al., 2017). The tracker of Jason-1 expected an ocean-like waveform and frequently failed over continental areas. The Envisat tracker was more robust but could fail due to steep topography or significant noise. Jason-2/3, Sentinel-3A/B, and Sentinel-6A all use an a-priori *Digital Elevation Model* (DEM) in combination with the real-time DORIS measurements to determine the reception window ensuring good tracking in complex areas but causing data gaps due to incorrect DEM data (Cretaux et al., 2017).

Special retracking algorithms such as the *Offset Center of Gravity* (OCOG, Wingham et al., 1986) must be applied to non-standard (continental) waveforms to find the leading edge for retrieving the range. The empirical OCOG retracker determines the gate representing the center of gravity of the waveform and subtracts the half-width of the waveform from this gate to calculate the leading edge position. The data used in this thesis is processed using the improved threshold retracker (Jinyum et al., 2006; Schwatke et al., 2015). This retracker distinguishes between multiple sub-waveforms reflected from different features within the footprint. Despite the advances in retracking algorithms, the range precision remains at decimeters for LRM missions and centimeters for SAR sensors in small inland waters (Nielsen et al., 2017).

3.1.4 Range Corrections

Once the range is obtained by the retracking of the received signal waveform, it has to be corrected for instrument biases, atmospheric delays, and geophysical effects. Table 3.1 lists the corrections and their typical impact on the range measurements of radar altimeters as described by Rosmorduc et al. (2016). Instrument biases are typically the least significant compared to the retracking precision over inland waters. Larger corrections of up to 2.3 m magnitude must be applied for atmospheric delays caused by particle interaction within the ionosphere and troposphere. The LRM and SAR altimeters use a secondary C-band frequency of 3.2 to 5.41 GHz to derive the electron content for direct ionosphere correction (eoPortal, 2024). However, the dual-frequency ionosphere correction is unreliable for inland applications due to possible land contamination (Dettmering & Schwatke, 2022). Therefore, all corrections for atmospheric delays must be derived from models for inland altimetry. Table 3.1 does not list ocean tides and tidal loading because they do not affect the reaches studied in this thesis. Still, the corrections for other geophysical effects, such as solid Earth tides and pole tides, must be applied.

These corrections and the range measurements are obtained in the *Multi-Version Altimetry* (MVA) format from the *Open Altimeter Database* (OpenADB, Schwatke et al., 2023). MVA contains not only the mission-specific standard corrections but also alternative corrections, e.g., from different troposphere models. Furthermore, MVA provides corrections for systematic orbit errors estimated with the *Multi-Mission Crossover Analysis* (MMXO) by Bosch et al. (2014). By harmonizing the applied corrections for all missions and utilizing the MMXO correction, data from different satellite altimetry missions can be easily combined without residual biases.

Besides the standard corrections, which are also used for ocean applications, the most significant errors in inland altimetry with a magnitude of multiple meters are caused by the position of the satellite above the target, the target's properties, or multiple targets within the footprint that can also affect the SAR stripes (depending on the intersection angle) as shown in Figure 3.2. Boergens et al. (2016) studied corrections for the off-nadir (or hooking) effect. When using Equation 3.1, the water body is assumed to be nadir below the satellite, but the sensor can also receive signal reflections from off-nadir water bodies within the radar footprint, which results in an erroneous range. This hooking effect can be corrected by fitting a parabola

Table 3.1 Corrections for instrument biases, atmospheric delays, geophysical effects, and target properties applied to satellite altimetry range measurements as described by Rosmorduc et al. (2016), Boergens et al. (2016), and **P2**.

Correction	Description	Magnitude [m]
Instrument Biases		
Ultra-Stable Oscillator	Clock drift	0.01
Centre of Gravity	Variations due to fuel consumption	0.01
Waveform Filters	Blocking certain frequencies in the signal	<0.10
Signal Delays by the Atmosphere		
Ionosphere	Electron content	0.5
Wet Troposphere	Water vapour and liquid water	0.5
Dry Troposphere	Atmospheric gases	2.3
Vertical Surface Variations by Geophysical Effects		
Solid Earth Tides	Deformations of the solid Earth by the attraction of the Sun and Moon	0.5
Pole Tides	Solid Earth deformation caused by motion of the rotational axis	0.02
Target Properties		
Hooking Effect	Off-nadir measurements	up to 3
River Slope	Ground track shift across sloping river	up to 3

to the off-nadir measurements to maximize the data coverage and precision over narrow rivers or without direct nadir measurements (Boergens et al., 2016). In the DAHITI approach (Schwatke et al., 2015), the hooking effect is mitigated by careful selection of the VS and discarding the off-nadir measurements through extended outlier rejection. Although the altimeter satellites nominally stay on the same orbit and are therefore assumed to intersect a river at the exact location each cycle, the satellite's ground track actually shifts by kilometers during the mission lifetime, as shown in Figure 3.3. Depending on the WSS of the river, this shift causes a significant error of up to several meters in the WSE time series (Halicki et al., 2023). This is much more significant than the order of magnitude of most of the common corrections applied to satellite altimetry (cf. Table 3.1). **P2** demonstrates that an improvement in the *Root Mean Square Error* (RMSE) by up to 30 cm or 66% can be achieved by the WSS correction. With the global WSS dataset published in **P3**, this correction can be applied to the majority of DAHITI stations and is also used in **P4**.

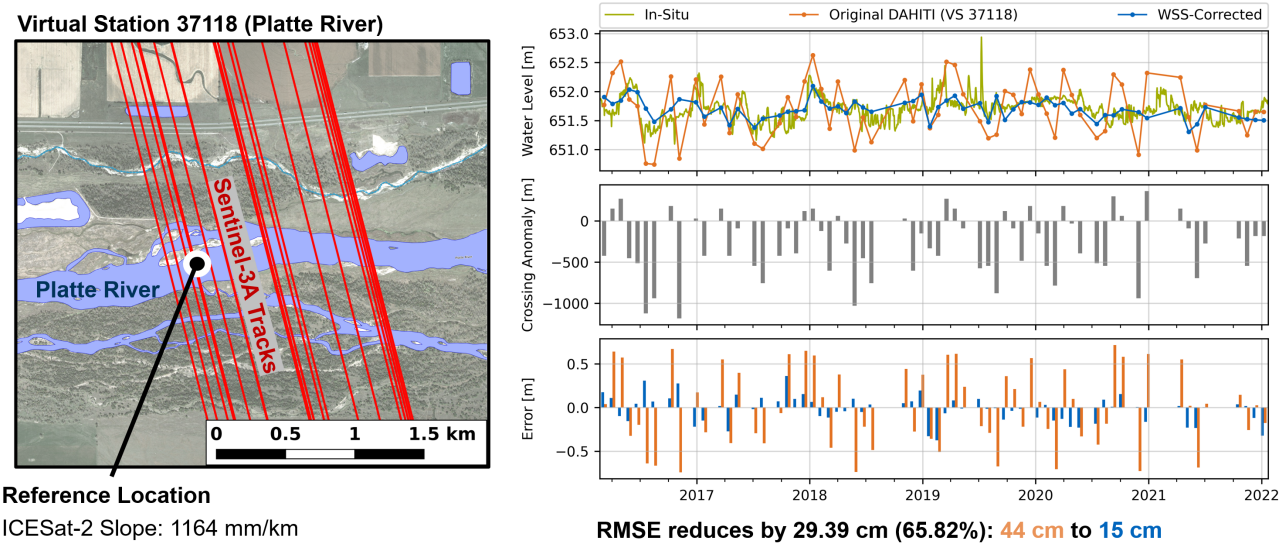

Figure 3.3 Slope correction at the Platte River for the DAHITI virtual station 37118. Left: Ground track shift of Sentinel-3A at the virtual station. Right: WSE time series without (orange) and with (blue) the WSS correction applied compared to the in-situ time series (green).

3.2 Water Surface Slope

A time-variable WSS profile can be derived from radar altimetry using WSE differences between consecutive VSs of the same satellite pass (i.e., with data from the same day) (Bjerklie et al., 2018; Garambois et al., 2017). However, this approach is limited by the orbit geometry to a small number of sites. Similar spatial constraints apply to estimating WSE profiles from fully focused SAR observations (Ehlers et al., 2025), which can monitor time-variability but require extensive processing. A higher spatial coverage and, in some cases, the time variability of WSS within an entire river system can be modeled using cubic spline (Nielsen et al., 2022; Zakharova et al., 2020) or B-spline (Boergens et al., 2021) functions. Despite their advantages, these methods face challenges due to uneven or limited data availability. A commonly used and more robust but coarse approach is deriving the average WSS from the average WSE at the VSs (Halicki et al., 2023; Tarpanelli et al., 2013; Tourian et al., 2016). However, the average WSE can be biased because of the different temporal sampling of the VSs.

A linear model is applied in **P1** using a least-squares approach to obtain the adjusted elevations of the VSs within the Lower Mississippi River and derive the WSS. The time differences are considered in the weighting of the data, resulting in a higher accuracy of the average WSS with less bias. **AP3** further includes Laplace and a-priori gradient conditions and data from long-repeat orbit missions such as Cryosat-2 to increase the spatial resolution and estimate the average WSS for several Polish rivers. Although the linear models used in **P1** and **AP3** generally align with the average in-situ gradient, they cannot capture the temporal WSS variations. Therefore, **P2** introduces an innovative approach to obtain instantaneous WSS measurements from lidar altimeters, addressing **O2** by highly accurate and spatial dense observations and **O3** by quantifying the temporal WSS variability.

3.2.1 Lidar Altimeters

The *Geoscience Laser Altimeter System* (GLAS) carried by the NASA *Ice, Cloud, and Land Elevation Satellite* (ICESat), which launched in 2003, was the first-ever operational lidar sensor in space (Remy et al., 2017). The primary objective of ICESat was to measure the elevation of the polar ice sheet and derive the ice mass changes to assess their impact on global sea level (Schenk & Csathó, 2012). GLAS consisted of three alternately operating infrared analog pulse lasers with a wavelength of 1064 nm and an energy of 70 mJ. The analog pulse laser accumulates the power of the received backscattered photons over time in a waveform comparable to pulse limited LRM altimetry, retrieving the WSE with Equation 3.1. Unlike radar altimetry, which operates with much longer wavelengths, lidar cannot penetrate clouds, but the backscattered signal can be associated with a significantly smaller footprint of about 70 m for GLAS. The first laser of GLAS failed after 37 days, and the second laser experienced rapid energy decay, so operations switched from continuous to periodical observations (Abdalati et al., 2010). Due to the long repeat cycle and the intermittent observation phases, ICESat is of little use for hydrogeodesy (Magruder et al., 2024). Nevertheless, GLAS proved to measure the WSE of inland waters accurately with an RMSE of 0.03 to 0.25 m and has the major advantage of its small footprint being unaffected by surrounding topography in contrast to radar altimetry (Urban et al., 2008).

ICESat-2, the follow-on mission of ICESat, was launched in 2018 into a polar 92° orbit and carries the photon-counting *Advanced Topographic Laser Altimeter System* (ATLAS). In contrast to the GLAS waveform detectors, the photon-counting detector can measure the time of flight of the individual photons and works with pulses of less energy (Degnan, 2002). ATLAS uses a wavelength of 532 nm and can determine the geolocation of each backscattered photon within a footprint of 17 m. Compared to GLAS the along-track ground sampling distance is improved from 150 m to 0.7 m. Furthermore, the coverage of ICESat-2 observations is increased by splitting the laser pulse into six beams. These beams are arranged into three pairs separated by 3.3 km on the ground, each of which consists of a low energy (weak) beam of 45 µJ and a high energy (strong) beam of 175 µJ. Within a pair, the strong and weak beams are separated by 90 m (Markus et al., 2017; Neumann et al., 2019).

ICESat-2 science data are available at different product levels (ATL##) from basic telemetry data (ATL01) over geolocated data of each received photon (ATL03) to surface-specific products such as inland water height (ATL13) used in this thesis. ATL13 does not contain the WSE for each single photon but average values over short segments of 75 to 100 received photons (Jasinski et al., 2023). Additionally, the ATL13 data is already filtered for photons received from potential inland waters based on water extent datasets such as HydroLakes (Messager et al., 2016) or *Global River Widths from Landsat* (GRWL, Allen and Pavelsky, 2018). These ancillary datasets are not time-variable, so the ATL13 product can contain non-water observations during low WSE, e.g., from river banks and bars.

Regardless of the product level, ICESat-2 data does not contain the required information (e.g., POD) for integration into the MVA structure, so the corrections cannot be harmonized with other satellite altimetry missions and the MMXO is not applicable. Therefore, the data cannot be used for multi-mission analysis. However, spaceborne lidar data are considered "ready-to-use" (Cretaux et al., 2017) and especially ICESat-2 data show high accuracy with an RMSE of $\sim$0.14 m for inland waters (Ryan et al., 2020; Xiang et al., 2021).

3.2.2 P2: Water Surface Slope from ICESat-2

The ATLAS sensor of ICESat-2 is used in **P2** to obtain WSS observations of rivers. Due to the high accuracy and precision of ATLAS, the intersection of a single beam with a river is sufficient to measure reach-scale WSS along the beam (along-track approach). Nevertheless, the preprocessed ATL13 data still contains outliers that are identified and rejected using a *Support Vector Regression* (SVR) and the *Absolute Deviation Around the Median* (ADM) within a moving window. The along-track WSS is fitted to the remaining WSE observations using linear regression and projected onto the river centerline vector to obtain the WSS along the river centerline. This along-track approach can only be applied when the intersection angle is small (a threshold of 65° is set in **P2**) because the confidence of fitting decreases as the intersection becomes more orthogonal. In such orthogonal cases, there is a high probability that multiple beams intersect the river reach, and the WSS is measured across-track using the difference in WSE and chainage between two intersections. The WSS measurements are binned at reach scale, referencing the SWORD reaches, which have been established as the community standard and facilitate data exchange and usage.

The validation in **P2** between 277 gauges shows an accuracy comparable to the science requirements of the SWOT mission (17 mm/km). Especially, the across-track approach is robust and accurate with an *Median Absolute Error* (MAE) of 24 mm/km. In contrast, the along-track slope requires additional angle-dependent outlier rejection based on the confidence of fit, and the remaining observations are still less accurate with an MAE of 57 mm/km. To maximize the spatial and temporal coverage, daily averages of both approaches are combined and show an MAE of 28 mm/km. However, the temporal resolution is still relatively low because of the long repeat orbit of ICESat-2 and occasional cloud cover. Therefore, ICESat-2 cannot be used to obtain meaningful WSS time series. Nevertheless, the time variability can be quantified by the standard deviation and extreme values of the daily reach-scale WSS, and this information grows with each additional mission cycle. This quantification of the time-variability is not possible with the approach of **P1** or other static datasets such as SRTM. Furthermore, **P2** demonstrates that the constant average ICESat-2 WSS can be used to correct the WSE measurements from radar altimetry and significantly improve the WSE time series (see Section 3.1.4). The MAE of the constant average combined WSS is 23 mm/km.

The methodology, results and validation, and WSE time series correction are described and discussed in detail in Appendix P2:

P2 Scherer, D., Schwatke, C., Dettmering, D., & Seitz, F. (2022). **ICESat-2 Based River Surface Slope and Its Impact on Water Level Time Series From Satellite Altimetry**. *Water Resources Research*, *58*, 1–25. https://doi.org/10.1029/2022WR032842

3.2.3 P3: Global River Slope Dataset

In **P3**, the approach developed in **P2** is applied at a global scale to all SWORD river reaches and published as the *ICESat-2 River Surface Slope* (IRIS) dataset. IRIS covers more than 70% of the global SWORD reaches because of the long-repeat orbit and the consequent dense ground track pattern of the satellite. However, most reaches are covered by less than six measurements within four years of observation because of the long-repeat orbit. Figure 3.4 shows the measurement principle with the six parallel beams and the resulting global IRIS dataset. The IRIS dataset and statistics (e.g., by river properties, cloud cover, and climate zones) are described and discussed in Appendix P3:

P3 Scherer, D., Schwatke, C., Dettmering, D., & Seitz, F. (2023). **ICESat-2 river surface slope (IRIS): A global reach-scale water surface slope dataset**. *Scientific Data*, *10*, 359. https://doi.org/10.1038/s41597-023-02215-x

Since the publication of **P3** and IRIS in 2023, it has been widely utilized within the hydrogeodesy community, and Christoffersen et al. (2023) developed a similar approach. DAHITI uses the IRIS data to correct WSE time series as demonstrated in **P2**. **AP3**, Dhote et al. (2024), Musaeus et al. (2024), and Normandin et al. (2024) use IRIS as a reference to compare their WSS results from multi-mission altimetry, SWOT, and ICESat-2. Rezende et al. (2023) use IRIS as a proxy for SWOT slopes to test a SWOT discharge algorithm, and it is also used to interpolate WSE from observations from VS to a nearby location (Rezende et al., 2025). Furthermore, Chen et al. (2024) use IRIS to update the water prediction flood inundation mapping system of the *National Oceanic and Atmospheric Administration* (NOAA). Using IRIS slopes improved the inundation accuracy by 16% over the previously used river slope data.

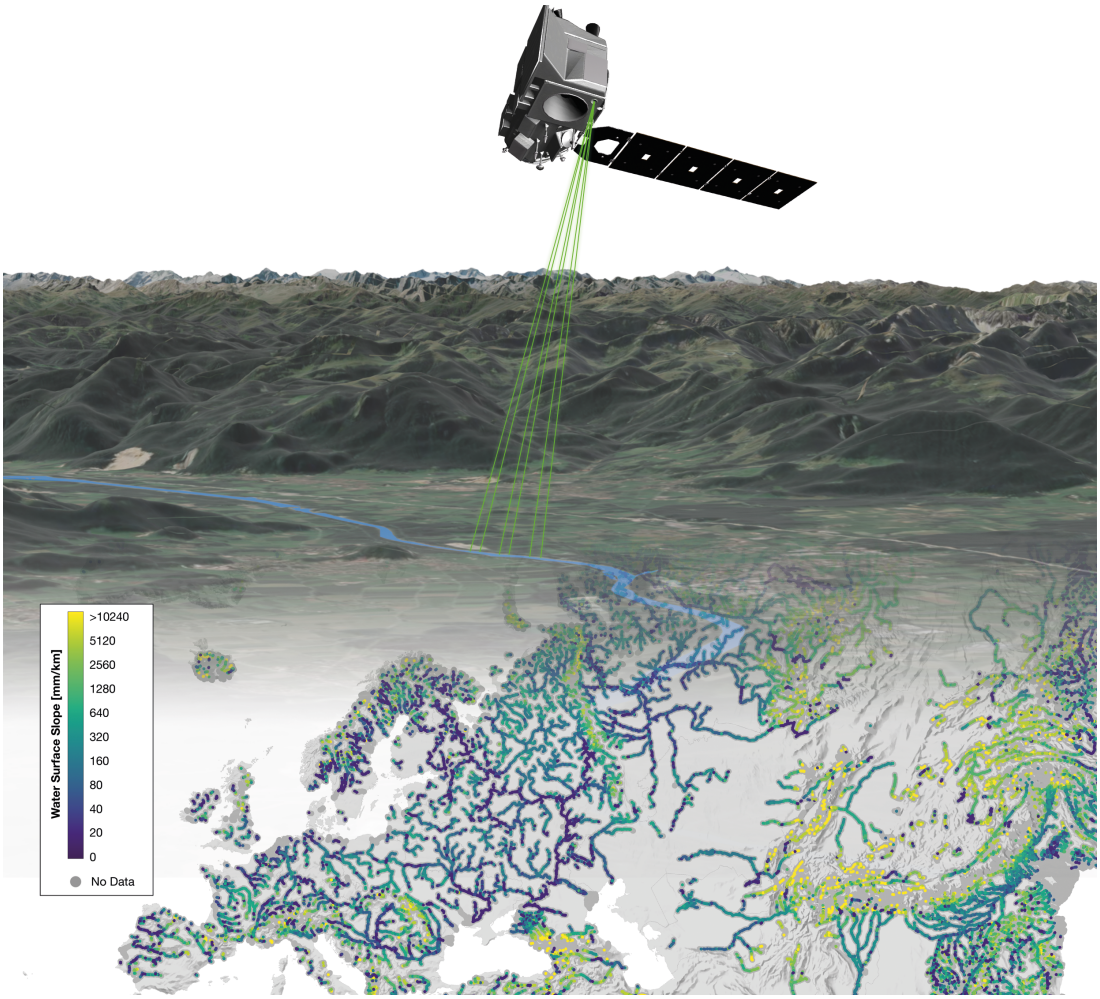

Figure 3.4 Global IRIS WSS dataset derived from ICESat-2's six parallel lidar beams

3.3 Water Surface Area

Time-variable water masks and WSA observed by satellite imagery are essential for **P1** and **P4** to derive the river bathymetry from a combination with satellite altimetry data (Sec. 3.4). **P1** uses 10 to 30 m resolution images acquired by the Landsat and Sentinel-2 missions. To meet objective **O2** and improve the results both in accuracy and transferability to smaller rivers, **P4** employs high-resolution (3 m) PlanetScope data, which, however, have a different spectral resolution and require a different approach to retrieve the WSA. The differences between the sensors and water classification methods are described in the following sections.

3.3.1 Multispectral Sensors

Landsat

The NASA Landsat program started in 1972 and was one of the first missions dedicated to terrain observation. The first satellite was equipped with a passive multispectral scanner system detecting red, green, blue, and *Near Infrared* (NIR) light with a resolution of 80 m. Further launches of Landsat satellites keep the program ongoing, resulting in the longest global environmental satellite record. With each launch, the sensors of the Landsat satellites improve in radiometric, spectral, and spatial resolution. Since the launch of Landsat-4 in 1982, the program reached a spatial resolution of 30 m with additional *Shortwave Infrared* (SWIR) and thermal infrared bands. Landsat imagery is provided in collections, ensuring consistent processing of all missions and sensor iterations, including, e.g., atmospheric corrections to convert the top of atmosphere reflectance to land surface reflectance (Wulder et al., 2022).

In contrast to nadir satellite altimetry, the spatial coverage of the optical sensors is nearly global. The imaging sensors onboard the early Landsat satellites utilize a rotating mirror to scan 185 km wide stripes across the ground track. The forward motion of the satellite is compensated by the *Scan Line Corrector* (SLC) system, which ensures that the scanned lines are parallel and perpendicular to the ground track. Landsat-7 data contains significant sensor errors (stripes of void pixels) caused by a failure of the SLC system in May 2003. Since Landsat-8, a sensor capable of scanning an entire line at once without a mirror is employed, making it less prone to such errors (Emery & Camps, 2017).

Additional void pixels are caused by clouds and cloud shadows, which is the primary limitation of multispectral satellite imagery. Especially within the tropics and sub-tropics, ground features such as rivers can be unobservable during rainy seasons (Eberhardt et al., 2016; Wulder et al., 2015). Clouds and cloud shadows are masked by a homogenous approach across all Landsat missions (Z. Zhu & Woodcock, 2012).

Satellite imagery from the Landsat-4, -5, -7, and -8 missions are used in **P1**. The spectral resolution of Landsat-1, -2, and -3 is not sufficient for the applied water classification (cf. Section 3.3.2), Landsat-6 failed to reach orbit, and Landsat-9 was not launched at the time of publication.

Sentinel-2

The ESA Sentinel-2 constellation consists of the Sentinel-2A and -2B satellites launched in 2015 and 2017. The satellites are equipped with identical multispectral imagers, which provide 12 spectral bands with similar characteristics as the recent Landsat sensors, and an equivalent cloud masking can be applied (Z. Zhu et al., 2015). The swath of Sentinel-2 is 290 km wide, and the spatial resolution is 10 m for the visible and 20 m for the used NIR and SWIR bands. In **P1**, Landsat and Sentinel-2 observations are jointly used by resampling all images to a 10 m resolution. This combined constellation can achieve a minimum revisit time below 5 days depending on the latitude (Wulder et al., 2015).

PlanetScope

P4 focuses on monitoring the discharge of small rivers (<100 m width) whose surface variations are often too low for detection with the coarse maximum 10 m resolution of the Landsat and Sentinel-2 constellation. In contrast, the nominal 3 m ground sampling resolution of the commercial PlanetScope cube satellite constellation is sufficient to detect such small rivers and their variations. The orbit altitude of the approximately 130 satellites varies so that the actual resolution ranges from 3.0 to 4.2 m. The constellation consists of three different instrument generations: The Dove Classic satellites launched in 2014 capture red, green, blue, and NIR channels within a 24 km wide swath. The updated Dove-R satellites were launched in 2019 with an increased scene size in the along-track direction from 8 to 16 km. With the launch of the latest Super Dove generation in 2020, the spectral resolution increased by four additional bands within the visible spectrum, and the scene size increased to 32.5 km × 19.6 km. With the large number of satellites, the constellation reaches a daily revisit time (PlanetScope, 2023). This increases the probability of monitoring the surface water extent at water level extremes and acquiring cloud-free images with a minimum time interval to the altimetry observations, which is important for the combination of both data (cf. Sec. 3.4).

3.3.2 Water Classification

P1 and **P4** describe two different automatic water classification approaches for multi-spectral satellite imagery. The approaches differ by the required spectral resolution. The resulting watermasks are used to calculate the WSA, which is required for fitting the hypsometric water-level-to-surface-area relationship and constructing the observed bathymetry in Section 3.4.

Automated Water Area Extraction Tool (AWAX)

The *Automated Water Area Extraction Tool* (AWAX), developed in **AP1** (Schwatke et al., 2019) and applied in **P1**, consists of two steps: (1) The automated water classification and (2) the filling of data gaps caused by clouds and sensor errors such as the SLC error based on a long-term water probability mask to monitor the time-variable surface extent of inland water bodies. In the first step, AWAX applies the following five proven water classification methods to cloud-masked Landsat and Sentinel-2 imagery:

- *Modified Normalized Difference Water Index* (MNDWI, H. Xu, 2006)
- *New Water Index* (NWI, Ding, 2009)
- *Automated Water Extraction Index for Non-Shadow Areas* ($AWEI_{nsh}$, Feyisa et al., 2014)
- *Automated Water Extraction Index for Shadow Areas* ($AWEI_{sh}$, Feyisa et al., 2014)
- *Tasseled Cap for Wetness* (TC_{wet}, Kauth and Thomas, 1976)

These indexes apply different combinations of the optical (red, green, blue) and infrared bands (NIR, SWIR1, SWIR2). The result of each index is a raster of continuous values, and its frequency histogram usually shows two distinct maxima representing water and land pixels. The indices differ in their maximum value range and significance of both maxima. Additionally, the threshold value separating both classes varies for each scene and index, e.g., depending on atmospheric conditions (Emery & Camps, 2017) or the ratio of mixed pixels (Ji et al., 2009). In general, the threshold value is assumed to be at a local minimum between both maxima. AWAX automatically calculates these thresholds and combines them for a robust classification.

Figure 3.5 shows an example of the automated threshold determination of AWAX. It is based on the assumption that the number of land and water pixels must be consistent for each index. The initial rough threshold is set to the commonly used default value of 0 for the MNDWI. The corresponding reference pixel is identified in the cumulative histogram of the MNDWI, and a search window of $\pm 0.05\%$ of the number of all pixels is defined around it. This search window is transferred to the cumulative histograms and

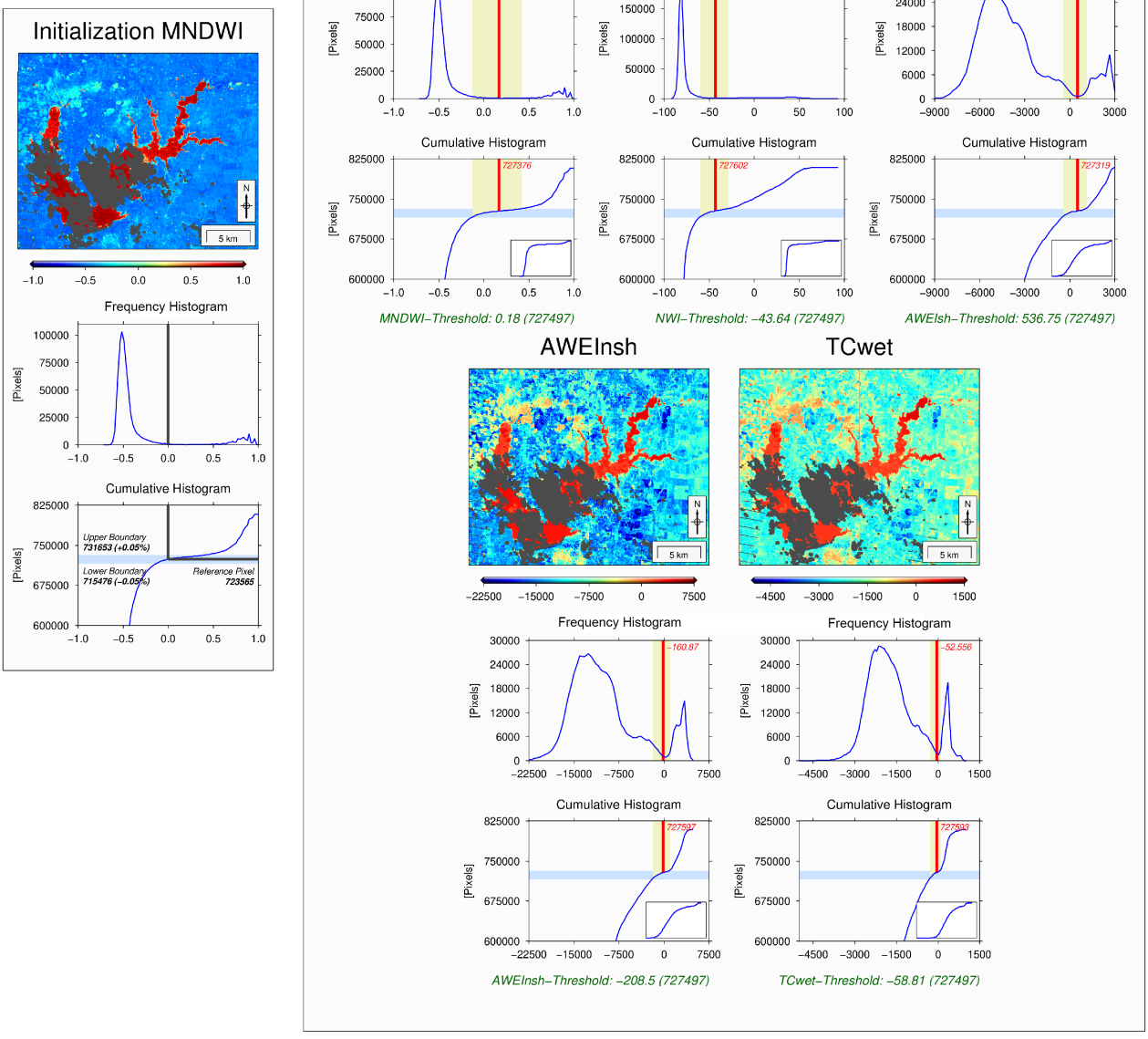

Figure 3.5 Example for the AWAX land-water threshold calculation (modified) from **AP1** (Schwatke et al., 2019). Left: Definition of a search window (light blue) in the cumulative histogram around the reference pixel representing the default threshold. Right: Individual minima (red) of each index in the frequency histograms within the transferred search window (light green). The final threshold based on the average pixel value of the individual minima is shown in green.

further to the frequency histograms of all water indices. For the frequency histogram of each index, the minimum value within the search window is determined and re-transferred to the cumulative histograms. The average of all pixel indexes representing the individual minima is used as a common threshold to classify water and land pixels into five binary water masks.

The binary water masks of the five indices are summed pixel-wise, leading to different confidences in the presence of water. Depending on the discrepancy between the indices, a pixel is either marked as land, water, or a data gap in the final mask. Data gaps caused by clouds, sensor errors, or index mismatches are filled by a long-term water probability mask. The probability mask is computed by dividing the number of water pixels accumulated over all obtained scenes by the number of accumulated valid pixels (i.e., land or water). Using an approach that iterates over the probability values p, the difference between the initial WSA with gaps (WSA_{init}) filled with a subset of the probability mask ($\text{WSA}_{fill}(p)$) and the WSA derived solely from the probability mask ($\text{WSA}(p)$) is minimized to obtain the best fill:

$$\min_{p} |(\text{WSA}_{init} + \text{WSA}_{fill}(p)) - \text{WSA}(p)| \tag{3.2}$$

Segment Anything Model (SAM)

The spectral resolution of the PlanetScope sensors is not sufficient to apply the AWAX approach because there are no SWIR channels. Therefore, **P4** employs a new classification method using the *Segment Anything Model* (SAM, Kirillov et al., 2023). SAM is an artificial intelligence model trained on over 1 billion masks on 11 million images. Although SAM was most probably not trained on water masks and satellite imagery, its zero-shot transfer capabilities based on minimal user inputs are sufficient to classify various features in satellite images (Osco et al., 2023), and SAM is also already used in the geospatial computation (Wu & Osco, 2023).

SAM provides two different methods, the SAM Generator and the SAM Predictor. The SAM Generator is an unsupervised algorithm that generates various masks for all detected image features. The SAM Predictor requires minimal user supervision by setting a small set of reference points both within and outside the feature of interest. Both methods require a three-band image. Instead of using a regular red, green, and blue channel combination, **P4** uses a false color image containing the NIR, a derived MNDWI, and the red bands to improve the contrast between water and land. Analogous to the AWAX approach, the resulting binary masks of the SAM Generator, SAM Predictor, and a standard MNDWI classification are summed pixel-wise to obtain different classes of water probability.

In contrast to the AWAX processing of Landsat and Sentinel-2 data, no cloud filling is applied in **P4** using SAM with PlanetScope data. Although the approach based on Equation 3.2 could be transferred to the resulting water masks, the number of processed PlanetScope scenes is not sufficient to obtain a robust water probability mask. The number of processed scenes is limited by the free-of-charge PlanetScope download quota. Instead, only cloud-free images are used in **P4**. This is feasible due to the daily revisit time of the PlanetScope satellites and the resulting high likelihood of acquiring cloud-free images with a minimum lag to the satellite altimetry.

3.4 River Bathymetry

The processed WSE from satellite altimetry and WSA from optical imagery must be combined to obtain river bathymetry and cross-sectional geometry to derive the geometric parameters (cross-sectional area A_i, wetted perimeter P_i, and depth d_i), which are required for the flow velocity, depth-dependent roughness, and discharge calculation as introduced in Chapter 2. The upper part of the geometry can be observed from the combined data, while the permanently submerged part of the geometry is estimated using empirical relationships and optimization. While the fundamental methods to derive the geometry are established in **P1**, **P4** focuses on increasing the accuracy of the unobserved part and quantifying the geometric uncertainties based on the WSE and WSA input uncertainties to fulfill objectives **O2** and **O3**.

The imaging sensors and their spatial and temporal resolution are the main differences between **P1** and **P4**. The 10 to 30 m Landsat and Sentinel-2 data used in **P1** are freely available, and nearly all images acquired within the *Area of Interest* (AOI) can be classified and cloud-filled using AWAX (see Section 3.3.2), but the temporal resolution is low causing large time lags between WSA and WSE observations. In contrast, **P4** uses 3 m resolution PlanetScope data, which is available daily but not free of charge. Because of the relatively high temporal variability of rivers, the time lag between WSE and WSA measurements should be minimal or synchronous for a meaningful combination. Therefore, the PlanetScope images are selected manually to be cloud-free and with minimal delay (typically less than a day) to the altimetry measurements. Because the average time lag is significantly longer in **P1**, it requires the fitting of a hypsometric model to assign the correct WSE to the images. Nevertheless, the hypsometric model is also used in **P4** for WSE estimation in seasons of permanent cloud coverage and outlier detection and mitigation.

The hypsometry model, or hypsometric curve, describes the relationship between elevation and area and is used in geomorphology to quantitatively compare the topography and landform processes such as erosion between different catchments (Willgoose & Hancock, 1998). The hypsometric curve is continuous and monotonic increasing and can be modeled using, e.g., (piecewise) linear or polynomial functions (Crétaux et al., 2016; Durand et al., 2024). Schwatke et al. (2020) use a modified function from Strahler (1952) that can model a large variety of hypsometric relationships given these conditions:

$$y = \left[\frac{x_{min} - x}{x_{min} - x_{ip}} \cdot \frac{x_{max} - x_{ip}}{x_{max} - x} \right]^{z} \cdot y_{scale} + y_{min} \tag{3.3}$$

where x_{min} and x_{max} define the minimum and maximum WSA, y_{min} the bed elevation, and y_{scale} the WSE variation. The parameters describing the shape of the curve (z) and the abscissa of its inflection point (x_{ip}) must be fitted to the data, and x_{min} and y_{min} are unknown. Figure 3.6 shows an example hypsometric curve of varying shape depending on the exponent z.

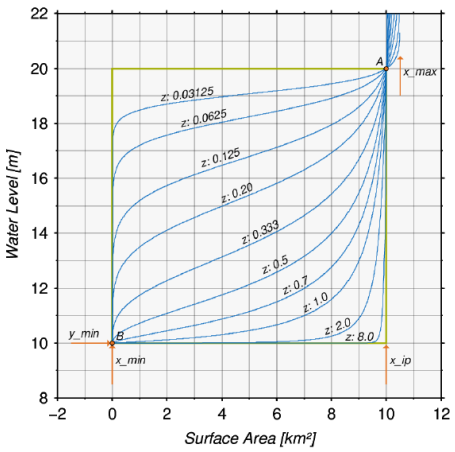

Figure 3.6 Shape of the modified Strahler hypsometric model depending on the exponent z (Schwatke et al., 2020).

The hypsometry is commonly used to describe lake bathymetry, which is basically a small catchment, to relate WSA and WSE (e.g. Carrea et al., 2023; Crétaux et al., 2016; Li et al., 2019; Schwatke et al., 2020). However, the application in lakes mainly involves the estimation of volume variations, which does not require the entire lake bathymetry, and the exact value of the unknowns is less important. Therefore, y_{min} can be assumed to be close to zero, and loose bounds can be given for x_{min} when fitting the model to the data. Similar to lakes, the bathymetry of a river (an even smaller catchment than a lake) can also be described with a hypsometric function (Durand et al., 2024) and Equation 3.6 is applied in **P1** and **P4**. In contrast to the relative lake volume variations, the unknown riverbed elevation (y_{min}) derived from depth estimates is important for estimating the absolute discharge values, which requires the entire river bathymetry. Although the unobserved submerged bathymetry is not reconstructed from the hypsometry, large errors in y_{min} can cause a poor fitting of the hypsometric curve due to the small area-to-depth relationship.

3.4.1 Depth Estimation

There is no satellite sensor capable of reliably measuring the depth of inland waters, which is required for fitting the hypsometry and reconstructing the submerged bathymetry. In some rare cases of clear waters, the depth can be measured using the ICESat-2 lidar alitimeter (Datta & Wouters, 2021; Xiao et al., 2023; N. Xu et al., 2022). However, these measurements are not suitable in rivers because of their high degree of turbidity (Coppo Frias et al., 2023; Henke, 2024). Instead, **P1** and **P4** use an empirical width-to-depth relationship derived from Moody and Troutman (2002). They use power-law regressions as proposed by Leopold and Maddock (1953), which are typically used in hydrology and geomorphology (Kenney, 1993), to relate the average water-surface width $\bar{w}$ and average depth $\bar{d}$ to discharge measurements of more than a thousand globally distributed cross-sections with different flow regimes ranging from mountainous streams to large alluvial rivers. Moody and Troutman (2002) obtain the following regression relations:

$$\bar{w} = 7.2Q^{0.50\pm0.02} \tag{3.4}$$

$$\bar{d} = 0.27Q^{0.39\pm0.01} \tag{3.5}$$

where the coefficients and exponents are empirical factors derived from the regression. When solving Equation 3.4 for the discharge Q these regression relations can be written as:

$$\bar{d} = 0.27\left(\frac{\bar{w}^2}{7.2^2}\right)^{0.39} \tag{3.6}$$

However, equation 3.6 must be used with caution as Kenney (1993) states that power-law regressions must not be treated like single-valued analytical functions, and rearrangements “may severely distort the results”. Additionally, the uncertainty of the exponents is disregarded. Nevertheless, considering the many unknowns and uncertainties in satellite monitoring of river discharge, this method still yields good results, as confirmed by the validation in **P1**, and the river width can be derived from the water masks resulting from Section 3.3.2. In **P1**, Equation 3.6 is used to estimate the depth for each synchronous data pair and retrieve the river bed elevation by subtracting the depth from the respective WSE. The median of all observations is then used as the final river bed elevation at the cross-section. Instead of the median, **P4** calculates the weighted average of the depth estimates with higher weights on the observations during low flow in order to reduce the overestimation caused by flood events with large widths when the river exceeds its banks. Still, the geometric parameters obtained from this empirically derived depth (see Section 3.4.2) may vary significantly and unrealistically between the multiple consecutive sections studied in **P4**. Therefore, the vector of bed elevations ($\mathbf{h_0}$) is further optimized with the same method used in Section 2.3.1. Constrained by the range of empirical depth estimates and under the assumption of gradually varied flow, the objective function minimizes the standard deviation in cross-sectional area at the mean WSE ($\bar{A}(x)$) between all cross-sections within the studied reach:

$$\min_{\mathbf{h_0}} \sigma\left(\left[\bar{A}(x_1), \ldots, \bar{A}(x_m)\right]\right) \tag{3.7}$$

3.4.2 Cross-Sectional Geometry

In **P1** and **P4**, the water masks resulting from Section 3.3.2 are aligned to a common pixel grid and ordered by the hypsometric WSE, resulting in a stack of water masks which is used to derive a map of the observable bathymetry as shown in Figure 3.7. Because of classification errors or changes in the river bed, there can still be inconsistencies in each pixel column (i.e., a pixel classified as land is classified as water in the masks above and below). **P1** follows Schwatke et al. (2020) and applies a moving window filter to mitigate these outliers. It sets the respective pixels' elevation in the bathymetry map when the majority of classes within the window indicate land. Instead of a single bathymetry map, **P4** computes three rasters. The first is based on the elevation of the minimum water elevation per pixel, the second on the maximum land elevation per pixel, and the third on the mean of the two rasters. In this way, the classification errors are preserved as uncertainty, which can be transferred to the geometric parameters and derived discharge to fulfill objective **O3**.

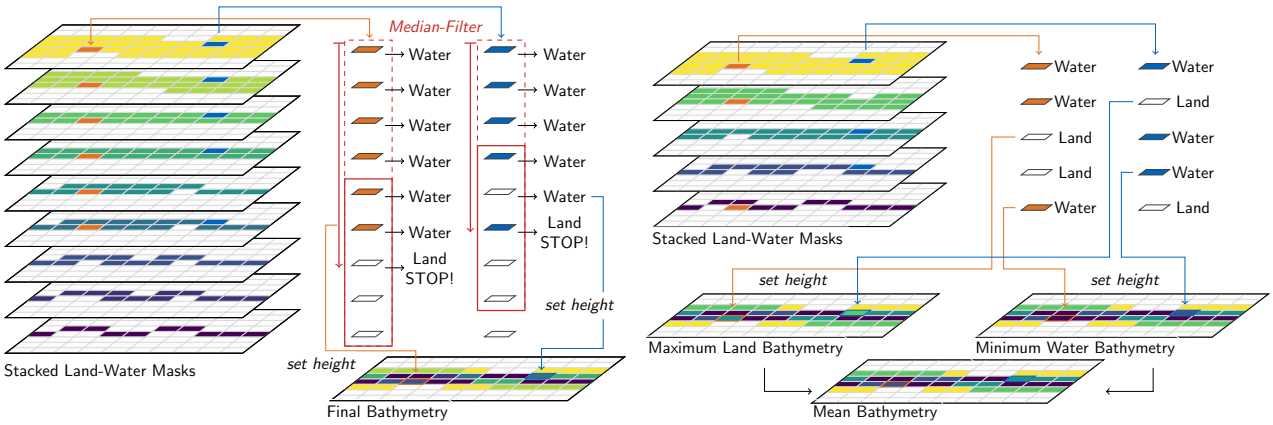

Figure 3.7 Schemes visualizing the processing of the river bathymetry raster based on the approach used in **P1** (left, modified from Schwatke et al. (2020)) and the approach used in **P4** (right). A moving window is used in **P1** to set the bottom elevation per pixel column of the stacked land-water masks sorted by WSE. In **P4**, two bathymetry rasters are derived from the minimum water and the maximum land elevation per pixel column to obtain a mean bathymetry raster with uncertainties.

The observable part of the cross-sectional geometry can be sampled along the cross-section. Following Bjerklie et al. (2018), the shape between the minimum observed WSE and the estimated river bed elevation is approximated with a parabola as shown on the left of Figure 3.8. This is the final cross-sectional geometry in **P1**, from which the cross-sectional parameters $A(t)$, $P(t)$, and $R(t)$ (see Section 2.2.3) can be derived depending on the WSE time series. As described in Section 3.4.1, the river bed elevation is optimized in **P4** under the assumption of gradually varied flow, and the geometries are adjusted respectively so that the difference between the cross-sectional area at mean flow is minimal. The center of Figure 3.8 shows the cross-sections after optimization. Addressing objective **O3**, the remaining range between the minimum and maximum bed elevation is used to quantify the uncertainty of the geometric parameters (Figure 3.8 right), which is transferred to the discharge uncertainty.

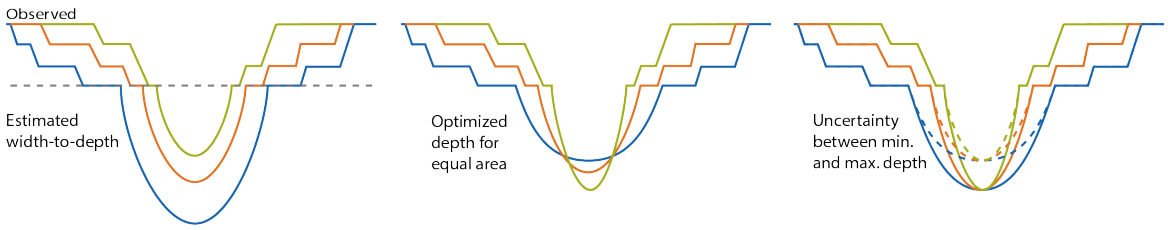

Figure 3.8 Processing of the cross-sectional geometries based on the empirical Equation 3.6 (left), the optimization with Equation 3.7 (center), and the resulting uncertainty based on the extreme values (right).

4 Discharge Algorithms and Results

Based on the hydraulic concepts introduced in Chapter 2 and with the different satellite observables and derivables described in Chapter 3, the two publications **P1** and **P4** focus on algorithms for the satellite monitoring of river discharge and discuss the results. While **P1** concentrates on the identification of the potential and limitations of the observations and methods (**O1**), **P4** also investigates innovative techniques to improve the hydraulic parameter estimation (**O2**) and provides reliable uncertainty quantification (**O3**).

4.1 P1: Initial Framework for Satellite-Derived Discharge

The Manning equation is chosen in **P1** as the fundamental hydraulic flow law because of its communitywide use, especially in the context of the SWOT mission (Durand et al., 2014; Garambois & Monnier, 2015; Hagemann et al., 2017), but also with multi-mission satellite data (Bjerklie et al., 2018; Sichangi et al., 2018; Zakharova et al., 2020). The required parameters are derived from different satellite sensors. The average WSS is calculated from satellite altimetry using linear adjustment of the VSs' elevation. The upper part of the cross-sectional geometry is observed by combining satellite altimetry and water masks from Landsat and Sentinel-2 images employing the AWAX algorithm developed in **AP1**. The unknown depth is estimated using the empirical width-to-depth relationship (Equation 3.6) to complete the cross-sectional geometry with a parabola. The roughness coefficient is calculated with Equation 2.9 using literature decision guides for adjustment factors that are selected by an expert based on satellite imagery.

The approach of **P1** is applied to the Lower Mississippi River, where extensive validation data are available so that a closed-loop test can be performed by substituting all satellite-derived parameters with in-situ observations. The WSS is validated against a dense network of in-situ WSE stations, showing that the results are well within the range of the in-situ WSS but partially deviate significantly from the average in-situ WSS. The spatial resolution depends on the location of VSs, and large errors occur between closely located adjacent stations. The WSE accuracy of the VSs depends on the respective sensor and river properties (width, intersection angle, etc.) that propagate to the WSS and make a global application challenging. Additionally, temporal WSS variations, which improved the results significantly, cannot be quantified using the linear adjustment approach. Except for small deviations that can be caused by erosion and sedimentation, the observable bathymetry shows good agreement with the in-situ multibeam bathymetric survey data. The estimation of the permanently submerged cross-sectional geometry succeeds in straight and gradually widening river sections but significantly underestimates the cross-sectional area in narrow and bending sections where the riverbed is affected by strong erosion that cannot be detected using the empirical width-to-depth relationship. However, such sections can be avoided judging from satellite imagery. Knowing the in-situ discharge, time-variable WSS, and geometry, the closed-loop test reveals that the roughness is the dominant error source for 12 out of the 16 cross-sections studied, caused by an incorrect selection of the adjustment factors using the coarse decision guides. The validation leads to the conclusion that errors from incorrect roughness values are most significant, while a better slope estimation would improve the results and general applicability, and errors from the bathymetry can be avoided by carefully selecting the study site.

The framework, results, and closed-loop validation are described and discussed in detail in Appendix P1:

P1 Scherer, D., Schwatke, C., Dettmering, D., & Seitz, F. (2020). **Long-Term Discharge Estimation for the Lower Mississippi River Using Satellite Altimetry and Remote Sensing Images**. *Remote Sensing*, *12*, 2693. https://doi.org/10.3390/rs12172693

4.2 P4: Discharge Monitoring with Roughness Optimization

With improved WSS measurements in **P2** and **P3**, **P4** addresses the roughness coefficient, identified in **P1** as the principal source of discharge error. To achieve **O2**, a new optimization approach based on the principle of mass conservation is developed, minimizing the discharge differences between consecutive cross-sections by adjusting the roughness coefficients using the L-BFGS-B algorithm described in Section 2.3.1. This method not only minimizes discharge errors resulting from inaccurate roughness coefficients but also minimizes the potential for observer bias present in **P1**, where roughness coefficients are selected based on a decision guide. Also concerning **O2**, the unknown depth of the unobserved cross-sectional geometry is optimized across multiple cross-sections to reduce the probability of outliers. In contrast to **P1**, **P4** uses high-resolution satellite imagery to transfer the approach to smaller rivers. Because of the lower spectral resolution, a novel deep-learning classification method is required to obtain water masks from the high-resolution images.

Furthermore, **P4** fulfills **O3** by transferring all uncertainties of the input quantities to the resulting discharge time series. This uncertainty range is not equivalent to statistical error propagation, which is challenging because of the complex and non-linear relationship between the input uncertainties (such as water extent classification errors) and the discharge. Instead, a 90% uncertainty range is computed using an ensemble of multiple computations with different parameter configurations based on the following observed and derived uncertainties:

- The WSS uncertainty is obtained from the IRIS WSS extremes (see Section 3.2.2).
- The uncertainty of the observed bathymetry is considered by constructing two additional bathymetry rasters representing possible extremes caused by false positive and false negative water classifications of the satellite imagery (see Section 3.4.2).
- The uncertainty of the unobserved bathymetry is derived from the remaining range of depth estimates after the depth optimization (see Section 3.4.2).
- The uncertainty of the entire cross-sectional geometry is influenced by the uncertainty of the WSE time series consisting of retracking and correction errors (see Section 3.1) which are obtained from DAHITI.
- The standard deviations of the roughness coefficients are obtained from the squared diagonal of the inverse Hessian matrix computed during the roughness optimization (see Section 2.3.1).

In this way, the uncertainty can be broken down into constituents based on the individual satellite observables, demonstrating further potential for improvement and addressing objective **O1**. For instance, a time-variable slope could reduce the uncertainty by up to 20%, especially in smaller upstream reaches.

The approach is transferred to 27 globally distributed rivers of different discharge domains to estimate discharge time series covering up to 22 years. The validation shows that 91% of the in-situ observations are within the 90% uncertainty range, which has a coefficient of variation of 43%. With a median NRMSE of 12% (132 m^3/s RMSE), the quality aligns with the GCOS standard of 15% (GCOS, 2022) and is comparable with the expected uncertainty of SWOT discharge of less than 30% in ungauged basins (Durand et al., 2023). The requirement of 10% measurement uncertainty, which marks a breakthrough according to GCOS (2022), is met for 7 out of the 27 studied rivers under difficult and diverse test conditions, highlighting the potential of satellite monitoring of river discharge without in-situ calibration (**O1**).

The optimization approach, results, and validation are described and discussed in detail in Appendix P4:

P4 Scherer, D., Schwatke, C., Dettmering, D., & Seitz, F. (2024). **Monitoring river discharge from space: An optimization approach with uncertainty quantification for small ungauged rivers**. *Remote Sensing of Environment*, *315*, 114434. https://doi.org/10.1016/j.rse.2024.114434

5 Conclusion

This thesis describes an extensive approach to the satellite monitoring of river discharge without calibration data, enabling its application in ungauged basins. The work addresses the declining number and uneven distribution of in-situ gauges, particularly in regions most vulnerable to water scarcity and hydrological extremes, to support the understanding and management of freshwater resources under a changing climate. The discharge estimates with uncertainties are valuable for hydrological models, such as the ongoing ESA project EO4FLOOD (Tarpanelli et al., 2025), which integrates discharge from the optimization approach. In contrast to recent advancements in hydrogeodesy, which focus on data from the unprecedented SWOT mission, this thesis leverages the large variety of multi-mission satellite observations, combining long-term measurements of WSE, WSS, and WSA with hydraulic methods based on the principle of mass conservation. This approach complements the SWOT mission by ensuring resilience against potential data gaps in SWOT data and offering discharge time series for decades prior to the launch of SWOT.

The thesis comprises four key publications, which address the research objectives defined in Section 1.2 to achieve the goal of long-term satellite monitoring of river discharge in ungauged basins. The advancements and key findings related to these objectives are discussed below.

O1 Identify the potential and limitations of uncalibrated satellite monitoring of river discharge

The potential of estimating river discharge from satellite observations without in-situ calibration is demonstrated for the Lower Mississippi River in **P1** with extensive validation and transferred to 27 rivers in **P4**, where the average quality meets the standards defined by GCOS (2022) and reveals no significant dependencies on the flow regime. In line with multiple state-of-the-art studies, the Manning equation and the necessary approximations of gradually varied flow prove to be valid and sufficient in the context of the scales and uncertainties of the satellite observables. However, it is important to avoid backwater-affected reaches, as the applied approximations can lead to significant errors in these conditions, as described in **P4**. Similarly, curved or narrowing reaches should be avoided since the erosion and sedimentation processes in these sections cannot be modeled using the empirical width-to-depth equation, which is also not valid for braided rivers. Most of these limiting conditions can be identified through satellite imagery.

In contrast, in straight and widening river sections, the geometric parameters of the Manning equation can be effectively derived from WSE and WSA observations by satellite altimetry and remote sensing optical imagery with high accuracy, as demonstrated by the validation in **P1**. The WSS can be obtained by a linear adjustment of WSE measurements from nadir radar altimetry as shown in **P1** but occasionally deviates significantly depending on the opportunistic spatial distribution of VSs. The WSS accuracy and spatial distribution are improved using lidar altimetry, but neither method can be used to derive a meaningful WSS time series, which would better constrain the discharge estimation and could reduce the resulting uncertainty by up to 20% as indicated in **P4**. The roughness coefficient is the most critical parameter, leading to significant errors when chosen manually using literature decision guides, as shown in **P1**, and causing large uncertainties in the optimization approach of **P4**.

The general applicability of the discharge approaches is limited by the inhomogeneous distribution of nadir altimetry discussed in **AP2** so that only reaches intersected by the nadir ground track can be monitored. Although WSE time series from multiple stations can be combined in **P4** using the IRIS dataset to increase temporal coverage, the temporal resolution of the discharge time series, which is limited by the repeat cycle of the altimeter satellites, remains coarse, so that many extreme events are likely missed.

O2 Investigate innovative techniques to improve the parameter estimation

The space-based observation of WSS can be improved by leveraging the unique multibeam lidar altimeter of the ICESat-2 mission with an innovative approach described in **P2**. The high accuracy and spatial resolution of ICESat-2 not only reduces the WSS errors but also enables the measurement of instantaneous WSS and the quantification of WSS variability. This approach can be transferred to the majority of SWORD river reaches, leading to the IRIS dataset published in **P3**, which provides reach-scale WSS globally. The quality of the IRIS dataset is reflected in its large impact within the hydrogeodesy community as described in Section 3.2.3. Besides the direct improvement of the discharge by the more accurate WSS, IRIS data can also be used to correct the WSE time series from nadir altimetry for the ground track shift. In steep rivers, this correction reduces the WSE RMSE by up to 30 cm or 66%, as demonstrated in **P2**. This also affects the accuracy of the satellite-derived bathymetry and cross-sectional geometries. Furthermore, the IRIS WSS is used to combine WSE measurements from multiple virtual stations of different missions within one reach. In this way, the temporal resolution of the resulting discharge time series, which depends on the resolution of the WSE time series, can be increased in **P4**.

Using a novel and robust deep-learning water classification in **P4**, high-resolution satellite imagery by PlanetScope, which lacks the spectral resolution required for established index-based classification, can be combined with WSE to obtain a fine-scale river bathymetry. With the increased spatial resolution compared to Landsat or Sentinel-2 imagery, the discharge approach can be transferred to significantly smaller rivers below 100 m width.

Following recent advances in approaches designed for the innovative SWOT mission, a major improvement within **P4** is the optimization of the roughness coefficient, mitigating the risk of observer bias when choosing this parameter manually. Based on the principle of mass conservation, the roughness coefficient is optimized to minimize the difference in discharge between multiple consecutive cross-sections within a reach. In contrast to the approach of **P1**, this unsupervised method only requires minimal expert input, such as the definition of coarse boundary values, and can quantify the roughness uncertainty.

O3 Provide reliable uncertainty quantification

The optimization approach of **P4** provides a confidence interval reflecting a reliable uncertainty quantification, ensuring that the discharge time series can be integrated into comprehensive hydrologic models. The uncertainty range is based on the uncertainty of the estimated hydraulic parameters, which further depend on the uncertainties of the satellite observables and derivables.

The WSS errors of the ICESat-2 measurement are low and likely neglectable, as demonstrated by the validation in **P2**. However, there is no method to obtain meaningful WSS time series from satellite observations prior to the launch of SWOT, and a constant WSS must be used. Therefore, there is a significant WSS uncertainty caused by the temporal variations, which can be approximated from the temporal sparse instantaneous ICESat-2 observations.

Geometric uncertainties caused by WSA classification errors or erosion and sedimentation are represented by two additional bathymetric rasters representing the possible extremes. Additionally, the depth of the unobserved bathymetry is optimized across multiple cross-sections, and the remaining range of depth estimates quantifies the uncertainty of the unobserved geometry. Furthermore, the uncertainties of the DAHITI WSE time series are considered in the uncertainty of the cross-sectional geometry.

The standard deviation of the roughness coefficients can be obtained from L-BFGS-B optimization. Each of the hydraulic parameters is individually varied from the optimal solution to their respective minimum and maximum values, generating an ensemble of extreme scenarios. The range between the 5th and 95th percentile of the ensemble results is used as the 90% uncertainty range. This range includes 91% of the validation data across all rivers studied in **P4**, confirming the reliability of the uncertainty quantification. With 43%, the coefficient of variation is reasonable given the number of unknowns in ungauged basins.

6 Outlook

Not all limitations identified in the scope of **O1** could be overcome in this thesis, but the optimization approach developed in **P4** is also not limited to the selected sensors and can be transferred to other observations of WSE, WSA, and WSS. It would be logical to include SWOT data in future developments. The groundbreaking coverage of WSE measurements within the wide swath, in contrast to nadir altimetry, would increase the number of applicable reaches significantly. First studies by Köhn and Nielsen (2024), Maubant et al. (2025), Yu et al. (2024), and Zhao et al. (2025) show that the SWOT WSE and WSS accuracy is considerably better compared to nadir altimetry and mainly within the science requirements (JPL, 2018) for inland waters of 10 to 25 cm and 17 mm/km, except for some outliers that occur especially in the Level 2 vectorized product. Monitoring WSA with optical sensors is still more accurate and robust than SWOT (Kistler, 2025) because SWOT, as any SAR imager, is affected by radar layover and other effects (JPL, 2024; Peral et al., 2024). Still, beyond the preprocessed pixel cloud product, the single-look complex SWOT data could further reduce the size of detectable water features. Although the synchronous SWOT observations of WSE and WSA would remove the dependency on fitting the hypsometric curve (except for outlier detection), the most accurate solution could be the combination of the wide-swath SWOT WSE with daily high-resolution satellite imagery such as PlanetScope. The spatially dense and time-variable SWOT WSS measurements would further constrain the optimization of the roughness coefficient, reduce the uncertainties, and allow the capture of hysteresis effects. The SWOT WSS could enhance the quantification of the temporal variability and extremes within IRIS and could potentially be used to obtain historical WSS time series using a rating curve approach with nadir altimetry.

Still, the limitation of the temporal resolution remains with the 10-day repeat cycle of SWOT (Cerbelaud et al., 2024). As there is no satellite constellation providing observations with high temporal resolution, temporal and spatial densification is required for a better capture of peak flow events. While there are several statistical and empirical approaches for spatiotemporal interpolation of WSE from satellite altimetry, the (sub-)daily PlanetScope data could be used to directly measure flood wave propagation by calculating the WSA time lag between reaches. The deep-learning water classification applied in **P4** could facilitate this approach. A similar method has been used by Sichangi et al. (2018) using daily MODIS imagery, but with PlanetScope, much smaller rivers and WSA variations can be measured, potentially providing improved accuracy and transferability. The spatiotemporal WSE densification could lead to a basin-scale discharge approach, integrating discharge estimates from multiple branches to further constrain the optimization of the unknown parameters similar to Durand et al. (2023).

The high-resolution PlanetScope imagery is required to monitor the small rivers studied in **P4**, but the optimization approach could also be applied to the lower-resolution Landsat and Sentinel-2 data when observing larger rivers. The threshold river width, above which the lower resolution is sufficient, could be studied in future research. Many peak flow events cannot be observed with satellite imagery due to cloud cover. Watermasks from the radar images acquired by the Sentinel-1 mission could be used besides the SWOT pixel cloud to refine the upper part of the observed bathymetry.

The current approach cannot be applied to braided rivers because the empirical width-to-depth relationship utilized is only valid in meandering rivers. However, a simplified depth estimation might be feasible because of the ephemeral character of braided rivers and the resulting shallow depth at low flows. Additionally, braided rivers show large variations in the riverbed because of high erosion and sedimentation, which would require up to yearly unique bathymetries to capture the temporal geometry variations. While the Manning equation yields good results in meandering rivers, it could be worth applying more sophisticated hydraulic models within braided rivers.

Bibliography

Abdalati, W., Zwally, H. J., Bindschadler, R., Csatho, B., Farrell, S. L., Fricker, H. A., Harding, D., Kwok, R., Lefsky, M., Markus, T., Marshak, A., Neumann, T., Palm, S., Schutz, B., Smith, B., Spinhirne, J., & Webb, C. (2010). The ICESat-2 laser altimetry mission. *Proceedings of the IEEE*, *98*, 735–751. https://doi.org/10.1109/JPROC.2009.2034765

Allen, G. H., & Pavelsky, T. (2018). Global extent of rivers and streams. *Science*, *361*, 585–588. https://doi.org/10.1126/science.aat063

Alsdorf, D. E., Rodríguez, E., & Lettenmaier, D. P. (2007). Measuring surface water from space. *Reviews of Geophysics*, *45*, RG2002. https://doi.org/10.1029/2006RG000197

Andreadis, K. M., Brinkerhoff, C. B., & Gleason, C. J. (2020). Constraining the Assimilation of SWOT Observations With Hydraulic Geometry Relations. *Water Resources Research*, *56*(5). https://doi.org/10.1029/2019wr026611

Andreadis, K. M., Coss, S. P., Durand, M. T., Gleason, C. J., Simmons, T. T., Tebaldi, N., Bjerklie, D. M., Brinkerhoff, C., Dudley, R. W., Gejadze, I., Larnier, K., Malaterre, P.-O., Oubanas, H., Allen, G. H., Bates, P. D., David, C. H., Domeneghetti, A., Marc, L. F., Frasson, R. P. d. M., … Yadav, B. (2025). A First Look at River Discharge Estimation From SWOT Satellite Observations. *Geophysical Research Letters*. https://doi.org/10.1029/2024GL114185

Arcement, G. J., & Schneider, V. R. (1989). Guide for selecting Manning's roughness coefficients for natural channels and flood plains. https://doi.org/10.3133/wsp2339

Battjes, J. A., & Labeur, R. J. (2017). Unsteady Flow in Open Channels. Cambridge University Press. https://doi.org/10.1017/9781316576878

Bauer-Gottwein, P., Christoffersen, L., Musaeus, A., Frías, M. C., & Nielsen, K. (2024). Hydraulics of Time-Variable Water Surface Slope in Rivers Observed by Satellite Altimetry. *Remote Sensing*, *16*, 4010. https://doi.org/10.3390/rs16214010

Beven, K. (2006). Searching for the Holy Grail of scientific hydrology: $Q_t = (S, R, \Delta t)A$ as closure. *Hydrology and Earth System Sciences*, *10*(5), 609–618. https://doi.org/10.5194/hess-10-609-2006

Bjerklie, D. M., Birkett, C. M., Jones, J. W., Carabajal, C., Rover, J. A., Fulton, J. W., & Garambois, P. A. (2018). Satellite remote sensing estimation of river discharge: Application to the Yukon River Alaska. *Journal of Hydrology*, *561*, 1000–1018. https://doi.org/10.1016/j.jhydrol.2018.04.005

Bjerklie, D. M., Dingman, S. L., Vorosmarty, C. J., Bolster, C. H., & Congalton, R. G. (2003). Evaluating the potential for measuring river discharge from space. *Journal of Hydrology*, *278*, 17–38. https://doi.org/10.1016/S0022-1694(03)00129-X

Blöschl, G., Bierkens, M. F., Chambel, A., Cudennec, C., Destouni, G., Fiori, A., Kirchner, J. W., McDonnell, J. J., Savenije, H. H., Sivapalan, M., Stumpp, C., Toth, E., Volpi, E., Carr, G., Lupton, C., Salinas, J., Széles, B., Viglione, A., Aksoy, H., … Zhang, Y. (2019). Twenty-three unsolved problems in hydrology (UPH) – a community perspective. *Hydrological Sciences Journal*, *64*, 1141–1158. https://doi.org/10.1080/02626667.2019.1620507

Boergens, E., Dettmering, D., Schwatke, C., & Seitz, F. (2016). Treating the Hooking Effect in Satellite Altimetry Data: A Case Study along the Mekong River and Its Tributaries. *Remote Sensing*, *8*, 91. https://doi.org/10.3390/rs8020091

Boergens, E., Schmidt, M., & Seitz, F. (2021). The use of B-splines to represent the topography of river networks. *GEM - International Journal on Geomathematics*, *12*(1). https://doi.org/10.1007/s13137-021-00188-w

Bosch, W., Dettmering, D., & Schwatke, C. (2014). Multi-Mission Cross-Calibration of Satellite Altimeters: Constructing a Long-Term Data Record for Global and Regional Sea Level Change Studies. *Remote Sensing*, *6*, 2255–2281. https://doi.org/10.3390/rs6032255

Brinkerhoff, C. B., Gleason, C. J., Feng, D., & Lin, P. (2020). Constraining Remote River Discharge Estimation Using Reach-Scale Geomorphology. *Water Resources Research*, *56*(11). https://doi.org/10.1029/2020wr027949

Brown, G. (1977). The average impulse response of a rough surface and its applications. *IEEE Transactions on Antennas and Propagation*, *25*, 67–74. https://doi.org/10.1109/TAP.1977.1141536

Broyden, C. G. (1970). The Convergence of a Class of Double-rank Minimization Algorithms 1. General Considerations. *IMA Journal of Applied Mathematics*, *6*(1), 76–90. https://doi.org/10.1093/imamat/6.1.76

Byrd, R. H., Peihuang, L., Nocedal, J., & Argonne National Lab., I. (1996). A limited-memory algorithm for bound-constrained optimization. https://doi.org/10.2172/204262

Carrea, L., Crétaux, J.-F., Liu, X., Wu, Y., Calmettes, B., Duguay, C. R., Merchant, C. J., Selmes, N., Simis, S. G. H., Warren, M., Yesou, H., Müller, D., Jiang, D., Embury, O., Bergé-Nguyen, M., & Albergel, C. (2023). Satellite-derived multivariate world-wide lake physical variable timeseries for climate studies. *Scientific Data*, *10*, 30. https://doi.org/10.1038/s41597-022-01889-z

Cerbelaud, A., David, C. H., Biancamaria, S., Wade, J., Tom, M., de Moraes Frasson, R. P., & Blumstein, D. (2024). Peak Flow Event Durations in the Mississippi River Basin and Implications for Temporal Sampling of Rivers. *Geophysical Research Letters*, *51*. https://doi.org/10.1029/2024GL109220

Cerbelaud, A., David, C. H., Pavelsky, T. M., Biancamaria, S., Garambois, P.-A., Kittel, C. M., Papa, F., Bates, P. D., Tourian, M. J., Durand, M. T., Frasson, R. P. d. M., Oubanas, H., Simard, M., Schumann, G. J.-P., Allen, G. H., Tarpanelli, A., Wongchuig, S., Wade, J., Tom, M., … Benveniste, J. (2025). Progress towards satellite requirements to capture water propagation in Earth's rivers. https://doi.org/10.22541/essoar.173627093.35248744/v1

Chaudhry, M. H. (2022). Open-Channel Flow. Springer International Publishing. https://doi.org/10.1007/978-3-030-96447-4

Chen, Y., Baruah, A., Devi, D., & Cohen, S. (2024). Updating the U.S. Hydrofabric Slope Parameter Using a Remote Sensing Dataset: Impact on Flood Inundation Mapping [Poster]. *American Geophysical Union (AGU)*.

Chow, V. T. (1959). Open-Channel Hydraulics. Blackburn Press.

Christoffersen, L., Bauer-Gottwein, P., Sørensen, L. S., & Nielsen, K. (2023). ICE2WSS; An R package for estimating river water surface slopes from ICESat-2. *Environmental Modelling Software*, *168*, 105789. https://doi.org/10.1016/j.envsoft.2023.105789

Colebrook, C., & White, C. (1937). Experiments with fluid friction in roughened pipes. *Proceedings of the Royal Society of London. Series A - Mathematical and Physical Sciences*, *161*, 367–381. https://doi.org/10.1098/rspa.1937.0150

Coppo Frias, M., Liu, S., Mo, X., Nielsen, K., Ranndal, H., Jiang, L., Ma, J., & Bauer-Gottwein, P. (2023). River hydraulic modeling with ICESat-2 land and water surface elevation. *Hydrology and Earth System Sciences*, *27*(5), 1011–1032. https://doi.org/10.5194/hess-27-1011-2023

Cretaux, J.-F., Arsen, A., Calmant, S., Kouraev, A., Vuglinski, V., Bergé-Nguyen, M., Gennero, M.-C., Nino, F., Abarca Del Rio, R., Cazenave, A., & Maisongrande, P. (2011). SOLS: A lake database to monitor in the Near Real Time water level and storage variations from remote sensing data. *Advances in Space Research*, *47*(9), 1497–1507. https://doi.org/10.1016/j.asr.2011.01.004

Cretaux, J.-F., Nielsen, K., Frappart, F., Papa, F., Calmant, S., & Benveniste, J. (2017). Hydrological Applications of Satellite Altimetry: Rivers, Lakes, Man-Made Reservoirs, Inundated Areas. In D. Stammer & A. Cazenave (Eds.), *Satellite Altimetry Over Oceans and Land Surfaces* (1st ed.). CRC Press. https://doi.org/10.1201/9781315151779-14

Crétaux, J.-F., Abarca-del-Río, R., Bergé-Nguyen, M., Arsen, A., Drolon, V., Clos, G., & Maisongrande, P. (2016). Lake Volume Monitoring from Space. *Surveys in Geophysics*, *37*, 269–305. https://doi.org/10.1007/s10712-016-9362-6

Datta, R. T., & Wouters, B. (2021). Supraglacial lake bathymetry automatically derived from ICESat-2 constraining lake depth estimates from multi-source satellite imagery. *The Cryosphere*, *15*, 5115–5132. https://doi.org/10.5194/tc-15-5115-2021

Degnan, J. J. (2002). Photon-counting multikilohertz microlaser altimeters for airborne and spaceborne topographic measurements. *Journal of Geodynamics*, *34*, 503–549. https://doi.org/10.1016/S0264-3707(02)00045-5

Depetris, P. J. (2021). The Importance of Monitoring River Water Discharge. *Frontiers in Water*, *3*, 745912. https://doi.org/10.3389/frwa.2021.745912

Dettmering, D., Ellenbeck, L., Scherer, D., Schwatke, C., & Niemann, C. (2020). Potential and limitations of satellite altimetry constellations for monitoring surface water storage changes—A case study in the Mississippi basin. *Remote Sensing*, *12*. https://doi.org/10.3390/rs12203320

Dettmering, D., & Schwatke, C. (2022). Ionospheric Corrections for Satellite Altimetry - Impact on Global Mean Sea Level Trends. *Earth and Space Science*, *9*. https://doi.org/10.1029/2021EA002098

Dhote, P. R., Agarwal, A., Singhal, G., Calmant, S., Thakur, P. K., Oubanas, H., Paris, A., & Singh, R. P. (2024). River Water Level and Water Surface Slope Measurement from Spaceborne Radar and Lidar Altimetry: Evaluation and Implications for Hydrological Studies in the Ganga River. *IEEE Journal of Selected Topics in Applied Earth Observations and Remote Sensing*, 1–20. https://doi.org/10.1109/JSTARS.2024.3379874

Ding, F. (2009). Study on Information Extraction of Water Body with a New Water Index (NWI). *Science of Surveying and Mapping*, *34*, 155–157.

Donlon, C. J., Cullen, R., Giulicchi, L., Vuilleumier, P., Francis, C. R., Kuschnerus, M., Simpson, W., Bouridah, A., Caleno, M., Bertoni, R., Rancaño, J., Pourier, E., Hyslop, A., Mulcahy, J., Knockaert, R., Hunter, C., Webb, A., Fornari, M., Vaze, P., ... Tavernier, G. (2021). The Copernicus Sentinel-6 mission: Enhanced continuity of satellite sea level measurements from space. *Remote Sensing of Environment*, *258*, 112395. https://doi.org/10.1016/j.rse.2021.112395

Durand, M. T., Dai, C., Moortgat, J., Yadav, B., de Moraes Frasson, R. P., Li, Z., Wadkwoski, K., Howat, I., & Pavelsky, T. M. (2024). Using river hypsometry to improve remote sensing of river discharge. *Remote Sensing of Environment*, *315*, 114455. https://doi.org/10.1016/j.rse.2024.114455

Durand, M. T., Gleason, C. J., Garambois, P. A., Bjerklie, D., Smith, L. C., Roux, H., Rodriguez, E., Bates, P. D., Pavelsky, T. M., Monnier, J., Chen, X., Baldassarre, G. D., Fiset, J.-M., Flipo, N., d. M. Frasson, R. P., Fulton, J., Goutal, N., Hossain, F., Humphries, E., ... Vilmin, L. (2016). An intercomparison of remote sensing river discharge estimation algorithms from measurements of river height, width, and slope. *Water Resources Research*, *52*, 4527–4549. https://doi.org/10.1002/2015WR018434

Durand, M. T., Gleason, C. J., Pavelsky, T. M., de Moraes Frasson, R. P., Turmon, M., David, C. H., Altenau, E. H., Tebaldi, N., Larnier, K., Monnier, J., Malaterre, P. O., Oubanas, H., Allen, G. H., Astifan, B., Brinkerhoff, C., Bates, P. D., Bjerklie, D., Coss, S., Dudley, R., ... Wang, J. (2023). A Framework for Estimating Global River Discharge From the Surface Water and Ocean Topography Satellite Mission. *Water Resources Research*, *59*. https://doi.org/10.1029/2021WR031614

Durand, M. T., Neal, J., Rodríguez, E., Andreadis, K. M., Smith, L. C., & Yoon, Y. (2014). Estimating reach-averaged discharge for the River Severn from measurements of river water surface elevation and slope. *Journal of Hydrology*, *511*, 92–104. https://doi.org/10.1016/j.jhydrol.2013.12.050

DVWK (Deutscher Verband für Wasserwirtschaft und Kulturbau e. V.) (1990). Hydraulische Methoden zur Erfassung von Rauheiten. I. Bestimmung von Rauheiten. II. Äquivalente Sandrauheiten und Stricklerbeiwerte fester und beweglicher Strömungsberandungen. Verlag Paul Parey.

Eberhardt, I., Schultz, B., Rizzi, R., Sanches, I., Formaggio, A., Atzberger, C., Mello, M., Immitzer, M., Trabaquini, K., Foschiera, W., & Luiz, A. J. B. (2016). Cloud Cover Assessment for Operational Crop Monitoring Systems in Tropical Areas. *Remote Sensing*, *8*, 219. https://doi.org/10.3390/rs8030219

Ehlers, F., Slobbe, C., Schlembach, F., Kleinherenbrink, M., & Verlaan, M. (2025). Polygon-Informed Cross-Track Altimetry (PICTA): Estimating river water level profiles with the Sentinel-6 altimeter. *Remote Sensing of Environment*, *316*, 114479. https://doi.org/10.1016/j.rse.2024.114479

Elmi, O., Tourian, M. J., Saemian, P., & Sneeuw, N. (2024). Remote Sensing-Based Extension of GRDC Discharge Time Series - A Monthly Product with Uncertainty Estimates. *Scientific Data 2024 11:1*, *11*, 1–12. https://doi.org/10.1038/s41597-024-03078-6

Emery, W., & Camps, A. (2017). Introduction to Satellite Remote Sensing. Elsevier. https://doi.org/10.1016/b978-0-12-809254-5.00001-4

eoPortal. (2024). Satellite Missions catalogue. ESA. Retrieved April 11, 2024, from https://www.eoportal.org/satellite-missions

ESA (European Space Agency). (2023). Sentinel-3 SRAL Land User Handbook. Version 1.1. https://sentinels.copernicus.eu/documents/247904/4871083/Sentinel-3+SRAL+Land+User+Handbook+V1.1.pdf

Escudier, P., Couhert, A., Mercier, F., Mallet, A., Thibaut, P., Tran, N., Amarouche, L., Picard, B., Carrere, L., Dibarboure, G., Ablain, M., Richard, J., Steunou, N., Dubois, P., Rio, M.-H., & Dorandeu, J. (2017). Satellite Radar Altimetry. In D. Stammer & A. Cazenave (Eds.), *Satellite Altimetry over Oceans and Land Surfaces* (1st ed.). CRC Press. https://doi.org/10.1201/9781315151779-1

Feyisa, G. L., Meilby, H., Fensholt, R., & Proud, S. R. (2014). Automated Water Extraction Index: A new technique for surface water mapping using Landsat imagery. *Remote Sensing of Environment*, *140*, 23–35. https://doi.org/10.1016/j.rse.2013.08.029

Fischenich, C. (2000). Robert Manning (A Historical Perspective) (EMRRP Technical Notes Collection No. ERDCTN-EMRRP-SR-10). U.S. Army Engineer Research and Development Center. Vicksburg, MS. www.wes.army.mil/el/emrrp

Fletcher, R. (1970). A new approach to variable metric algorithms. *The Computer Journal*, *13*(3), 317–322. https://doi.org/10.1093/comjnl/13.3.317

Frias, M. C., Vesterhauge, A. R., Olesen, D. H., Bandini, F., Grosen, H., Nielsen, S. Y., & Bauer-Gottwein, P. (2025). Combining UAS LiDAR, Sonar, and Radar Altimetry for River Hydraulic Characterization. *Drones 2025, Vol. 9, Page 31*, *9*, 31. https://doi.org/10.3390/DRONES9010031

Garambois, P. A., Calmant, S., Roux, H., Paris, A., Monnier, J., Finaud-Guyot, P., Montazem, A. S., & da Silva, J. S. (2017). Hydraulic visibility: Using satellite altimetry to parameterize a hydraulic model of an ungauged reach of a braided river. *Hydrological Processes*, *31*, 756–767. https://doi.org/10.1002/hyp.11033

Garambois, P. A., & Monnier, J. (2015). Inference of effective river properties from remotely sensed observations of water surface. *Advances in Water Resources*, *79*, 103–120. https://doi.org/10.1016/j.advwatres.2015.02.007

Gauckler, P. G. (1868). Du mouvement de l'eau dans les conduites. *Annales des ponts et chaussées*, *15*, 229–281.

GCOS (Global Climate Observing System). (2022). The 2022 GCOS ECVs Requirements. World Meteorological Organization. https://library.wmo.int/idurl/4/58111

Gerber, F., Blake, L., & Savola, N. (2023, December). optimParallel-python: Type hints (Version v0.1.3). Zenodo. https://doi.org/10.5281/zenodo.10426043

Gerber, F., & Furrer, R. (2019). optimParallel: An R Package Providing a Parallel Version of the L-BFGS-B Optimization Method. *The R Journal*, *11*(1), 352–358. https://doi.org/10.32614/RJ-2019-030

Gleason, C. J., & Durand, M. T. (2020). Remote sensing of river discharge: A review and a framing for the discipline. *Remote Sensing*, *12*, 1–28. https://doi.org/10.3390/rs12071107

Goldfarb, D. (1970). A family of variable-metric methods derived by variational means. *Mathematics of Computation*, *24*(109), 23–26. https://doi.org/10.1090/s0025-5718-1970-0258249-6

Gommenginger, C., Thibaut, P., Fenoglio-Marc, L., Quartly, G., Deng, X., Gómez-Enri, J., Challenor, P., & Gao, Y. (2011). Retracking Altimeter Waveforms Near the Coasts. Springer Berlin Heidelberg. https://doi.org/10.1007/978-3-642-12796-0_4

Hagemann, M. W., Gleason, C. J., & Durand, M. T. (2017). BAM: Bayesian AMHG-Manning Inference of Discharge Using Remotely Sensed Stream Width, Slope, and Height. *Water Resources Research*, *53*, 9692–9707. https://doi.org/10.1002/2017WR021626

Halicki, M., Schwatke, C., & Niedzielski, T. (2023). The impact of the satellite ground track shift on the accuracy of altimetric measurements on rivers: A case study of the Sentinel-3 altimetry on the Odra/Oder River. *Journal of Hydrology*, *617*, 128761. https://doi.org/10.1016/j.jhydrol.2022.128761

Hannah, D. M., Demuth, S., van Lanen, H. A. J., Looser, U., Prudhomme, C., Rees, G., Stahl, K., & Tallaksen, L. M. (2011). Large-scale river flow archives: Importance, current status and future needs. *Hydrological Processes*, *25*, 1191–1200. https://doi.org/10.1002/hyp.7794

Henke, N. (2024). Gewässertiefen aus dem Weltall: Analyse von Laseraltimetermessungen über Seen und Flüssen [Bachelor's thesis]. Technische Universität München.

IPCC (Intergovernmental Panel on Climate Change). (2022). The Ocean and Cryosphere in a Changing Climate: Special Report of the Intergovernmental Panel on Climate Change. Cambridge University Press. https://doi.org/10.1017/9781009157964

Jain, M. K., Kothyari, U. C., & Raju, K. G. R. (2004). A GIS based distributed rainfall-runoff model. *Journal of Hydrology*, *299*, 107–135. https://doi.org/10.1016/j.jhydrol.2004.04.024

Jaramillo, F., Aminjafari, S., Castellazzi, P., Fleischmann, A., Fluet-Chouinard, E., Hashemi, H., Hubinger, C., Martens, H. R., Papa, F., Schöne, T., Tarpanelli, A., Virkki, V., Wang-Erlandsson, L., Abarca-del-Rio, R., Borsa, A., Destouni, G., Di Baldassarre, G., Moore, M.-L., Posada-Marín, J. A., … Salazar, J. F. (2024). The Potential of Hydrogeodesy to Address Water-Related and Sustainability Challenges. *Water Resources Research*, *60*(11). https://doi.org/10.1029/2023wr037020

Jasinski, M., Gsfc, N., Stoll, J., Hancock, D., Robbins, J., Nattala, J., Morison, J., Jones, B., Ondrusek, M., Parrish, C., Ssai, C. C., Jasinski, M., Stoll, J., Hancock, D., Robbins, J., Nattala, J., Morison, J., Jones, B., Ondrusek, M., … Carabajal, C. (2023). ICESat-2 Algorithm Theoretical Basis Document (ATBD) for Along Track Inland Surface Water Data, ATL13, Version 6. https://doi.org/10.5067/03JYGZ0758UL

Ji, L., Zhang, L., & Wylie, B. (2009). Analysis of Dynamic Thresholds for the Normalized Difference Water Index. *Photogrammetric Engineering & Remote Sensing*, *75*, 1307–1317. https://doi.org/10.14358/PERS.75.11.1307

Jinyum, G., Cheiway, H., Xiaotao, C., & Yuting, L. (2006). Improved threshold retracker for satellite altimeter waveform retracking over coastal sea*. *Progress in Natural Science*, *16*, 732–738. https://doi.org/10.1080/10020070612330061

JPL (Jet Propulsion Laboratory). (2018). Surface Water and Ocean Topography Mission (SWOT) Project Science Requirements Document (tech. rep. No. JPL D-61923) (Rev B). Jet Propulsion Laboratory, California Institute of Technology. Pasadena, CA.

JPL (Jet Propulsion Laboratory). (2024). SWOT Science Data Products User Handbook (tech. rep.) (Internal Document JPL D-109532). Jet Propulsion Laboratory, California Institute of Technology. Pasadena, CA.

Julien, P. Y. (2018). River mechanics. Cambridge University Press. https://doi.org/10.1017/9781316107072

Kauth, R. J., & Thomas, G. S. (1976). The Tasselled Cap – A Graphic Description of the Spectral-Temporal Development of Agricultural Crops as Seen by LANDSAT. *Proceedings of the LARS Symposia*, Paper 159.

Kenney, B. C. (1993). On the validity of empirical power laws. *Stochastic Hydrology and Hydraulics*, *7*, 179–194. https://doi.org/10.1007/BF01585597

Kirillov, A., Mintun, E., Ravi, N., Mao, H., Rolland, C., Gustafson, L., Xiao, T., Whitehead, S., Berg, A. C., Lo, W.-Y., Dollár, P., & Girshick, R. (2023). Segment Anything. https://doi.org/10.48550/arXiv.2304.02643

Kistler, C. (2025). Surface Area Estimation for Lakes and Reservoirs Using SWOT KaRIn Measurements [Master's thesis]. Technische Universität München.

Köhn, S. J., & Nielsen, K. (2024, December). Validation of SWOT HR PIXC 2.0 based water levels on Danish lakes. https://doi.org/10.22541/essoar.173325114.47640060/v1

Krabbenhoft, C. A., Allen, G. H., Lin, P., Godsey, S. E., Allen, D. C., Burrows, R. M., DelVecchia, A. G., Fritz, K. M., Shanafield, M., Burgin, A. J., Zimmer, M. A., Datry, T., Dodds, W. K., Jones, C. N., Mims, M. C., Franklin, C., Hammond, J. C., Zipper, S., Ward, A. S., … Olden, J. D. (2022). Assessing placement bias of the global river gauge network. *Nature Sustainability*, *5*, 586–592. https://doi.org/10.1038/s41893-022-00873-0

Kummu, M., de Moel, H., Ward, P. J., & Varis, O. (2011). How Close Do We Live to Water? A Global Analysis of Population Distance to Freshwater Bodies (M. Perc, Ed.). *PLoS ONE*, *6*, e20578. https://doi.org/10.1371/journal.pone.0020578

Larnier, K., Monnier, J., Garambois, P.-A., & Verley, J. (2020). River discharge and bathymetry estimation from SWOT altimetry measurements. *Inverse Problems in Science and Engineering*, *29*(6), 759–789. https://doi.org/10.1080/17415977.2020.1803858

Larnier, K., & Monnier, J. (2023). Hybrid Neural Network - Variational Data Assimilation algorithm to infer river discharges from SWOT-like data. *Computational Geosciences*, *27*, 853–877. https://doi.org/10.1007/s10596-023-10225-2

Le Coz, J., Renard, B., Bonnifait, L., Branger, F., & Le Boursicaud, R. (2014). Combining hydraulic knowledge and uncertain gaugings in the estimation of hydrometric rating curves: A Bayesian approach. *Journal of Hydrology*, *509*, 573–587. https://doi.org/10.1016/j.jhydrol.2013.11.016

Lecher, K., Lühr, H.-P., & Zanke, U. C. E. (Eds.). (2021, June). Taschenbuch der Wasserwirtschaft (10th ed.). Springer Vieweg.

Leopold, L. B., & Maddock, T. (1953). The hydraulic geometry of stream channels and some physiographic implications. https://doi.org/10.3133/pp252

Li, X., Long, D., Huang, Q., Han, P., Zhao, F., & Wada, Y. (2019). High-temporal-resolution water level and storage change data sets for lakes on the Tibetan Plateau during 2000–2017 using multiple altimetric missions and Landsat-derived lake shoreline positions. *Earth System Science Data*, *11*, 1603–1627. https://doi.org/10.5194/essd-11-1603-2019

Liu, D. C., & Nocedal, J. (1989). On the limited memory BFGS method for large scale optimization. *Mathematical Programming*, *45*, 503–528. https://doi.org/10.1007/BF01589116

Liu, J., Bauer-Gottwein, P., Frias, M. C., Musaeus, A. F., Christoffersen, L., & Jiang, L. (2023). Stage-Slope-Discharge Relationships Upstream of River Confluences Revealed by Satellite Altimetry. *Geophysical Research Letters*, *50*(23). https://doi.org/10.1029/2023gl106394

LUBW (Landesanstalt für Umweltschutz Baden-Württemberg). (2002). Hydraulik naturnaher Fließgewässer: Teil 2 – Neue Berechnungsverfahren für naturnahe Gewässerstrukturen (Landesanstalt für Umweltschutz Baden-Württemberg, Ed.; 1st ed.). Landesanstalt für Umweltschutz Baden-Württemberg.

Magruder, L. A., Farrell, S. L., Neuenschwander, A., Duncanson, L., Csatho, B., Kacimi, S., & Fricker, H. A. (2024). Monitoring Earth's climate variables with satellite laser altimetry. *Nature Reviews Earth & Environment*, *5*, 120–136. https://doi.org/10.1038/s43017-023-00508-8

Manning, R. (1891). On the flow of water in open channels and pipes. *Transactions of the Institution of Civil Engineers of Ireland*, *20*, 161–207. https://doi.org/10.48495/r207ts96k

Marchi, M., Castellanos-Acuña, D., Hamann, A., Wang, T., Ray, D., & Menzel, A. (2020). ClimateEU, scale-free climate normals, historical time series, and future projections for Europe. *Scientific Data*, *7*, 428. https://doi.org/10.1038/s41597-020-00763-0

Markus, T., Neumann, T., Martino, A., Abdalati, W., Brunt, K., Csatho, B., Farrell, S., Fricker, H., Gardner, A., Harding, D., Jasinski, M., Kwok, R., Magruder, L., Lubin, D., Luthcke, S., Morison, J., Nelson, R., Neuenschwander, A., Palm, S., … Zwally, J. (2017). The Ice, Cloud, and land Elevation Satellite-2 (ICESat-2): Science requirements, concept, and implementation. *Remote Sensing of Environment*, *190*, 260–273. https://doi.org/10.1016/j.rse.2016.12.029

Maubant, L., Dodd, L., & Tregoning, P. (2025). Assessing the Accuracy of SWOT Measurements of Water Bodies in Australia. *Geophysical Research Letters*, *52*, e2024GL114084. https://doi.org/10.1029/2024GL114084

Messager, M. L., Lehner, B., Grill, G., Nedeva, I., & Schmitt, O. (2016). Estimating the volume and age of water stored in global lakes using a geo-statistical approach. *Nature Communications*, *7*, 13603. https://doi.org/10.1038/ncomms13603

Moody, J. A., & Troutman, B. M. (2002). Characterization of the spatial variability of channel morphology. *Earth Surface Processes and Landforms*, *27*, 1251–1266. https://doi.org/10.1002/esp.403

Mueller, D. S., Abad, J. D., García, C. M., Gartner, J. W., García, M. H., & Oberg, K. A. (2007). Errors in Acoustic Doppler Profiler Velocity Measurements Caused by Flow Disturbance. *Journal of Hydraulic Engineering*, *133*, 1411–1420. https://doi.org/10.1061/(ASCE)0733-9429(2007)133:12(1411)

Musaeus, A. F., Kittel, C. M. M., Luchner, J., Frias, M. C., & Bauer-Gottwein, P. (2024). Hydraulic River Models From ICESat-2 Elevation and Water Surface Slope [e2023WR036428 2023WR036428]. *Water Resources Research*, *60*(6), e2023WR036428. https://doi.org/10.1029/2023WR036428

Neumann, T. A., Martino, A. J., Markus, T., Bae, S., Bock, M. R., Brenner, A. C., Brunt, K. M., Cavanaugh, J., Fernandes, S. T., Hancock, D. W., Harbeck, K., Lee, J., Kurtz, N. T., Luers, P. J., Luthcke, S. B., Magruder, L., Pennington, T. A., Ramos-Izquierdo, L., Rebold, T., … Thomas, T. C. (2019). The Ice, Cloud, and Land Elevation Satellite – 2 mission: A global geolocated photon product derived from the Advanced Topographic Laser Altimeter System. *Remote Sensing of Environment*, *233*, 111325. https://doi.org/10.1016/j.rse.2019.111325

Nielsen, K., Stenseng, L., Andersen, O. B., & Knudsen, P. (2017). The performance and potentials of the CryoSat-2 SAR and SARIn modes for lake level estimation. *Water (Switzerland)*, *9*. https://doi.org/10.3390/w9060374

Nielsen, K., Zakharova, E., Tarpanelli, A., Andersen, O. B., & Benveniste, J. (2022). River levels from multi mission altimetry, a statistical approach. *Remote Sensing of Environment*, *270*, 112876. https://doi.org/10.1016/j.rse.2021.112876

Nikuradse, J. (1932). Gesetzmäßigkeiten der turbulenten Strömung in glatten Rohren. *VDI-Forschungsheft*, (356).

Niwa, Y., & Fujii, Y. (2020). A conjugate BFGS method for accurate estimation of a posterior error covariance matrix in a linear inverse problem. *Quarterly Journal of the Royal Meteorological Society*, *146*, 3118–3143. https://doi.org/10.1002/qj.3838

Nocedal, J., & Wright, S. J. (2006). Numerical Optimization. Springer New York. https://doi.org/10.1007/978-0-387-40065-5

Normandin, C., Frappart, F., Baghdadi, N., Bourrel, L., Luque, S. P., Ygorra, B., Kitambo, B., Papa, F., Riazanoff, S., & Wigneron, J.-P. (2024). First results of the surface water ocean topography (SWOT) observations to rivers elevation profiles in the Cuvette Centrale of the Congo Basin. *Frontiers in Remote Sensing*, *5*. https://doi.org/10.3389/frsen.2024.1466695

Normandin, C., Frappart, F., Diepkilé, A. T., Marieu, V., Mougin, E., Blarel, F., Lubac, B., Braquet, N., & Ba, A. (2018). Evolution of the Performances of Radar Altimetry Missions from ERS-2 to Sentinel-3A over the Inner Niger Delta. *Remote Sensing*, *10*(6), 833. https://doi.org/10.3390/rs10060833

Osco, L. P., Wu, Q., de Lemos, E. L., Gonçalves, W. N., Ramos, A. P. M., Li, J., & Marcato, J. (2023). The Segment Anything Model (SAM) for remote sensing applications: From zero to one shot. *International Journal of Applied Earth Observation and Geoinformation*, *124*, 103540. https://doi.org/10.1016/j.jag.2023.103540

Oubanas, H., Gejadze, I., Malaterre, P.-O., Durand, M. T., Wei, R., Frasson, R. P. M., & Domeneghetti, A. (2018). Discharge Estimation in Ungauged Basins Through Variational Data Assimilation: The Potential of the SWOT Mission. *Water Resources Research*, *54*(3), 2405–2423. https://doi.org/10.1002/2017wr021735

Papageorgiou, M., Leibold, M., & Buss, M. (2012). 4. Minimierung einer Funktion mehrerer Variablen ohne Nebenbedingungen. Springer Berlin Heidelberg. https://doi.org/10.1007/978-3-540-34013-3_4

Paris, A., Dias de Paiva, R., Santos da Silva, J., Medeiros Moreira, D., Calmant, S., Garambois, P. A., Collischonn, W., Bonnet, M.-P., & Seyler, F. (2016). Stage-discharge rating curves based on satellite altimetry and modeled discharge in the Amazon basin. *Water Resources Research*, *52*(5), 3787–3814. https://doi.org/10.1002/2014wr016618

Pavelsky, T. M. (2014). Using width-based rating curves from spatially discontinuous satellite imagery to monitor river discharge. *Hydrological Processes*. https://doi.org/10.1002/hyp.10157

Peral, E., Esteban-Fernández, D., Rodríguez, E., McWatters, D., Bleser, J.-W. D., Ahmed, R., Chen, A. C., Slimko, E., Somawardhana, R., Knarr, K., Johnson, M., Jaruwatanadilok, S., Chan, S., Wu, X., Clark, D., Peters, K., Chen, C. W., Mao, P., Khayatian, B., … Srinivasan, K. (2024). KaRIn, the Ka-Band Radar Interferometer of the SWOT Mission: Design and in-Flight Performance. *IEEE Transactions on Geoscience and Remote Sensing*, *62*, 1–27. https://doi.org/10.1109/TGRS.2024.3405343

PlanetScope. (2023). Planet Imagery Product Specifications. https://assets.planet.com/docs/Planet_Combined_Imagery_Product_Specs_letter_screen.pdf

Remy, F., Memin, A., & Velicogna, I. (2017). Applications of Satellite Altimetry to Study the Antarctic Ice Sheet. In D. Stammer & A. Cazenave (Eds.), *Satellite Altimetry Over Oceans and Land Surfaces* (1st ed., pp. 505–522). CRC Press. https://doi.org/10.1201/9781315151779-15

Rezende, I., Fatras, C., Oubanas, H., Gejadze, I., Malaterre, P.-O., Peña-Luque, S., & Domeneghetti, A. (2025). Reconstruction of Effective Cross-Sections from DEMs and Water Surface Elevation. *Remote Sensing*, *17*(6), 1020. https://doi.org/10.3390/rs17061020

Rezende, I., Pierre-Olivier, Oubanas, H., Gejadze, I., Fatras, C., Peña-Luque, S., & Quittard, D. (2023). Global Discharge Estimation from SWOT Satellite and reference DEMs [Poster]. *Hydrospace Conference*. https://web.archive.org/web/20240831223116/https://az659834.vo.msecnd.net/eventsairwesteuprod/production-nikal-public/142f43253a3b4740b99e359a54b98eb3

Rhoads, B. L. (2020). River dynamics: Geomorphology to support management. Cambridge University Press. https://doi.org/10.1017/9781108164108

Riggs, R. M., Allen, G. H., Wang, J., Pavelsky, T. M., Gleason, C. J., David, C. H., & Durand, M. T. (2023). Extending global river gauge records using satellite observations. *Environmental Research Letters*, *18*(6), 064027. https://doi.org/10.1088/1748-9326/acd407

Rosgen, D. (1996). Applied River Morphology (2nd). Wildland Hydrology.

Rosmorduc, V., Benveniste, J., Bronner, E., Dinardo, S., Lauret, O., Maheu, C., Milagro, M., Picot, N., Ambrozio, A., Escolà, R., Garcia-Mondejar, A., Restano, M., Schrama, E., & Terra-Homem, M. (2016). Radar Altimetry Tutorial (J. Benveniste & N. Picot, Eds.; tech. rep.). https://www.altimetry.info

Ryan, J. C., Smith, L. C., Cooley, S. W., Pitcher, L. H., & Pavelsky, T. M. (2020). Global Characterization of Inland Water Reservoirs Using ICESat-2 Altimetry and Climate Reanalysis. *Geophysical Research Letters*, *47*, 1–10. https://doi.org/10.1029/2020GL088543

Santos da Silva, J., Calmant, S., Seyler, F., Rotunno Filho, O. C., Cochonneau, G., & Mansur, W. J. (2010). Water levels in the Amazon basin derived from the ERS 2 and ENVISAT radar altimetry missions. *Remote Sensing of Environment*, *114*(10), 2160–2181. https://doi.org/10.1016/j.rse.2010.04.020

Schenk, T., & Csathó, B. (2012). A new methodology for detecting ice sheet surface elevation changes from laser altimetry data. *IEEE Transactions on Geoscience and Remote Sensing*, *50*, 3302–3316. https://doi.org/10.1109/TGRS.2011.2182357

Scherer, D., Schwatke, C., Dettmering, D., & Seitz, F. (2020). Long-Term Discharge Estimation for the Lower Mississippi River Using Satellite Altimetry and Remote Sensing Images. *Remote Sensing*, *12*, 2693. https://doi.org/10.3390/rs12172693

Scherer, D., Schwatke, C., Dettmering, D., & Seitz, F. (2022). ICESat-2 Based River Surface Slope and Its Impact on Water Level Time Series From Satellite Altimetry. *Water Resources Research*, *58*, 1–25. https://doi.org/10.1029/2022WR032842

Scherer, D., Schwatke, C., Dettmering, D., & Seitz, F. (2023). ICESat-2 river surface slope (IRIS): A global reach-scale water surface slope dataset. *Scientific Data*, *10*, 359. https://doi.org/10.1038/s41597-023-02215-x

Scherer, D., Schwatke, C., Dettmering, D., & Seitz, F. (2024). Monitoring river discharge from space: An optimization approach with uncertainty quantification for small ungauged rivers. *Remote Sensing of Environment*, *315*, 114434. https://doi.org/10.1016/j.rse.2024.114434

Schumm, S. A. (1977). The Fluvial System. John Wiley & Sons.

Schwatke, C., Dettmering, D., Bosch, W., & Seitz, F. (2015). DAHITI - An innovative approach for estimating water level time series over inland waters using multi-mission satellite altimetry. *Hydrology and Earth System Sciences*, *19*(10), 4345–4364. https://doi.org/10.5194/hess-19-4345-2015

Schwatke, C., Dettmering, D., Passaro, M., Hart-Davis, M., Scherer, D., Müller, F. L., Bosch, W., & Seitz, F. (2023). OpenADB: DGFI-TUM's Open Altimeter Database. *Geoscience Data Journal*. https://doi.org/10.1002/gdj3.233

Schwatke, C., Dettmering, D., & Seitz, F. (2020). Volume Variations of Small Inland Water Bodies from a Combination of Satellite Altimetry and Optical Imagery. *Remote Sensing*, *12*, 1606. https://doi.org/10.3390/rs12101606

Schwatke, C., Halicki, M., & Scherer, D. (2024). Generation of High-Resolution Water Surface Slopes From Multi-Mission Satellite Altimetry. *Water Resources Research*, *60*. https://doi.org/10.1029/2023WR034907

Schwatke, C., Scherer, D., & Dettmering, D. (2019). Automated Extraction of Consistent Time-Variable Water Surfaces of Lakes and Reservoirs Based on Landsat and Sentinel-2. *Remote Sensing*, *11*, 1010. https://doi.org/10.3390/rs11091010

Seyler, F., Calmant, S., da Silva, J. S., Moreira, D. M., Mercier, F., & Shum, C. (2013). From TOPEX/Poseidon to Jason-2/OSTM in the Amazon basin. *Advances in Space Research*, *51*, 1542–1550. https://doi.org/10.1016/j.asr.2012.11.002

Shanno, D. F. (1970). Conditioning of quasi-Newton methods for function minimization. *Mathematics of Computation*, *24*(111), 647–656. https://doi.org/10.1090/s0025-5718-1970-0274029-x

Shumilova, O., Tockner, K., Sukhodolov, A., Khilchevskyi, V., Meester, L. D., Stepanenko, S., Trokhymenko, G., Hernández-Agüero, J. A., & Gleick, P. (2023). Impact of the Russia–Ukraine armed conflict on water resources and water infrastructure. *Nature Sustainability*, *6*, 578–586. https://doi.org/10.1038/s41893-023-01068-x

Sichangi, A., Wang, L., & Hu, Z. (2018). Estimation of River Discharge Solely from Remote-Sensing Derived Data: An Initial Study Over the Yangtze River. *Remote Sensing*, *10*, 1385. https://doi.org/10.3390/rs10091385

Stammer, D., & Cazenave, A. (2017, October). Satellite Altimetry over Oceans and Land Surfaces (D. Stammer & A. Cazenave, Eds.). CRC Press. https://doi.org/10.1201/9781315151779

Strahler, A. N. (1952). Hypsometric (area-altitude) analysis of erosional topography. *GSA Bulletin*, *63*(11), 1117–1142. https://doi.org/10.1130/0016-7606(1952)63[1117:HAAOET]2.0.CO;2

Strickler, A. (1923). Beiträge zur frage der geschwindigkeitsformel und der rauhigkeitszahlen für ströme, kanäle und geschlossene leitungen. *Bulletin technique de la Suisse romande*, *49*(26), 315. https://doi.org/10.5169/seals-38271

Tarpanelli, A., Barbetta, S., Brocca, L., & Moramarco, T. (2013). River discharge estimation by using altimetry data and simplified flood routing modeling. *Remote Sensing*, *5*, 4145–4162. https://doi.org/10.3390/rs5094145

Tarpanelli, A., Santi, E., Tourian, M. J., Filippucci, P., Amarnath, G., & Brocca, L. (2019). Daily River Discharge Estimates by Merging Satellite Optical Sensors and Radar Altimetry Through Artificial Neural Network. *IEEE Transactions on Geoscience and Remote Sensing*, *57*, 329–341. https://doi.org/10.1109/TGRS.2018.2854625

Tarpanelli, A., Schumann, G., Kittel, C., Andersson, J., Barbetta, S., Bauer-Gottwein, P., Cantoni Igomez, E., Chewning, C., Ciabatta, L., Dettmering, D., Elmi, O., Filippucci, P., Gal, L., González-Jiménez, M., Gustafsson, D., Hundecha, Y., Larnicol, G., Larnier, K., Massari, C., … Volden, E. (2025). Earth Observation data for Advancing Flood Forecasting: EO4FLOOD project [Project website: https://eo4flood.org/]. https://doi.org/10.5194/egusphere-egu25-6671

Thompson, J. R., Gosling, S. N., Zaherpour, J., & Laizé, C. L. (2021). Increasing Risk of Ecological Change to Major Rivers of the World With Global Warming. *Earth's Future*, *9*. https://doi.org/10.1029/2021EF002048

Tourian, M. J., Sneeuw, N., & Bárdossy, A. (2013). A quantile function approach to discharge estimation from satellite altimetry (ENVISAT). *Water Resources Research*, *49*, 4174–4186. https://doi.org/10.1002/wrcr.20348

Tourian, M. J., Tarpanelli, A., Elmi, O., Qin, T., Brocca, L., Moramarco, T., & Sneeuw, N. (2016). Spatiotemporal densification of river water level time series by multimission satellite altimetry. *Water Resources Research*, *52*, 1140–1159. https://doi.org/10.1002/2015WR017654

Turnipseed, D. P., & Sauer, V. B. (2010). Discharge measurements at gaging stations. U.S. Geological Survey. https://doi.org/10.3133/tm3A8

UN (United Nations). (2024). The United Nations World Water Development Report 2024: Water for Prosperity and Peace. UNESCO.

Urban, T. J., Schutz, B. E., & Neuenschwander, A. L. (2008). A Survey of ICESat Coastal Altimetry Applications: Continental Coast, Open Ocean Island, and Inland River. *Terrestrial, Atmospheric and Oceanic Sciences*, *19*, 1. https://doi.org/10.3319/TAO.2008.19.1-2.1(SA)

Vicente-Serrano, S. M., Lopez-Moreno, J.-I., Beguería, S., Lorenzo-Lacruz, J., Sanchez-Lorenzo, A., García-Ruiz, J. M., Azorin-Molina, C., Morán-Tejeda, E., Revuelto, J., Trigo, R., Coelho, F., & Espejo, F. (2014). Evidence of increasing drought severity caused by temperature rise in southern Europe. *Environmental Research Letters*, *9*(4), 044001. https://doi.org/10.1088/1748-9326/9/4/044001

Vuilleumier, P., & Egido, A. (2023). The Sentinel-3 Next Generation Topography (S3NG-TOPO) Mission; Enhancing Continuity, Performance and Hydrology Capabilities [Presentation]. https://doi.org/10.24400/527896/A03-2023.3823

Wang, H., & He, G. (2022). Rivers: Linking nature, life, and civilization. *River*, *1*, 25–36. https://doi.org/10.1002/rvr2.7

Wilby, R. L. (2019). A global hydrology research agenda fit for the 2030s. *Hydrology Research*, *50*(6), 1464–1480. https://doi.org/10.2166/nh.2019.100

Willgoose, G., & Hancock, G. (1998). Revisiting the hypsometric curve as an indicator of form and process in transport-limited catchment. *Earth Surface Processes and Landforms*, *23*, 611–623. https://doi.org/10.1002/(SICI)1096-9837(199807)23:7<611::AID-ESP872>3.0.CO;2-Y

Wingham, D., Rapley, C., & D, G. (1986). New Techniques in Satellite Altimeter Tracking Systems. *Digest - International Geoscience and Remote Sensing Symposium (IGARSS)*, 1339–1344.

Wu, Q., & Osco, L. P. (2023). samgeo: A Python package for segmenting geospatial data with the Segment Anything Model (SAM). *Journal of Open Source Software*, *8*(89), 5663. https://doi.org/10.21105/joss.05663

Wulder, M. A., Hilker, T., White, J. C., Coops, N. C., Masek, J. G., Pflugmacher, D., & Crevier, Y. (2015). Virtual constellations for global terrestrial monitoring. *Remote Sensing of Environment*, *170*, 62–76. https://doi.org/10.1016/j.rse.2015.09.001

Wulder, M. A., Roy, D. P., Radeloff, V. C., Loveland, T. R., Anderson, M. C., Johnson, D. M., Healey, S., Zhu, Z., Scambos, T. A., Pahlevan, N., Hansen, M., Gorelick, N., Crawford, C. J., Masek, J. G., Hermosilla, T., White, J. C., Belward, A. S., Schaaf, C., Woodcock, C. E., ... Cook, B. D. (2022). Fifty years of Landsat science and impacts. *Remote Sensing of Environment*, *280*, 113195. https://doi.org/10.1016/j.rse.2022.113195

Xiang, J., Li, H., Zhao, J., Cai, X., & Li, P. (2021). Inland water level measurement from spaceborne laser altimetry: Validation and comparison of three missions over the Great Lakes and lower Mississippi River. *Journal of Hydrology*, *597*. https://doi.org/10.1016/j.jhydrol.2021.126312

Xiao, W., Hui, F., Cheng, X., & Liang, Q. (2023). An automated algorithm to retrieve the location and depth of supraglacial lakes from ICESat-2 ATL03 data. *Remote Sensing of Environment*, *298*, 113730. https://doi.org/10.1016/j.rse.2023.113730

Xu, H. (2006). Modification of normalised difference water index (NDWI) to enhance open water features in remotely sensed imagery. *International Journal of Remote Sensing*, *27*, 3025–3033. https://doi.org/10.1080/01431160600589179

Xu, N., Ma, Y., Zhou, H., Zhang, W., Zhang, Z., & Wang, X. H. (2022). A Method to Derive Bathymetry for Dynamic Water Bodies Using ICESat-2 and GSWD Data Sets. *IEEE Geoscience and Remote Sensing Letters*, *19*, 1–5. https://doi.org/10.1109/LGRS.2020.3019396

Ye, A., Zhou, Z., You, J., Ma, F., & Duan, Q. (2018). Dynamic Manning's roughness coefficients for hydrological modelling in basins. *Hydrology Research*, *49*, 1379–1395. https://doi.org/10.2166/nh.2018.175

Yu, L., Zhang, H., Gong, W., & Ma, X. (2024). Validation of Mainland Water Level Elevation Products From SWOT Satellite. *IEEE Journal of Selected Topics in Applied Earth Observations and Remote Sensing*, *17*, 13494–13505. https://doi.org/10.1109/JSTARS.2024.3435363

Zakharova, E., Nielsen, K., Kamenev, G., & Kouraev, A. (2020). River discharge estimation from radar altimetry: Assessment of satellite performance, river scales and methods. *Journal of Hydrology*, *583*(January), 124561. https://doi.org/10.1016/j.jhydrol.2020.124561

Zhang, Y., Zheng, H., Zhang, X., Leung, L. R., Liu, C., Zheng, C., Guo, Y., Chiew, F. H. S., Post, D., Kong, D., Beck, H. E., Li, C., & Blöschl, G. (2023). Future global streamflow declines are probably more severe than previously estimated. *Nature Water*, *1*, 261–271. https://doi.org/10.1038/s44221-023-00030-7

Zhao, Y., Fu, J., Pang, Z., Jiang, W., Zhang, P., & Qi, Z. (2025). Validation of Inland Water Surface Elevation from SWOT Satellite Products: A Case Study in the Middle and Lower Reaches of the Yangtze River. *Remote Sensing*, *17*, 1330. https://doi.org/10.3390/rs17081330

Zhu, C., Byrd, R. H., Lu, P., & Nocedal, J. (1997). Algorithm 778: L-BFGS-B: Fortran subroutines for large-scale bound-constrained optimization. *ACM Transactions on Mathematical Software*, *23*, 550–560. https://doi.org/10.1145/279232.279236

Zhu, Z., Wang, S., & Woodcock, C. E. (2015). Improvement and expansion of the Fmask algorithm: cloud, cloud shadow, and snow detection for Landsats 4–7, 8, and Sentinel 2 images. *Remote Sensing of Environment*, *159*, 269–277. https://doi.org/10.1016/j.rse.2014.12.014

Zhu, Z., & Woodcock, C. E. (2012). Object-based cloud and cloud shadow detection in Landsat imagery. *Remote Sensing of Environment*, *118*, 83–94. https://doi.org/10.1016/j.rse.2011.10.028

List of Figures

List of Tables

Acronyms

ADCP	*Acoustic Doppler Current Profiler*
ADM	*Absolute Deviation Around the Median*
AOI	*Area of Interest*
ATLAS	*Advanced Topographic Laser Altimeter System*
AWAX	*Automated Water Area Extraction Tool*
$AWEI_{nsh}$	*Automated Water Extraction Index for Non-Shadow Areas*
$AWEI_{sh}$	*Automated Water Extraction Index for Shadow Areas*
BFGS	*Broyden–Fletcher–Goldfarb–Shanno Algorithm*
DAHITI	*Database for Hydrological Time Series of Inland Waters*
DEM	*Digital Elevation Model*
DORIS	*Doppler Orbitography and Radiopositioning Integrated by Satellite*
ECV	*Essential Climate Variable*
ERS	*European Remote Sensing*
ESA	*European Space Agency*
GCOS	*Global Climate Observing System*
GLAS	*Geoscience Laser Altimeter System*
GRACE	*Gravity Recovery and Climate Experiment*
GRDC	*Global Runoff Data Centre*
GRWL	*Global River Widths from Landsat*
ICESat	*Ice, Cloud, and Land Elevation Satellite*
IRIS	*ICESat-2 River Surface Slope*
L-BFGS-B	*Limited-Memory BFGS Algorithm with Box Constraints*
LRM	*Low Resolution Mode*
MAE	*Median Absolute Error*
MMXO	*Multi-Mission Crossover Analysis*
MNDWI	*Modified Normalized Difference Water Index*
MODIS	*Moderate Resolution Imaging Spectroradiometer*
MVA	*Multi-Version Altimetry*
NASA	*National Aeronautics and Space Administration*
NIR	*Near Infrared*
NOAA	*National Oceanic and Atmospheric Administration*
NRMSE	*Normalized Root Mean Square Error*
NWI	*New Water Index*
OCOG	*Offset Center of Gravity*
OpenADB	*Open Altimeter Database*
POD	*Precise Orbit Determination*
RMSE	*Root Mean Square Error*
SAM	*Segment Anything Model*
SAR	*Synthetic Aperture Radar*
SLC	*Scan Line Corrector*
SLR	*Satellite Laser Ranging*
SNR	*Signal-to-Noise Ratio*
SRTM	*Shuttle Radar Topography Mission*
SVR	*Support Vector Regression*
SWIR	*Shortwave Infrared*
SWOT	*Surface Water and Ocean Topography*
TC_{wet}	*Tasseled Cap for Wetness*
VS	*Virtual Station*
WSA	*Water Surface Area*
WSE	*Water Surface Elevation*
WSS	*Water Surface Slope*

Appendix

P1 Long-Term Discharge Estimation for the Lower Mississippi River Using Satellite Altimetry and Remote Sensing Images

Scherer, D., Schwatke, C., Dettmering, D., & Seitz, F. (2020). **Long-Term Discharge Estimation for the Lower Mississippi River Using Satellite Altimetry and Remote Sensing Images**. *Remote Sensing*, *12*, 2693. https://doi.org/10.3390/rs12172693

Date of Publication: 20 August 2020

Abstract

Despite increasing interest in monitoring the global water cycle, the availability of in situ gauging and discharge time series is decreasing. However, this lack of ground data can partly be compensated for by using remote sensing techniques to observe river stages and discharge. In this paper, a new approach for estimating discharge by combining water levels from multi-mission satellite altimetry and surface area extents from optical imagery with physical flow equations at a single cross-section is presented and tested at the Lower Mississippi River. The datasets are combined by fitting a hypsometric curve, which is then used to derive the water level for each acquisition epoch of the long-term multi-spectral remote sensing missions. In this way, the chance of detecting water level extremes is increased and a bathymetry can be estimated from water surface extent observations. Below the minimum hypsometric water level, the river bed elevation is estimated using an empirical width-to-depth relationship in order to determine the final cross-sectional geometry. The required flow gradient is derived from the differences between virtual station elevations, which are computed in a least square adjustment from the height differences of all multi-mission satellite altimetry data that are close in time. Using the virtual station elevations, satellite altimetry data from multiple virtual stations and missions are combined to one long-term water level time series. All required parameters are estimated purely based on remote sensing data, without using any ground data or calibration. The validation at three gauging stations of the Lower Mississippi River shows large deviations primarily caused by the below average width of the predefined cross-sections. At 13 additional cross-sections situated in wide, uniform, and straight river sections nearby the gauges the Normalized Root Mean Square Error (NRMSE) varies between 10.95% and 28.43%. The Nash-Sutcliffe Efficiency (NSE) for these targets is in a range from 0.658 to 0.946.

Contribution

D.S. developed the methodology, performed the validation, and wrote the paper. C.S. provided the DAHITI data and contributed to the methodology. D.D. and F.S. contributed to the manuscript writing and helped with the discussions of the applied methods and results. All authors have read and agreed to the published version of the manuscript.

Criteria	Own Contribution
Idea and conceptual design	90%
Data acquisition and preparation	80%
Implementation and realisation	90%
Analysis and discussion	90%
Figure compilation	95%
Manuscript structure and writing	80%
Overall contribution	88%

remote sensing

MDPI

Article

Long-Term Discharge Estimation for the Lower Mississippi River Using Satellite Altimetry and Remote Sensing Images

Daniel Scherer *, Christian Schwatke, Denise Dettmering and Florian Seitz

Deutsches Geodätisches Forschungsinsitut der Technischen Universität München (DGFI-TUM), Arcisstraße 21, 80333 München, Germany; christian.schwatke@tum.de (C.S.); denise.dettmering@tum.de (D.D.); florian.seitz@tum.de (F.S.)

* Correspondence: daniel.scherer@tum.de; Tel.: +49-89-23031-1109

Received: 26 June 2020; Accepted: 17 August 2020; Published: 20 August 2020

Abstract: Despite increasing interest in monitoring the global water cycle, the availability of in situ gauging and discharge time series is decreasing. However, this lack of ground data can partly be compensated for by using remote sensing techniques to observe river stages and discharge. In this paper, a new approach for estimating discharge by combining water levels from multi-mission satellite altimetry and surface area extents from optical imagery with physical flow equations at a single cross-section is presented and tested at the Lower Mississippi River. The datasets are combined by fitting a hypsometric curve, which is then used to derive the water level for each acquisition epoch of the long-term multi-spectral remote sensing missions. In this way, the chance of detecting water level extremes is increased and a bathymetry can be estimated from water surface extent observations. Below the minimum hypsometric water level, the river bed elevation is estimated using an empirical width-to-depth relationship in order to determine the final cross-sectional geometry. The required flow gradient is derived from the differences between virtual station elevations, which are computed in a least square adjustment from the height differences of all multi-mission satellite altimetry data that are close in time. Using the virtual station elevations, satellite altimetry data from multiple virtual stations and missions are combined to one long-term water level time series. All required parameters are estimated purely based on remote sensing data, without using any ground data or calibration. The validation at three gauging stations of the Lower Mississippi River shows large deviations primarily caused by the below average width of the predefined cross-sections. At 13 additional cross-sections situated in wide, uniform, and straight river sections nearby the gauges the Normalized Root Mean Square Error (NRMSE) varies between 10.95% and 28.43%. The Nash-Sutcliffe Efficiency (NSE) for these targets is in a range from 0.658 to 0.946.

Keywords: river discharge; satellite altimetry; remote sensing; bathymetry; Manning; roughness; flow gradient; DAHITI

1. Introduction

Water is essential for all aspects of life on Earth and the global water cycle influences the climate decisively. In particular, freshwater is elementary as people's livelihood. While rivers store only 0.006% of the global freshwater resources, they are the main source for freshwater consumption and irrigation [1]. With growing needs of the Earth's increasing population and growing attention of climate change, water management developments are required to be sustainable. River discharge measurements provide the foundation for water resource planning, decision making, and design and operation of related infrastructure [2]. Moreover, they are of extreme importance for monitoring

hydrological change in space and time. As discharge combines a variety of different flow and transfer processes within the up-stream catchment, it is an essential hydrological variable widely used for tuning and calibrating hydrological models [3]. Such models help to increase our knowledge about the global water cycle. While the water cycle is affected by global warming, it also influences the climate. As water cycles between the land, oceans, and atmosphere, it changes the dynamics and thermodynamics of the climate system [4].

In situ discharge is usually calculated using the water level measured at a gauge and a functional relation (rating curve), which is calibrated and regularly adjusted by in situ velocity measurements and depth soundings [5,6]. Establishing and maintaining such a discharge station is an involved and complicated process, which is cost- and time-intensive [7]. Thus, despite the need for increased attention to the global water cycle and freshwater resources, the number of freely available in situ discharge time-series in public databases such as the Global Runoff Data Centre (GRDC) is rapidly declining since about 1980, especially in remote areas outside Europe or the USA [8]. Therefore, there is a strong motivation to estimate discharge with remote sensing techniques.

In contrast to discharge, which cannot be measured directly from remote sensing data [9], many hydrological and hydraulic variables such as inundated area [10], lake surface area [11,12], and river widths [13–15] can be measured reliably with multispectral or hyperspectral sensors on board of satellites [16,17], such as the MODIS, Landsat, and Sentinel-2 satellites. In addition to the widely used sensors covering the visible and infrared spectrum, water surface area can also be acquired using other techniques such as SAR or passive microwave radiometers [16,18]. Although intended to monitor oceans, satellite altimetry can presently be used to measure water levels of inland water bodies such as lakes and reservoirs [19–22]. Furthermore, satellite altimetry is capable of measuring the water level and longitudinal topography of rivers wider than 200 m [23,24]. Combining water level and surface area data, reservoir bathymetry and storage variations can be derived but are limited by the minimum observed water level [25,26]. Rating curves between previously sampled in situ discharge measurements and water level from satellite altimetry observations [27–29] are established to allow discharge estimation beyond the period of the in situ time series. These approaches are constrained by the need for in situ discharge measurements in order to establish and maintain the rating curve similar to. Estimating discharge solely from remote sensing data, however, is a big challenge, but allows to obtain discharge data even in remote, low developed, or crisis-affected regions where it may not be possible to maintain a network of gauging stations, although these regions are among those most affected by water scarcity [30,31].

With the announcement and preparation of the Surface Water and Ocean Topography (SWOT) mission, which will synchronously measure water level, water surface slope, and inundated areas [32], several studies discussed discharge estimation based on remote sensing data using basic hydraulic flow laws, e.g., the Manning formula [33], which requires an estimated roughness coefficient. The developed algorithms can be divided into two approaches: The At-a-station Hydraulic Geometry (AHG), estimates discharge based on the hydraulic parameters at single stations. Reach averaging methods such as the At-Many-stations Hydraulic Geometry (AMHG) combine multiple AHG relations along river reaches, which interact stably and predictably, considering the river equilibrium and conservation of mass [9,34,35].

Durand et al. [36] developed an reach averaging algorithm called MetroMan that calculates a best estimate of reach averaged river bathymetry and roughness coefficient based on input measurements of water level and water surface slope using the Metropolis algorithm in a Bayesian Markov Chain Monte Carlo scheme to estimate discharge with an normalized root-mean-squared error (NRMSE) of 36% in a case study for the river Severn. Water levels and time variable slopes are derived from gauge measurements. Additionally, a high resolution LiDAR digital elevation model (DEM) is used for the floodplain. This method sucessfully estimates the roughness coefficient, but underestimates the cross-sectional area. In a previous study [37], the authors emphasize the importance of time variable flow gradient data, which will be measured by SWOT. Other studies notice only small errors when

using a constant value [38,39]. The GaMo algorithm by Garambois and Monnier [40] works similar to MetroMan, using an AMHG approach, synthetic SWOT such as data and the Levenberg-Marquardt solver to estimate the unknown parameters. The method is tested on 91 synthetic test cases and the river Garonne. Overall the NRMSE is about 15% without using in situ data. Bjerklie et al. [41] estimate the bankfull discharge of the Yukon River at two locations in Alaska using a combination of the Manning formula and the Prandtl-von Karman equation in an AHG approach. The roughness coefficient is expressed by the Froude number, which is estimated using the meander length and the water surface slope, derived from satellite altimetry [42]. A parabolic cross-sectional shape is assumed using four Landsat scenes and an empirical dataset of hydraulic parameters measured at a large variety of rivers in the US. On average, the uncalibrated discharge results are within 20% of the validation data. In a recent study, Zakharova et al. [38] use an AHG approach to estimate daily discharge for the Ob river in Siberia from radar altimetry and a selection of nine Landsat scenes. The NRMSE is 23% using depth information from topographic maps and 20% after calibration of the parameters of the Manning formula. Kebede et al. [43] estimate discharge time series for the Lhasa River using only Landsat and SRTM data. The NRMSE is in a range of 25.7% to 41.4% and the NSE is between 0.886 and 0.956.

No universally applicable approach can be found in a comparison [44] of algorithms for the upcoming SWOT mission, which shows the need for further algorithm improvements to handle special cases such as extreme flood events or braided rivers. However, for most rivers there is at least one approach, but not always the same one, that can estimate the discharge within an NRMSE of 35%. There are several other studies that estimate discharge from remote sensing data (e.g., [45,46]). However, these require in situ data for calibration. The biggest challenge is the estimation of the flow velocity. Besides the mentioned methods using hydraulic flow laws, MODIS data was used to estimate the velocity by measuring the time lag of width variations between two stations [47].

In this paper, we use only remote sensing data without calibration, because we are aiming to develop a method applicable to ungauged regions. However, a large variety of in situ data is required for the validation. Therefore, we chose the well surveyed Lower Mississipi River as study area. In contrast to existing similar AHG and also reach averaging approaches, we use significantly more remote sensing and satellite altimetry data. In addition to satellite altimetry, the Database for Hydrological Time Series over Inland Waters (DAHITI) [21] provides long-term land-water masks and surface area time series since 1982 using satellite imagery from Landsat and Sentinel-2. Observational data gaps in these satellite images caused by clouds or sensor errors are filled using a long-term water occurrence mask allowing us to use every available satellite image [12]. To obtain a long-term water level time series from satellite altimetry observations available in DAHITI, we combine multiple virtual stations of the Envisat, Jason-2/-3, and Sentinel-3A/-3B missions covering different observation periods. We further increase the temporal coverage of available data by fitting a hypsometric function to synchronized satellite altimetry and surface area observations. Using the resulting hypsometry, we can predict the water level for each surface area observation derived from the images of the Landsat mission, which launched more than 20 years before the first satellite altimetry measurements over inland waters. The long-term satellite altimetry and remote sensing data allows us to construct large parts of the river bathymetry using observed instead of estimated data, because there are multiple occurrences of low water levels. Based on the predicted geometry, the velocity is estimated with the Manning Formula. The required roughness coefficient is estimated similar to other studies using adjustment factors [38,43,47]. The flow gradient is derived from satellite altimetry measurements at multiple stations along the river. The resulting discharge time series are validated using in situ data. In situ measurements are substituted for the estimated parameters in order to analyze each parameter's error and its effect on the residuals in the resulting discharge time series.

The article is structured as follows. In Section 2 we introduce the selected study areas and describe the data used for processing and validation. In Section 3 the methodology for estimating river discharge from remote sensing data is explained. In Section 4 the results are presented and validated

for each study area. The paper concludes with a discussion of the results in Section 5 and a conclusion (Section 6).

2. Study Area and Data

Section 2.1 gives an overview of the Lower Mississippi River and the selected study areas. The results of our study are validated with in situ data which are described in Section 2.2. For the method of this paper, only remote sensing and satellite altimetry data are required which we describe in Section 2.3. Additionally, a river centerline is required (Section 2.4).

2.1. Study Areas

The Lower Mississippi River is an alluvial river, with a gradual longitudinal profile. Although the river is maintained to allow safe navigation for ships and barges, it is still naturally shaped with shallows, meander, and without artificial dams. Nevertheless, it is modified by human activities such as riverbank protections to prevent further natural meandering [48]. A long-term assessment of the historical trends in hydrology, sedimentation, and channel geometry shows a large spatial and temporal variability of morphological trends in the study area [49]. The Mississippi River basin has a drainage area of 3.23 million km^2 and the water transported by the river comes mostly from winter snowfall, frontal storms, and convective storms [50]. Measurements at Vicksburg between 1931 and 2017 show a mean daily discharge of 17,543 m^3/s with a peak of 65,411 m^3/s recorded in May 2011 [51]. The three selected study areas for this paper are located along a 525 km long segment of the Lower Mississippi River between the cities of Greenville (MS, USA) and Baton Rouge (LA, USA). Figure 1 shows an overview map of the river segment and study areas (red). Each study area includes one of the in situ gauges at Vicksburg, Natchez, and Tarbert Landing, that we use to validate the respective results. The study areas also include river reaches up- and downstream of the gauge locations where we apply our methodology to additional cross-sections. However, the study area at Tarbert Landing covers only the river reaches downstream of the gauge, because the flow is diverted into the Atchafalaya River at the Old River Control Complex [52] which is located just upstream the gauge.

2.2. In-Situ Validation Data

We use in situ data collected and distributed by the United States Army Corps of Engineering (USACE) and the United States Geological Survey (USGS) to validate the predicted river bathymetry, the resulting discharge time series, and the satellite altimetry time series.

2.2.1. Water Levels and Discharge

In situ discharge time series of the Mississippi River at Vicksburg, available from the USGS National Water Information System (NWIS) [53], and at Natchez and Tarbert Landing, available from the USACE RiverGages.com website [54] are used to validate the resulting discharge time series of this paper. Additionally, water level time series from the stage gauges at Greenville, Vicksburg, Natchez, Knox Landing, Red River Landing, St. Francisville, and Baton Rouge, available from RiverGages.com are used to evaluate the quality of the input satellite altimetry data (see Section 2.3.1). The gauge locations are shown in Figure 1.

2.2.2. River Bathymetry

Multibeam and singlebeam bathymetric point cloud data collected by the USACE in several hydrographic surveys between June 2018 and September 2019 are available on the eHydro website [55]. Additional multibeam data collected for the 2013 hydrographic survey are available on the the USACE New Orleans District website [56] for areas not covered by the more recent surveys. The point cloud data is merged, interpolated, and exported as a raster with CloudCompare [57]. The surveyed bathymetry is used to evaluate the quality of the predicted bathymetry.

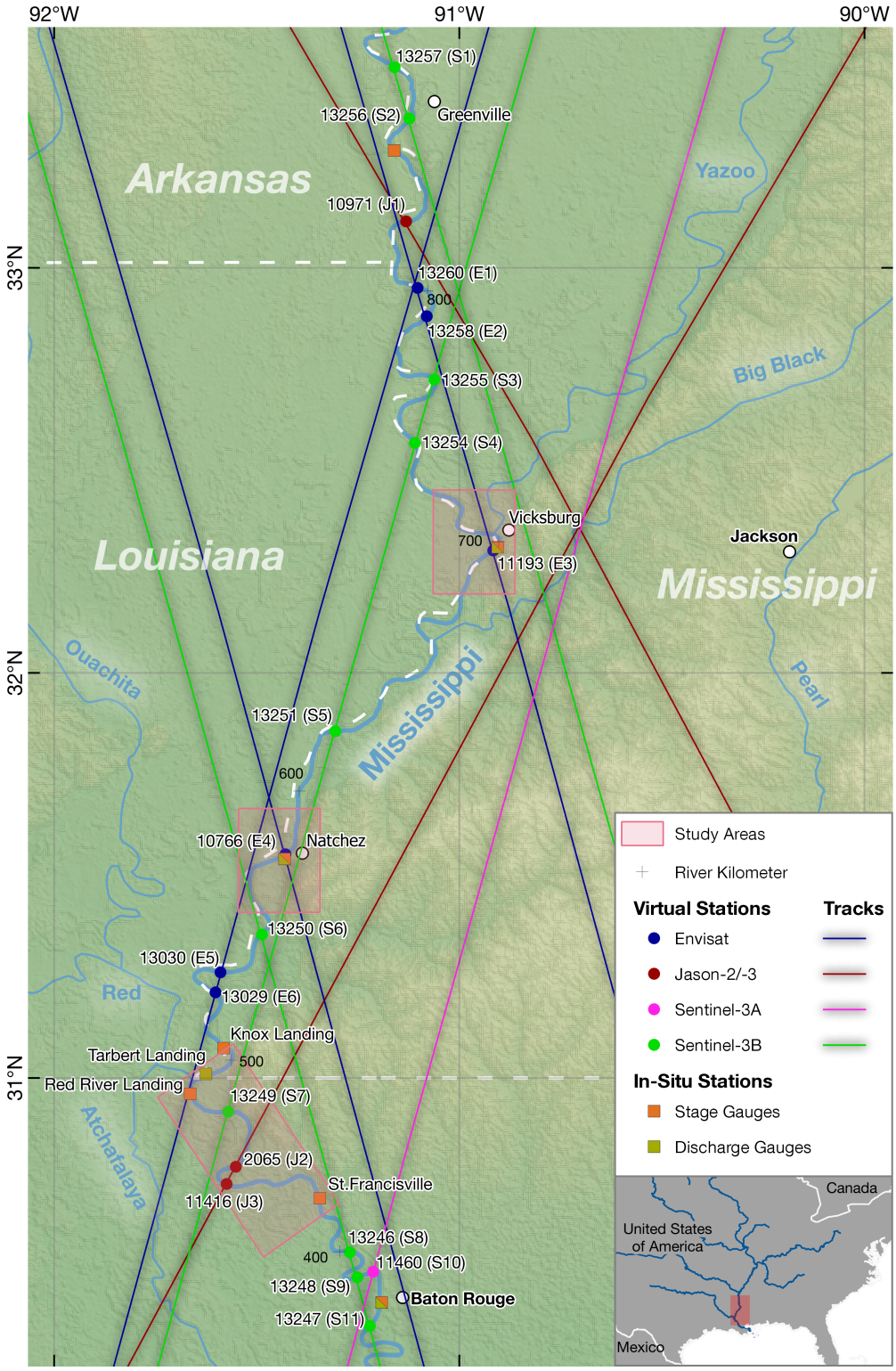

Figure 1. Overview of study areas, discharge and water level gauge locations, satellite altimetry tracks, and virtual stations with the DAHITI identifier and the short identifier used in this paper (brackets).

2.3. Remote Sensing Data

All remotely sensed data used in this study are processed and provided by the Database for Hydrological Time Series over Inland Waters (DAHITI) [21], which is developed and maintained by the Deutsches Geodätisches Forschungsinstitut der Technischen Universität München (DGFI-TUM). All datasets are freely available on the DAHITI website (http://dahiti.dgfi.tum.de) after registration.

2.3.1. Satellite Altimetry

Satellite altimetry provides profiled along-track data nearly globally, only limited by the orbital parameters of the satellite. As the sensors are measuring in nadir direction only, the available data is limited to the satellite's ground track. Unlike ocean applications, the major challenge of satellite altimetry over inland waters are the different reflections caused from multiple land and water features within the sensor footprint. Depending on the sensor, the reflection of water bodies narrower than 300 m may be too weak and unidentifiable in the received radar waveform to measure the water level. Comparisons to in situ time series reveal a Root Mean Square Error (RMSE) of a few centimeters (for larger lakes) up to some decimeters for smaller rivers [21]. Satellite altimetry water level measurements are possible also in remote areas with no infrastructure at so-called virtual stations where the ground track of the satellite crosses a river of suitable width. However, in contrast to continuous in situ observations, the temporal resolution is low, with one observation every 10 to 35 days depending on the mission.

Within the study area, 21 virtual stations at the Lower Mississippi River are available on the DAHITI website [21]. To achieve homogeneous altimetry data over multiple satellite missions and sensors a multi-mission cross-calibration is performed in the preprocessing of the DAHITI data [58]. Additionally, an extended outlier rejection is applied and a Kalman filter approach is used to estimate water level time series. In this study, we use time series of water heights with respect to the EIGEN-6c4 global gravity field model and formal errors from the Kalman filtering derived from measurements by the Envisat, Jason-2/-3, and Sentinel-3A/-3B missions. Figure 1 shows the nominal tracks of the altimetry satellites passing the study area and the available virtual stations at the Mississippi River. The identifiers of the virtual stations are assigned by DAHITI. An additional short identifier for this paper is shown in brackets. The time series at each station contains one averaged water level per crossing and additionally the formal error and acquisition date. Figure 2 shows a Hovmöller diagram [59] of the satellite altimetry data with every available measurement plotted as its deviation from the mean height which is shown per station in brackets at the y-axis.

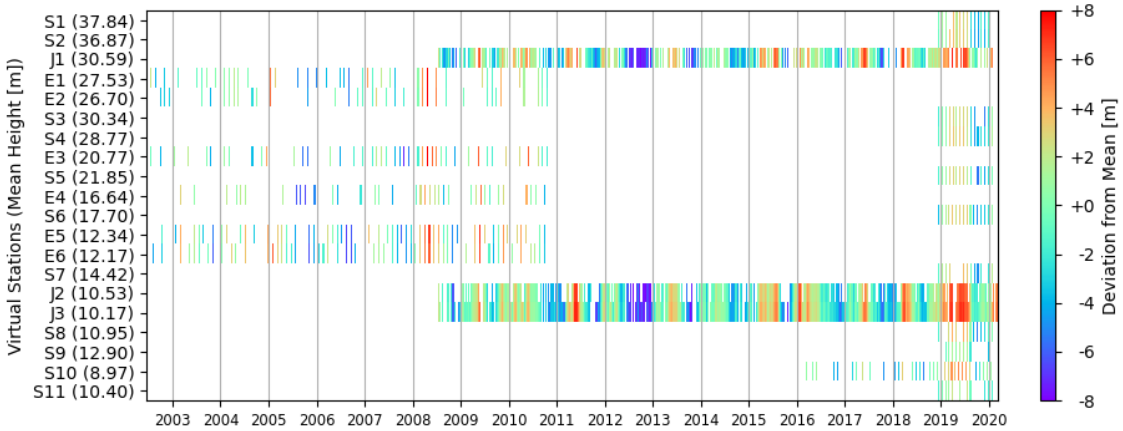

Figure 2. Measured height anomalies for each virtual station. The mean height per station is provided in brackets at the y-axis.

Envisat orbited the Earth from 2002 to 2010 with a repeat cycle of 35 days. Jason-2 (launched in 2008) and its successor Jason-3 (launched in 2016) are on an orbit with a repeat cycle of 10 days. The orbits of Sentinel-3A (launched in 2016) and the structurally identical satellite Sentinel-3B (launched in 2018) are congruent but shifted and thus interleaved with a repeat cycle of 27 days each. For a comparison of the water level time series measured at the virtual and in situ stations, Table 1 shows the closest gauge per virtual station, the along river distance, the number n of synchronous observations and the respective median offset, RMSE, NRMSE, and the squared Pearson correlation coefficient R_P^2. The last column shows the number of removed in situ outliers detected by a simple outliers detection

algorithm which is required because the in situ data is preliminary [54]. The average RMSE is 0.46 m and the mean R_P^2 is 0.976.

Table 1. Satellite altimetry comparison with in situ gauges showing the distance between the two locations, the number # of synchronous observations and the respective median offset, RMSE, NRMSE and the squared Pearson correlation coefficient R_P^2. The arrows indicate whether the stage (•) or combined stage and discharge (○) gauge is located upstream (↑) or downstream (↓) of the virtual station.

Station (DAHITI ID)	Gauge	Distance [km]		#	Offset [m]	RMSE [%]	NRMSE	R_P^2	Outliers
S1 (13257)	Greenville •	28.08	↓	13	2.35	0.35	0.99	0.994	40
S2 (13256)		11.69	↓	14	1.04	0.11	0.31	0.999	40
J1 (10971)		24.29	↑	282	−1.85	0.68	2.11	0.965	40
E1 (13260)		47.97	↑	42	−3.68	0.73	2.34	0.951	40
E2 (13258)		58.16	↑	36	−4.37	0.39	1.24	0.985	40
S3 (13255)	Vicksburg ○	66.64	↓	12	3.89	0.37	1.38	0.991	28
S4 (13254)		42.86	↓	14	2.67	0.53	2.01	0.969	28
E3 (11193)		1.70	↑	46	−0.17	1.13	5.44	0.901	28
S5 (13251)	Natchez ○	39.08	↓	13	2.07	0.43	2.13	0.976	24
E4 (10766)		0.70	↓	34	0.19	0.47	2.86	0.978	24
S6 (13250)		28.28	↑	14	−1.66	0.51	2.60	0.976	24
E5 (13030)	Knox Landing •	31.57	↓	50	1.18	0.44	3.98	0.986	50
E6 (13029)		17.38	↓	53	0.67	0.79	7.03	0.948	50
S7 (13249)	Red River Landing •	11.40	↑	10	−0.29	0.22	1.49	0.995	42
J2 (2065)		31.99	↑	299	−1.50	0.50	4.23	0.981	42
J3 (11416)	St. Francisville •	27.67	↓	347	1.32	0.49	5.48	0.979	9
S8 (13246)		21.77	↑	11	−0.78	0.20	1.71	0.997	9
S9 (13248)	Baton Rouge ○	15.39	↓	7	1.22	0.21	1.78	0.989	39
S10 (11460)		11.29	↓	29	0.73	0.14	1.80	0.998	39
S11 (13247)		5.10	↑	8	0.07	0.53	5.08	0.970	39

2.3.2. Water Surface Extent

The DAHITI land-water masks and water occurrence masks used in this study, are extracted using the Automated Water Area Extraction Tool (AWAX) [12], originally designed to extract the time-variable surface area of lakes and reservoirs. Using five different indices, AWAX calculates a land-water mask for every multispectral satellite image acquired by the Landsat-4/-5/-7/-8 missions whose spatial resolution is 30 m and the Sentinel-2A/-2B satellites which use a similar bandwidth as Landsat, but the spatial resolution improved to 10 m and 20 m, respectively. Additionally, a quality mask indicating data gaps caused by voids, clouds, cloud shadows, or snow is extracted for every scene. All land-water masks are stacked to get a long-term water occurrence mask, which is used in an iterative approach to fill the remaining data gaps in the land-water masks for every scene. This leads to a gapless water surface area time series which can be obtained from DAHITI for selected targets together with the void free land-water masks and the water occurrence masks. In this paper, subsets of the void free land-water masks are used to compute the water surface extent and river width of the Mississippi River within the study area. On average, 407 land-water masks per target are used in this paper. The maximum number of available land-water masks is 524 and the minimum 223. The respective scenes were acquired between January 1983 and December 2019 with an average interval of 21 days. From 17 June 2002, the date of the first available altimetry measurement, the average interval is 15 days.

2.4. River Centerline

The determination of the flow gradient and sinuosity requires a continuous river centerline, which is available from OpenStreetMaps (OSM) [60]. The centerline is used to measure the distances between the stations and to define the river kilometer of the virtual-stations, gauges, and cross-sections.

3. Methodology

In this section, we describe the methodology used to estimate river discharge from remote sensing data at a given cross-section (CS) in detail. The methodology is similar to the AHG relations. Therefore, the fundamental equations to calculate discharge and flow velocity, described in Section 3.1, require the determination of the at-a-station hydrographic parameters shown in Figure 3. All parameters at a CS that are a function of stage are elements of the AHG [35].

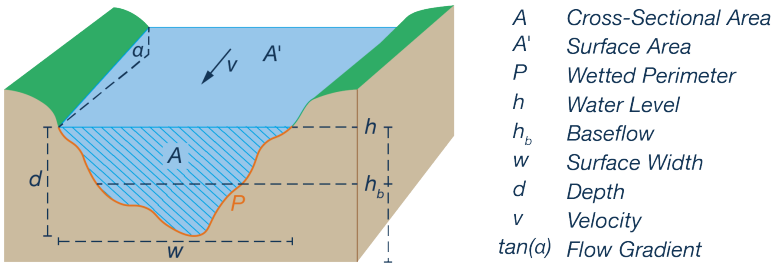

Figure 3. At-a-station hydrographic parameters.

Next, we describe the estimation of the shown parameters, starting with the flow gradient which requires a linear adjustment of the satellite altimetry data (Section 3.2) to derive the elevation differences between the virtual stations. Additionally, the resulting elevations enable us to combine short-term satellite altimetry data from multiple virtual stations to one long-term time series. In Section 3.3, we estimate the geometric parameters by synchronizing the long-term water level time series with land-water masks to fit a hypsometric curve, construct a bathymetry, and extract the cross-sectional geometry. The hypsometry fitting requires the estimation of the river depth using empirically established width to depth relations. The estimation of the roughness coefficient using geomorphological adjustment factors is described in Section 3.4. Figure 4 shows a detailed flowchart of the explained approach with the processing steps and data grouped by the describing sections.

3.1. Discharge and Velocity Calculation

In this paper, commonly established equations are used to calculate the hydraulic parameters and derive a discharge time series. The fundamental equation to calculate the discharge Q at a river CS for time t is defined as follows [35]:

$$Q(t) = \sum_{i=1}^{n} \bar{v}_i(t) \cdot A_i(t) \quad (1)$$

where n is the number of subsections of CS, $\bar{v}_i$ is the mean velocity in the subsection, and A_i is the cross-sectional area of the subsection. The CS is divided to consider the velocity distribution [61]. We divide each channel in 30 subsections analogous to the recommendation for in situ measurements [5].

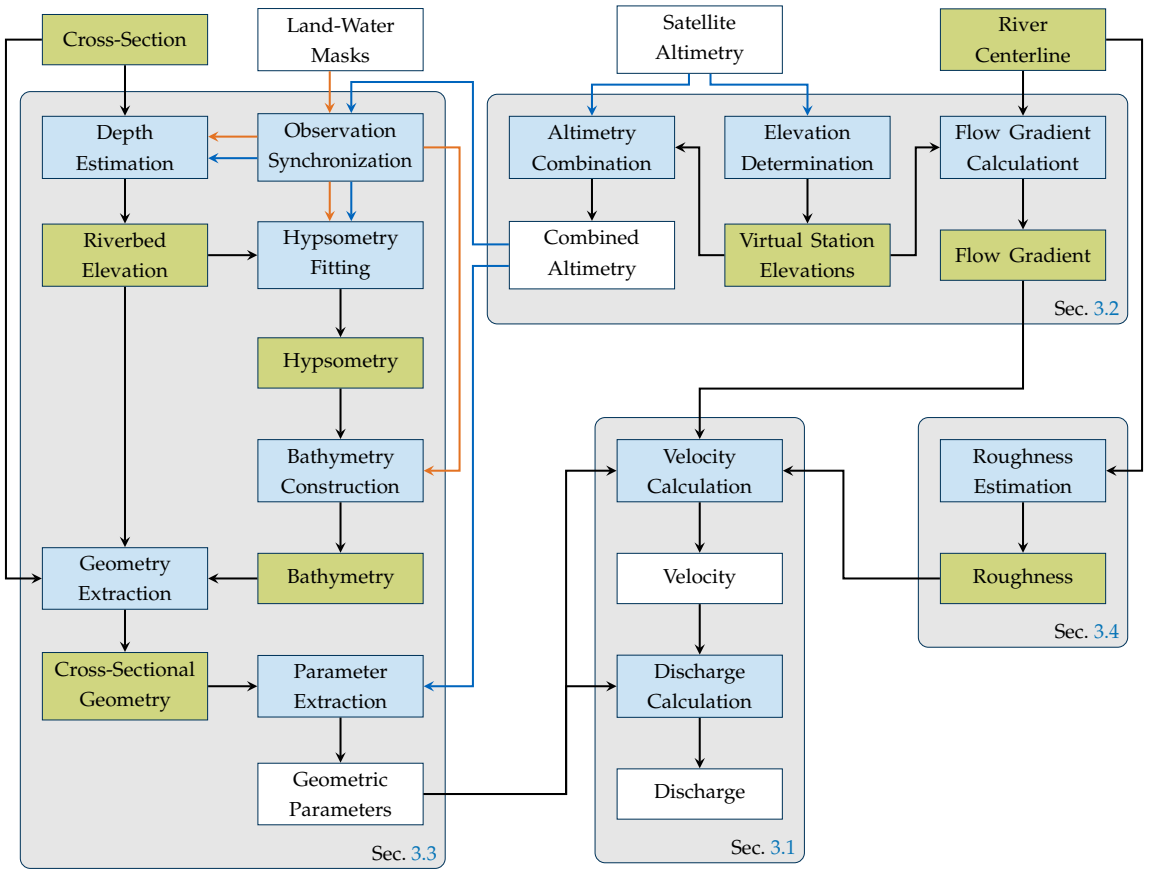

Figure 4. Methodology flowchart with time series data (white), constant data (green), processing steps (blue), and sections (gray). Orange arrows represent data derived from land-water masks and blue arrows represent satellite altimetry.

The mean velocity $\bar{v}$ is calculated with the Gauckler-Manning-Strickler formula [33], which is also known as the Manning Formula:

$$\bar{v}_i(t) = k_{st} \cdot R_i(t)^{\frac{2}{3}} \cdot I^{\frac{1}{2}} \tag{2}$$

where k_{st} is the roughness coefficient and I is the flow gradient, both assumed to be constant over the width of a given CS and time in this study even if they are actually variable. This simplification is necessary to adapt the equation to the possibilities of remote sensing data. R_i is the variable hydraulic radius of the subsection, which is expressed as:

$$R_i(t) = \frac{A_i(t)}{P_i(t)} \tag{3}$$

where A_i is the cross-sectional area and P_i is the wetted perimeter of the subsection. Both variables are related to the change of the water level h over time obtained from the satellite altimetry time series. The estimations of each parameter are described in the following sections, starting with I in Section 3.2, followed by A and P in Section 3.3 and k_{st} in Section 3.4.

3.2. Elevation Determination

The elevation differences of the virtual stations are required for two purposes. First, to calculate the flow gradient (Section 3.2.1) and second, to combine short-term satellite altimetry data of multiple virtual stations to one long-term water level time series per study area by subtracting the virtual station elevations (Section 3.2.2). The mean value of each virtual station is not accurate enough to be used as the reference elevation. Therefore, the elevations of all virtual stations are determined using a linear

least-squares adjustment of the observed water level differences, which is applicable for alluvial rivers with a gradual longitudinal profile without flow control structures so we can assume the functional model for the difference between two stations to be linear:

$$\Delta h_{ij}(t) = h_i(t) - h_j(t) \tag{4}$$

The most downstream station is defined as reference station with elevation 0. The elevations of all u remaining stations are unknown. For every water level measurement $h_i(t)$ at every station i the temporally closest measurement $h_j(t)$ is searched at each remaining station j. If the time difference $\Delta t_{ij}(t)$ between two measurements is lower than a threshold of 3 days, the water level difference $\Delta h_{ij}(t)$ is added as an observation b to the vector of observations $\mathbf{l}$ and $\Delta t_{ij}(t)$ is considered to be Δt_b. Although a lower threshold would be beneficial to obtain more accurate values, it is not feasible with the satellite altimetry constellation over the past 18 years because of the low temporal resolution of the water level measurements. At the end of the iterations, $\mathbf{l}$ has the shape $(k, 1)$, where k is the number of observed water level differences. With a linear least-squares adjustment [62] the unknown elevations $\mathbf{x}$ above the reference station can be estimated:

$$\mathbf{x} = (\mathbf{A}^\mathsf{T}\mathbf{P}\mathbf{A})^{-1}\mathbf{A}^\mathsf{T}\mathbf{P}\mathbf{l} \tag{5}$$

where $\mathbf{A}$ is a (k, u)-design matrix indicating the stations i and j of each observation b. The weights, or diagonal elements of the weighting matrix $\mathbf{P}$, are calculated for every observation b using the time differences Δt_b of the water level measurements at the two stations as follows:

$$p_{bb} = \frac{1}{1 + \Delta t_b} \tag{6}$$

Additionally, this method provides the inaccuracies of the adjusted heights to evaluate the accuracy of the derived data.

3.2.1. Flow Gradient Calculation

The flow gradient I at a CS is calculated by the elevation difference Δx of two virtual stations upstream and downstream of the CS and their distance s along the river:

$$I = \frac{\Delta x}{s} \tag{7}$$

The distance s is extracted from the river centerline. Δx is calculated using $\mathbf{x}$.

3.2.2. Altimetry Combination

Figures 1 and 2 show that the altimetry observations are not evenly distributed in space and time. To achieve a long-term discharge estimation, we combine water level data from multiple selected virtual stations within and nearby the study area by subtracting the linear adjusted station elevation x_i (Equation (5)) from every water level observation in the time series of each respective virtual station i. For the combination to be valid, it must be ensured that the flow between the selected virtual stations is not interrupted or diverted. Appendix A describes further offsets that are applied to the long-term water level time series in order to validate the derived bathymetry.

3.3. Geometric Parameters

To estimate the parameters A and P, a geometric representation of the river's cross-sectional shape is required. The location of the CS is defined by two coordinates at the river bank, which are manually selected using the river centerline and the DAHITI water occurrence mask to assure the CS includes the maximum contiguous water extent but no standing water nearby the river. We first construct the

river bathymetry within an area of interest (AOI) enclosing the CS (Section 3.3.1). Then, we extract the cross-sectional geometry and geometric parameters from the bathymetry (Section 3.3.2). The AOI is square-shaped with an edge length of 1.5 times the distance between the coordinates defining the CS and centered on the midpoint of the CS. The chosen size of the AOI ensures that the AOI includes the morphologic features of the respective reach and a wide surface area range to derive a robust area-height relationship in the following steps.

3.3.1. Bathymetry

The bathymetry is constructed using the method by Schwatke et al. [26] whose details and adaption to rivers are described in the following paragraphs. It combines water levels from satellite altimetry and land-water masks to estimate the bathymetry and volume variations of lakes and reservoirs. The two datasets are combined by fitting a hypsometry, which considers the water level as a monotonically increasing function of surface area. To adapt this method to the application on rivers, we clip the land-water masks to the AOI and remove non-contiguous water surfaces using image segmentation methods which ensures that the area-height relationship is monotonically increasing within the AOI.

Observation Synchronization

The fitting of the hypsometric curve requires contemporaneous observations of water level measured by satellite altimetry and surface area derived from land-water masks. As the altimetry and multispectral sensors are onboard of different satellites which do not acquire data synchronously, the observations have to be synchronized. For an optimized fitting result, it is best to have a large number of observations with a high correlation of water level and surface area. The correlation is expected to decrease with a longer time between the observations, because of changing conditions of water level and inundated area. To get a suitable data set, the synchronizing process iterates from a long to a short time delta between the observations, reducing the number of pairs with every iteration. Once the pairs have a correlation higher than a threshold of 0.75, the iteration stops, and the data is used in the following processing steps. If no iteration yields a sufficient correlation, the threshold is lowered and the iterations are repeated. As the relation of surface area and water level is not necessarily linear, the correlation coefficient by Spearman [63] is used.

Depth Estimation

In contrast to the study by Schwatke et al. [26] which only requires a good quality topography above the minimum water level to estimate volume variations, it is necessary for our methodology to also characterize the submerged topography or bathymetry and thus, the river bed elevation h_0 in order to estimate the cross-sectional geometry. Using h_0 we can optimize the fitting of the hypsometric function and estimate the cross-sectional geometry below the minimum water level. The elevation of the riverbed is required in order to optimize the fitting of the hypsometric curve to the observed synchronized data and limit the predictions to a reasonable minimum water level. Moody and Troutman [64] studied the relationship of depth, width, and discharge for a large dataset of world-wide distributed rivers, from small mountain streams to large alluvial rivers. They obtained the following regression relations:

$$\bar{w} = 7.2Q^{0.50} \tag{8}$$

$$\bar{d} = 0.27Q^{0.39} \tag{9}$$

where Q is the discharge, $\bar{w}$ is the mean water-surface width and $\bar{d}$ is the mean depth at a CS. By solving Equation (8) for Q and substituting Q in Equation (9) with the resulting term, $\bar{d}$ can be calculated by measurements of $\bar{w}$:

$$\bar{d} = 0.27\left(\frac{\bar{w}^2}{7.2^2}\right)^{0.39} \tag{10}$$

To estimate the bed elevation h_0, the cross-sectional river width $w(t)$ is extracted from the land-water masks of the synchronized observations. $w(t)$ is inserted in Equation (10) to calculate $\bar{d}(t)$, which is subtracted from the synchronous water level $h(t)$ to obtain $h_0(t)$. Finally, we use the median result of all synchronous observations as h_0.

Hypsometry Fitting

Because the land-water masks are clipped to the AOI and contain only contiguous water surfaces, a fixed area-height relationship of the river reach can be described by a hypsometric curve. Due to the bathymetry and the surrounding topography, the adjusted hypsometric function must always be monotonically increasing. Following Schwatke et al. [26], we fit a modified hypsometric Strahler [65] function to the synchronous observations of water level y and surface area x within the AOI:

$$y = \left[\frac{x_{min} - x}{x_{min} - x_{ip}} \cdot \frac{x_{max} - x_{ip}}{x_{max} - x} \right]^z \cdot y_{scale} + y_{min} \tag{11}$$

Six parameters of Equation (11) have to be fitted to the x and y data. x_{min} defines the minimum surface area and x_{max} the maximum surface area of the hypsometric curve. The minimum water level is defined as y_{min} and the variations of water level is defined by y_{scale}. The exponent z describes the shape of the hypsometric curve and x_{ip} represents the abscissa of the curves inflection point. To limit and improve the resulting curve, bounds are given to the fitting process. In contrast to [26], we set the minimum water level boundary y_{min} to the estimated river bed elevation h_0. The function is necessary because, although for the period from January 1983 until 2002 land-water masks are available, there are no contemporaneous satellite altimetry observations. Using the hypsometric function we obtain water levels for each land-water mask and increase the number of data. Additionally, the use of a hypsometric function fitted to water level and surface area observations reduces the influence of observational errors in the satellite altimetry data. In contrast to a width-height relationship, the variation amplitude of the area-height relationship is larger and incorrectly classified pixels in the land-water masks have a smaller effect on the resulting water level.

Bathymetry Construction

In this step, all available land-water masks are stacked and sorted by the respective hypsometric water level. Analogous to [26], each pixel column is analyzed and filtered with a median filter to obtain a bathymetric layer whose pixel values represent the respective minimum water level, disregarding outliers. Figure 5a shows the resulting bathymetry within the AOI and the CS between the user defined coordinates A and B.

3.3.2. Cross-Sectional Geometry

We use evenly spaced samples along the CS with a distance of 1 m to obtain the cross-sectional geometry from the bathymetric raster. However, the geometry is incomplete below the baseflow h_b, which is the minimum water level either observed by satellite altimetry or estimated using the hypsometry for the minimum observed surface area. Therefore, we fill the gap between h_b and the river bed elevation h_0 with a parabola as proposed by Bjerklie et al. [41]. The parabola is fitted to the two lowest points of the observed geometry and their midpoint whose ordinate is replaced by the predicted bed elevation. Figure 5b shows the resulting complete cross-sectional profile with the sampled geometry above h_b and the parabolic fill to h_0 below h_b.

3.3.3. Geometric Parameter Extraction

Using the cross-sectional geometry, the geometric parameters A and P are extracted for each water level h in the combined long-term satellite altimetry time series 3.2.2. P is the length of the profile line below h and A is the area of the polygon enclosed by the profile line and the water line at h.

As we split the CS in subsections, P_i is only the part of the wetted perimeter touching the river bed in the subsection and not the border part to a neighboring subsection. Figure 5b illustrates an example subsection i and the respective parameters A_i and P_i.

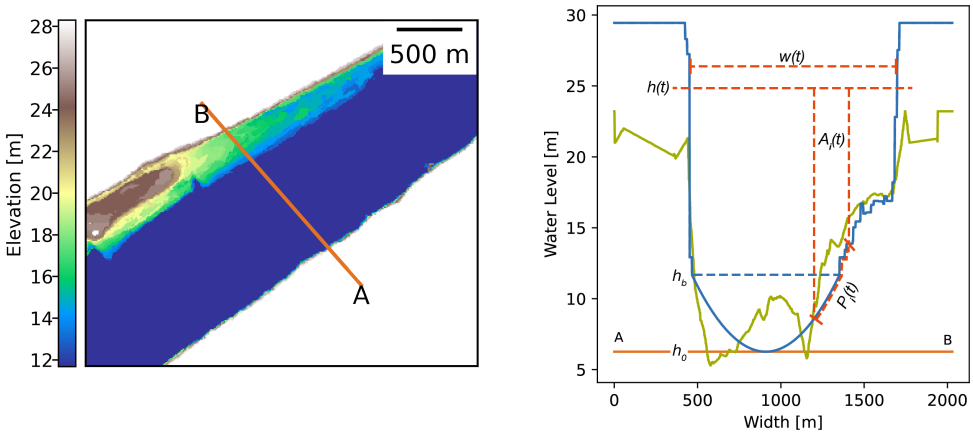

(**a**) Bathymetry (**b**) Cross-sectional geometry

Figure 5. Constructed bathymetry (**a**) within the AOI and extracted cross-sectional geometry (**b**) with geometric parameters downstream of Vicksburg at CS 694.7. The solid blue line in (**b**) shows the estimated cross-sectional profile and the green line the bathymetric survey data as reference. The dashed blue line shows the observed baseflow h_b and the solid orange line the estimated river bed elevation h_0. $A_i(t)$ is the area of subsection i defined by the water level $h(t)$ at the top and the wetted perimeter $P_i(t)$ at the bottom.

3.4. Roughness Estimation

The roughness of the river bed is specified by the roughness coefficient k_{st} which can be interchanged with the expression $\frac{1}{n}$ where n is the Gauckler Manning coefficient. The lower the value of k_{st}, the higher is the disturbance of flow from the river bed. The roughness coefficient can be determined objectively based on different factors [66,67]:

$$k_{st} = \frac{1}{(n_b + n_1 + n_2 + n_3 + n_4)m} \tag{12}$$

In Equation (12), n_b is a base value for the channel material, n_1 is a correction factor for surface irregularities, n_2 is a value for variations in shape and size of the channel CS, n_3 is a value for obstructions and n_4 is a value for vegetation and flow conditions. Arcement and Schneider [67] provide a decision guide to select suitable adjustment factors. m is a correction factor for the channel meandering depending on the sinuosity s:

$$m = \begin{cases} 1.00 & \text{if } 1.0 < s \leq 1.2 \\ 1.15 & \text{if } 1.2 < s \leq 1.5 \\ 1.30 & \text{if } 1.5 < s \end{cases} \tag{13}$$

s is calculated using a segment of the river centerline around the selected CS that has a length of 20 times the maximum width, since this distance is likely to include at least one meander wavelength [68–70]. This method was also used in other related studies, e.g., for the Yangtze River [47], the Lhasa River [43] and two siberian rivers [38]. Except for m, we use constant adjustment factors for all cross-sections. Because the Lower Mississippi River is an alluvial and meandering river with a low flow gradient and as there are many locks and dams at the Upper Mississippi River we assume the bed material

to be fine sand or firm soil, which is confirmed by in situ surveys [71]. Therefore, we set the base value n_b to 0.02 according to the decision guide [67]. Each CS is selected to be situated in straight river segments without obstructions or irregularities such as banks or multiple channels. Therefore, the adjustment factors for irregularity n_1, shape and size variation n_2, and obstruction n_3 are set to 0. The vegetation factor n_4 is set to 0, as well, because the effect of bank vegetation in wide channels with small depth-to-width ratios is small [67]. Depending on the degree of meandering the resulting k_{st} is 38.46, 43.48, or 50.00. These values are comparable to literature values for natural channels with moderate sediment transport ($k_{st} = 35$), natural channels with solid bed and no irregularities ($k_{st} = 40$), and maintained channels with solid sand and clay or gravel ($k_{st} = 50$) [72]. Therefore, the estimated values are plausible and suitable to estimate the velocity.

4. Results and Validation

In this section, we present and validate the results for the Lower Mississippi River. Section 4.1 covers the estimated flow gradient and different validation methods. In Section 4.2, we present and validate the estimated cross-sectional geometries and resulting discharge time series for multiple CS within each of the three study areas shown in Figure 1.

4.1. Flow Gradient

Figure 6 shows the virtual stations at the adjusted elevations above the reference station S11 (12347) and the flow gradient I of the resulting longitudinal profile in blue. Additionally, the upper table shows the maximum, median, and minimum flow gradient between the water level gauges for validation. In order to obtain these statistics, we calculate the flow gradient between the gauges for each date that is consistently included across all in situ time series. We ignore any resulting gradient below 0, assuming bad data or extreme events. This shows the high variability of the flow gradient.

The most extreme values occur around Knox Landing which is nearest to the Old River Control Complex where the flow is partially diverted into the Atchafalaya River. Figure 6 also shows a longitudinal profile in black which is derived from single beam soundings conducted in 2019. The sounding data includes the measured water level at the survey site. The Baton Rouge water level measured at the survey date and the constant offset between the Baton Rouge gauge and virtual station 13247 (see Table 1) is subtracted to equalize the variation due to surveys at different dates and the datum difference between in situ and altimetry data.

A comparison of the satellite altimetry derived flow gradient and the in situ statistics shows that the estimates are mostly within the range of the measurements and close to the median gradient. The largest deviations occur between stations located close to each other. The flow gradient does not change continuously, but discretely at each virtual station. Therefore, large deviations are possible at nearby river segments with a virtual station in between.

Table 2 shows the uncertainties of the resulting station elevations as a formal error from the linear adjustment. The uncertainties are largest for virtual stations of the Envisat mission and lowest for the Jason and Sentinel-3 missions.

Table 2. Uncertainties δ of the adjusted virtual station (VS) elevations in millimeters.

VS:	**S1**	**S2**	**J1**	**E1**	**E2**	**S3**	**S4**	**E3**	**S5**	**E4**	**S6**	**E5**	**E6**	**S7**	**J2**	**J3**	**S8**	**S9**	**S10**
δ [mm]:	27	26	20	51	51	21	21	48	21	68	18	42	42	23	18	18	20	23	36

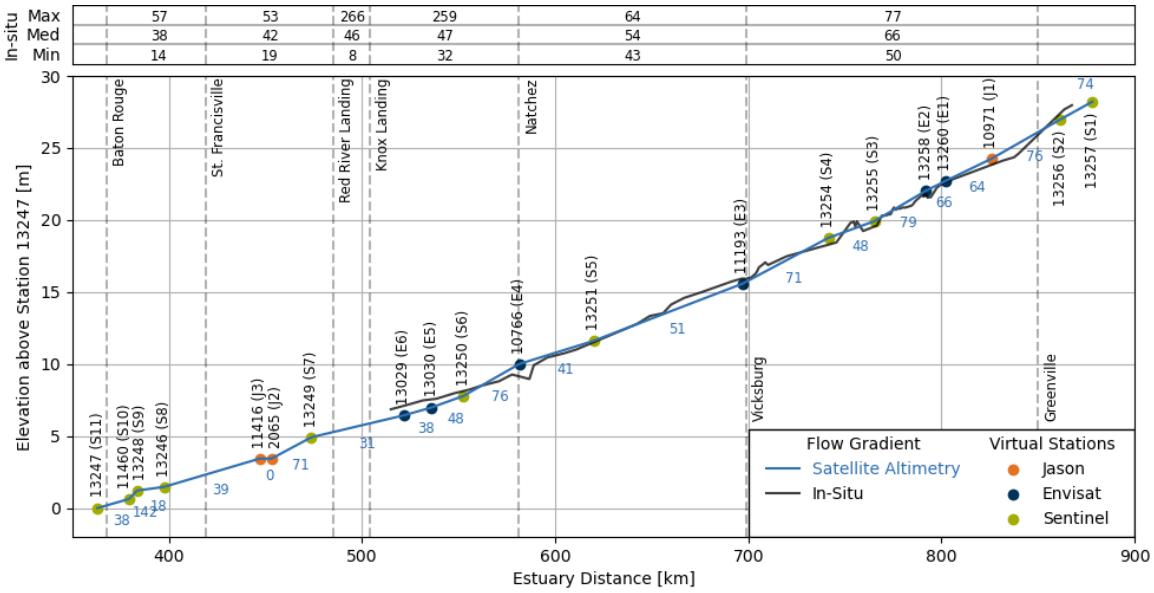

Figure 6. Flow Gradient [10^{-6}] of the Lower Mississippi River (blue numbers) derived from adjusted virtual station elevations. A longitudinal profile derived from bathymetric survey data is shown in black. The dashed lines represent the locations of in situ water level gauges. The minimum, median, and maximum flow gradient between the gauges is shown at the top.

4.2. Geometry and Discharge

The methodology presented in this paper can be applied at any location along the river since the input data is not bound to a specific location. However, it may not be suited for every river segment. For example, it can be expected that the estimated river bed elevation and thus the channel geometry is incorrect in curved river segments, because of strong erosion along the thalweg [69]. For this study, we focus on the three in situ discharge gauge locations within the study area at Vicksburg, Natchez, and Tarbert Landing. For each study area, we examine a CS at the gauge and four to five additional nearby locations. Using the DAHITI water occurrence mask, the additional CSs are selected to be situated in reaches with geomorphologic features such as straight and wide river segments without irregularities such as sand banks or multiple channels. Therefore, the additional CSs are expected to be most suitable for the application of the methodology. Each CS is numbered according to the respective estuary distance in kilometers. Figure 7 shows a map for each study area with each gauge, VS, and CS. Additionally, the figure shows the DAHITI water occurrence masks.

To validate the cross-sectional geometric parameters, we compared the estimated geometry with in situ bathymetric survey data. We validate the resulting discharge time series against the measured discharge at the gauge located within each study area. The validation is quantified by the Nash–Sutcliffe efficiency (NSE) [73], the root mean square error (RMSE), the normalized RMSE (NRMSE), and the squared Pearson correlation coefficient R_p^2. The discharge estimation results for the three study areas and selected cross-sectional geometries are presented in Sections 4.2.1–4.2.3. The supplementary material contains figures for each CS.

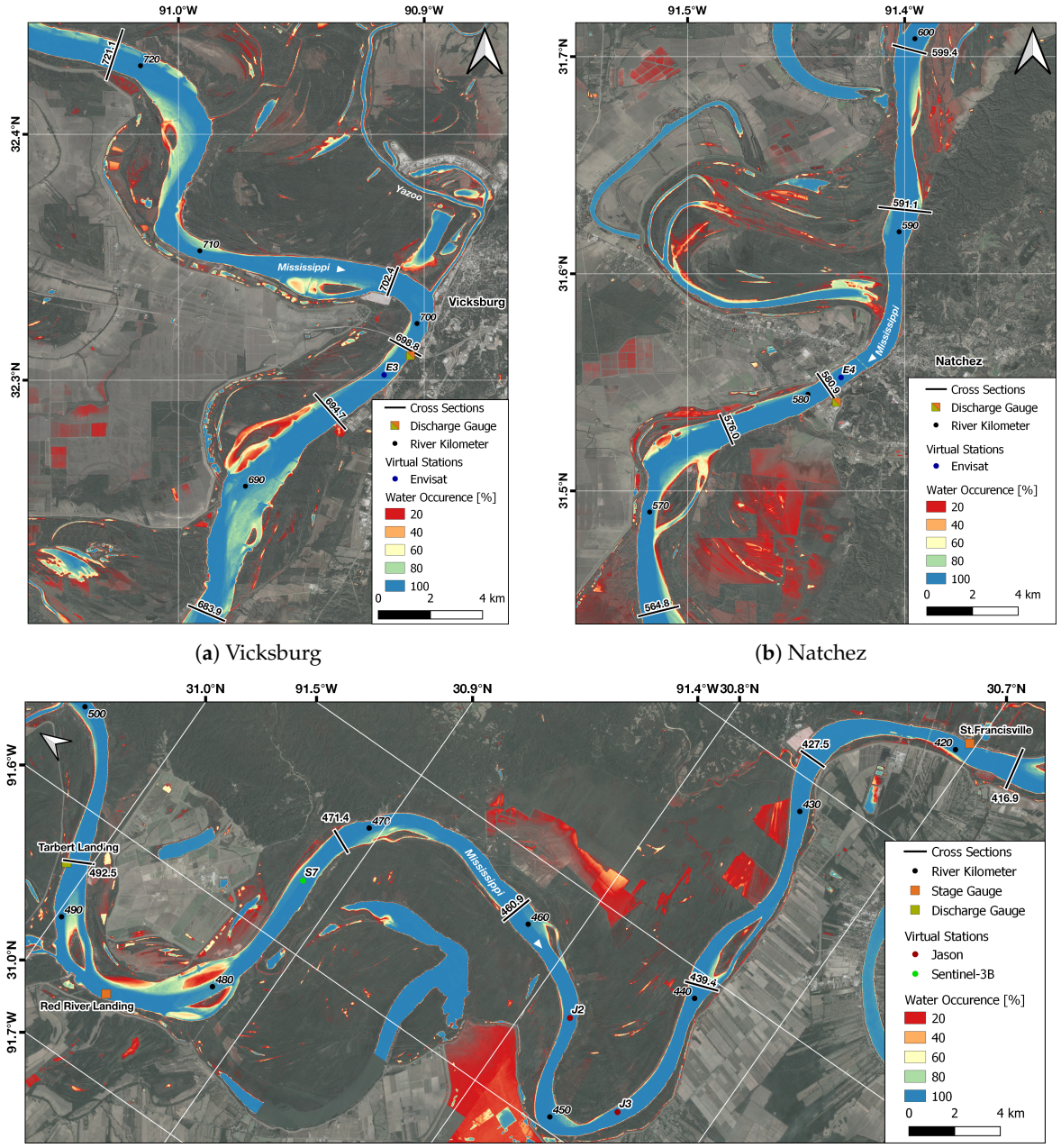

(**a**) Vicksburg

(**b**) Natchez

(**c**) Tarbert Landing.

Figure 7. Water occurrence, gauges, virtual stations, and cross-sections within the study areas.

4.2.1. Vicksburg

First, we present the results for each CS within the study area around the Vicksburg gauge shown in Figure 7a. We use satellite altimetry data from virtual stations E3, J1, and S4 which are combined as described in Section 3.2.2 to one single water level time series with 361 observations in the time period from 17 June 2002 to 12 March 2020. We use the same long-term water level time series at each CS within the study area. 458 surface area observations are available between 13 January 1983 and 1 June 2019. On the left side of Table 3, we show the estimated parameters used to derive the velocity and discharge for each CS at Vicksburg. The flow gradient I is inconsistent because virtual station E3 is located between CS 698.8 and CS 694.7. The roughness k_{st} changes depending on the sinuosity of the river as described in Section 3.4. The cross-sectional area A and hydraulic radius R are given as percentage of the respective in situ values below the maximum observed water level for validation. The estimated bed elevation h_0 is given as the deviation from the in situ data. To estimate the geometric parameters

of the CSs, the long-term water level time series and the observations of surface area within each AOI are synchronized per CS. The number of synchronized pairs, the squared Spearman correlation coefficient R_S^2 of water level and surface area, and the average time difference Δt are listed on the right side of Table 3. The results are validated using in situ data of the Vicksburg gauge provided by the USGS which is available for 330 matching days in the time period from 2 January 2008 to 6 March 2020.

Table 3. Estimated Parameters (left), discharge validation results (center), and observations synchronization statistics (right) at Vicksburg using combined altimetry data from E3, J1, and S4. A and P are given as percentage and h_0 as deviation of the respective in situ data. The synchronization statistics shows the resulting number of surface area and water level observation pairs, the area-height correlation coefficient R_S^2, and the average time Δt between the synchronized observations.

	Parameters						Discharge Validation				Synchronization		
CS	I [10^{-6}]	k_{st}	A [%]	R [%]	Δh_0 [m]	ΔQ [m^3/s]	NSE	NRMSE [%]	RMSE [m^3/s]	R_P^2	Pairs	R_S^2	Δt [Days]
683.9	51	50.00	92.72	109.31	2.70	−2130.80	0.873	17.34	3827	0.974	239	0.681	5.00
694.7	51	43.48	98.14	104.40	0.97	−4321.02	0.658	28.43	6275	0.976	239	0.704	5.00
698.8	71	38.46	60.72	60.96	20.78	−13457.17	−1.112	70.69	15604	0.960	239	0.634	5.00
702.4	71	38.46	102.47	105.63	3.84	−1938.45	0.844	19.24	4246	0.978	239	0.748	5.00
721.1	71	50.00	97.38	161.45	0.37	1471.94	0.929	12.96	2861	0.975	239	0.720	5.00

Figure 8 shows the fitted hypsometry, estimated bathymetry, and extracted cross-sectional geometry at CS 721.1 upstream the Vicksburg gauge. Figure 8 and Table 3 show, that the river bed elevation is correctly estimated at CS 721.1. Therefore, the cross-sectional geometry matches the bathymetric survey data. However, R is overestimated but the in situ value could be too low due to interpolation in the upper area.

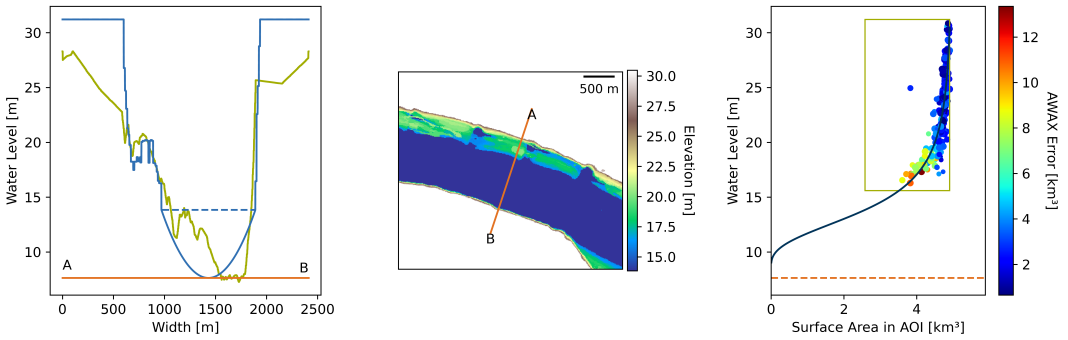

(**a**) Cross-sectional geometry (**b**) Bathymetry (**c**) Hypsometry

Figure 8. Estimated geometry, bathymetry, and hypsometry upstream of the Vicksburg Gauge (CS 721.1). The blue line in (**a**) shows the estimated and the green line the in situ cross-sectional geometry. Additionally, the figure shows the predicted bed elevation h_0 (orange) and minimum observed water level h_b (dashed blue). The bathymetry (**b**) is shown within the AOI defined by the CS which is represented by the orange line. The hypsometry (**c**) was used to construct the bathymetry. The dashed orange line represents h_0 which was used as boundary condition to fit the hypsometric function (dark blue) to the synchronized observations. The color of the observations shows the surface area error within the entire land-water mask not limited to the AOI. The green rectangle shows the bounds of the entire available water level and surface area observations.

Figure 9 shows the fitted hypsometry, estimated bathymetry, and extracted cross-sectional geometry at the Vicksburg gauge (CS 698.8). In contrast to CS 721.1 (Figure 8), a wrong h_0 is estimated because the river is narrower than the average reach, causing the geometry to be significantly underestimated with an area of only 60.72% of the actual size. Furthermore, a bridge obscures the satellite images of parts of the river. Consequently, the residuals of the discharge time series shown in

Figure 10 are much larger at CS 698.8 (red) than at CS 721.1 (blue) compared to in situ data (green). CS 694.7 (orange) has the worst results of the CSs whose locations are not defined by the gauge but morphological features.

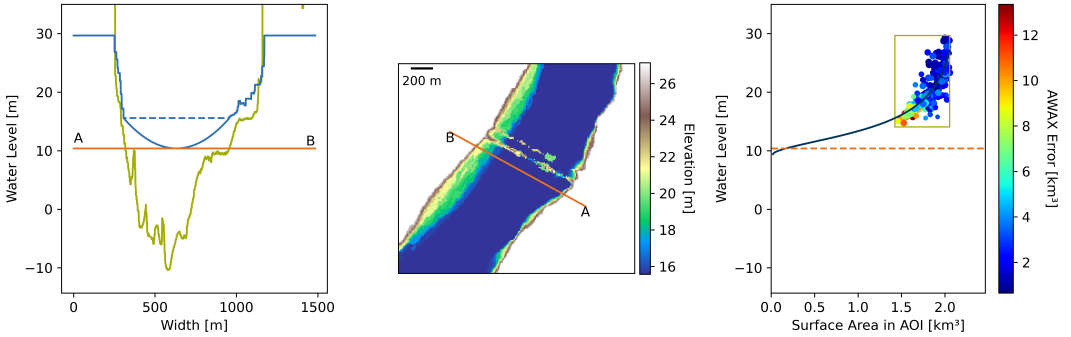

(**a**) Cross-sectional geometry (**b**) Bathymetry (**c**) Hypsometry

Figure 9. Estimated geometry, bathymetry, and hypsometry at the Vicksburg Gauge (CS 698.8). For details see Figure 8.

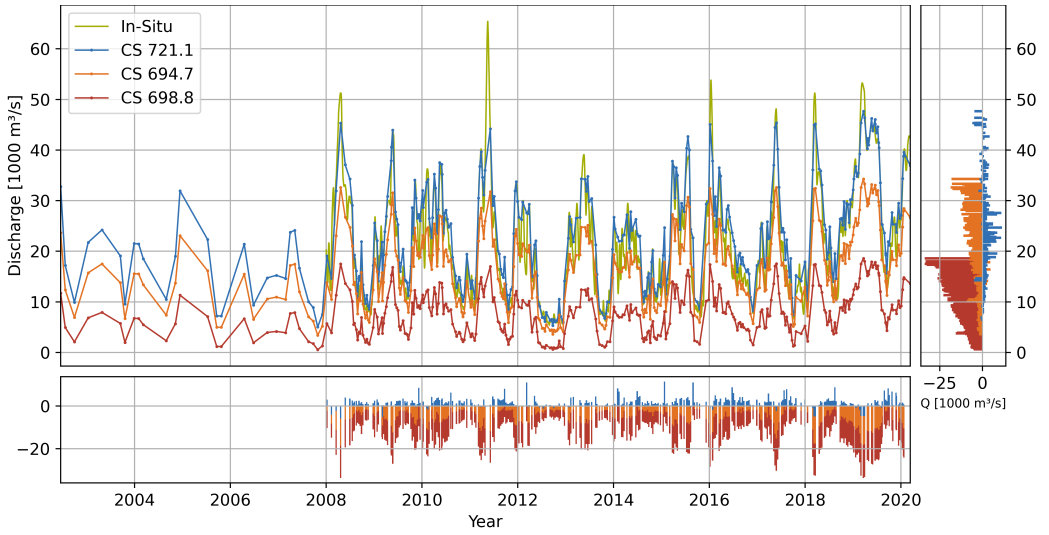

Figure 10. Discharge time series with residuals per time (horizontal) and discharge (vertical) of selected cross-sections around the Vicksburg gauge.

4.2.2. Natchez

Satellite altimetry data from virtual stations E4, J1, S5, and S6 is used for the study area around the Natchez gauge at CS 580.9 shown in Figure 7b. The combined time series contains 360 observations in the time period between 8 March 2003 and 12 March 2020. 459 land-water masks are available from 7 November 1984 to 1 June 2019. Similar to Vicksburg, the Natchez gauge is located on a narrow river segment. The four additional selected CSs are in regular, straight, and widening reaches. Table 4 shows the estimated parameters, the validation results of the estimated discharge time series, and the statistics of the observation synchronization per CS. The in situ time series for Natchez is not daily but contains a record every 14 days on average with 585 entries in the time period from 3 January 2000 to 10 September 2019. To increase the number of validation data, we fit a rating curve using daily water level measurements at Natchez (see Appendix B). Therefore, 343 entries in the time period between 7 January 1984 and 28 November 2019 can be used to validate the estimated discharge. Although errors could be introduced by using the rating curve, we assume the result is good enough for validation.

Similar to Vicksburg, a virtual station (E4) is just in the middle of the study area, so the flow gradient is not consistent. Meandering in the study area is low, causing the k_{st} to be constant across all CSs.

Table 4. Estimated Parameters (left), discharge validation results (center), and observations synchronization statistics (right) at Natchez using combined altimetry data from E4, J1, S5, and S6. For details see Table 3.

	Parameters						Discharge Validation				Synchronization		
CS	I [10^{-6}]	k_{st}	A [%]	R [%]	Δh_0 [m]	ΔQ [m^3/s]	NSE	NRMSE [%]	RMSE [m^3/s]	R_P^2	Pairs	R_S^2	Δt [Days]
564.8	76	50.00	125.53	140.19	−2.43	4094.80	0.785	21.92	5059	0.963	232	0.829	5.14
576.0	76	50.00	99.43	118.78	−0.86	1625.15	0.921	13.26	3060	0.966	232	0.572	5.14
580.9	76	50.00	59.14	83.75	11.90	−9632.32	−0.002	47.27	10912	0.956	232	0.714	5.14
591.1	41	50.00	76.13	111.05	1.54	−3714.84	0.745	23.83	5500	0.966	232	0.715	5.14
599.4	41	50.00	87.92	104.37	7.10	−3516.56	0.754	23.42	5405	0.967	232	0.655	5.14

Similar to CS 698.8 at Vicksburg the cross-sectional area is underestimated at the location of the Natchez gauge (CS 580.9), because the estimated river bed elevation is too high due to the below-average river width. A figure showing the cross-sectional geometry of CS 580.9 as well as every other CS is provided in the supplemetary materials. Therefore, the estimated discharge time series for CS 580.9 at the Natchez gauge (red) shown in Figure 11 has the largest residuals compared to the rated in situ discharge time series (green). CS 576.0 (blue) and CS 591.1 (orange) are the best and worst performing additional CSs which are selected by geomorphologic features. For CS 580.9 and CS 591.1 the negative residuals increase with rising discharge. There is no systematic error visible for CS 576.0.

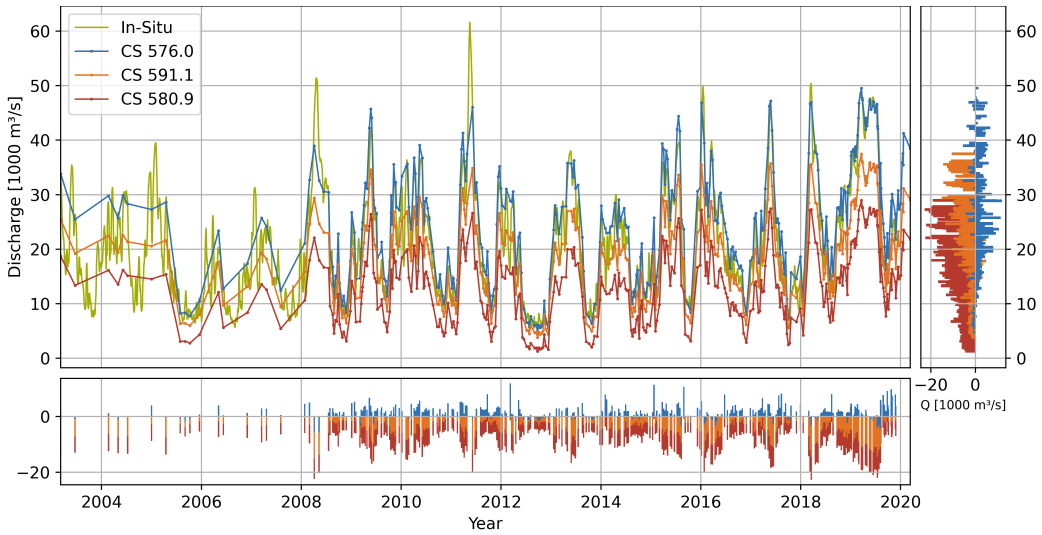

Figure 11. Discharge time series with residuals per time (horizontal) and discharge (vertical) of selected cross-sections at Natchez.

4.2.3. Tarbert Landing

The third study area shown in Figure 7c is located at and below the Tarbert Landing discharge gauge. Upstream Tarbert Landing is the Old River Control Complex, where the Mississippi River is partially diverted into the Atchafalaya River. Therefore, a validation with the Tarbert Landing discharge would be invalid for estimates in the upstream reach, so we extended the study area downstream to the St. Francisville gauge. We also do not use Envisat data from the nearby virtual stations E5 or E6 as they are upstream of the Old River Control Complex. We combine satellite altimetry data from virtual stations J2, S7, S9, and S10 to a time series of 360 observations between 16 July 2008 and 9 March 2020. 379 land-water masks are available from 7 November 1984 to 21 November 2018. Table 5 shows the estimated parameters, discharge validation results, and synchronization statistics for each CS. The flow

gradient varies throughout the study area as multiple virtual stations are located along the reach. The k_{st} is not consistent because of different degrees of meandering along the river. The estimated discharge time series were validated against daily in situ data for Tarbert Landing provided by the USACE for the time period from 3 January 1984 to 28 November 2019. The estimated and in situ time series can be compared at 344 matching days.

Table 5. Estimated Parameters (left), discharge validation results (center), and observations synchronization statistics (right) at Tarbert Landing using combined altimetry data from J2, S7, S9, and S10. For details see Table 3.

	Parameters						Discharge Validation				Synchronization		
CS	I $[10^{-6}]$	k_{st}	A [%]	R [%]	Δh_0 [m]	ΔQ [m^3/s]	**NSE**	**NRMSE** [%]	**RMSE** [m^3/s]	R_P^2	**Pairs**	R_S^2	Δt [Days]
416.9	39	50.00	115.52	117.83	6.41	1191.17	0.933	12.12	2226	0.981	148	0.899	4.12
427.5	39	43.48	116.25	117.48	−0.71	1188.82	0.924	12.97	2381	0.982	148	0.847	4.12
439.4	39	50.00	103.66	100.79	2.69	−109.32	0.946	10.95	2011	0.978	148	0.818	4.12
460.9	72	43.48	107.07	109.58	2.58	1541.46	0.925	12.86	2361	0.980	147	0.712	4.00
471.4	72	43.48	102.30	112.37	3.66	−555.25	0.926	12.76	2344	0.979	147	0.794	4.00
492.5	31	43.48	99.76	101.60	−0.70	−4914.37	0.389	36.73	6745	0.980	136	0.582	4.38

Figure 12 shows the hypsometry, bathymetry, and cross-sectional geometry of CS 492.5 at the Tarbert Landing discharge gauge. Although the estimated geometry matches the surveyed bathymetry, which is also apparent from the low A and R deviations, the resulting time series deviates largely from the in situ data with an NRMSE of 36.73% and an NSE of 0.389. This is presumably caused by an erroneously low flow gradient, which is probably introduced by the upstream flow diversion. Figure 13 shows the estimated discharge and residuals compared to the in situ time series (green) for CS 492.5 at the Tarbert Landing gauge (red) and the best (CS 439.4, blue) and worst (CS 460.9, orange) performing additional CS selected by geomorphologic features.

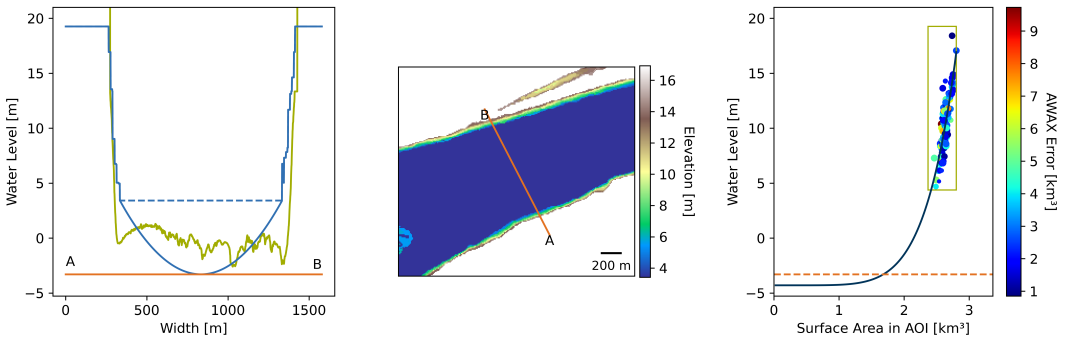

(**a**) Cross-sectional geometry (**b**) Bathymetry (**c**) Hypsometry

Figure 12. Estimated geometry, bathymetry, and hypsometry at Tarbert Landing (CS 492.5). For details see Figure 8.

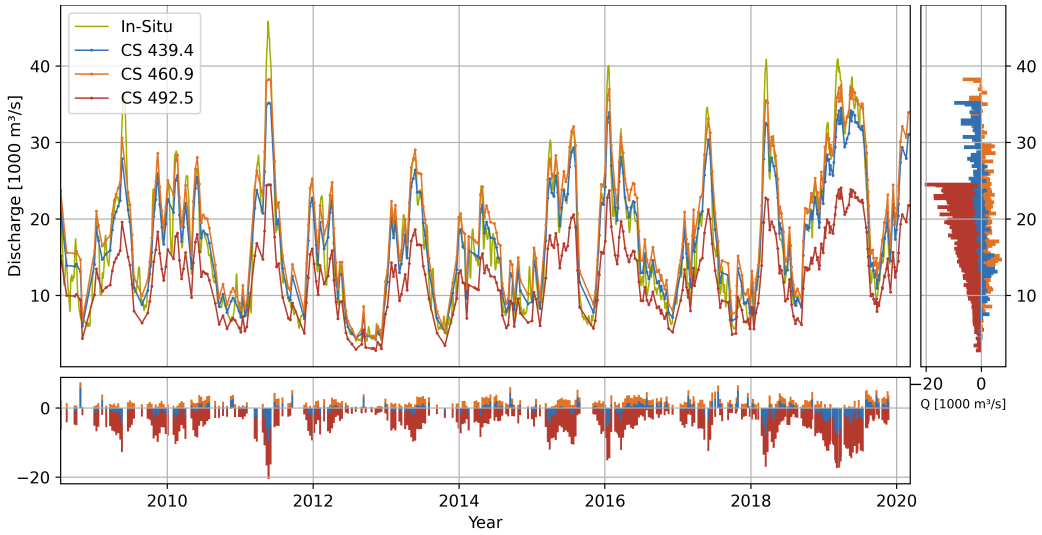

Figure 13. Discharge time series with residuals per time (horizontal) and discharge (vertical) of selected cross-sections at Tarbert Landing.

5. Discussion

This study is the first application of the DAHITI land-water and water occurrence masks on rivers. These masks and the modified hypsometric function were previously only used to determine the surface area, extent, and volume of lakes and reservoirs [12,26]. The study shows that also for large alluvial rivers that are morphologically more dynamic than lakes or reservoirs, the water occurrence mask can be used to extract a large amount of void-free land-water masks to fill data gaps caused by clouds, cloud shadows, instrument errors or ice. Additionally, the modified hypsometric function can be used to derive the water level within a river reach based on the respective surface area. However, it cannot be concluded that the approach is applicable to smaller rivers whose size does not exceed a few image pixels, or braided rivers which are morphologically much more dynamic than the Mississippi.

We showed in Section 4.1 that the elevation differences between virtual stations of multiple missions with different observation periods can be estimated accurately within river segments without flow disruptions such as the Lower Mississippi River. This can be seen from the low inaccuracies resulting from the linear adjustment shown in Table 2. Additionally, a comparison with the in situ values (Figure 6) shows that the estimates are within the range of the variable in situ gradient and in general close to the median value. The largest deviations occur between adjacent stations. In contrast to the calculation of the flow gradient using SRTM or other DEM data which is limited to a short period of observation, the usage of multi-mission satellite altimetry allows the calculation of an average flow gradient over time. Using the mean values of each virtual station is not sufficient to calculate the flow gradient as these do not monotonically increasing with the estuary distance (see Figure 2) which would result in a negative flow gradient. However, the continuity and variability of the flow gradient cannot be determined using our approach. The spatial resolution of the estimated flow gradient is limited by the fixed orbits of the satellite altimetry missions, but may be increased using long-repeat orbit missions such as Cryosat-2. In most cases a high spatial resolution of the flow gradient is of minor importance, but at Tarbert Landing (CS 492.5) a higher resolution would be beneficial to detect possibly rapid changes due to the upstream flow diversion. Deriving a variable flow gradient from a satellite-based sensor will first become possible with the SWOT mission.

The roughness coefficient is estimated using multiple adjustment factors, a method that has been well established in several studies [38,43,47,67]. Most of the adjustment factors are set to 0, because we select only uniform sections without irregularities such as eroded banks, abrupt changes in CS size, or obstructions based on the DAHITI water occurrence mask. However, the method is useful because different rates of meandering could be considered. There is no in situ data available for validation,

but the calculated roughness coefficients are within the ranges of literature values for natural and maintained channels with solid bed materials which are common in alluvial rivers.

Our method differs from classical state of the art AHG approaches [38,41,43] by the construction of the river bathymetry which uses as many observational data from satellite altimetry and remote sensing images as possible and a hypsometric function which was originally developed for lakes [26]. Our results for 16 cross-sections show that the hypsometry can also be fitted to surface area and satellite altimetry observations over large alluvial rivers to increase the number of water level observations when the river depth is estimated correctly. The depth estimation succeeds for straight, wide, and uniform cross-sections with a median deviation of 2.4 m. We are able to manually identify such river segments using the DAHITI water occurrence mask. The method and its limitation to specific river segments might be transferable to similar rivers, because the empirical width-depth relationship used is derived from a large dataset of world-wide distributed rivers. The geometry extracted from the estimated bathymetry is validated using bathymetric survey data. Overall, the cross-sectional area is underestimated with an average coverage of 96.51% of the actual area. However, the average hydraulic radius is overestimated with 109.97% of the surveyed data, because of the medium spatial resolution of the Landsat mission and the parabola that is used to extend the geometry below the baseflow. The larger hydraulic radius leads to an increased velocity and thus discharge estimation, while the reduced area causes an underestimation of the discharge.

Using long-term satellite altimetry time series combined from multiple virtual stations enables the estimation of discharge time series over a period of up to 18 years. The validation at 16 cross-sections against the closest in situ measurements yields a median Normalized Root Mean Square Error (NRMSE) of 18.29% with a minimum of 10.95% and a maximum of 70.69%. The median Nash-Sutcliffe Efficiency (NSE) is 0.858 with a minimum of -1.112 and a maximum of 0.946. However, the resulting errors are significantly high at the three gauge locations. At Vicksburg and Natchez this is caused by the below average river width, which leads to an underestimation of the river depth and the depending geometric parameters. At Tarbert Landing the extracted channel geometry is correct, but the estimated flow gradient is most likely too low. At the 13 other cross-sections, which are not defined by the gauge locations but are selected to be in straight, wide, and uniform river segments, the median NRMSE is 13.26% with a minimum of 10.95% and a maximum of 28.43%. The median NSE at these cross-sections is 0.921 with a minimum of 0.658 and a maximum of 0.946. These errors are within the range of results from an intercomparison of state of the art studies [44].

In contrast to the variable distribution of errors, the correlations between estimated and in situ discharge are consistently high at all cross-sections with values above 0.95. Figure 14a–c show the linear regressions of estimated and in situ discharge for each CS. It is apparent that the discharge is predominantly underestimated at each CS and the deviation increases with rising discharge. At Tarbert Landing the results of the selected CS are very consistent, while they are more widely spread at Natchez and Vicksburg.

To evaluate the quality of the estimated geometric parameters, we substitute the estimated cross-sectional geometry with a geometry extracted from the bathymetric survey data and calculate an additional time series for each CS. Figure 14d–f show the relation of these new estimates and the in situ discharge. The estimates improve for CS 698.8 at the Vicksburg gauge and CS 580.9 at the Natchez gauge which is expected as the geometry is clearly underestimated. This emphasizes the high importance of correctly estimated geometric parameters. However, the estimated discharge at CS 580.9 is now consistently too high. This could be caused by an overestimated flow gradient which is much smaller downstream at CS 576.0 and CS 564.8 where the estimated discharge decreased using the bathymetric survey data. At Tarbert Landing the estimates do not change significantly, which confirms that the geometric parameters are estimated well.

Next, we use the in situ flow gradient time-series derived from in situ water-level time series (see Figure 6) to substitute the estimated constant slope. The variable flow gradient is used in two analyses. First, Figure 14g–i show the relation of in situ discharge and estimates using bathymetric

survey data and variable in situ flow gradient. In this analysis, all parameters are extracted from in situ data except the roughness which has to be estimated anyway and the input water level time series which is obtained from satellite altimetry. Compared to the results shown in Figure 14d–f, the estimates improve e.g., at the Tarbert Landing (CS 492.5) and Natchez gauge (CS 580.9) where we expected the estimated gradient to be wrong. However, at some CS (e.g., CS 460.9) there is a higher discharge deviation using the variable gradient and bathymetric survey data. Therefore, we assume that the estimated roughness must be wrong at those places. In the second analysis, we use the estimated bathymetry and the variable in situ flow gradient. Figure 14j–l show the respective relation of in situ data and estimates. Again, the results are worst at the narrow CS 698.8 and 580.9 where the estimated bathymetry is too shallow. The use of the variable flow gradient shows no improvement in the results of these CS compared to Figure 14a–c. At Natchez, the results get more consistent at the different CS while they are more widely spread at Tarbert Landing using the variable flow gradient.

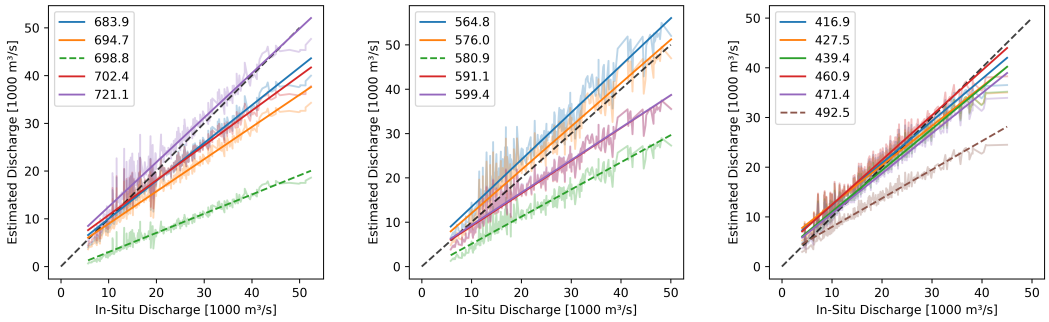

(**a**) Vicksburg (**b**) Natchez (**c**) Tarbert Landing

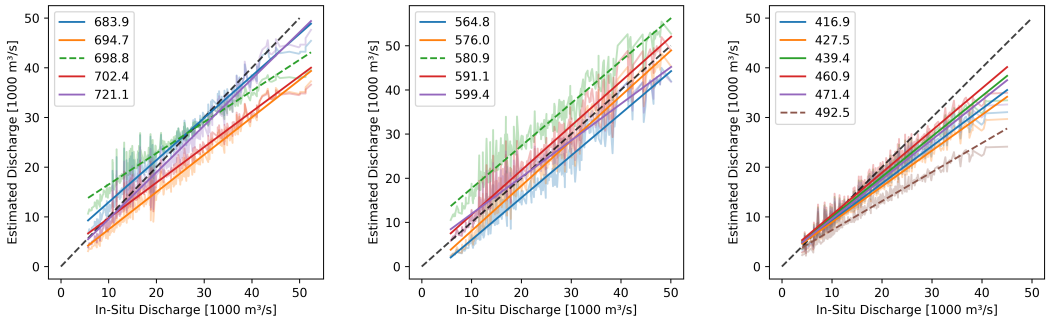

(**d**) Vicksburg (**e**) Natchez (**f**) Tarbert Landing

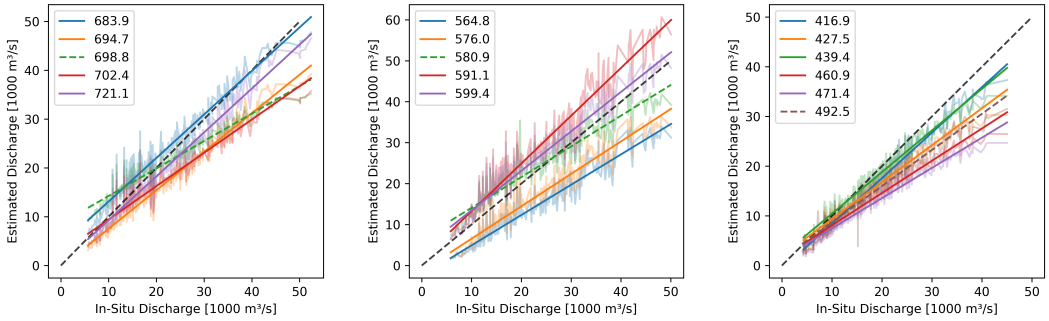

(**g**) Vicksburg (**h**) Natchez (**i**) Tarbert Landing

Figure 14. *Cont.*

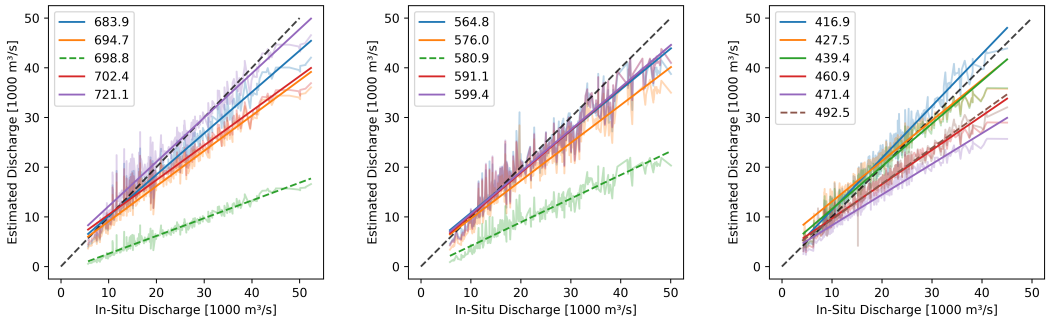

(**j**) Vicksburg (**k**) Natchez (**l**) Tarbert Landing

Figure 14. In-Situ vs. estimated discharge and linear regression for each CS using all estimated parameters (**a**–**c**), bathymetric survey data (**d**–**f**), bathymetric survey data and variable in situ flow gradients (**g**–**i**), and variable in situ flow gradient and estimated bathymetry (**j**–**l**). The black dashed lines show the optimum relation. The colored dashed lines represent the CS at the gauges.

Table 6 shows the NRMSE values per CS for each substitute and additionally the assumed significant factor for further improvements of the methodology which is chosen as follows: If the NRMSE increases or the improvements are only marginal using substituted values of I, A and P, we assume the roughness to be significant for further improvements. If the NRMSE decreases significantly by either substituting I or A and P we assume the respective substitute to be significant for further improvements but only when the effect is not negated using all substitutes.

Table 6. Errors of the discharge estimation using estimated parameters and respective increase (+) or decrease (−) using in situ substitutions per CS. The right column shows the significant parameter causing the largest error.

CS	Estimated	Substitute			Significant Parameter
		I	A and P	I, A, and P	
	NRMSE[%]	Δ NRMSE[%]	Δ NRMSE[%]	Δ NRMSE[%]	
721.1	12.96	−1.02	−2.13	+0.65	Roughness
702.4	19.24	+3.19	+3.97	+7.24	Roughness
698.8	70.69	+5.03	−49.11	−47.87	Bathymetry
694.7	28.43	−2.72	+0.30	−2.31	Roughness
683.9	17.34	−2.58	−4.90	−3.79	Roughness
599.4	23.42	−9.76	−11.25	−6.09	All
591.1	23.83	−9.96	−10.69	+4.24	Roughness
580.9	47.27	+13.40	−14.32	−30.78	Bathymetry
576.0	13.26	+8.42	−0.27	+16.95	Roughness
564.8	21.92	−6.60	+0.29	+17.76	Roughness
492.5	36.73	−14.84	+2.46	−12.23	Gradient
471.4	12.76	+19.92	+3.84	+24.11	Roughness
460.9	12.86	+9.80	-1.51	+18.72	Roughness
439.4	10.95	−0.47	+3.49	+1.03	Roughness
427.5	12.97	+1.27	+10.77	+7.67	Roughness
416.9	12.12	+1.47	+8.50	+3.06	Roughness

At CS 721.1, 702.4, 683.9, 591.1, 576.0, 564.8, 471.4, 460.9, 427.5, and 416.9 single or no substituted parameters lead to improvements while the errors increase when all parameters are substituted. As we expect the results to improve using the substituted parameters, the estimated roughness must be the cause of error. At CS 694.7 and 439.4 the estimation improves using the substitutes but the remaining error is still high compared to the improvements. Therefore, the roughness must also be the significant parameter at these locations to gain further improvements. At CS 698.8 and 580.9 the results

significantly improve by substituting the geometric parameters. These are predominantly the narrow CS at the gauges where the bathymetry construction failed caused by the underestimation of the river depth. At CS 599.4 the substitution leads to significant improvements but the remaining errors are still high. Therefore, all parameters (I, A, P, and the roughness) are significant for improvements. CS 492.5 is the only location where the result improve significantly using the in situ flow gradient and the effect was not dampened by substituting the bathymetry. Here, the estimated flow gradient is probably incorrect due to the flow diversion just upstream of Tarbert Landing.

Although the number of 16 CS as test locations might be too low to be statistically significant and the CS are manually selected, the substitution of parameters shows that the largest cause of error is the incorrect roughness value. This is probably not only caused by the coarse estimation of the roughness coefficient using adjustment factors but also by the used flow formula itself. To estimate the flow velocity we use the Manning formula which is the most commonly used relation between velocity and water level described by a friction factor. However, being an empirical equation, the Manning formula has no theoretical basis. It is inhomogeneous in terms of dimensional analysis and the value of the roughness coefficient has no direct relation on the properties that cause bed roughness. Furthermore, using the Manning formula we can only obtain an average velocity over width and depth, and complex characteristics as backwater effects, negative flow gradients or uneven velocity distributions due to meandering cannot be considered. We minimize the effect of generalization in width by dividing the CS in multiple subsections but to overcome the velocity distribution over depth and the other mentioned challenges a more sophisticated formula will be required. Some improvements can be expected by using a variable roughness coefficient as it is the standard for non-remote sensing methods and already used by Bjerklie et al. [41] with remote sensing data.

6. Conclusion and Outlook

In this paper, we present an approach to determine long-term river discharge time series using solely satellite altimetry and remote sensing data at the Lower Mississippi River. The methodology does not require calibration and works at cross-sections in straight, wide, and uniform reaches of the river and possibly at comperable large alluvial rivers. At river segments without flow disruptions, a linear adjustment of the virtual station elevations allows us to combine satellite altimetry data from multiple virtual stations and missions to one single long-term water level time series. At the Lower Mississippi River, the constant flow gradient derived from the virtual station elevations shows a high agreement with the average of the variable flow gradient calculated using in situ data. The roughness coefficient is estimated using multiple adjustment factors similar to many state of the art studies. Using long-term optical remote sensing data and a hypsometric function, further water levels can be derived from surface areas in addition to the satellite altimetry observations. In this way, we can cover a wider range of water levels and use it in combination with the respective water surface extents to construct large parts of the river bathymetry. The remaining part of the bathymetry below the baseflow is approximated using a parabola and an estimation of the river bed elevation which is based on an empirical width-to-depth relationship that shows limitations in below average wide cross-sections.

In straight, wide, and uniform river reaches, the NRMSE varies between 10.95% and 28.43% and is comparable with other studies without calibration. The NSE is in a range from 0.658 to 0.946. The NRMSE increases up to 70.69% at CS not defined by the planform shape of the river but by gauges which are predominantly located in narrow reaches where depth is underestimated in our approach.

To discuss the significance of the parameters in the Manning formula, we substitute in situ measurements of bathymetry and variable flow gradient for the respective estimated parameters. Except for narrow CS where the in situ bathymetry leads to the smallest residuals, overall roughness is the most significant parameter for further improvements of the methodology. The in situ flow gradient was only significant at one CS of the study where the spatial resolution of the satellite altimetry was too low to detect a larger change of the flow gradient.

The case study at the Lower Mississippi river shows that the approach is limited to selected regular and uniform reaches where the flow is not disturbed by obstacles, bends, or abrupt changes in width. Such conditions cause an underestimation of the channel depth using the empirical width-depth relationship. However, potentially suitable reaches can be identified based on the DAHITI water occurrence mask. At CS in these reaches, the geometry can be approximated well, because of the large number of synchronized water level and surface area observations and the derived hypsometry. Since the estimated flow gradient matches the mean of the variable in situ data, only the difficult to determine roughness coefficient remains as a limiting factor for the application of the methodology in suitable reaches.

For future studies, improvements of the roughness estimation and selection of cross-sections will be a particular challenge. In particular, the applicability and potential of more sophisticated flow equations should be examined. Additionally, the transferability to other targets such as smaller, braided, or non-alluvial rivers should be studied. The principle of mass conservation and reach averaging could be used to reduce the currently wide range of errors. Using water levels derived from surface areas with a hypsometry [26] would extend the resulting discharge time series over the period of the Landsat mission starting with the launch of Landsat 4 in 1982. The implementation of additional remote sensing missions gives new possibilities. Cryosat-2 data could be used to increase the spatial resolution of the estimated flow gradient and in future, the time synchronous observations of water level, surface area, and time variable flow gradient by the SWOT mission could be used to improve all aspects of our methodology while the effort of an implementation of SWOT data should be small.

Supplementary Materials: Supplementary Materials are available online at http://www.mdpi.com/2072-4292/12/17/2693/s1.

Author Contributions: D.S. developed the methodology, performed the validation, and wrote the paper. C.S. provided the DAHITI data and contributed to the methodology. D.D. and F.S. contributed to the manuscript writing and helped with the discussions of the applied methods and results. All authors have read and agreed to the published version of the manuscript.

Funding: This research received no external funding. The APC was funded by the Technical University of Munich (TUM) in the framework of the Open Access Publishing Program

Acknowledgments: We thank the US Geological Survey (USGS) and the US Army Corps of Engineering (USACE) for providing the in situ data. We thank three anonymous reviewers for their valuable comments that helped to improve the manuscript.

Conflicts of Interest: The authors declare no conflict of interest.

Appendix A

To validate the cross-sectional geometry (Section 3.3) with in situ bathymetry, we apply two offsets, Δh_g and Δh_{cs} to the long-term water level time series $h(t)$ to get an individual time series $h_{cs}(t)$ for each cross-section cs:

$$h_{cs}(t) = h(t) + \Delta h_g + \Delta h_{cs} \tag{A1}$$

where Δh_g is the median of the differences between the long-term satellite altimetry time series and the time series of a nearby water level gauge g, and Δh_{cs} is the height difference between the cross-section and that gauge. To obtain Δh_{cs}, we determine the gauge elevations analogous to the virtual stations using Equations (4)–(6) and estimate the elevation at the position of the cross-section using a linear interpolation between the gauge elevations. Δh_{cs} is the difference between the interpolated elevation and the elevation of gauge g.

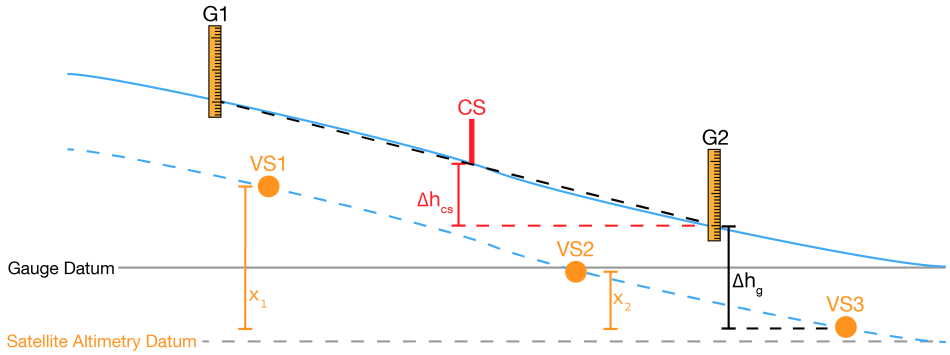

Figure A1. Illustration of the determined elevations showing three virtual stations (VS1-3), two gauges (G1 and G2), and a cross-section (CS) along a river (blue). The dashed blue line shows the river relative to the satellite altimetry datum. The elevations x_1 and x_2 above the reference station VS3 are the results of a linear adjustment of the satellite altimetry data. x_1 and x_2 are subtracted from measurements at VS1 and VS2 respectively to combine all VS to one long-term time series. The two offsets Δh_g and Δh_{cs} are necessary for the validation of the cross-sectional geometry with bathymetric survey data to compensate for the different datums and the shift in location.

Appendix B

In contrast to Vicksburg and Tarbert Landing, the time resolution of the in situ discharge time series for Natchez provided by the USACE is not daily but contains a record every 14 days on average with 585 entries in the time period from 3 January 2000 to 10 September 2019. However, only 21 in situ observations match a date in the estimated discharge time series and can be used for the validation. In order to increase the number of validation data, an additional discharge time series is estimated using a rating curve based on daily water level measurements at Natchez, which are also provided by the USACE. To consider the hysteresis effect [6], we use the rating curve formula by Jones [74–76]:

$$Q = Q_n \sqrt{1 + \frac{1}{SC} \frac{\Delta h}{\Delta t}} \tag{A2}$$

where Q_n is the estimated discharge for the water level h using a simple rating curve, in our case an exponential function, and t denotes time. The parameters of the exponential function, as well as the river bed slope S and the flood wave celerity C are fitted to the observed data for each year separately to consider changes in the channel geometry over time. For years when the fitting fails, parameters fitted to the entire observational period are used. The RMSE of the rated data is 1225 m^3/s compared to the original observations. The respective NRMSE is 5.66% and the R_P^2 is 0.978.

References

1. Gleick, P.H. Water resources. In *Encyclopedia of Climate and Weather*, 2nd ed.; Schneider, S.H., Ed.; Oxford University Press: New York, NY, USA, 2012; Volume 2, pp. 817–823.
2. Marsh, T.J. Capitalising on river flow data to meet changing national needs—A UK perspective. *Flow Meas. Instrum.* **2002**, *13*, 291–298.
3. Hunger, M.; Döll, P. Value of river discharge data for global-scale hydrological modeling. *Hydrol. Earth Syst. Sci.* **2008**, *12*, 841–861.
4. Chahine, M.T. The hydrological cycle and its influence on climate. *Nature* **1992**, *359*, 373–380.
5. Boyer, M.C. Streamflow Measurement. In *Handbook of Applied Hydrology*; Chow, V.T., Ed.; McGraw-Hill: New York, NY, USA, 1964; Chapter 15.
6. Holmes, R.R. Streamflow Rating. In *Handbook of Applied Hydrology*, 2nd ed.; Singh, V.P., Ed.; McGraw-Hill: New York, NY, USA, 2016; Chapter 6.
7. Holmes, R.R. Streamflow Data. In *Handbook of Applied Hydrology*, 2nd ed.; Singh, V.P., Ed.; McGraw-Hill: New York, NY, USA, 2016; Chapter 5.

8. Hannah, D.M.; Demuth, S.; van Lanen, H.A.J.; Looser, U.; Prudhomme, C.; Rees, G.; Stahl, K.; Tallaksen, L.M. Large-scale river flow archives: Importance, current status and future needs. *Hydrol. Process.* **2011**, *25*, 1191–1200.
9. Gleason, C.J.; Smith, L.C. Toward global mapping of river discharge using satellite images and at-many-stations hydraulic geometry. *Proc. Natl. Acad. Sci. USA* **2014**, *111*, 4788–4791.
10. Pekel, J.F.; Cottam, A.; Gorelick, N.; Belward, A.S. High-resolution mapping of global surface water and its long-term changes. *Nature* **2016**, *540*, 418–422.
11. Klein, I.; Gessner, U.; Dietz, A.J.; Kuenzer, C. Global WaterPack—A 250 m resolution dataset revealing the daily dynamics of global inland water bodies. *Remote Sens. Environ.* **2017**, *198*, 345–362.
12. Schwatke, C.; Scherer, D.; Dettmering, D. Automated Extraction of Consistent Time-Variable Water Surfaces of Lakes and Reservoirs Based on Landsat and Sentinel-2. *Remote Sens.* **2019**, *11*, 1010.
13. Pavelsky, T.M.; Smith, L.C. RivWidth: A Software Tool for the Calculation of River Widths From Remotely Sensed Imagery. *IEEE Geosci. Remote Sens. Lett.* **2008**, *5*, 70–73.
14. Allen, G.H.; Pavelsky, T. Global extent of rivers and streams. *Science* **2018**, *361*, 585–588.
15. Yang, X.; Pavelsky, T.M.; Allen, G.H.; Donchyts, G. RivWidthCloud: An Automated Google Earth Engine Algorithm for River Width Extraction From Remotely Sensed Imagery. *IEEE Geosci. Remote Sens. Lett.* **2020**, *17*, 217–221.
16. Alsdorf, D.E.; Rodríguez, E.; Lettenmaier, D.P. Measuring surface water from space. *Rev. Geophys.* **2007**, *45*, RG2002.
17. Mladenova, I.E.; Nearing, G.S.; Bolten, J.D.; Lakshmi, V. Remote Sensing Techniques and Data Assimilation for Hydrologic Modeling. In *Handbook of Applied Hydrology*, 2nd ed.; Singh, V.P., Ed.; McGraw-Hill: New York, NY, USA, 2016; Chapter 8.
18. Kugler, Z.; Nghiem, S.; Brakenridge, G. L-Band Passive Microwave Data from SMOS for River Gauging Observations in Tropical Climates. *Remote Sens.* **2019**, *11*, 835.
19. Birkett, C.M. The contribution of TOPEX/POSEIDON to the global monitoring of climatically sensitive lakes. *J. Geophys. Res.* **1995**, *100*, 25179.
20. Berry, P.A.M. Global inland water monitoring from multi-mission altimetry. *Geophys. Res. Lett.* **2005**, *32*, L16401.
21. Schwatke, C.; Dettmering, D.; Bosch, W.; Seitz, F. DAHITI—An innovative approach for estimating water level time series over inland waters using multi-mission satellite altimetry. *Hydrol. Earth Syst. Sci.* **2015**, *19*, 4345–4364.
22. Biancamaria, S.; Frappart, F.; Leleu, A.S.; Marieu, V.; Blumstein, D.; Desjonquères, J.D.; Boy, F.; Sottolichio, A.; Valle-Levinson, A. Satellite radar altimetry water elevations performance over a 200 m wide river: Evaluation over the Garonne River. *Adv. Space Res.* **2017**, *59*, 128–146.
23. Liu, G.; Schwartz, F.; Tseng, K.H.; Shum, C.K.; Lee, S. Satellite altimetry for measuring river stages in remote regions. *Environ. Earth Sci.* **2018**, *77*, 639.
24. Boergens, E.; Buhl, S.; Dettmering, D.; Klüppelberg, C.; Seitz, F. Combination of multi-mission altimetry data along the Mekong River with spatio-temporal kriging. *J. Geod.* **2017**, *91*, 519–534.
25. Getirana, A.; Jung, H.C.; Tseng, K.H. Deriving three dimensional reservoir bathymetry from multi-satellite datasets. *Remote Sens. Environ.* **2018**, *217*, 366–374.
26. Schwatke, C.; Dettmering, D.; Seitz, F. Volume Variations of Small Inland Water Bodies from a Combination of Satellite Altimetry and Optical Imagery. *Remote Sens.* **2020**, *12*, 1606.
27. Kouraev, A.V.; Zakharova, E.A.; Samain, O.; Mognard, N.M.; Cazenave, A. Ob' river discharge from TOPEX/Poseidon satellite altimetry (1992–2002). *Remote Sens. Environ.* **2004**, *93*, 238–245.
28. Tourian, M.J.; Sneeuw, N.; Bárdossy, A. A quantile function approach to discharge estimation from satellite altimetry (ENVISAT). *Water Resour. Res.* **2013**, *49*, 4174–4186.
29. Tourian, M.J.; Schwatke, C.; Sneeuw, N. River discharge estimation at daily resolution from satellite altimetry over an entire river basin. *J. Hydrol.* **2017**, *546*, 230–247.
30. Degefu, D.M.; Weijun, H.; Zaiyi, L.; Liang, Y.; Zhengwei, H.; Min, A. Mapping Monthly Water Scarcity in Global Transboundary Basins at Country-Basin Mesh Based Spatial Resolution. *Sci. Rep.* **2018**, *8*, 1–10.
31. Oki, T.; Quiocho, R.E. Economically challenged and water scarce: Identification of global populations most vulnerable to water crises. *Int. J. Water Resour. Dev.* **2020**, *36*, 416–428.

32. Biancamaria, S.; Lettenmaier, D.P.; Pavelsky, T.M. The SWOT Mission and Its Capabilities for Land Hydrology. *Surv. Geophys.* **2016**, *37*, 307–337.
33. Manning, R. On the flow of water in open channels and pipes. *Trans. Inst. Civ. Eng. Irel.* **1891**, *20*, 161–207.
34. Gleason, C.J.; Smith, L.C.; Lee, J. Retrieval of river discharge solely from satellite imagery and at-many-stations hydraulic geometry: Sensitivity to river form and optimization parameters. *Water Resour. Res.* **2014**, *50*, 9604–9619.
35. Julien, P.Y. *River Mechanics*; Cambridge University Press: New York, NY, USA, 2018.
36. Durand, M.; Neal, J.; Rodríguez, E.; Andreadis, K.M.; Smith, L.C.; Yoon, Y. Estimating reach-averaged discharge for the River Severn from measurements of river water surface elevation and slope. *J. Hydrol.* **2014**, *511*, 92–104.
37. Durand, M.; Rodriguez, E.; Alsdorf, D.E.; Trigg, M. Estimating River Depth From Remote Sensing Swath Interferometry Measurements of River Height, Slope, and Width. *IEEE J. Sel. Top. Appl. Earth Obs. Remote. Sens.* **2010**, *3*, 20–31.
38. Zakharova, E.; Nielsen, K.; Kamenev, G.; Kouraev, A. River discharge estimation from radar altimetry: Assessment of satellite performance, river scales and methods. *J. Hydrol.* **2020**, *583*, 124561.
39. Bjerklie, D.M.; Lawrence Dingman, S.; Vorosmarty, C.J.; Bolster, C.H.; Congalton, R.G. Evaluating the potential for measuring river discharge from space. *J. Hydrol.* **2003**, *278*, 17–38.
40. Garambois, P.A.; Monnier, J. Inference of effective river properties from remotely sensed observations of water surface. *Adv. Water Resour.* **2015**, *79*, 103–120.
41. Bjerklie, D.M.; Birkett, C.M.; Jones, J.W.; Carabajal, C.; Rover, J.A.; Fulton, J.W.; Garambois, P.A. Satellite remote sensing estimation of river discharge: Application to the Yukon River Alaska. *J. Hydrol.* **2018**, *561*, 1000–1018.
42. Bjerklie, D.M. Estimating the bankfull velocity and discharge for rivers using remotely sensed river morphology information. *J. Hydrol.* **2007**, *341*, 144–155.
43. Kebede, M.G.; Wang, L.; Yang, K.; Chen, D.; Li, X.; Zeng, T.; Hu, Z. Discharge Estimates for Ungauged Rivers Flowing over Complex High-Mountainous Regions based Solely on Remote Sensing-Derived Datasets. *Remote Sens.* **2020**, *12*, 1064.
44. Durand, M.; Gleason, C.J.; Garambois, P.A.; Bjerklie, D.; Smith, L.C.; Roux, H.; Rodriguez, E.; Bates, P.D.; Pavelsky, T.M.; Monnier, J.; et al. An intercomparison of remote sensing river discharge estimation algorithms from measurements of river height, width, and slope. *Water Resour. Res.* **2016**, *52*, 4527–4549.
45. Sichangi, A.W.; Wang, L.; Yang, K.; Chen, D.; Wang, Z.; Li, X.; Zhou, J.; Liu, W.; Kuria, D. Estimating continental river basin discharges using multiple remote sensing data sets. *Remote Sens. Environ.* **2016**, *179*, 36–53.
46. Moramarco, T.; Barbetta, S.; Bjerklie, D.M.; Fulton, J.W.; Tarpanelli, A. River Bathymetry Estimate and Discharge Assessment from Remote Sensing. *Water Resour. Res.* **2019**, *55*, 6692–6711.
47. Sichangi, A.; Wang, L.; Hu, Z. Estimation of River Discharge Solely from Remote-Sensing Derived Data: An Initial Study Over the Yangtze River. *Remote Sens.* **2018**, *10*, 1385.
48. Knox, J.C. The Mississippi River System. In *Large Rivers*; Gupta, A., Ed.; John Wiley & Sons, Ltd: Chichester, UK, 2007; pp. 145–182.
49. Little, C.D.; Biedenharn, D.S. *Mississippi River Hydrodynamic and Delta Management Study (MRHDM)—Geomorphic Assessment*; Technical Report 14-5; US Army Engineer Research and Development Center (ERDC): Vicksburg, MS, USA, 2014.
50. Wohl, E.E. Hydrology and Discharge. In *Large Rivers*; Gupta, A., Ed.; John Wiley & Sons, Ltd: Chichester, UK, 2007; pp. 29–44.
51. The Global Runoff Data Centre, 56068 Koblenz, Germany. GRDC Data Download Portal. 2020. Available online: https://portal.grdc.bafg.de/(accessed on 5 August 2020)
52. Lewis, J.; Brown, G.; Ayers, S. *Investigation of Discharge Measurements of the Lower Mississippi River below Natchez, MS*; Technical Report 3; US Army Corps of Engineering: Vicksburg, MS, USA, 2017.
53. U.S. Geological Survey. USGS Water Data for the Nation. 2016. Available online: https://waterdata.usgs.gov/nwis (accessed on 10 December 2019)
54. US Army Corps of Engineers. Rivergages.com. 2019. Available online: http://rivergages.mvr.usace.army.mil (accessed on 10 December 2019).

55. US Army Corps of Engineers. USACE Hydrographic Surveys Powered by eHydro. 2019. Available online: https://geospatial-usace.opendata.arcgis.com/datasets/4b8f2ba307684cf597617bf1b6d2f85d (accessed on 10 December 2019).
56. US Army Corps of Engineers, N.O.D. Multibeam Bathymetric Data for the Lower Mississippi River. 2013. Available online: mvn.usace.army.mil/Missions/Engineering/Channel-Improvement-and-Stabilization-Program/2013MBMR/ (accessed on 10 December 2019).
57. Girardeau-Montaut, D. CloudCompare (version 2.9.1). 2019. Available online: http://www.cloudcompare.org/ (accessed on 10 December 2019).
58. Bosch, W.; Dettmering, D.; Schwatke, C. Multi-Mission Cross-Calibration of Satellite Altimeters: Constructing a Long-Term Data Record for Global and Regional Sea Level Change Studies. *Remote Sens.* **2014**, *6*, 2255–2281.
59. Hovmöller, E. The Trough-and-Ridge diagram. *Tellus* **1949**, *1*, 62–66.
60. OpenStreetMap Contributors. Planet Dump. 2017. Available online: https://planet.osm.org (accessed on 10 December 2019).
61. Einstein, H.A. Der hydraulische oder Profil-Radius. *Schweiz. Bauztg.* **1934**, *103/104*, 89–91.
62. Niemeier, W. *Ausgleichungsrechnung*; De Gruyter: Tubingen, Germany, 2008; p. 512.
63. Spearman, C. The Proof and Measurement of Association between Two Things. *Am. J. Psychol.* **1987**, *100*, 441.
64. Moody, J.A.; Troutman, B.M. Characterization of the spatial variability of channel morphology. *Earth Surf. Process. Landforms* **2002**, *27*, 1251–1266.
65. Strahler, A.N. Hypsometric (Area-Altitude) Analysis of Erosional Topography. *GSA Bull.* **1952**, *63*, 1117–1142.
66. Cowan, W. Estimating hydraulic roughness coefficients. *Agric. Eng.* **1956**, *37*, 473–475.
67. Arcement, G.J.; Schneider, V.R. *Guide for Selecting Manning's Roughness Coefficients for Natural Channels and Flood Plains*; Technical Report; U.S. Geological Survey: Washington, DC, USA, 1989.
68. Fitzpatrick, F.A.; Waite, I.R. *Revised Methods for Characterizing Stream Habitat in the National Water-Quality Assessment Program*; Technical Report; Geological Survey (U.S.): Washington, DC, USA, 1998.
69. Leopold, L.B.; Wolman, M.G.; Miller, J.P. *Fluvial Processes in Geomorphology*; Dover Publications, Inc.: New York, NY, USA, 1964.
70. Gordon, N.D.; McMahon, T.A.; Finlayson, B.L.; Gippel, C.J.; Nathan, R.J. *Stream Hydrology: An Introduction for Ecologists*, 2nd ed.; John Wiley & Sons, Ltd: Hoboken, NJ, USA, 2004.
71. Gaines, R.A.; Priestas, A.M. *Particle Size Distribution of Bed Sediments along the Mississippi River, Grafton, Illinois, to Head of Passes, Louisiana, November 2013*; Technical Report 7; US Army Corps of Engineers: Vicksburg, MS, USA, 2016.
72. Lecher, K. (Ed.) *Taschenbuch der Wasserwirtschaft*, 9th ed.; Springer-Vieweg: Wiesbaden, Germany, 2012.
73. Nash, J.; Sutcliffe, J. River flow forecasting through conceptual models part I—A discussion of principles. *J. Hydrol.* **1970**, *10*, 282–290.
74. Jones, B.E. *A Method of Determining the Daily Discharge of Rivers if Variable Slope*; Technical Report; U.S. Geological Survey: Reston, VA, USA, 1916.
75. Perumal, M.; Shrestha, K.B.; Chaube, U.C. Reproduction of Hysteresis in Rating Curves. *J. Hydraul. Eng.* **2004**, *130*, 870–878.
76. Zakwan, M. Spreadsheet-based modelling of hysteresis-affected curves. *Appl. Water Sci.* **2018**, *8*, 1–5.

P2 ICESat-2 Based River Surface Slope and Its Impact on Water Level Time Series From Satellite Altimetry

Scherer, D., Schwatke, C., Dettmering, D., & Seitz, F. (2022). **ICESat-2 Based River Surface Slope and Its Impact on Water Level Time Series From Satellite Altimetry**. *Water Resources Research*, *58*, 1–25. https://doi.org/10.1029/2022WR032842

Date of Publication: 25 October 2022

Abstract

The water surface slope (WSS) of rivers is essential for estimating flow velocity and discharge. It is also helpful as a correction applied to range measurements of satellite altimetry missions to derive water level time series at a virtual station. Using radar altimetry, WSS can only be roughly estimated and is limited to wide rivers because of its coarse spatiotemporal resolution. In contrast, the lidar sensor onboard ICESat-2 can also observe small rivers. Using ICESat-2's unique measurement geometry with six parallel laser beams, we derive instantaneous WSS along and across the satellite's ground track, time-variable WSS (with an average of five days of records in the studied epoch between October 2018 and October 2021), and average WSS on reach-scale. Although the method can be applied globally, this study is limited to 815 reaches in Europe and North America where sufficient validation data is available. We compare the ICESat-2 WSS with time-variable WSS derived from multiple gauges and constant data from the "SWOT River Database" (SWORD). For 89% of the studied reaches, ICESat-2 can be used to estimate the average WSS with a median absolute error of 23 mm/km. We also show the possible performance gain at multiple virtual stations in the "Database for Hydrological Time Series of Inland Waters" (DAHITI, https://dahiti.dgfi.tum.de), applying the WSS as a correction for altimetry satellites' ground track variability. We correct 137 virtual stations for the derived ICESat-2 WSS and yield improvements in the root mean square error (RMSE) by up to 30 cm or 66%.

Contribution

Conceptualization, D.S.; data curation: C.S.; funding acquisition: D.D., F. S.; methodology: D.S.; project administration: D.D., F.S.; software: D.S.; supervision: D.D., F.S.; validation: D.S.; visualization: D.S.; writing – original draft: D.S.; writing–review and editing: C.S., D.D., F.S.

Criteria	Own Contribution
Idea and conceptual design	85%
Data acquisition and preparation	75%
Implementation and realisation	90%
Analysis and discussion	90%
Figure compilation	95%
Manuscript structure and writing	80%
Overall contribution	86%

Water Resources Research

RESEARCH ARTICLE
10.1029/2022WR032842

ICESat-2 Based River Surface Slope and Its Impact on Water Level Time Series From Satellite Altimetry

Daniel Scherer[1], Christian Schwatke[1], Denise Dettmering[1], and Florian Seitz[1]

[1]Department of Aerospace and Geodesy, TUM School of Engineering and Design, Deutsches Geodätisches Forschungsinstitut der Technische Universität München (DGFI-TUM), Munich, Germany

Key Points:

- Simultaneous obs. from Ice, Cloud, and Land Elevation Satellite 2's (ICESat-2's) unique multibeam lidar altimeter are used to estimate instantaneous reach-scale water surface slope (WSS)
- For 89% of 815 studied reaches, we find ICESat-2 can be used to estimate WSS with a median absolute error of 23 mm/km relative to gauge data
- We correct water level time series from radar satellite altimetry for the derived WSS and obtain improvements of up to 30 cm (66%) root mean square error

Correspondence to:
D. Scherer,
daniel.scherer@tum.de

Citation:
Scherer, D., Schwatke, C., Dettmering, D., & Seitz, F. (2022). ICESat-2 based river surface slope and its impact on water level time series from satellite altimetry. *Water Resources Research*, *58*, e2022WR032842. https://doi.org/10.1029/2022WR032842

Received 8 JUN 2022
Accepted 25 OCT 2022

Author Contributions:
Conceptualization: Daniel Scherer
Data curation: Christian Schwatke
Funding acquisition: Denise Dettmering, Florian Seitz
Methodology: Daniel Scherer
Project Administration: Denise Dettmering, Florian Seitz
Software: Daniel Scherer
Supervision: Denise Dettmering, Florian Seitz
Validation: Daniel Scherer
Visualization: Daniel Scherer
Writing – original draft: Daniel Scherer

Abstract The water surface slope (WSS) of rivers is essential for estimating flow velocity and discharge. It is also helpful as a correction applied to range measurements of satellite altimetry missions to derive water level time series at a virtual station. Using radar altimetry, WSS can only be roughly estimated and is limited to wide rivers because of its coarse spatiotemporal resolution. In contrast, the lidar sensor onboard Ice, Cloud, and Land Elevation Satellite 2 (ICESat-2) can also observe small rivers. Using ICESat-2's unique measurement geometry with six parallel laser beams, we derive instantaneous WSS along and across the satellite's ground track, time-variable WSS (with an average of 5 days of records in the studied epoch between October 2018 and October 2021), and average WSS on reach-scale. Although the method can be applied globally, this study is limited to 815 reaches in Europe and North America where sufficient validation data is available. We compare the ICESat-2 WSS with time-variable WSS derived from multiple gauges and constant data from the "SWOT River Database." For 89% of the studied reaches, ICESat-2 can be used to estimate the average WSS with a median absolute error of 23 mm/km. We also show the possible performance gain at multiple virtual stations (VS) in the "Database for Hydrological Time Series of Inland Waters" (https://dahiti.dgfi.tum.de), applying the WSS as a correction for altimetry satellites' ground track variability. We correct 137 VS for the derived ICESat-2 WSS and yield improvements in the root mean square error by up to 30 cm or 66%.

1. Introduction

The water surface slope (WSS), hydraulic gradient, or flow gradient of a river is the slope of the hydraulic grade line, that is, the change of the pressure head per distance unit (Gliński et al., 2011; Herrmann & Bucksch, 2014; Julien, 2018b). It is typically defined positive for an decreasing water surface elevation (WSE) in downstream direction (Julien, 2018b). WSS is not stationary but changes over time and space. Especially in natural rivers that are non-uniform and unsteady, the WSS is variable over time because of morphological changes of the river bed and flood waves (Julien, 2018a). Locally, WSS may differ from larger-scale averages and change with every reach because of local characteristics like cascades, pools, or tributary estuaries (Rhoads, 2020; Schumm, 2005). While the WSS of an alluvial river is gradual, bedrock causes natural discontinuities in semi-alluvial rivers (Julien, 2018b). In hydrology, WSS is a critical parameter required to calculate flow velocity and discharge (Manning, 1891; Rhoads, 2020). The flow velocity derived from WSS is also essential for densifying spatial or temporal low-resolution water level measurements from non-repeating satellite altimetry missions such as Cryosat-2 (Tourian et al., 2016). Generally, the WSS can be used to correct any satellite altimetry mission to compensate for the satellites' ground track variability when calculating long-term water level time series at fixed locations, so-called virtual stations (VS).

WSE measurements of the "Shuttle Radar Topography Mission" (SRTM) are regularly used to derive WSS (Cohen et al., 2018; Kebede et al., 2020; LeFavour & Alsdorf, 2005; Sichangi et al., 2018). However, because of its relatively large height error, WSS estimates from SRTM data are only appropriate on a large scale (LeFavour & Alsdorf, 2005). For river discharge estimation and satellite altimetry correction, though, smaller-scale WSS are favorable. Additionally, SRTM captured only a short epoch of 11 days in February 2000, and the WSS observed during this time may not represent the respective average WSS.

There are only a few methods capable of detecting small-scale local changes of WSS with high resolution. Airborne lidar (Mandlburger et al., 2020) and radar (Jiang et al., 2020) sensors or measurements from field campaigns (Carr et al., 2019; Pitcher et al., 2020) are suitable because of the continuous local mapping of the WSE. However, such airborne or field campaigns require significant personnel and cost-intensive effort, so they

Writing – review & editing: Christian Schwatke, Denise Dettmering, Florian Seitz

can only be applied occasionally to selected reaches but are not suitable to continuously observe the WSS of an entire river system. Therefore, the WSS observations may not agree with the actual average WSS, similar to methods using SRTM data.

Better suited for operational usage, WSE measurements between two stations, such as gauges, with a known distance along the river and without flow disturbances in between can be used to estimate WSS. The local scales depend on the distribution of stations along the river. Although such WSS estimates represent only a mean between the stations and small-scale deviations may not be captured, temporal changes of the long-term mean WSS can be monitored by the temporal continuous WSE measurements.

In-situ gauging stations are the most accurate WSE sources as the pressure head is continuously measured by a probe in a housing sheltered from disturbances, for example, weather (Sauer & Turnipseed, 2010). However, maintaining a network of gauging stations is challenging (Calmant & Seyler, 2006), limiting the number of monitored sites and increasing the probability of undetected flow disturbances or significant changes in WSS between two gauges. Therefore, WSS estimates between two in-situ stations may not always be meaningful, especially, when both stations do not reference the same vertical datum. Often, gauge data can not be used to derive WSS because the vertical datum is not specified. Additionally, from a global view, the spatial distribution of gauges is uneven, concentrated in developed countries and absent in remote areas, which is apparent from the availability of the derived discharge data (Hannah et al., 2011).

In contrast, satellite altimetry provides homogeneously distributed data globally. However, the number of potential VS depends on the satellite orbit and how the track crosses a river of interest. It may miss meridional flowing rivers parallel to its ground track or cross meandering rivers multiple times within a short distance. Overall, the temporal resolution of WSE measurements by satellite altimetry is significantly lower than that of gauges. Classical pulse-limited radar or low-resolution mode (LRM) altimeters measure only in nadir direction and may have a significant error for narrow rivers due to the large radar footprint (Calmant et al., 2016). Still, for rivers wider than 200 m the WSE can be derived from LRM altimetry with an root mean square error (RMSE) of a few decimeters (Schwatke et al., 2015; Sulistioadi et al., 2015). WSE measurements using synthetic aperture radar (SAR) can be used for rivers that are up to 40 m narrow with similar accuracy (Halicki & Niedzielski, 2022), and the more modern techniques like interferometric SAR (SARIn) and laser altimeters are still more accurate and applicable for even more narrow rivers. Furthermore, modern sensors such as the planned "Surface Water and Ocean Topography" (SWOT) mission measure not only in nadir direction but within a swath so that WSS can be instantaneously derived within one pass (Langhorst et al., 2019).

Despite the challenges and uncertainties, satellite altimetry is widely used to estimate WSS, predominantly to derive river discharge (Gleason & Durand, 2020; Sichangi et al., 2016). In a study for two arctic rivers, SARIn and SAR data from the CryoSat-2, SARAL, and Sentinel-3A missions were used to model the longitudinal river profile using a time-variable cubic spline function (Zakharova et al., 2020). In this way, it was possible to estimate WSS at any location and time for a 175 km segment of the Ob River. However, no satisfactory satellite altimetry data could be retrieved for the Pur River. The average relative model error was 22%, with error estimates ranging from 1.4 to 10 mm/km for WSS between 1 and 13 mm/km. However, the authors state these errors might be underestimated. A linear model was used to derive constant WSS of the Mississippi River with a least-squares approach based on Jason-2/-3, ENVISAT ("Environmental Satellite"), and Sentinel-3A/B data (Scherer et al., 2020). The average absolute median deviation of the WSS between the VS compared to the WSS measurements between seven gauges was 12 mm/km with a median relative error of 19.4%. WSS could also be derived from a topographic model of the Mekong River which used B-Splines on a directed tree graph fitted to multi-mission satellite altimetry WSE observations (Boergens et al., 2021). However, the model was limited by the uneven distribution of observations and quality suffered in regions with sparse data.

Without applying a model, WSE differences between consecutive intersections of the same satellite altimetry passes with two reaches of the Yukon River were used to estimate WSS (Bjerklie et al., 2018). The resulting WSS ranged between 30 and 140 mm/km and were within the range of 10–320 mm/km observed by field measurements. In a similar way, WSS was determined for the Xingu River using WSE measurements of 10 consecutive crossings of the ENVISAT mission (Garambois et al., 2017). Although these studies may yield good results, methods using consecutive crossings of one satellite altimetry pass are limited to a small number of sites by the orbit geometry of the respective mission. In contrast, ICESat data of different passes observed within 2 days difference were used to estimate WSS for the Congo River (O'Loughlin et al., 2013). Because of the long repeat

cycle of ICESat, it is more likely to get useable data for any global river with this method. However, there may be errors introduced due to the time lag between the asynchronous WSE observations.

In this paper, we use WSE measurements acquired by the follow-on mission of ICESat, the "Ice, Cloud, and Land Elevation Satellite 2" (ICESat-2). Similar to ICESat, it is placed on a long-repeat orbit and therefore, covers many reaches but revisits them only every 91 days. Compared to ICESat, the coverage of ICESat-2 is increased by its new sensor, the "Advanced Topographic Laser Altimeter System" (ATLAS), which measures the Earth's topography along the ground track of three parallel pairs of laser beams spaced 3.3 km apart (Markus et al., 2017; Neumann et al., 2019). This increases the probability of simultaneous WSE measurements at different locations within a river reach.

The novel approach presented in this study uses ICESat-2's unique measurement geometry to derive instantaneous reach-scale river WSS. Two methods, (a) the across-track and (b) the along-track, are combined in this approach. In the across-track method, we calculate the WSS between the simultaneous WSE measurements of ICESat-2's parallel beams intersecting a reach. Additionally, we fit the WSS to all WSE observations of each individual beam intersecting the river reach and project it to the river centerline in the along-track method. Both methods are combined into a time-variable WSS to maximize the temporal and spatial coverage. Furthermore, an average reach-scale WSS is computed. In this way, we aim to derive global average reach-scale WSS and its variability in future studies.

Amongst other data required for this study, the used ICESat-2 data set is described in Section 2. The approach to derive WSS is described in Section 3. The resulting WSS are compared with time-variable WSS between in-situ gauges in Section 4 where we also show the impact of applying the reach-scale WSS as a correction to VS hydrographs.

2. Study Areas and Data

For this study, we select rivers in Europe and North America where a sufficient number of in-situ data are available for validation. The maps of these regions (Figure 1) contain all reaches defined by the "SWOT River Database" (SWORD, see Section 2.2). Only the bold reaches are studied in this paper because the selection of the studied reaches is limited by the availability of in-situ gauges suitable for validation and their connectivity so that there are no dams, weirs, major riffles, or confluences in between the gauges. All the in-situ sources are given in Section 2.3. No WSS can be derived for the purple reaches because no or insufficient data is available from ICESat-2. The ICESat-2 data is described in Section 2.1. Table A1 in the appendix lists the characteristics of the studied river sections according to SWORD and the in-situ sources used which we describe in Section 2.3. Although strongly limited by the spatial distribution of suitable gauges, we include as diverse reaches as possible, especially regarding the nominal slope and width. Figure 1 also shows the orbit ground tracks of the Jason-2/3 and Sentinel-3A/B missions and the VS used in this study. We describe the radar satellite altimetry data in Section 2.4.

2.1. ATLAS/ICESat-2 ATL13 L3A Inland Water Surface Height Product

The primary data used in this study are WSE measurements acquired by ICESat-2 provided within the "ATLAS/ICESat-2 L3A Along Track Inland Surface Water Data" (ATL13) (Jasinski et al., 2021b) product by the "National Snow & ICE Data Center" (NSIDC). The satellite is placed on a 91-day repeat orbit with an inclination of 92° (Markus et al., 2017). The ATLAS sensor onboard ICESat-2 is a photon-counting lidar, measuring the time an emitted photon travels to Earth and back to the sensor. ATLAS emits photons along three pairs of beams, which each consist of a high energy (175 ± 17 μJ) "strong" beam and a low energy (45 ± 5 μJ) "weak" beam. Each beam illuminates a footprint of approximately 17 m in diameter at a pulse rate of 10kHz (i.e., one pulse every 0.7 m) (Neumann et al., 2019). However, because of the low reflectance of water, a maximum of 2.9 photons per meter can be observed by the sensor over inland waters, depending on the water and atmospheric conditions (Jasinski et al., 2021a).

Two global studies (Cooley et al., 2021; Ryan et al., 2020) validate the "ATLAS/ICESat-2 L3A Land and Vegetation Height (ATL08)" data, which reportedly contain very similar water level observations to the ATL13 data (Ryan et al., 2020). For lakes and reservoirs, there is no significant difference in the accuracy between the strong and weak beams (Cooley et al., 2021). In contrast to radar altimetry, the lidar sensor can not penetrate clouds, so

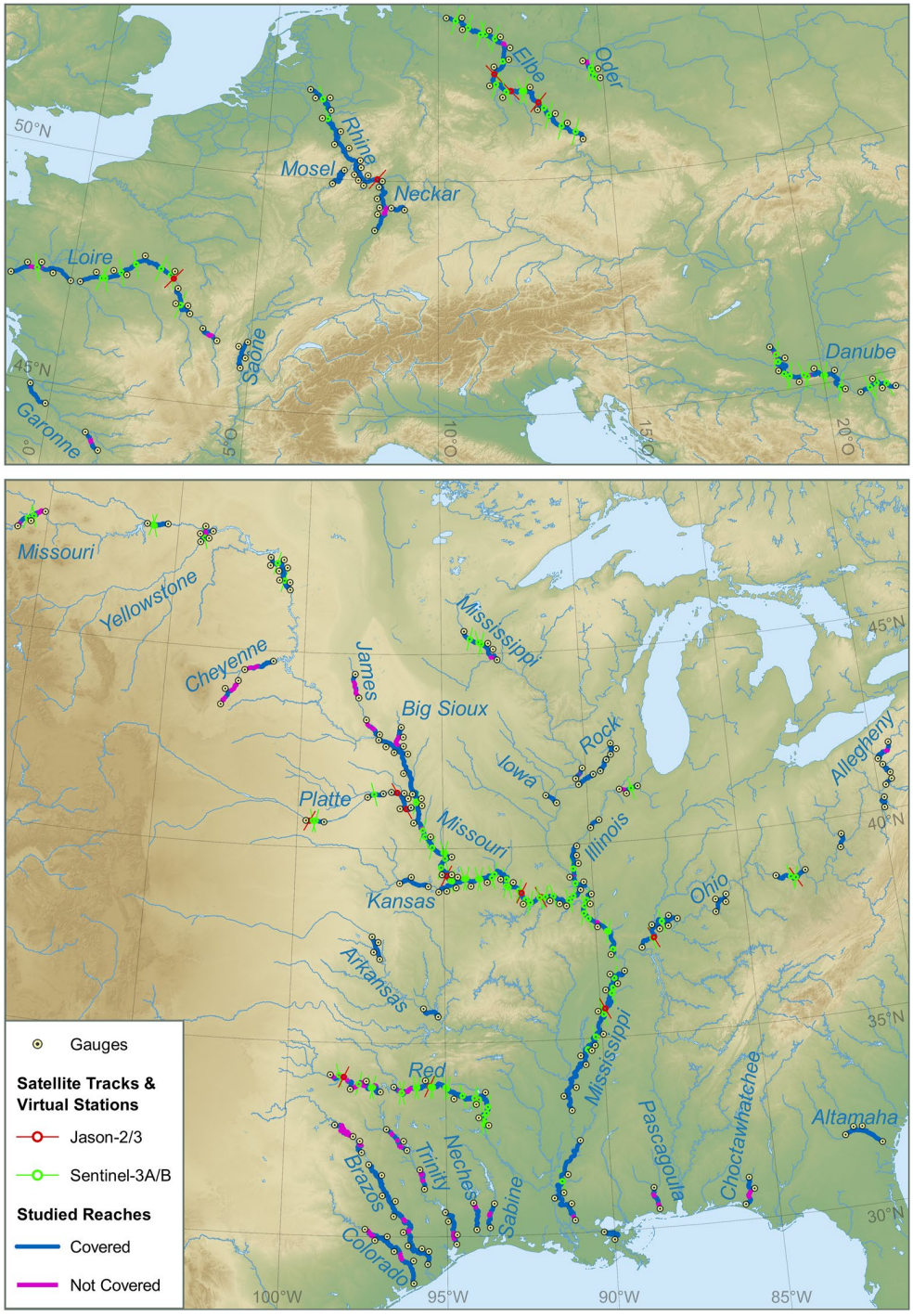

Figure 1. Regions with studied reaches, in-situ gauges we use for validation, and virtual stations to which we apply the water surface slope correction. Top: Europe. Bottom: North America.

there are missing observations in overcast conditions. The median standard deviation of ICESat-2 observations over inland waters is reported to be 0.017 m, with a mean error of 0.14 m (Cooley et al., 2021; Ryan et al., 2020). A regional study validating ATL13 data at the Mekong River reports similar results with an RMSE of 0.24 m and a median standard deviation of 0.04 m (Lao et al., 2022).

The ATL13 product does not contain photon-level observations but representative values over short segments of 75–100 consecutive received photons above inland water bodies. These short segments have an along-track length of 30 to several hundred meters, depending on the number of received signal photons per pulse. In this paper, we use the "ht_water_surf" parameter, the mean water surface height, with reference to the WGS84 ellipsoid per beam and short segment (Jasinski et al., 2021a). We apply the EIGEN-6C4 geoid (Foerste et al., 2014) to have a common reference of the ICESat-2 WSE data with other satellite altimetry data used in this study. Additionally, we use the spacecraft orientation parameter to identify the strong and weak beams and compare the respective results.

2.2. SWOT River Database (SWORD)

To determine the angle and chainage at which the beam ground tracks of ICESat-2 intersect a river, we use the high-resolution (30 m) river centerlines from SWORD (Version v1) (Altenau et al., 2021a). SWORD is based on the "Global River Widths from Landsat" (GRWL) data set (Allen & Pavelsky, 2018), which contains river centerlines processed from Landsat imagery at mean annual flow. For SWORD, the GRWL centerlines were segmented at natural and artificial river obstructions, basin boundaries, tributary junctions, or otherwise approximately every 10 km. SWORD also includes data on river obstructions and topology, which we use to determine whether two stations are connected without flow disturbances in between. Additionally, SWORD contains constant WSS data per reach, which we use as a benchmark to compare our results besides in-situ gauging data. The SWORD WSS are estimated by fitting a linear regression to elevation data from the MERIT Hydro data set (Altenau et al., 2021a; Yamazaki et al., 2019). MERIT Hydro is derived from MERIT DEM which comprises remote sensing data from the SRTM and "Advanced Land Observing Satellite" (ALOS) missions, with removed noise, height errors, and tree canopy biases (Yamazaki et al., 2017). Furthermore, SWORD contains the width of each reach at mean annual flow, which we use to filter the ICESat-2 observations.

2.3. In-Situ Water Level Time Series From Gauges

We validate the WSS using in-situ WSE data observed at multiple pairs of gauges. The in-situ data of single gauges are also used to determine error measures for satellite-derived hydrographs at VS before and after applying the WSS as a correction. We retrieve the in-situ data for Germany from the "Wasserstraßen- und Schifffahrtsverwaltung des Bundes" (WSV) provided by the "Bundesanstalt f"ur Gewässerkunde" (BfG), for the United States from the "U.S. Army Corps of Engineering" (USACE) and the "U.S. Geological Survey" (USGS), for France from "Hydroportail", and for Serbia from the "Republic Hydrometeorological Service of Serbia" (HIDMET). The number of gauges per river and their vertical datum is listed for each source in Table A1 in the appendix. We only use in-situ data from gauges with a given vertical datum to get an accurate WSE difference between a pair of gauges. In case the given vertical datum varies per gauge within a source, it is converted to the common datum given in Table A1. If a conversion is not possible, the gauge is discarded.

2.4. DAHITI Water Level Time Series From Radar Altimetry

We use water level time series derived from radar satellite altimetry data from the "Database for Hydrological Time Series of Inland Waters" (DAHITI, www.dahiti.dgfi.tum.de) (Schwatke et al., 2015) in this study. The data is provided at VS, which are located at the intersections of a satellite's orbit ground track with a river. We select the Jason-2/3 and Sentinel-3A/B missions for this study. These satellites orbit Earth in a repeating pattern, revisiting the same location every 10 and 27 days, respectively. However, the orbit repeatability at the equator crossing of altimetry satellites is designed to be within ± 1 km (Tapley et al., 1994) so that the exact location where they cross a river is not stationary. For the selected missions, the empirical repeatability magnitude is in a range of 1.5–1.7 km. With a global median river WSS of 469 mm/km (Frasson et al., 2019), these slight deviations at the assumed to be stationary VS can cause a WSE error of up to 1 m on average.

The Jason-2/3 satellites are equipped with a LRM altimeter, which scans a circular area with a diameter of several kilometers (Calmant et al., 2016). Special retracking software must be used for smaller rivers to treat the so-called "hooking" or "off-nadir" effect and signal noise caused by ambient topographic features (Boergens et al., 2016; Frappart et al., 2006; Schwatke et al., 2015). The sensor onboard Sentinel-3A/B is a SAR altimeter, which has an improved along-track resolution of about 300 m (Calmant et al., 2016). Atmospheric, geophysical, and

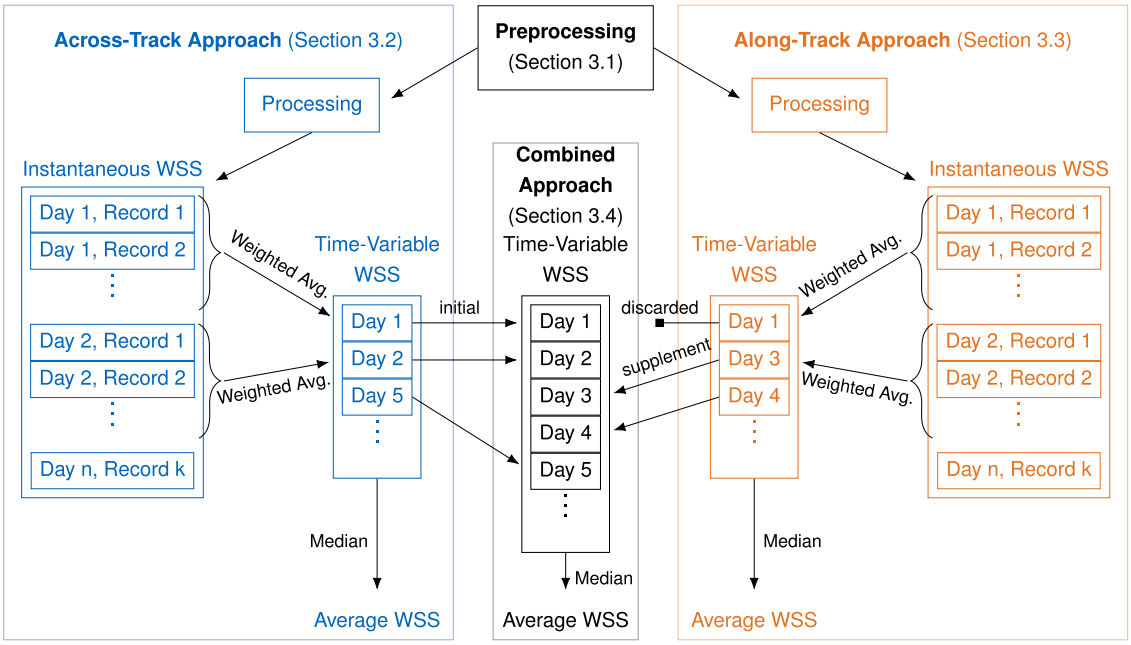

Figure 2. Processing flow and data structure. After preprocessing (Section 3.1) the instantaneous water surface slope (WSS) is estimated using the across-track (blue, Section 3.2) and along-track (orange, Section 3.3) approach. The results are reduced to a time-variable WSS with daily resolution using a weighted average. Both approaches are combined (black, Section 3.4) using the across-track time-variable data supplemented by the along-track data while duplicate along-track data is discarded. An average value is derived for each approach by calculating the median of each time-variable WSS.

instrument corrections must be applied to estimate accurate WSE from satellite altimetry measurements (Calmant et al., 2016). All mutual and satellite-specific corrections are already applied to the time series data retrieved from DAHITI. Additionally, the DAHITI data are corrected by inter-mission biases from a multi-mission cross-over analysis to allow the combination of WSE data from different missions (Bosch et al., 2014; Schwatke et al., 2015).

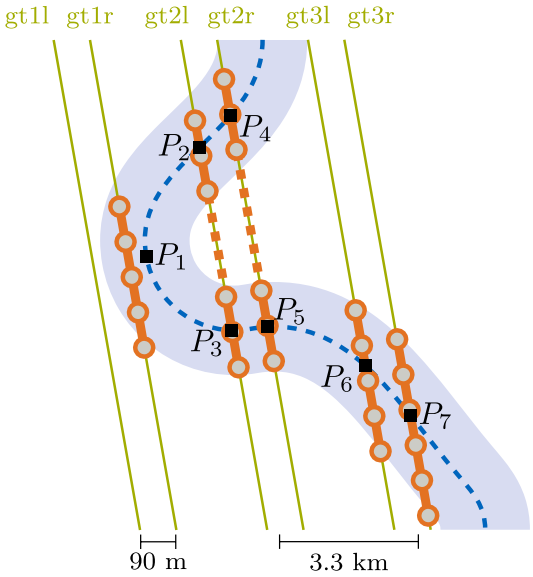

Figure 3. Schematic of Ice, Cloud, and Land Elevation Satellite 2 ATL13 observations (circles) of one cycle within a reach area of interest (light-blue polygon), segmented as features (orange) per beam (green) with reference points (squares) at the centerline (dashed blue) intersections or the nearest centerline point. Features with multiple intersections (dashed orange) are split.

3. Methodology

In this paper, we use two methods to estimate instantaneous, time-variable, and average reach-scale WSS from ICESat-2 observations: (a) Across-track WSE differences of two beams (Section 3.2) and (b) along-track WSE linear trends of single beams (Section 3.3). Both methods have advantages and disadvantages depending on the intersection angle of the orbit ground track with the reach centerline. Therefore, we also estimate time-variable and average WSS using a combined approach (Section 3.4). Figure 2 shows the processing flow and data structure after preprocessing.

3.1. Preprocessing

The processing is performed for each given SWORD reach and starts by selecting all ATL13 observations within the reach area of interest (AOI). To construct the reach AOI, we buffer the SWORD reach center line by the reach's width plus four times its width standard deviation. The AOI of a schematic river reach is shown in Figure 3 as a light-blue polygon. Each beam and cycle of the ATL13 data intersecting with the AOI is handled as an individual feature. Each feature is intersected with the SWORD reach centerline to determine the intersection location as feature reference point P_i and its chainage. In case there are multiple intersections, the feature is split in between.

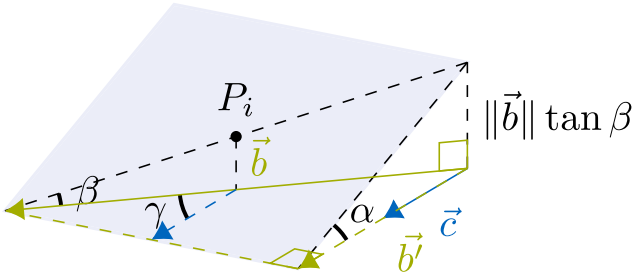

Figure 4. Schematic of an Ice, Cloud, and Land Elevation Satellite 2 beam ground track $\vec{b}$ crossing a river (blue polygon) with centerline tangent vector $\vec{c}$ at an angle γ, along-track water surface slope (WSS) ($\tan\beta$), and along-river WSS ($\tan\alpha$).

If a feature is not intersecting the river centerline, the nearest point of the centerline to the feature is taken as the reference point P_i. Figure 3 shows a schematic of the feature definition with a significantly reduced number of observations for simplicity.

We use the WSE of the already preprocessed ATL13 inland water body height data. Outliers within each feature are detected and removed similar to the DAHITI approach (Schwatke et al., 2015). For this purpose, an absolute deviation around the median (ADM) is calculated using a rolling window along the beam ground track. The windows size is seven observations for features with more than 20 data points across the river. Otherwise, the ADM of all observations is used. All observations with an ADM of more than 5 cm are assumed to be outliers and rejected. Additionally, we use the type ("inland_water_body_type") and cloud ("cloud_flag_asr_atl09") flags from the ATL13 data. Observations, which are not flagged as reservoir, river, or estuary are rejected as well as observation marked cloudy with at least low confidence (flags 0–3). If there are along-track gaps of more than 500 m in the remaining observations, we split the data into clusters at these gaps and use only the cluster with the largest number of observations. Further outliers are detected using a linear support vector regression (SVR). Contrary to the standard DAHITI approach (Schwatke et al., 2015) for radar altimetry, we do not use a zero-slope constraint for the SVR. WSE observations that deviate more than 5 cm from the SVR fit are rejected as outliers.

3.2. Across-Track WSS Estimation

For each feature reference position P_i, we calculate a reference WSE using the average of the valid WSE observations weighted by their inverse distance to P_i. Next, the chainage difference between all possible pairs of reference positions P_i of the same cycle, so also between features of the same beam (e.g., P_4 and P_5 in Figure 3), are calculated. Pairs of reference positions with a chainage distance below 1,000 m are disregarded, assuming the baseline is too short for estimating a meaningful WSS. Between the remaining pairs of reference positions, the WSS is calculated by dividing their WSE difference by their chainage difference. Negative WSS estimates are rejected assuming outliers. In order to reduce the multiple instantaneous results to a reach scale time-variable across-track WSS with daily temporal resolution (i.e., a WSS time series, cf. Figure 2), the daily weighted average is used. The weights are defined as the inverse of the sum of the standard deviations of the WSE observations in both features used to calculate the instantaneous WSS records. In this step samples from different locations within the reach are combined and treated as if the WSS is not changing over the reach. While this does not reflect the real behavior of a river, we assume the SWORD reaches to be homogeneous so that the local WSS variability is of minor significance. Additionally, we derive an average reach-scale across-track WSS by calculating the median of the time-variable WSS values.

3.3. Along-Track WSS Estimation

The spatial resolution of the ICESat-2 ATLAS instrument is high enough (approx. 0.7 m (Jasinski et al., 2021a)) to detect along-track water level differences with small error (approx. 0.061 m (Jasinski et al., 2021a)) in cloud-free conditions within a single river crossing of a beam, respectively one feature (the ATL13 observations assigned to a reference position P_i). Figure 4 shows a schematic of such a feature. Because of the high spatial resolution, precision, and accuracy, we can estimate the along-track WSS ($\tan\beta$) by fitting a linear regression to the ATL13 short segment WSE observations and their along-track position. We use a fitting instead of the difference of the maximum and minimum WSE to cope with undetected outliers. However, for hydraulic applications, the along-river WSS ($\tan\alpha$) is required instead of $\tan\beta$. In order to estimate $\tan\alpha$ at a reference position P_i, the vector of the features beam ground track segment $\vec{b}$ is projected onto the river centerline tangent vector $\vec{c}$:

$$\vec{b'} = \frac{\vec{b} \cdot \vec{c}}{\|\vec{c}\|^2} \vec{c} \tag{1}$$

$\vec{c}$ is the connecting vector between the upstream and downstream SWORD nodes of the SWORD node closest to P_i. Then, the WSS $\tan\alpha$ can be calculated by dividing the fitted WSE difference by the length of the river section intersected by the beam ground track $\left(\|\vec{b'}\|\right)$ as follows:

$$\tan\alpha = \frac{\|\vec{b}\|\tan\beta}{\|\vec{b'}\|}\mathrm{sgn}\left(\vec{b}\cdot\vec{c}\right) \tag{2}$$

Note the multiplication by the sign of the scalar product of $\vec{b}$ and $\vec{c}$ in order to preserve the slope direction in the rare cases the river slope is negative. However, negative WSS results are rejected assuming outliers.

Using a Students t-distribution the WSS confidence interval (CI) is calculated at a 95% confidence level based on the standard error of the linear fitting of $\tan\beta$ (Niemeier, 2008). The CI is used as an outlier criteria to reject linear fits with high uncertainty. We use an angle-dependent outlier threshold $\mathrm{CI}_{th}(\gamma)$, which allows a higher CI for less orthogonal and thus longer intersections. At such intersections we assume a larger CI caused by small-scale WSS variations such as riffles and waves but better results than for shorter more orthogonal intersections with a possible lower CI. Additionally, the angle-dependent outlier threshold rejects any result from an intersection angle larger then the given maximum angle. $\mathrm{CI}_{th}(\gamma)$ is calculated as follows:

$$\mathrm{CI}_{th}(\gamma) = \begin{cases} \mathrm{CI}_{\max} - \dfrac{\mathrm{CI}_{\max}}{\gamma_{\max}}\gamma' & \text{if}\gamma' < \gamma_{\max} \\ 0, & \text{otherwise} \end{cases} \tag{3}$$

with

$$\gamma' = \begin{cases} 180° - \gamma & \text{if}\gamma > 90° \\ \gamma, & \text{otherwise} \end{cases} \tag{4}$$

and

$$\gamma = \arccos\frac{\vec{b}\cdot\vec{c}}{\|\vec{c}\|\|\vec{b}\|} \tag{5}$$

where γ is the intersection angle of the beam $\vec{b}$ with the reach centerline $\vec{c}$, $\mathrm{CI}_{\max}$ is the defined maximum CI parameter, and $\gamma_{\max}$ is the defined maximum intersection angle parameter. In this study, we use $\mathrm{CI}_{\max} = 300$ mm/km and $\gamma_{\max} = 65°$ as a result of empirical tests. Analogous to Section 3.2 and as shown in Figure 2 a weighted average is used to calculate time-variable mean values with daily temporal resolution where γ'^{-1} is used as weight. The median value of this time-variable WSS is used as an average reach scale along-track WSS.

3.4. Combined WSS Estimation

In order to increase the spatial and temporal coverage, we merge both, the across- and along-track methods, in one combined approach. This combination is necessary because depending on the intersection angle between the orbit ground track and the river centerline, it is possible that only one approach yields a WSS estimate. We expect the along-track method to yield results in situations where the across-track method can not be applied because of lacking simultaneous intersections with meridional reaches. On the other hand, orthogonal crossings with zonal reaches are favorable for the across-track approach, increasing the probability of multiple beams crossing the same reach. Therefore, the days of record in the WSS time series from both methods may differ.

As shown in Figure 2, the combination of both approaches is executed based on the time-variable WSS results with daily resolution. Because the across-track approach proves to be more accurate (see Section 4), its time series is used as the initial data. This time series is then supplemented by records from the along-track time series for dates on which no across-track observations are available. Thus, in the combined approach, the across-track WSS is used for each available day, while the along-track WSS is only used for days without across-track WSS. The average combined WSS is determined using the median of the combined time-variable WSS.

Table 1
Instantaneous Water Surface Slope Validation Results by Method and Used Beams With the Median Absolute Error (MAE), Coverage of the Studied Reaches, and Median 95% Confidence Interval (CI) of the Fitting

Method	Beams	n_{est}	n_{val}[a]	MAE $\left[\frac{mm}{km}\right]$	Coverage (%)	Med. CI $\left[\frac{mm}{km}\right]$
Across	All	18,178	20,021	24	82	
	Strong	4,889	5,345	23	78	
	Weak	4,382	4,839	23	75	
Along	All	4,455	4,645	57	78	30
	Strong	2,609	2,749	61	74	25
	Weak	1,846	1,896	52	62	36
Along[b]	All	12169	13183	133	96	79
	Strong	6,360	6,912	133	94	62
	Weak	5,809	6,271	134	94	110

[a]Estimates may be validated repeatedly when associated with multiple pairs of gauges. [b]Without outlier rejection.

4. Results and Discussion

We use two different methods to validate the WSS derived from ICESat-2 data. In Section 4.1, we compare the ICESat-2 WSS against time-variable in-situ WSS derived from two gauges enclosing the respective reach. The accuracy of the in-situ WSS depends on the gauge distance and river characteristics. We do not expect this data to reflect small-scale WSS variations between the gauges, but there is no more accurate time-variable WSS source covering large regions. As an alternative validation and to better quantify the quality of the ICESat-2 WSS, we apply the average combined WSS as a correction to water level time series from radar satellite altimetry in Section 4.2.

4.1. Validation Against Pairs of Gauges

To validate the method against in-situ WSS, we manually select pairs of in-situ gauges and determine their distance using the high-resolution SWORD centerline. We then calculate an in-situ WSS time series for each pair based on the difference between the two WSE time series. We apply our method to all SWORD reaches between the gauges of each pair and validate the instantaneous (Section 4.1.1), time-variable (Section 4.1.2), and average (Section 4.1.3) ICESat-2 WSS against the in-situ WSS time series, or the median in-situ WSS, respectively. The number of validation pairs is limited by the spatial distribution of the gauges, the epoch overlap with ICESat-2, and the availability of essential metadata such as the vertical datum, gauge zero, and exact location. We omit pairs of gauges with an average negative slope, mismatching vertical datums, or manually detected errors in the SWORD centerline between the gauges. In this way, 205 pairs of in-situ gauges are defined with 815 unique SWORD reaches located between the defined pairs. However, 132 reaches are located at the end and beginning of consecutive pairs of gauges, that is, within two validation sets, so there are more validation data than individual estimates. We manually select the pairs of gauges to ensure that they are connected without flow disturbances, that is, weirs, dams, or waterfalls.

4.1.1. Instantaneous WSS

Table 1 shows the results of the instantaneous WSS validated against the in-situ WSS. The median absolute error (MAE) refers to all validations, that is, if a reach is associated with multiple pairs of gauges, the WSS estimates are validated repeatedly. The along-track method is shown twice, with and without applying the angle-dependent outlier rejection. Each method is validated for strong and weak beams separately and with the data from all beams. Along-track results rejected as outliers because of a negative WSS fit are not listed in Table 1. Negative WSS fits occur for both beams with an equal probability of 35%. Table 1 also lists the percentage of the studied reaches covered by the respective method and subset of beams. Additionally, it shows the median CI for the along-track method.

Applying the across-track method to the data from all beams yields significantly more results than applying it to the strong or weak beams separately because there are more combinations possible between the intersections. Therefore, using all beams maximizes the coverage. However, the loss of coverage is not as significant as the loss of estimates when using only the strong or weak beams. Furthermore, the MAE is consistent at around 23 mm/km for any subset of beams with the across-track method. The MAE is significantly larger for the along-track method (57 mm/km), especially without the angle-dependent outlier rejection (133 mm/km). There is no difference in the MAE depending on the used beams with the along-track method. However, the CI is noticeably larger for the weak beams before outlier rejection. Figure 5 shows the absolute errors of the along-track method by the intersection angle and CI. Additionally, it shows the angle-dependent confidence threshold (black line) used for outlier rejection. Applying the outlier rejection to the results of the along-track method reduces the number of estimates by 63% and there are significantly fewer records than for the across-track method. Furthermore, the coverage of the studied reaches decreases, especially for the weak beams. However, the MAE improves by 57% with the application of the outlier rejection.

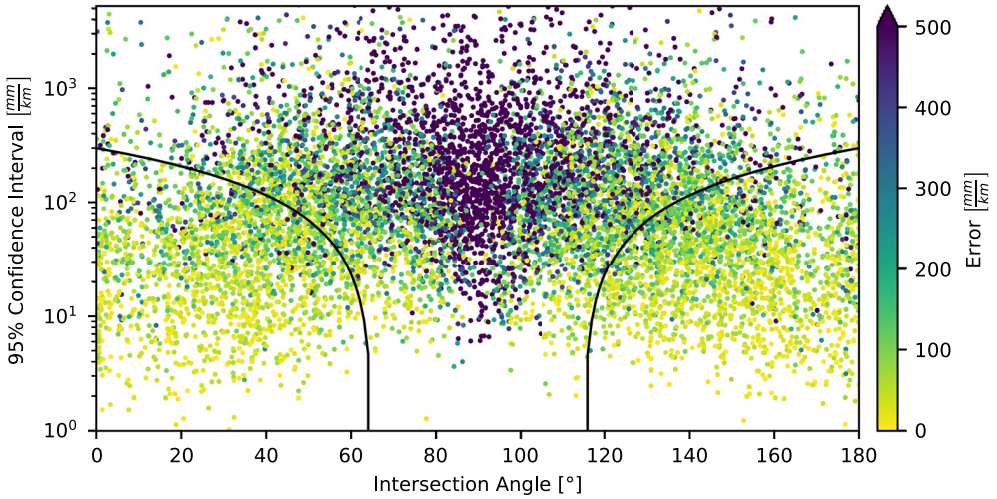

Figure 5. Along-Track water surface slope absolute errors by intersection angle and confidence interval with the applied angle-depended outlier threshold (black line). Estimates above the line are rejected.

Overall, the results in Table 1 show no notable difference in quality between the strong and weak beams throughout the methods, except for the number of estimates and coverage, which are higher for the strong beams. The covered percentage of the studied reaches is practically the same for both approaches, with 82% for the across-track method and 78% for the along-track method after the outlier rejection.

Figure 6 shows on the left the along-track WSS error by the length of the intersection between the satellite's ground track and the river surface area. The orange line shows the median error in a 200 m window. Additionally, the point color indicates the relative data point density. It shows a higher probability of large errors for shorter intersections. For intersections longer than 500 m, the rolling median along-track WSS error stays below 100 mm/km. The shortest intersection yielding a valid along-track WSS estimate is 66.2 m long. On the right, Figure 6 shows the across-track WSS error by the average width of the river reach according to SWORD data. The orange line shows the median error in a 100 m window. The narrowest river reach with an observed across-track WSS is 42 m wide. Although the probability of large errors rises with narrower reaches, the rolling median error stays below 55 mm/km.

As an example for fitting the along-track WSS and estimating the reference WSE for the across-track method, Figures 7–9 show selected intersection features with the Danube and Mississippi River. At the top, the figures show different types of outliers detected and rejected before the WSS estimation. The bottom plots show the along-track WSS fitted to the valid ATL13 observations and the elevation at the reference position (the

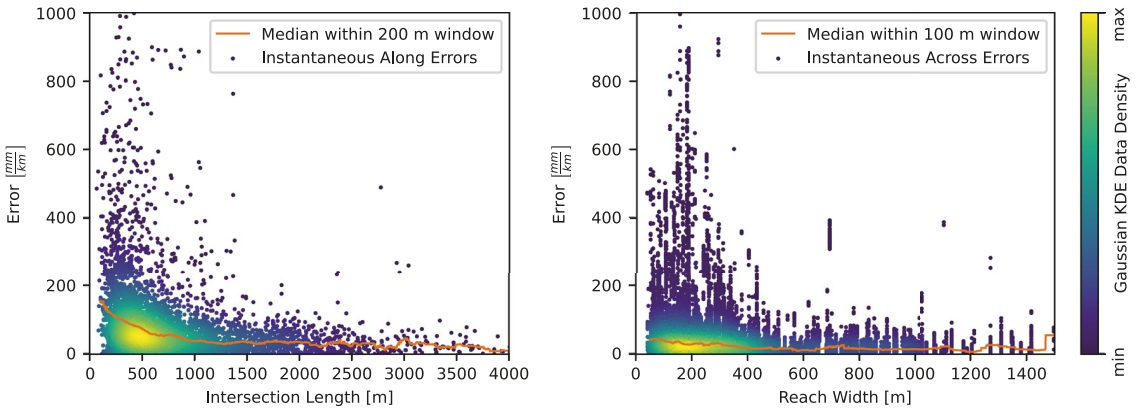

Figure 6. Left: Along-Track water surface slope (WSS) absolute errors by intersection length. Right: Across-Track WSS absolute errors by reach width. The orange lines show the rolling median within a 200 and 100 m window, respectively. The point color indicates the relative data point density.

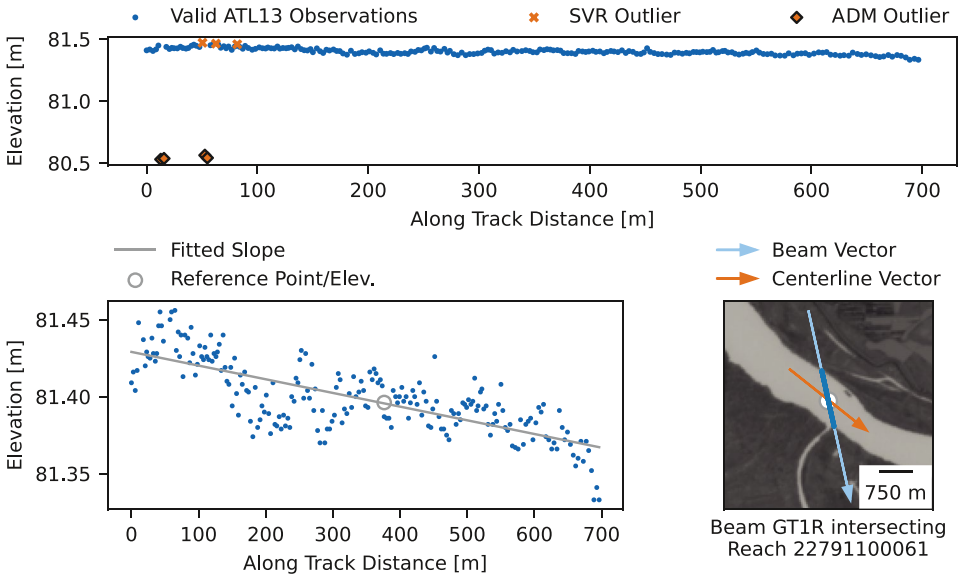

Figure 7. Beam GT1R (strong) intersecting reach 22791100061 (Danube) on 29 February 2020. Top: All ATL13 observations, including rejected outliers. Lower-left: Along-track Elevation of the ATL13 observations after outlier rejection with fitted along-track water surface slope (WSS) (89 mm/km, confidence interval: 10 mm/km). Lower-right: Beam GT1R intersecting the river centerline vector at an angle of 34° with ATL13 observations after outlier rejection. The resulting along-river WSS is 107 mm/km.

intersection with the centerline), which is used to calculate the across-track WSS in combination with simultaneous observations at other reference positions. The maps show the centerline and beam vector with the valid ATL13 observations and the feature reference location above a Sentinel-2 scene from the same month. The outliers in Figure 7 are caused by incorrect range measurements and detected by the ADM and SVR thresholds. The outliers in Figure 9 are caused by an additional intersection with the reach AOI. The WSE observations of the first intersection are considered outliers because the data is split into clusters at along-track gaps greater than 500 m and only the largest cluster is used. Figures 7 and 8 show the simultaneous intersection of the adjacent

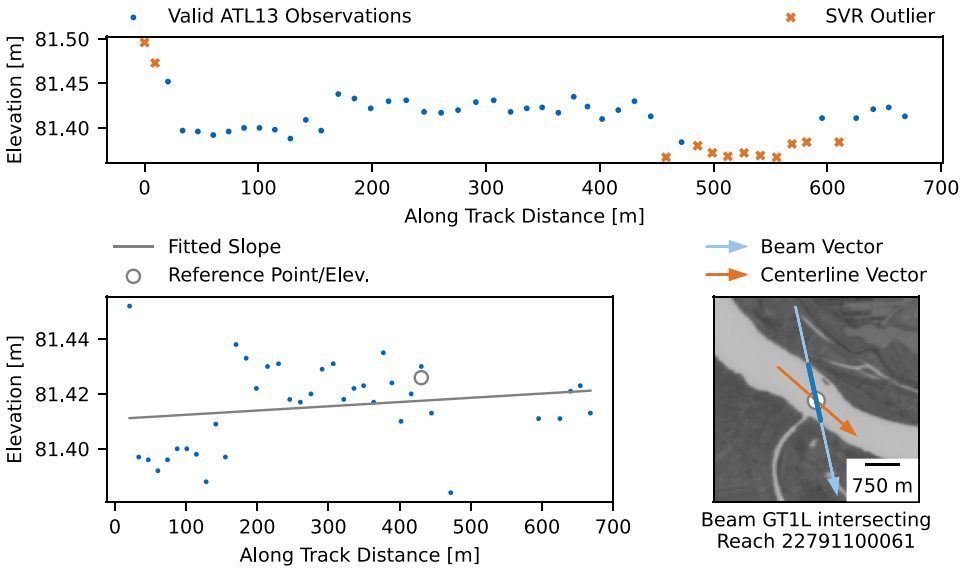

Figure 8. Lower-right: Beam GT1L (weak) intersecting reach 22791100061 (Danube) on 29 February 2020 at an angle of 32°. Top: ATL13 observations including outliers. Lower-left: water surface slope (WSS) fitted to valid ATL13 data. The resulting along-river WSS of −18 mm/km (confidence interval: 28 mm/km) is rejected.

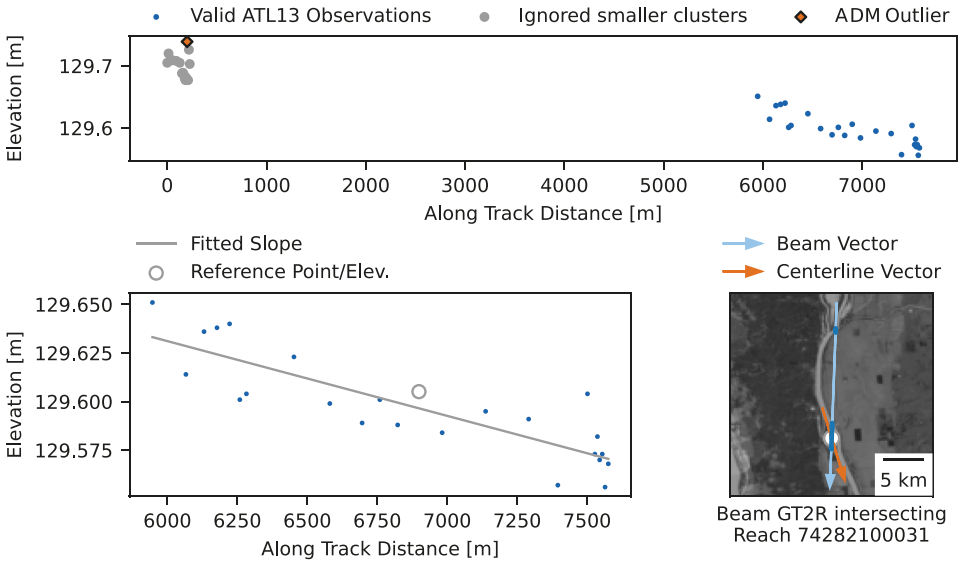

Figure 9. Lower-right: Beam GT2R (strong) intersecting reach 74282100031 (Mississippi) on 12 April 2020 at an angle of 19°. Top: ATL13 observations including outliers. Lower-left: water surface slope (WSS) fitted to valid ATL13 data. The resulting along-river WSS is 41 mm/km (confidence interval: 11 mm/km).

strong GT1R and weak GT1L beam with the same reach of the Danube River. There are significant less photon returns for the weak beam resulting in a lower spatial resolution of the ATL13 short segment data. Therefore, the WSS of −18 mm/km fitted to the weak data is not meaningful and gets rejected because it is negative. In contrast, the WSS fitting to the WSE of the strong beam is much more confident and accurate with a result of 107 mm/km while the in-situ WSS is 52 mm/km.

4.1.2. Time-Variable WSS

We do not distinguish between strong and weak beams for the time-variable WSS because the instantaneous WSS validation reveals no significant difference in quality (see Section 4.1.1). As mentioned in Sections 3.2 and 3.3, we use a weighted average to estimate time-variable WSS with daily temporal resolution using the WSE standard deviation or the intersection angle as the weight for the across- and along-track methods, respectively. Additionally, we combine both methods (Section 3.4) to increase the spatial and temporal resolution. Thus, there are three different WSS time series for each reach which we validate against the in-situ WSS. Table 2 shows the results of the validation.

There are 2,868 and 2,272 daily records for the across- and along-track methods. Combining both methods, we retrieve 3,671 estimates distributed over 726 reaches. 89% of the 815 studied reaches are covered by the combined approach, which is a 7% respectively 11% increase compared to using only the across- or along-track method (cf. Table 1). The median MAE slightly decreases by 2 mm/km for the across-track method using daily averages compared to the instantaneous results (cf. Table 1). For the along-track method, the MAE stays at 57 mm/km, and with 28 mm/km, the MAE of the combined time series is similar to the across-track method, which is plausible because the across-track method is preferred in the combination.

The temporal resolution of the combined WSS time series is sparse, with a maximum of 15 and a median of 5 records within the studied epoch from October 2018 to October 2021 because of the 91-day orbit repetition time. The median RMSE is 32, 80, and 49 mm/km for the across, along, and combined time series, and the median normalized RMSE (NRMSE) is 23%, 45%, and 35%, respectively. The mean in-situ WSS is used for the normalization of the RMSE. 79 reaches, about 10% of the studied reaches, do not have more than one daily WSS record. For the others, the median correlation coefficient is poor, especially for the combined method with only 0.35. Hence, even if the errors are small, the temporal variations are not well captured for most of the reaches. Therefore, the benefit of the daily WSS records is questionable or limited to individual reaches. On the other hand, local differences in WSS could cause the deviation of the ICESat-2 derived WSS over a relatively short baseline compared to the in-situ WSS measured along a much longer baseline.

Table 2
Time-Variable Water Surface Slope Validation Results Including the Absolute Error, Root Mean Square Error (RMSE), Normalized RMSE (NRMSE), Correlation Coefficient, and the Number of Records per Time Series

Measure	Method	Min	Mean	Med	Max	Std	n_{est}	n_{val}[a]
Abs. error[b] $\left[\frac{mm}{km}\right]$	Across	0	65	22	2,138	144	2,868	3,067
	Along	0	106	57	3,355	183	2,272	2,359
	Combined	0	75	28	3,267	158	3,671	3,886
RMSE[c] $\left[\frac{mm}{km}\right]$	Across	0	76	32	1,295	137	663	766
	Along	0	133	80	2,728	193	635	732
	Combined	0	98	49	2,728	177	726	841
NRMSE[c] (%)	Across	0	46	23	1,155	93	663	766
	Along	0	95	54	3,836	224	635	732
	Combined	0	68	35	3,836	198	726	841
Correlation[d]	Across	0.00	0.51	0.49	1.00	0.39	573	639
	Along	0.00	0.53	0.48	1.00	0.40	496	549
	Combined	0.00	0.44	0.35	1.00	0.38	647	729
Number of records[c]	Across	1	4	4	14	3	663	
	Along	1	4	3	12	2	635	
	Combined	1	5	5	15	3	726	

Note. The minimum, mean, median, maximum, and standard deviation values are given per quality measure and method. [a]Estimations may be validated repeatedly when associated with multiple pairs of gauges. [b]Per record in all time series. [c]Per time series. [d]Per time series with more than one record.

Figure 10 shows selected good performing WSS time series estimated with the combined approach (blue) and the in-situ data (orange). The amplitude and temporal variability are well captured for the shown reaches, especially at the reaches of the rivers Loire and Ohio. Note, that the number of records varies per reach and the record interval is inconsistent within the time series. The interval is not necessarily coherent with the 91-day repeat orbit but can be lower when the reach is intersected by two ICESat-2 tracks (e.g., the shown reach of the Missouri River) or larger when there are outliers, no data due to cloud coverage, or the reach is only partially intersected by an ICESat-2 track.

4.1.3. Average WSS

We derive an average reach-scale WSS by calculating the median value of the daily WSS estimates. We compare this average WSS with the median of the in-situ WSS time series and the constant WSS provided with the SWORD data, which is derived from the MERIT Hydro DEM (see Section 2.2). Table 3 shows the MAE and coverage of the WSS from the three approaches and the SWORD WSS compared to the median in-situ WSS. The SWORD coverage is 100% because of the large swath width of the SRTM mission. However, the MAE of SWORD with 71 mm/km is more than three times larger than the MAE of the combined approach with 23 mm/km. Additionally, the histogram of the SWORD WSS in Figure 11 shows a tendency to values below 50 mm/km, which does not fit the distribution of the median in-situ WSS between the studied pairs of gauges. The different distributions of the in-situ WSS and the ICESat-2 or SWORD WSS might be biased because of the variable number of reaches between the pairs of gauges.

4.2. Correcting WSE Time Series From Radar Satellite Altimetry for WSS

To better quantify the quality of the ICESat-2 WSS, we apply the average combined WSS as a correction to DAHITI water level time series derived from satellite altimetry at 137 VS. As described in Section 2.4, the altimetry satellites do not cross a river precisely at the same position but within a range of approximately ±1 km. Combined with a meandering river, this range leads to a variation of river crossing positions of up to 5.7 km at the studied VS. Still, the observations of all orbit repetition cycles within this range are typically aggregated in one time series per VS. To apply the WSS to the DAHITI time series, we intersect the respective orbit of each time

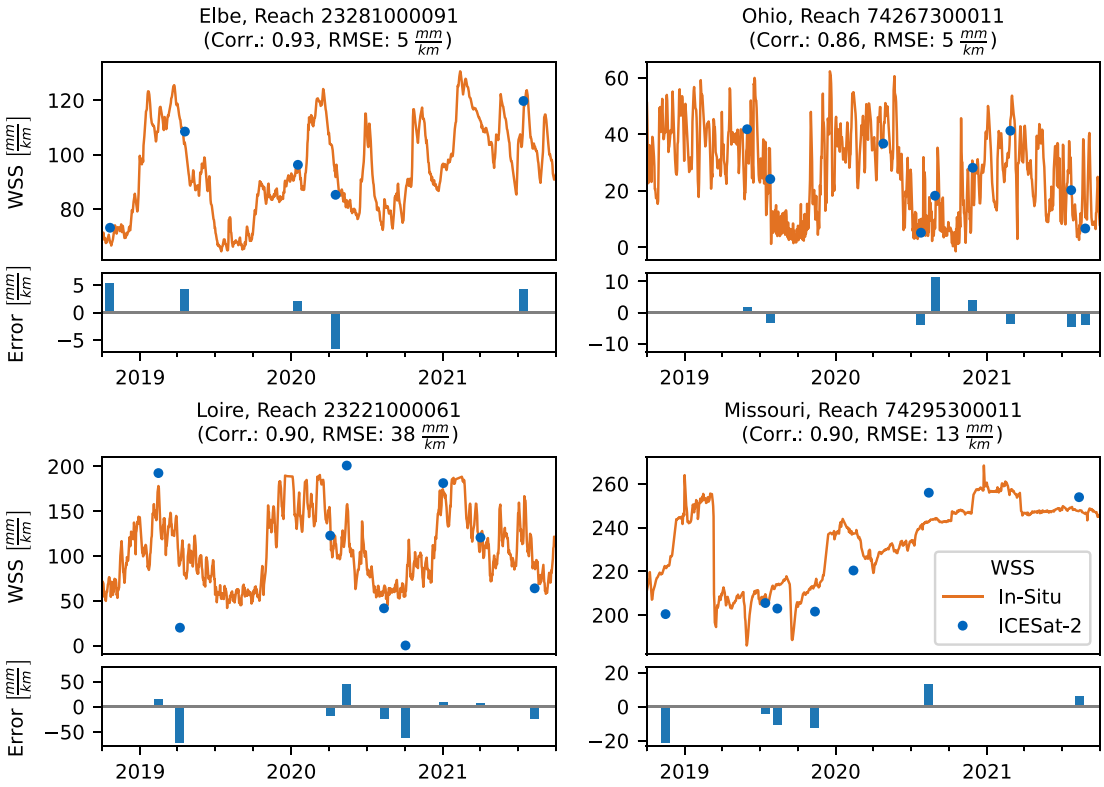

Figure 10. Water surface slope (WSS) time series for selected reaches of the rivers Elbe, Ohio, Loire, and Missouri. Blue dots show estimates using the combined approach. The in-situ WSS is shown in orange and the errors below. The correlation coefficient and root mean square error are given above each time series.

series record with the SWORD river centerline and determine the chainage of each intersection. By subtracting the VS reference point chainage, we get the crossing anomaly which is multiplied by the WSS to get the slope correction for each time series record. Outliers with errors above 75 cm in the DAHITI time series are removed before the comparison.

For this study, we select 137 VS from DAHITI. The VS must be adjacent to a gauge to validate the original DAHITI and WSS-corrected water level time series. Additionally, we selected only VS located between pairs of gauges so that we can compare the impact of the average ICESat-2 derived and SWORD WSS with the median in-situ WSS. We select only VS for which we can clearly and unambiguously determine the intersection of the orbits with the river centerline. For example, VS in curved reaches with multiple intersections and VS where the river runs nearly parallel to the satellite's ground track, which makes the exact measuring location hard to detect, are not part of this study. Furthermore, we do not use VS prone to the off-nadir effect caused by nearby water bodies because its errors likely exceed those caused by WSS. Tables B1 and B2 in the appendix list each studied VS with the mission, the reach, the amplitude of the crossing positions, the applied WSS, and the relative and absolute RMSE differences to the original DAHITI time series RMSE after applying the WSS as a correction. The relative RMSE difference is the percentage of the absolute RMSE difference from the RMSE before applying the correction.

Table 3
Coverage of the Studied Reaches and Median Absolute Errors (MAE) of the Average Reach-Scale Water Surface Slope (WSS) per Method and the SWORD WSS w.r.t. the Median In-Situ WSS

	MAE $\left[\frac{\text{mm}}{\text{km}}\right]$	Coverage [%]	n_{est}	n_{val}[a]
Across	19	81	663	780
Along	47	78	635	752
Combined	23	89	726	855
SWORD	71	100	811	943

[a]Estimates may be validated repeatedly when associated with multiple pairs of gauges.

Figure 12 shows histograms of the absolute and relative RMSE difference between the original DAHITI and the WSS-corrected time series for the in-situ, ICESat-2, and SWORD WSS. The RMSE improves by 30 cm or 66% in the best case. However, the histograms show only minor improvements for many VS and even an increased RMSE at some VS. For 88 VS (64% of the studied VS), the RMSE difference is insignificant between −2 and 2 cm using the WSS from ICESat-2. Overall, the correction based on the ICESat-2 WSS makes the most significant improvements with an RMSE difference below

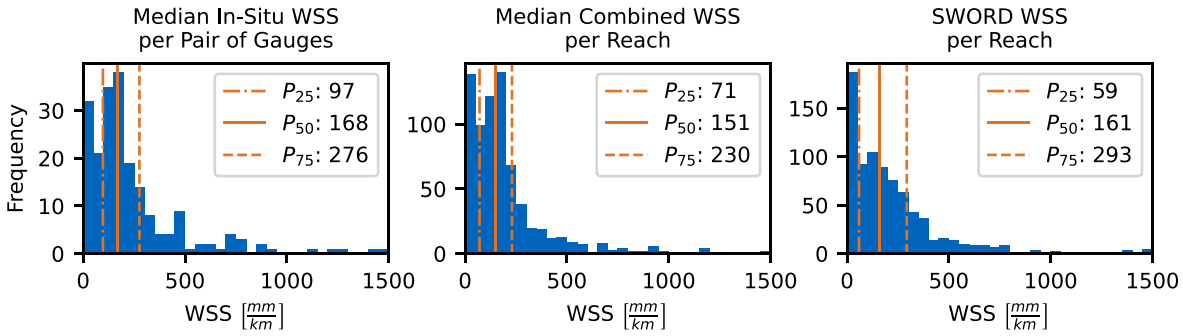

Figure 11. Histograms of the median in-situ water surface slope (WSS) per pair of gauges, the combined Ice, Cloud, and Land Elevation Satellite 2 WSS per reach, and the SWOT River Database WSS per reach.

−2 cm for 43 VS (31% of the studied VS) and a mean improvement of −2.20 cm RMSE (−8.24% NRMSE). The in-situ WSS performs similarly, with 44 VS (32% of the studied VS) improving by more than 2 cm and a mean improvement of −1.90 cm RMSE (−7.04% NRMSE). For some pairs of gauges used for validation, the SWORD connectivity differs from our manual determination. Therefore, a reduced set of results with only the stations between pairs of gauges connected according to SWORD is shown in orange in Figure 12. Even with the reduced set of VS, the WSS from ICESat-2 performs best. The correction based on the SWORD WSS has the lowest performance, with 37 VS (27% of the studied VS) improving by more than 2 cm and a mean improvement of −1.51 cm RMSE (−4.69% NRMSE). Using the SWORD WSS also results in the most considerable RMSE deterioration of +8 cm or +76%.

Figure 13 shows the absolute and relative RMSE differences after applying the WSS correction compared to the original DAHITI time series plotted depending on the reach WSS by source. The figure demonstrates, that most of the insignificant differences between −2 and 2 cm apparent in Figure 12 occur for VS in reaches of small WSS, shown in more detail in the plots on the right of Figure 13. The WSS correction's overall impact increases with a steeper WSS. However, there are VS where the RMSE increases or does not change significantly even in reaches with a steeper WSS. Since this occurs regardless of the used WSS source, either the reach-scale WSS is too coarse to reflect the local WSS, or the temporal WSS variability is so significant that an average WSS is not sufficient. With the ICESat-2 derived WSS correction, most degradations occur with WSS below 200 mm/km. However, for a WSS of more than 100 mm/km, the maximum RMSE improvements reach 5 cm or 30%. Although there are some outliers apparent, especially for the SWORD WSS, the majority of VS improves when correcting for WSS larger than 100 mm/km.

Figures 14 and 15 show, as an example, the original DAHITI and WSS-corrected water level time series at VS 37118 (Platte) and VS 13443 (Loire) compared to in-situ gauging data from USGS and Hydroportail, respectively. Both VS are derived from Sentinel-3A, and the combined WSS from this study is used for the WSS correction. The center plots show the crossing anomaly, that is, the difference of the nominal VS chainage to the chainage where the respective orbit crosses the river centerline. The bottom plots show the water level error w.r.t. the in-situ time series with and without the WSS correction. VS 37118 (Figure 14) shows a significant improvement in the time series, with the RMSE reduced by 29.39 cm or 65.82%. The combined WSS from this study used for correction is 1,164 mm/km, and the crossing anomaly magnitude is 1,545 m. At VS 13443 (Figure 15), the crossing anomaly magnitude is slightly larger (1,777 m), but the WSS of 430 mm/km used for correction is significantly lower than for VS 37118. Still, the RMSE improvements of 15.89 cm or 49.42% can be observed in the error bars and time series.

5. Conclusion

In this study, we successfully derive river WSS from ICESat-2 ATL13 observations at reach scale. The instantaneous results of the described methods, the across- and along-track approach, have median errors of 24 and 57 mm/km, respectively. We detect no difference in quality between WSS originating from strong or weak beam measurements. Only the confidence of fitting the along-track WSS is significantly lower for the weak beams. For the along-track approach, an angle-dependent outlier rejection is required, reducing the number of observations

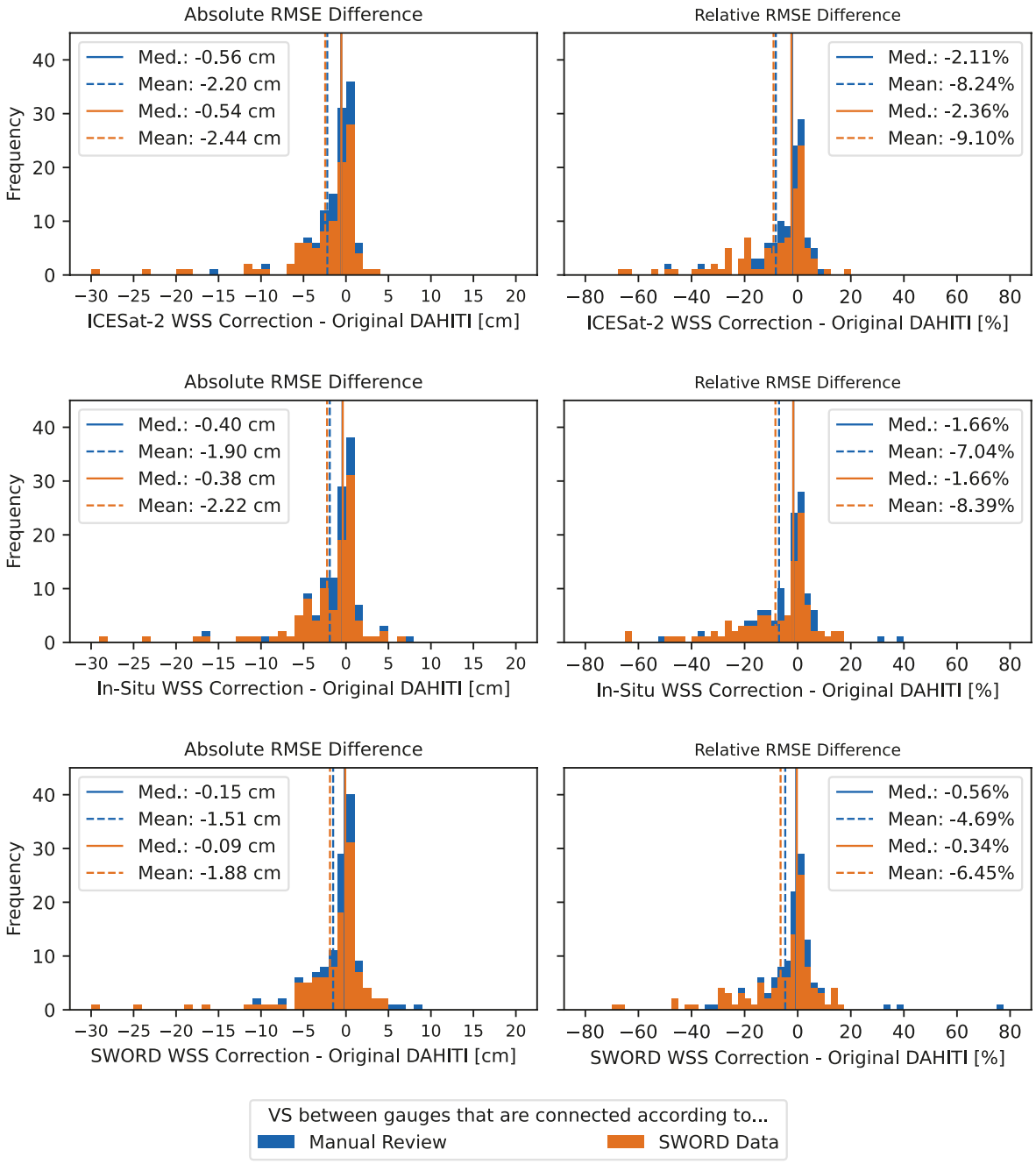

Figure 12. Histograms of the absolute (left) and relative (right) root mean square error difference applying the median combined (top), SWOT River Database (SWORD) (center), and median in-situ (bottom) water surface slope as a correction to the original Database for Hydrological Time Series of Inland Waters (DAHITI) water level time series. The in-situ histograms show all studied virtual stations in blue and a subset (orange) between pairs of gauges that are connected judging by SWORD data.

and coverage significantly but improving the estimated WSS quality. Overall, the across-track method has lower errors than the along-track method. The combined daily observations of both approaches cover 89% of the studied reaches with an MAE of 28 mm/km. However, the time variability of the WSS can not be estimated with confidence because although the median RMSE is low (49 mm/km), the median correlation coefficient of the time-variable WSS w.r.t. in-situ WSS between gauges is only 0.35. Additionally, the temporal resolution of the time-variable WSS is very sparse, with a median of only five records within the studied epoch of 2 years. Besides,

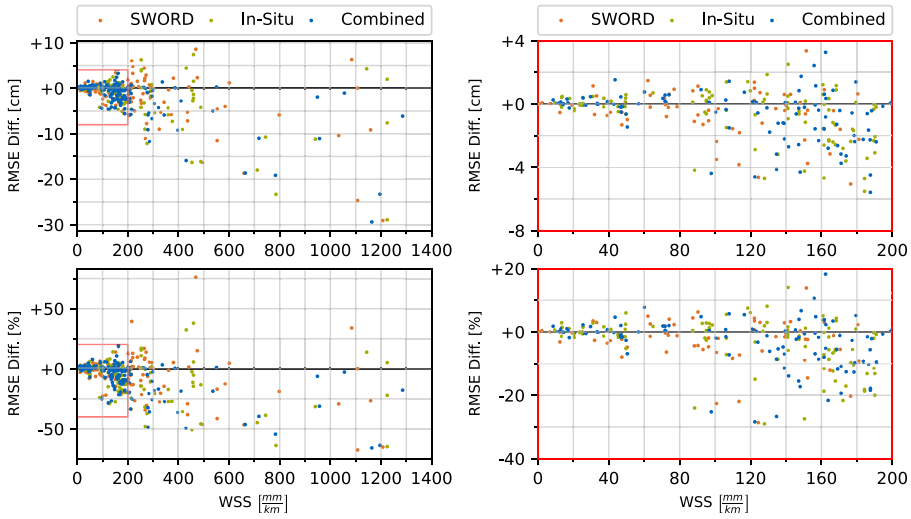

Figure 13. Root mean square error difference after applying the water surface slope (WSS)-correction compared to the original Database for Hydrological Time Series of Inland Waters time series for the 137 studied virtual stations. Negative values mean improvements due to the application of the WSS correction. The plots on the right show the regions of smaller WSS for more detail.

an average WSS is calculated for each reach also covering 89% of the reaches with an MAE of 23 mm/km w.r.t. average gauge data.

WSS can be an important correction for water level time series derived from radar satellite altimetry at VS when other errors like the off-nadir effect are not prevailing. To apply the WSS as a correction, the crossing chainage

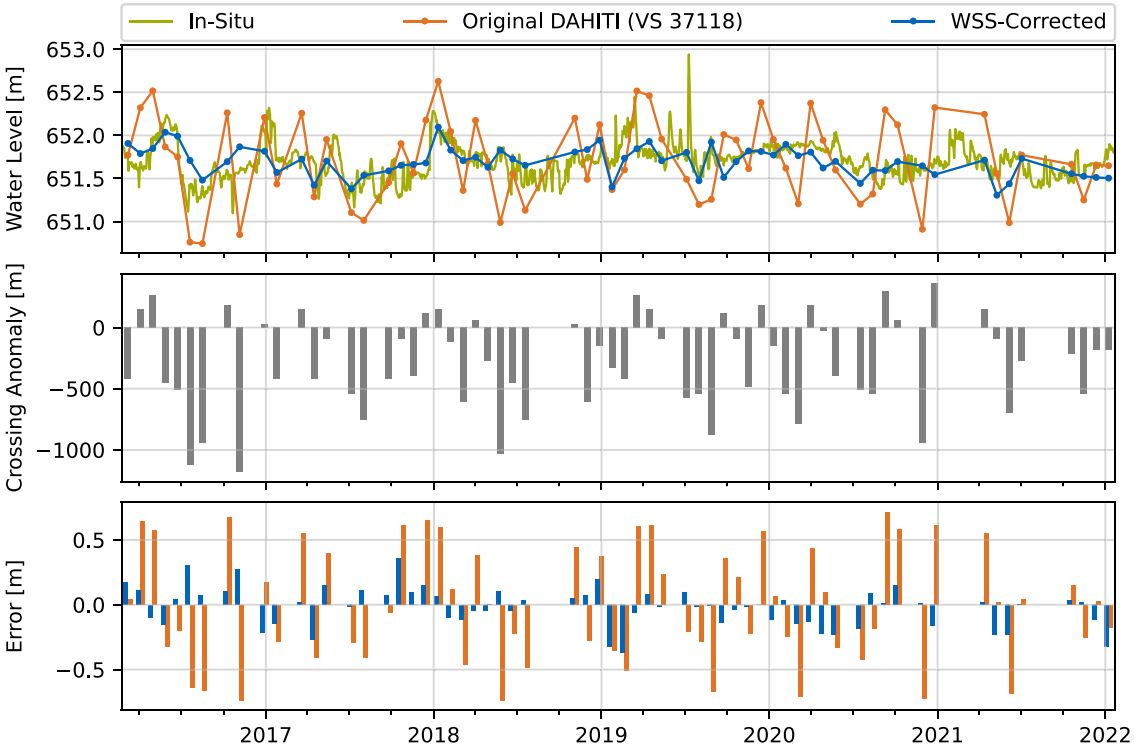

Figure 14. Top: Original Database for Hydrological Time Series of Inland Waters (DAHITI) and water surface slope (WSS)-corrected water level time series for virtual stations (VS) 37118 at the Platte River compared to the in-situ time series provided by U.S. Geological Survey (Station 06770200 near Kearney, Nebraska). Center: Crossing anomaly of the orbit ground tracks w.r.t. the VS nominal location. Bottom: Water level errors with and without the WSS correction applied.

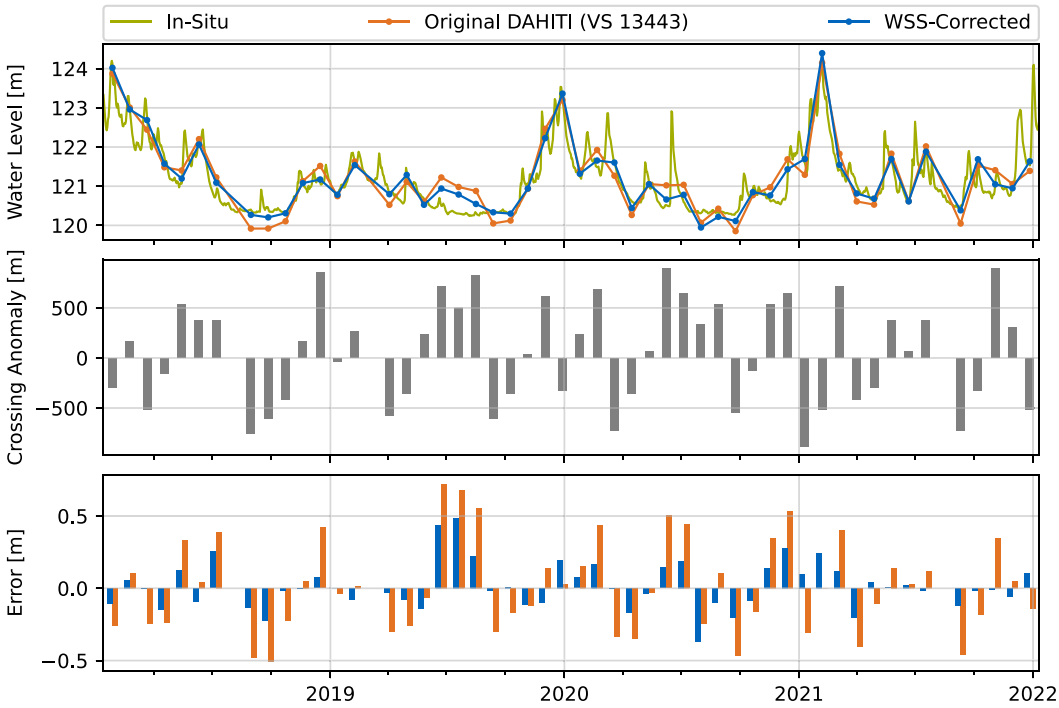

Figure 15. Top: Original Database for Hydrological Time Series of Inland Waters (DAHITI) and water surface slope (WSS)-corrected water level time series for virtual stations (VS) 13443 at the Loire River compared to the in-situ time series provided by Hydroportail (Station K418001010 at Gien). Center: Crossing anomaly of the orbit ground tracks w.r.t. the VS nominal location. Bottom: Water level errors with and without the WSS correction applied.

of the satellite orbit must be unambiguously determinable. Applying the WSS correction to the studied VS of the Sentinel-3A/B and Jason-2/3 missions improves the RMSE by up to 30 cm or 66%. However, the mean RMSE improvement is only 2.2 cm or 8.24% as for 64% of the studied VS, the impact is insignificant and sometimes leads to deterioration. A much more significant impact is expected for the calculation of reach-scale hydrographs of long repeat orbit missions like CryoSat-2, for which the WSS correction is mandatory because of the large crossing anomaly within the reach. Compared to using the ICESat-2 WSS from this study, the correction based on the SWORD WSS derived from DEM data has a lower impact, with a mean RMSE improvement of 1.51 cm or 4.69%. Overall, at VS situated in reaches with an average WSS below 100 mm/km, the WSS correction has no significant effect, presumably because the impact is lower than the radar altimeters accuracy. Still, a larger WSS should be considered an important source of error worth correcting, even with the less accurate WSS from SWORD.

The computational effort of the methodology to derive WSS from ICESat-2 is manageable, so the aim to apply the approach to all SWORD reaches globally is achievable. However, a denser cloud cover may affect observations of reaches in climate zones different from the studied area. Therefore, it must be determined whether the achieved coverage of 89% also applies globally.

Compared to the 91-day repeat orbit of ICESat-2, WSS time series derived from the upcoming SWOT mission will likely have a higher temporal resolution because the time interval of SWOT revisiting a reach is about 11 days due to its 120 km swath width and a 21-day repeat orbit (Biancamaria et al., 2016). Additionally, SWOT will use a Ka-band Radar Interferometer (KaRin) instrument, which can penetrate clouds in contrast to the ICESat-2 laser altimeter. Therefore, more data will be available for regions of high cloud coverage. SWOT is specifically designed to observe WSS and the science requirements of SWOT aim for a slope accuracy of 17 mm/km (Biancamaria et al., 2016), which would be better than the median results of this study. The airborne AirSWOT mission mounted with the same sensor as SWOT demonstrated that 90% of the slope errors were in the range of the required 17 mm/km with an MAE of 8.3 mm/km (Altenau et al., 2017). However, whether SWOT-derived WSS can match the accuracy of ICESat-2 with 23 mm/km must be studied after the launch of SWOT.

Appendix A: Studied Rivers With Characteristics and In-Situ Sourcess

Table A1 groups the studied rivers by the sources of in situ water level elevations used for validation. For each river, the characteristics are given according to the SWOT River Database (SWORD).

Table A1
Data Sources for the In-Situ Water Surface Elevation Data Used in This Study With the Median Width, Length, and Median Slope of the Studied River Sections According to SWOT River Database

In-situ source	River	Number of gauges	Median width (m)	Studied length (km)	Median Slope $\left[\frac{mm}{km}\right]$	Vertical datum
Bundesanstalt für Gewässerkunde (BfG)						Normalnull
	Elbe	15	171	591	201	
	Mosel	2	131	74	283	
	Neckar	2	107	33	218	
	Oder	3	174	44	309	
	Rhine	20	345	477	156	
U.S. Army Corps of Engineers (USACE)						NAVD88
	Mississippi	20	829	1,392	86	
U.S. Geological Survey (USGS)						NAVD88
	Allegheny	10	209	189	422	
	Altamaha	4	169	151	108	
	Arkansas	6	170	127	683	
	Big Sioux	4	45	127	184	
	Brazos	14	84	843	194	
	Cheyenne	5	51	200	928	
	Choctawhatchee	3	75	121	160	
	Colorado (Texas)	6	63	359	252	
	Illinois	9	277	178	12	
	Iowa	2	252	29	302	
	James	4	48	160	81	
	Kansas	6	179	161	332	
	Mississippi	12	829	1,392	86	
	Missouri	37	257	1,620	180	
	Neches	2	90	105	173	
	Ohio	12	685	392	25	
	Pascagoula	2	92	83	79	
	Platte	9	257	252	1,046	
	Red	11	155	809	210	
	Rock	7	160	178	157	
	Sabine	2	87	92	83	
	Trinity	9	80	330	134	
	Yellowstone	3	313	33	198	
Republic Hydrometeorological Service of Serbia (HIDMET)						Adriatic
	Danube	11	664	348	7	
Hydroportail						IGN 1969

Table A1
Continued

In-situ source	River	Number of gauges	Median width (m)	Studied length (km)	Median Slope $\left[\frac{mm}{km}\right]$	Vertical datum
	Garonne	4	184	113	289	
	Loire	17	318	476	310	
	Saône	4	234	59	21	

Appendix B: Detailed Results of the VS Water Surface Slope (WSS) Correction

Tables B1 and B2 list the WSS-corrected results for each studied virtual station (VS) and WSS source in Europe and North America, respectively.

Table B1
Results of the WSS Correction for Virtual Stations in Europe

				WSS $\left[\frac{mm}{km}\right]$			Rel. RMSE difference (%)			Abs. RMSE difference (cm)		
River VS ID	Mis.	Reach ID	Crossing ampl. (m)	1	2	3	1	2	3	1	2	3
Danube												
14383	S3A	22737900241	2,017	13	1	10	+0.99	+0.09	+0.67	+0.12	+0.01	+0.08
17612	S3B	22737900251	1,770	9	2	13	+1.79	+0.49	+2.91	+0.25	+0.07	+0.41
15558	S3B	22737900271	2,262	18	0	13	−1.79	+0.00	−1.41	−0.26	+0.00	−0.20
17227	S3B	22750000011	1,146	25	33	31	+2.23	+2.99	+2.78	+0.38	+0.51	+0.47
17970	S3A	22770000021	1,685	47	63	37	+2.03	+2.51	+1.62	+0.44	+0.55	+0.35
15195	S3B	22770000021	1,401	47	63	37	−1.36	−1.35	−1.28	−0.20	−0.20	−0.19
16850	S3B	22770000081	1,614	60	0	50	+7.77	+0.00	+6.00	+0.75	+0.00	+0.58
21581	S3A	22770000141	1,634		73	50		−6.38	−5.21		−0.80	−0.65
18403	S3A	22770000221	1,740	48	0	49	−1.55	+0.00	−1.50	−0.19	+0.00	−0.18
17363	S3B	22770000231	1,992	43	215	49	−0.19	+39.36	+0.85	−0.03	+5.96	+0.13
17364	S3B	22791100061	1,117	47	74	45	−0.89	−1.04	−0.87	−0.18	−0.21	−0.18
16479	S3B	22791100071	1,484	47	0	45	−1.75	+0.00	−1.66	−0.51	+0.00	−0.49
Elbe												
13618	S3A	23281000071	1,649	17	74	50	+0.56	+4.03	+2.42	+0.08	+0.61	+0.37
13631	S3B	23281000111	2,398	122	124	128	−28.40	−28.64	−29.03	−4.60	−4.64	−4.70
13619	S3A	23281000141	1,933	121	200	128	+0.91	+12.24	+1.93	+0.13	+1.80	+0.28
13620	S3A	23281000151	2,023	145	213	141	+0.67	+6.64	+0.49	+0.11	+1.04	+0.08
13621	S3B	23281000171	1,222	147	79	141	−1.75	−1.19	−1.63	−0.27	−0.19	−0.26
13627	S3A	23283000041	1,784	164	0	172	−21.61	−0.00	−21.66	−2.80	−0.00	−2.80
13626	J23	23283000081	1,565	200	222	204	+0.97	+1.64	+1.08	+0.20	+0.35	+0.23
13623	S3A	23283000091	1,611	178	221	190	−12.63	−13.18	−13.12	−2.00	−2.09	−2.08
13630	S3A	23285000011	1,587	204	475	190	−20.11	+14.97	−19.98	−3.11	+2.32	−3.09
13632	J23	23285000021	1,372	213	260	212	−4.74	−5.00	−4.73	−1.14	−1.20	−1.14
13635	S3B	23285000091	1,406	216	227	212	−25.14	−26.59	−24.56	−4.72	−4.99	−4.61
13634	S3A	23285000101	2,524	211	12	212	−33.54	−3.17	−33.53	−5.75	−0.54	−5.75
13649	J23	23285000141	1,071	188	441	204	−2.11	+1.45	−2.18	−0.43	+0.29	−0.44
13650	S3A	23285000161	1,909	298	127	289	−2.78	−6.03	−3.39	−0.56	−1.21	−0.68
13651	S3A	23285000181	1,000	296	202	289	−10.54	−8.38	−10.40	−1.76	−1.40	−1.74

Table B1
Continued

River VS ID	Mis.	Reach ID	Crossing ampl. (m)	WSS $\left[\frac{mm}{km}\right]$ 1	WSS 2	WSS 3	Rel. RMSE difference (%) 1	Rel. RMSE difference (%) 2	Rel. RMSE difference (%) 3	Abs. RMSE difference (cm) 1	Abs. RMSE difference (cm) 2	Abs. RMSE difference (cm) 3
13652	S3B	23285000211	1,410	304	110	264	−18.07	−8.36	−17.19	−3.38	−1.56	−3.22
13653	S3A	23285000241	1,409	124	251	256	−3.23	+0.55	+0.85	−0.57	+0.10	+0.15
Loire												
13412	S3A	23221000171	1,728	174	165	186	−12.55	−12.06	−13.13	−3.28	−3.16	−3.43
13417	S3B	23227000021	1,605	321	32	360	−16.91	−2.65	−17.21	−4.25	−0.67	−4.32
13415	S3A	23227000031	1,499	344	373	360	−27.39	−27.09	−27.29	−5.88	−5.82	−5.86
13419	S3B	23227000061	2,288	536	553	376	−18.65	−17.00	−27.13	−5.00	−4.56	−7.28
13420	S3A	23227000091	1,532	205	284	431	−4.66	+5.33	+32.31	−0.64	+0.73	+4.44
13421	S3A	23227000151	1,879	398	274	417	−36.29	−30.59	−35.60	−9.21	−7.77	−9.04
13443	S3A	23227000181	1,777	430	269	453	−49.42	−34.22	−50.73	−15.89	−11.00	−16.31
13399	J23	23227000191	732	276	1,084	453	−4.91	+33.92	−2.46	−0.91	+6.30	−0.46
13578	S3A	23227000251	1,268	411	254	459	−18.69	−21.61	−14.54	−2.85	−3.29	−2.22
Oder												
13660	S3A	24222100071	1,889	279	436	267	−48.60	−38.18	−47.94	−9.12	−7.17	−9.00
13661	S3A	24222100071	1,790	279	436	267	−32.36	−29.14	−31.79	−5.86	−5.28	−5.76
18752	S3A	24222100081	1,790	270	295	267	−0.10	+5.08	−0.68	−0.02	+0.80	−0.11
18753	S3A	24222300011	3,687	285	324	276	−35.81	−27.61	−37.18	−11.67	−9.00	−12.11
Rhine												
13593	S3A	23261000141	1,842	195	242	191	−0.67	+1.36	−0.82	−0.16	+0.32	−0.19
13584	S3A	23261001811	1,428	123	20	127	+0.18	−0.14	+0.23	+0.08	−0.06	+0.10
13654	J23	23263000081	954	71	71	93	+1.86	+1.89	+2.70	+0.35	+0.36	+0.51

Note. 1: Combined WSS from this study, 2: SWORD WSS, 3: In-Situ WSS. SWORD, SWOT River Database; RMSE, root mean square error; WSS, water surface slope; VS, virtual stations.

Table B2
Results of the WSS Correction for Virtual Stations in North America

River VS ID	Mis.	Reach ID	Crossing ampl. (m)	WSS $\left[\frac{mm}{km}\right]$ 1	WSS 2	WSS 3	Rel. RMSE difference (%) 1	Rel. RMSE difference (%) 2	Rel. RMSE difference (%) 3	Abs. RMSE difference (cm) 1	Abs. RMSE difference (cm) 2	Abs. RMSE difference (cm) 3
Illinois												
15094	S3A	74282100021	2,841	44	31	14	+4.65	+3.47	+1.44	+1.52	+1.14	+0.47
14256	S3A	74282100071	2,573	16	62	18	+1.05	+4.98	+1.15	+0.31	+1.47	+0.34
18655	S3A	74282700071	1,541	27	143	25	−0.49	+3.25	−0.62	−0.09	+0.60	−0.12
Mississippi												
11484	J23	74210000281	2,677	34	72	95	−0.06	+0.18	+0.48	−0.03	+0.08	+0.22
13250	S3B	74230300051	1,816	39	0	41	+0.78	−0.00	+0.86	+0.16	−0.00	+0.18
17172	S3B	74255000021	1,213	57	266	87	+0.02	+7.78	+0.50	+0.00	+1.67	+0.11
22858	S3A	74255000071	2,108	100	139	94	−1.93	−1.56	−1.91	−0.52	−0.42	−0.52
15411	S3B	74257000021	4,936	50	151	98	−2.65	+13.87	+2.17	−0.64	+3.35	+0.52
15412	S3B	74257000031	2,374	106	148	95	−1.49	+0.39	−2.61	−0.35	+0.09	−0.62
36325	S3A	74259000021	2,668	72	122	95	+0.51	+0.67	+0.49	+0.17	+0.22	+0.16

Table B2
Continued

River VS ID	Mis.	Reach ID	Crossing ampl. (m)	WSS $\left[\frac{mm}{km}\right]$ 1	WSS 2	WSS 3	Rel. RMSE difference (%) 1	Rel. RMSE difference (%) 2	Rel. RMSE difference (%) 3	Abs. RMSE difference (cm) 1	Abs. RMSE difference (cm) 2	Abs. RMSE difference (cm) 3
14252	S3A	74259000021	1,984	72	122	95	+1.77	+4.35	+2.83	+0.56	+1.37	+0.89
15776	S3B	74270100131	1,771	129	140	106	−1.19	−0.56	−1.96	−0.25	−0.11	−0.40
15777	S3B	74270500021	2,464	108	39	106	+5.74	+0.43	+5.54	+1.43	+0.11	+1.38
17170	S3B	74270500021	1,393	108	39	106	−7.26	−3.51	−7.18	−1.51	−0.73	−1.49
14253	S3A	74270700061	1,929	97	139	97	+0.47	+2.87	+0.47	+0.10	+0.60	+0.10
16793	S3B	74270700221	2,306	72	162	97	+0.46	+3.02	+1.29	+0.14	+0.90	+0.38
14254	S3A	74270900021	1,443	74	122	97	+2.02	+3.49	+2.66	+0.57	+0.99	+0.76
16794	S3B	74270900031	5,748	98	113	88	−25.22	−21.96	−24.02	−4.39	−3.82	−4.18
36755	S3B	74289500091	1,704	386	361	459	+0.35	−1.22	+5.63	+0.09	−0.33	+1.53
22867	S3A	74289500101	1,555	550	601	459	+1.07	+4.60	−5.29	+0.27	+1.18	−1.36
18656	S3A	74289500131	2,287	141	301	459	−13.89	−0.06	+37.94	−2.70	−0.01	+7.39
Missouri												
15096	S3A	74291100171	1,554	210	469	179	+5.67	+76.12	+0.96	+0.64	+8.58	+0.11
19674	S3B	74291100241	1,578	187	279	178	−10.23	−6.26	−10.45	−1.65	−1.01	−1.69
22888	S3A	74291100281	1,870	179	114	177	−9.58	−7.30	−9.54	−2.38	−1.82	−2.37
14790	S3A	74291300011	1,754	169	213	161	−11.68	−13.22	−11.51	−2.63	−2.98	−2.59
17590	S3B	74291300061	1,804	156	96	161	−0.37	−1.91	−0.17	−0.08	−0.40	−0.03
36834	J23	74291300061	1,346	156	96	161	−6.93	−4.70	−7.07	−1.57	−1.07	−1.60
22889	S3B	74291500021	1,369	148	176	161	−17.28	−20.28	−18.72	−4.31	−5.06	−4.67
22890	S3A	74291500031	2,199	169	93	168	−5.51	−5.56	−5.55	−1.29	−1.30	−1.30
14470	S3A	74291500061	1,752	147	47	168	−15.49	−7.97	−15.50	−2.57	−1.32	−2.57
36891	J23	74291500061	1,565	136	47	168	−5.36	−2.31	−5.90	−1.22	−0.53	−1.34
17213	S3B	74291500141	1,419	162	238	161	+3.88	+9.66	+3.73	+0.61	+1.53	+0.59
15649	S3B	74291700011	1,617	162	41	161	−7.96	−2.71	−7.95	−1.56	−0.53	−1.56
17214	S3B	74291700041	1,899	157	125	161	+4.79	+2.99	+5.09	+1.14	+0.71	+1.21
14151	S3A	74291900031	2,544	179	19	168	+5.17	−0.32	+4.30	+1.39	−0.09	+1.15
18020	S3A	74291900041	1,708	167	267	168	+3.44	+8.84	+3.52	+0.86	+2.21	+0.88
15283	S3B	74291900091	1,668	139	288	166	−11.34	−11.07	−12.33	−2.21	−2.16	−2.40
16835	S3B	74291900091	1,700	139	288	166	−6.95	+0.81	−6.65	−1.23	+0.14	−1.17
22891	S3A	74291900121	1,807	162	102	151	+2.30	−1.99	+1.19	+0.35	−0.30	+0.18
18661	S3A	74291900131	2,498	138	88	151	−4.76	−4.40	−4.61	−1.20	−1.11	−1.16
16456	S3B	74293300021	4,395	188	206	184	−17.82	−12.02	−18.69	−4.49	−3.03	−4.71
17455	S3B	74293300021	1,465	188	206	184	−18.41	−19.59	−18.19	−5.58	−5.94	−5.52
37033	J23	74293300041	1,222	184	181	457	−9.15	−9.11	−11.34	−2.24	−2.23	−2.78
22892	S3A	74293300071	1,772	177	205	123	−2.61	−2.05	−3.14	−0.57	−0.45	−0.69
16457	S3B	74293300101	1,918	171	0	123	−19.40	+0.00	−14.92	−3.75	+0.00	−2.89
22894	S3A	74293300131	1,521	199	134	190	+0.19	−1.47	−0.20	+0.04	−0.29	−0.04
22895	S3B	74293500011	1,912	203	50	190	−11.42	−4.84	−11.38	−2.33	−0.99	−2.33
22896	S3B	74293700011	1,628	202	152	190	−1.45	−2.39	−2.01	−0.24	−0.40	−0.34
19675	S3A	74293700061	2,416	191	151	21	−9.30	−8.85	−1.71	−2.39	−2.28	−0.44
18662	S3A	74293700081	2,055	186	250	21	−1.51	+0.17	−0.74	−0.61	+0.07	−0.30
38434	S3A	74295100031	2,501	135	101	150	−26.70	−22.63	−27.44	−4.13	−3.50	−4.25

Table B2
Continued

River VS ID	Mis.	Reach ID	Crossing ampl. (m)	WSS $\left[\frac{mm}{km}\right]$ 1	WSS 2	WSS 3	Rel. RMSE difference (%) 1	Rel. RMSE difference (%) 2	Rel. RMSE difference (%) 3	Abs. RMSE difference (cm) 1	Abs. RMSE difference (cm) 2	Abs. RMSE difference (cm) 3
22897	S3B	74295100031	1,026	135	101	135	−8.61	−6.44	−8.66	−3.17	−2.37	−3.19
14950	S3A	74297700211	2,282	92	87	118	+4.83	+4.42	+7.52	+0.90	+0.83	+1.41
16234	S3B	74297700251	1,794	116	72	120	+5.44	−0.34	+6.09	+0.74	−0.05	+0.83
18664	S3A	74299300181	2,006	162	90	141	−5.11	−4.30	−5.79	−0.83	−0.69	−0.94
14413	S3A	74299300181	2,333	162	90	141	+18.25	+6.29	+14.02	+3.26	+1.12	+2.50
19687	S3A	74299900021	2,096	664	659	711	−46.40	−46.53	−44.80	−18.63	−18.68	−17.99
22909	S3A	74299900041	1,938	949	798	1,144	−6.26	−18.86	+13.78	−1.95	−5.86	+4.28
Ohio												
14904	S3A	74265000091	1,687	14	0	24	−0.14	+0.00	−0.21	−0.05	+0.00	−0.08
36357	J23	74265000091	1,602	14	0	24	+0.01	+0.00	+0.03	+0.01	+0.00	+0.01
16549	S3B	74267100061	1,741	12	77	65	+0.15	+2.30	+1.73	+0.06	+0.93	+0.70
15867	S3B	74267700151	1,913	30	0	25	+1.70	+0.00	+1.49	+0.46	+0.00	+0.40
36420	J23	74267700161	1,418	34	13	25	+0.10	+0.03	+0.07	+0.04	+0.01	+0.03
36421	S3A	74267700161	1,571	34	13	25	−0.06	−0.06	−0.07	−0.02	−0.02	−0.02
Platte												
37079	J23	74294100031	2,050	718	553	744	−39.59	−41.46	−38.70	−11.00	−11.51	−10.75
37089	J23	74294300041	1,264	957	1,033	941	−31.12	−29.21	−31.46	−11.07	−10.39	−11.18
15689	S3B	74294500011	1,091	1,196	1,108	785	−63.72	−67.53	−63.79	−23.29	−24.68	−23.31
37117	S3A	74294500211	1,814	1,286	1,159	1,225	−17.77	−26.56	−22.09	−6.12	−9.15	−7.61
37118	S3A	74294500221	1,545	1,164	1,207	1,225	−65.82	−65.12	−64.75	−29.39	−29.08	−28.91
37120	J23	74294500231	1,530	1,055	1,108	1,225	−2.77	+0.08	+5.11	−1.07	+0.03	+1.98
Red												
35699	S3B	74223700061	1,570	147	272	129	+3.97	+13.77	+2.97	+0.84	+2.91	+0.63
35705	S3B	74223700081	2,054	156	0	129	+10.62	+0.00	+8.13	+2.43	+0.00	+1.86
35708	S3B	74223900031	3,045	150	216	141	−0.59	+1.84	−0.85	−0.21	+0.66	−0.30
35713	S3B	74223900051	1,650	106	7	141	+0.79	+0.04	+1.61	+0.24	+0.01	+0.50
35720	S3B	74225000031	1,652	131	171	177	−6.13	−5.51	−5.49	−1.78	−1.60	−1.60
35722	S3A	74225000051	1,825	170	167	147	−1.12	−1.14	−1.23	−0.42	−0.42	−0.46
35730	S3A	74225000091	1,995	146	151	147	−2.30	−2.29	−2.30	−0.63	−0.63	−0.63
35741	S3A	74225000151	1,606	140	180	164	+0.30	+2.31	+1.23	+0.08	+0.63	+0.34
35742	S3B	74225000161	1,897	187	211	164	−5.63	−5.45	−5.63	−2.27	−2.20	−2.27
35752	S3A	74225000201	1,644	158	251	164	−8.55	−9.78	−8.67	−2.31	−2.65	−2.35
35750	S3B	74225000201	1,507	158	251	164	−1.66	+0.52	−1.59	−0.39	+0.12	−0.38
35751	J23	74225000201	1,941	171	251	253	−10.83	−14.33	−14.39	−3.17	−4.19	−4.21
35757	S3A	74225000241	1,678	263	212	253	+0.64	−0.51	+0.36	+0.19	−0.15	+0.11
35759	S3B	74225000251	1,535	149	265	253	+6.70	+16.92	+15.57	+1.74	+4.40	+4.05
35764	S3B	74225000301	1,556		219	253		+9.26	+10.85		+3.28	+3.84
35763	S3A	74225000301	2,947		219	253		+12.83	+17.04		+4.70	+6.24
35779	S3B	74227100161	1,486	294	152	294	−25.73	−14.51	−25.73	−6.67	−3.76	−6.67
35781	S3A	74227100171	1,867	336	380	294	+3.25	+5.20	+1.70	+1.39	+2.21	+0.72
35783	S3A	74227100221	2,195	282	329	306	−20.70	−20.38	−20.79	−5.37	−5.29	−5.40
35796	J23	74227700011	1,465		584	488		−12.73	−13.31		−4.02	−4.20

Table B2
Continued

River VS ID	Mis.	Reach ID	Crossing ampl. (m)	WSS $\left[\frac{mm}{km}\right]$ 1	WSS 2	WSS 3	Rel. RMSE difference (%) 1	Rel. RMSE difference (%) 2	Rel. RMSE difference (%) 3	Abs. RMSE difference (cm) 1	Abs. RMSE difference (cm) 2	Abs. RMSE difference (cm) 3
35797	S3A	74227700021	1,617	783	495	488	−54.40	−46.27	−45.82	−19.14	−16.28	−16.12
Yellowstone												
38432	S3A	74298100021	1,828	50	343	174	−6.91	−14.61	−17.10	−1.46	−3.08	−3.60

Note. 1: Combined WSS from this study, 2: SWORD WSS, 3: In-Situ WSS. SWORD, SWOT River Database; RMSE, root mean square error; WSS, water surface slope; VS, virtual stations.

Data Availability Statement

The results of this study are available at Zenodo via https://doi.org/10.5281/zenodo.7098114. The ICESat-2 ATL13 data used for the WSS estimation in the study are available at the National Snow & Ice Datacenter (NSIDC) via https://doi.org/10.5067/ATLAS/ATL13.005 (Jasinski et al., 2021b). The SWOT River Database (SWORD) (Version v1) used for the reach definition and centerlines in the study are available at Zenodo via https://doi.org/10.5281/zenodo.4917236 (Altenau et al., 2021b). The water level time series from the Database for Hydrological Time Series of Inland Waters (DAHITI) used to assess the impact of correcting virtual stations for water surface slope are available at https://dahiti.dgfi.tum.de (Schwatke et al., 2015).

Acknowledgments
This work was funded by the Deutsche Forschungsgemeinschaft (DFG, German Research Foundation)—Project number 324641997, Grant DE 2174/10-2. Open access funding enabled and organized by Projekt DEAL. We thank the Wasserstraßen- und Schifffahrtsverwaltung des Bundes (WSV), Bundesanstalt für Gewässerkunde (BfG), U.S. Army Corps of Engineering (USACE), U.S. Geological Survey (USGS), Hydroportail, and the Republic Hydrometeorological Service of Serbia (HIDMET) for providing the in-situ data.

References

Allen, G. H., & Pavelsky, T. (2018). Global extent of rivers and streams. *Science*, *361*(6402), 585–588. https://doi.org/10.1126/science.aat0636

Altenau, E. H., Pavelsky, T. M., Durand, M. T., Yang, X., Frasson, R. P. D. M., & Bendezu, L. (2021a). The Surface Water and Ocean Topography (SWOT) Mission River Database (SWORD): A global river network for satellite data products. *Water Resources Research*, *57*(7), e2021WR030054. https://doi.org/10.1029/2021WR030054

Altenau, E. H., Pavelsky, T. M., Durand, M. T., Yang, X., Frasson, R. P. D. M., & Bendezu, L. (2021b). SWOT River Database (SWORD) (version v1) [Dataset]. Zenodo. https://doi.org/10.5281/zenodo.4917236

Altenau, E. H., Pavelsky, T. M., Moller, D., Lion, C., Pitcher, L. H., Allen, G. H., et al. (2017). AirSWOT measurements of river water surface elevation and slope: Tanana River, AK. *Geophysical Research Letters*, *44*(1), 181–189. https://doi.org/10.1002/2016GL071577

Biancamaria, S., Lettenmaier, D. P., & Pavelsky, T. M. (2016). The SWOT mission and its capabilities for land hydrology. *Surveys in Geophysics*, *37*(2), 307–337. https://doi.org/10.1007/s10712-015-9346-y

Bjerklie, D. M., Birkett, C. M., Jones, J. W., Carabajal, C., Rover, J. A., Fulton, J. W., & Garambois, P.-A. (2018). Satellite remote sensing estimation of river discharge: Application to the Yukon River Alaska. *Journal of Hydrology*, *561*, 1000–1018. https://doi.org/10.1016/j.jhydrol.2018.04.005

Boergens, E., Dettmering, D., Schwatke, C., & Seitz, F. (2016). Treating the hooking effect in satellite altimetry data: A case study along the Mekong River and its tributaries. *Remote Sensing*, *8*(2), 91. https://doi.org/10.3390/rs8020091

Boergens, E., Schmidt, M., & Seitz, F. (2021). The use of B-splines to represent the topography of river networks. *GEM: International Journal on Geomathematics*, *12*(1), 21. https://doi.org/10.1007/s13137-021-00188-w

Bosch, W., Dettmering, D., & Schwatke, C. (2014). Multi-mission cross-calibration of satellite altimeters: Constructing a long-term data record for global and regional sea level change studies. *Remote Sensing*, *6*(3), 2255–2281. https://doi.org/10.3390/rs6032255

Calmant, S., Crétaux, J. F., & Rémy, F. (2016). Principles of radar satellite altimetry for application on inland waters. *Microwave Remote Sensing of Land Surfaces: Techniques and Methods*, 175–218. https://doi.org/10.1016/B978-1-78548-159-8.50004-9

Calmant, S., & Seyler, F. (2006). Continental surface waters from satellite altimetry. *Comptes Rendus Geoscience*, *338*(14–15), 1113–1122. https://doi.org/10.1016/j.crte.2006.05.012

Carr, A. B., Trigg, M. A., Tshimanga, R. M., Borman, D. J., & Smith, M. W. (2019). Greater water surface variability revealed by new Congo River field data: Implications for satellite altimetry measurements of large rivers. *Geophysical Research Letters*, *46*(14), 8093–8101. https://doi.org/10.1029/2019GL083720

Cohen, S., Wan, T., Islam, M. T., & Syvitski, J. P. (2018). Global river slope: A new geospatial dataset and global-scale analysis. *Journal of Hydrology*, *563*(January), 1057–1067. https://doi.org/10.1016/j.jhydrol.2018.06.066

Cooley, S. W., Ryan, J. C., & Smith, L. C. (2021). Human alteration of global surface water storage variability. *Nature*, *591*(7848), 78–81. https://doi.org/10.1038/s41586-021-03262-3

Foerste, C., Bruinsma, S., Abrykosov, O., Lemoine, J.-M., Marty, J. C., Flechtner, F., et al. (2014). EIGEN-6C4 the latest combined global gravity field model including GOCE data up to degree and order 2190 of GFZ Potsdam and GRGS Toulouse. https://doi.org/10.5880/icgem.2015.1

Frappart, F., Calmant, S., Cauhopé, M., Seyler, F., & Cazenave, A. (2006). Preliminary results of ENVISAT RA-2-derived water levels validation over the Amazon basin. *Remote Sensing of Environment*, *100*(2), 252–264. https://doi.org/10.1016/j.rse.2005.10.027

Frasson, R. P. D. M., Pavelsky, T. M., Fonstad, M. A., Durand, M. T., Allen, G. H., Schumann, G., et al. (2019). Global relationships between river width, slope, catchment area, meander wavelength, sinuosity, and discharge. *Geophysical Research Letters*, *46*(6), 3252–3262. https://doi.org/10.1029/2019GL082027

Garambois, P. A., Calmant, S., Roux, H., Paris, A., Monnier, J., Finaud-Guyot, P., et al. (2017). Hydraulic visibility: Using satellite altimetry to parameterize a hydraulic model of an ungauged reach of a braided river. *Hydrological Processes*, *31*(4), 756–767. https://doi.org/10.1002/hyp.11033

Gleason, C. J., & Durand, M. T. (2020). Remote sensing of river discharge: A review and a framing for the discipline. *Remote Sensing*, *12*(7), 1–28. https://doi.org/10.3390/rs12071107

Gliński, J., Horabik, J., & Lipiec, J. (2011). Hydraulic gradient. In J. Gliński, J. Horabik, & J. Lipiec (Eds.), *Encyclopedia of agrophysics*. (p. 368). Springer. https://doi.org/10.1007/978-90-481-3585-1_680

Halicki, M., & Niedzielski, T. (2022). The accuracy of the Sentinel-3A altimetry over Polish rivers. *Journal of Hydrology*, *606*(April), 127355. https://doi.org/10.1016/j.jhydrol.2021.127355

Hannah, D. M., Demuth, S., van Lanen, H. A. J., Looser, U., Prudhomme, C., Rees, G., et al. (2011). Large-scale river flow archives: Importance, current status and future needs. *Hydrological Processes*, *25*(7), 1191–1200. https://doi.org/10.1002/hyp.7794

Herrmann, H., & Bucksch, H. (2014). Hydraulic gradient. In *Dictionary geotechnical engineering/wörterbuch geotechnik* (p. 697). Springer. https://doi.org/10.1007/978-3-642-41714-6_81759

Jasinski, M., Stoll, J., Hancock, D., Robbins, J., Nattala, J., Morison, J., et al. (2021a). *Algorithm theoretical basis document (ATBD) for inland water data products, ATL13, version 5, technical report* (Vol. 2). NASA Goddard Space Flight Center. https://doi.org/10.5067/RI5QTGTSVHRZ

Jasinski, M., Stoll, J., Hancock, D., Robbins, J., Nattala, J., Morison, J., et al. (2021b). ATLAS/ICESat-2 L3A inland water surface height, version 5 [Dataset]. Boulder, Colorado USA. https://doi.org/10.5067/ATLAS/ATL13.005

Jiang, L., Bandini, F., Smith, O., Jensen, I. K., & Bauer-Gottwein, P. (2020). The value of distributed high-resolution UAV-borne observations of water surface elevation for river management and hydrodynamic modeling. *Remote Sensing*, *12*(7), 1171. https://doi.org/10.3390/rs12071171

Julien, P. Y. (2018a). *River dynamics, chapter 11* (2nd ed.). Cambridge University Press. https://doi.org/10.1017/cbo9781139164016.009

Julien, P. Y. (2018b). Steady flow in rivers, chap. 5. In *River mechanics* (2nd ed.). Cambridge University Press. https://doi.org/10.1017/9781316107072.006

Kebede, M. G., Wang, L., Yang, K., Chen, D., Li, X., Zeng, T., & Hu, Z. (2020). Discharge estimates for ungauged rivers flowing over complex high-mountainous regions based solely on remote sensing-derived datasets. *Remote Sensing*, *12*(7), 1064. https://doi.org/10.3390/rs12071064

Langhorst, T., Pavelsky, T. M., Frasson, R. P. D. M., Wei, R., Domeneghetti, A., Altenau, E. H., et al. (2019). Anticipated improvements to river surface elevation profiles from the surface water and ocean topography mission. *Frontiers of Earth Science*, *7*(May), 1–13. https://doi.org/10.3389/feart.2019.00102

Lao, J., Wang, C., Nie, S., Xi, X., & Wang, J. (2022). Monitoring and analysis of water level changes in Mekong River from ICESat-2 spaceborne laser altimetry. *Water*, *14*(10), 1613. https://doi.org/10.3390/w14101613

LeFavour, G., & Alsdorf, D. (2005). Water slope and discharge in the Amazon River estimated using the shuttle radar topography mission digital elevation model. *Geophysical Research Letters*, *32*(17), 1491. https://doi.org/10.1029/2005GL023836

Mandlburger, G., Weiß, R., & Artz, T. (2020). Mapping of water surface levels and slopes with single photon LiDAR—A case study at the river Rhine. *The International Archives of the Photogrammetry, Remote Sensing and Spatial Information Sciences: ISPRS Archives*, *43*(B1), 57–64. https://doi.org/10.5194/isprs-archives-XLIII-B1-2020-57-2020

Manning, R. (1891). On the flow of water in open channels and pipes. *Transactions of the Institution of Civil Engineers of Ireland*, *20*, 161–207.

Markus, T., Neumann, T., Martino, A., Abdalati, W., Brunt, K., Csatho, B., et al. (2017). The Ice, Cloud, and Land Elevation Satellite-2 (ICESat-2): Science requirements, concept, and implementation. *Remote Sensing of Environment*, *190*, 260–273. https://doi.org/10.1016/j.rse.2016.12.029

Neumann, T. A., Martino, A. J., Markus, T., Bae, S., Bock, M. R., Brenner, A. C., et al. (2019). The Ice, Cloud, and Land Elevation Satellite-2 Mission: A global geolocated photon product derived from the advanced topographic laser altimeter system. *Remote Sensing of Environment*, *233*(September), 111325. https://doi.org/10.1016/j.rse.2019.111325

Niemeier, W. (2008). *Ausgleichungsrechnung: Statistische Auswertemethoden*. De Gruyter. https://doi.org/10.1515/9783110206784

O'Loughlin, F., Trigg, M. A., Schumann, G. J., & Bates, P. D. (2013). Hydraulic characterization of the middle reach of the Congo River. *Water Resources Research*, *49*(8), 5059–5070. https://doi.org/10.1002/wrcr.20398

Pitcher, L. H., Smith, L. C., Cooley, S. W., Zaino, A., Carlson, R., Pettit, J., et al. (2020). Advancing field-based GNSS surveying for validation of remotely sensed water surface elevation products. *Frontiers of Earth Science*, *8*(November), 1–20. https://doi.org/10.3389/feart.2020.00278

Rhoads, B. L. (2020). The vertical dimension of rivers: Longitudinal profiles, profile Adjustments, and step-pool morphology. In *River dynamics geomorphology to support management (chapter 13)*. Cambridge University Press. https://doi.org/10.4324/9781351218986-13

Ryan, J. C., Smith, L. C., Cooley, S. W., Pitcher, L. H., & Pavelsky, T. M. (2020). Global characterization of inland water reservoirs using ICESat-2 altimetry and climate reanalysis. *Geophysical Research Letters*, *47*(17), 1–10. https://doi.org/10.1029/2020GL088543

Sauer, V. B., & Turnipseed, D. P. (2010). Stage measurement at gaging stations. In *Techniques and methods (chapter 3-A7)*. U.S. Geological Survey. https://doi.org/10.3133/tm3A7

Scherer, D., Schwatke, C., Dettmering, D., & Seitz, F. (2020). Long-term discharge estimation for the lower Mississippi River using satellite altimetry and remote sensing images. *Remote Sensing*, *12*(17), 2693. https://doi.org/10.3390/rs12172693

Schumm, S. A. (2005). Valley morphology. In *River variability and complexity (chapter 12)*. Cambridge University Press. https://doi.org/10.1017/CBO9781139165440.015

Schwatke, C., Dettmering, D., Bosch, W., & Seitz, F. (2015). DAHITI—An innovative approach for estimating water level time series over inland waters using multi-mission satellite altimetry. *Hydrology and Earth System Sciences*, *19*(10), 4345–4364. https://doi.org/10.5194/hess-19-4345-2015

Sichangi, A. W., Wang, L., & Hu, Z. (2018). Estimation of river discharge solely from remote-sensing derived data: An initial study over the Yangtze river. *Remote Sensing*, *10*(9), 1385. https://doi.org/10.3390/rs10091385

Sichangi, A. W., Wang, L., Yang, K., Chen, D., Wang, Z., Li, X., et al. (2016). Estimating continental river basin discharges using multiple remote sensing data sets. *Remote Sensing of Environment*, *179*, 36–53. https://doi.org/10.1016/j.rse.2016.03.019

Sulistioadi, Y. B., Tseng, K. H., Shum, C. K., Hidayat, H., Sumaryono, M., Suhardiman, A., et al. (2015). Satellite radar altimetry for monitoring small rivers and lakes in Indonesia. *Hydrology and Earth System Sciences*, *19*(1), 341–359. https://doi.org/10.5194/hess-19-341-2015

Tapley, B. D., Ries, J. C., Davis, G. W., Eanes, R. J., Schutz, B. E., Shum, C. K., et al. (1994). Precision orbit determination for TOPEX/POSEIDON. *Journal of Geophysical Research*, *99*(C12), 24383. https://doi.org/10.1029/94JC01645

Tourian, M. J., Tarpanelli, A., Elmi, O., Qin, T., Brocca, L., Moramarco, T., & Sneeuw, N. (2016). Spatiotemporal densification of river water level time series by multimission satellite altimetry. *Water Resources Research*, *52*(2), 1140–1159. https://doi.org/10.1002/2015WR017654

Yamazaki, D., Ikeshima, D., Sosa, J., Bates, P. D., Allen, G. H., & Pavelsky, T. M. (2019). MERIT Hydro: A high-resolution global hydrography map based on latest topography dataset. *Water Resources Research*, *55*(6), 5053–5073. https://doi.org/10.1029/2019WR024873

Yamazaki, D., Ikeshima, D., Tawatari, R., Yamaguchi, T., O'Loughlin, F., Neal, J. C., et al. (2017). A high-accuracy map of global terrain elevations. *Geophysical Research Letters*, *44*(11), 5844–5853. https://doi.org/10.1002/2017GL072874

Zakharova, E., Nielsen, K., Kamenev, G., & Kouraev, A. (2020). River discharge estimation from radar altimetry: Assessment of satellite performance, river scales and methods. *Journal of Hydrology*, *583*(January), 124561. https://doi.org/10.1016/j.jhydrol.2020.124561

P3 ICESat-2 river surface slope (IRIS): A global reach-scale water surface slope dataset

Scherer, D., Schwatke, C., Dettmering, D., & Seitz, F. (2023). **ICESat-2 river surface slope (IRIS): A global reach-scale water surface slope dataset**. *Scientific Data*, *10*, 359. https://doi.org/10.1038/s41597-023-02215-x

Date of Publication: 6 June 2023

Abstract

The global reach-scale "ICESat-2 River Surface Slope" (IRIS) dataset comprises average and extreme water surface slopes (WSS) derived from ICESat-2 observations between October 2018 and August 2022 as a supplement to 121,583 reaches from the "SWOT Mission River Database" (SWORD). To gain full advantage of ICESat-2's unique measurement geometry with six parallel lidar beams, the WSS is determined across pairs of beams or along individual beams, depending on the intersection angle of spacecraft orbit and river centerline. Combining both approaches maximizes spatial and temporal coverage. IRIS can be used to research river dynamics, estimate river discharge, and correct water level time series from satellite altimetry for shifting ground tracks. Additionally, by referencing SWORD as a common database, IRIS may be used in combination with observations from the recently launched SWOT mission.

Contribution

D.S. developed the methodology and wrote the manuscript. C.S. curated the data. D.D. and F.S. supervised the study and contributed to the discussion of the results. All authors reviewed the manuscript.

Criteria	Own Contribution
Idea and conceptual design	85%
Data acquisition and preparation	50%
Implementation and realisation	90%
Analysis and discussion	90%
Figure compilation	95%
Manuscript structure and writing	80%
Overall contribution	82%

scientific data

OPEN

DATA DESCRIPTOR

ICESat-2 river surface slope (IRIS): A global reach-scale water surface slope dataset

Daniel Scherer ✉, Christian Schwatke, Denise Dettmering & Florian Seitz

The global reach-scale "ICESat-2 River Surface Slope" (IRIS) dataset comprises average and extreme water surface slopes (WSS) derived from ICESat-2 observations between October 2018 and August 2022 as a supplement to 121,583 reaches from the "SWOT Mission River Database" (SWORD). To gain full advantage of ICESat-2's unique measurement geometry with six parallel lidar beams, the WSS is determined across pairs of beams or along individual beams, depending on the intersection angle of spacecraft orbit and river centerline. Combining both approaches maximizes spatial and temporal coverage. IRIS can be used to research river dynamics, estimate river discharge, and correct water level time series from satellite altimetry for shifting ground tracks. Additionally, by referencing SWORD as a common database, IRIS may be used in combination with observations from the recently launched SWOT mission.

Background & Summary

The water surface slope (WSS) is a fundamental parameter for calculating river discharge, one of the Essential Climate Variables (ECVs) as defined by the Global Climate Observing System[1]. River discharge critically contributes to the characterization of the Earth's hydrological cycle and climate and, thus, its determination on a global scale is of great scientific relevance. Additionally, correcting water surface elevation (WSE) observations from satellite altimetry for WSS can significantly improve the accuracy of the resulting water level time series[2,3]. Depending on the river's morphology, regulation, bed material, and basin size, the WSS can be highly variable in both space and time[4].

Various methods exist to measure WSS based on field surveys, gauges, airborne sensors, or satellites. However, most of them face difficulties in capturing the temporal and/or spatial variability of WSS at global scale. Although they are very accurate, field surveys and airborne campaigns can only cover relatively small study areas within a short period of time because of the high human and financial effort. Gauge records are usually available over long periods at a high sampling rate, but their suitability to derive WSS is limited to free-flowing river segments covered by multiple gauges. Due to the small number of free-flowing rivers in developed areas[5] and the lack of gauging stations in remote areas, global WSS coverage with gauges cannot be achieved. In contrast, radar satellite altimetry provides a globally distributed network of so-called virtual stations, but at the same time lacks simultaneous observations over short distances and provides much fewer measurements compared to gauges[6]. Additionally, the distribution of virtual stations along a river is irregular, so that radar satellite altimetry cannot be used to derive a globally homogeneous WSS dataset. Another space-based technique is the use of digital elevation models (DEM) such as the "Shuttle Radar Topography Mission" (SRTM) or the "Advanced Spaceborne Thermal Emission and Reflection Radiometer" (ASTER) data, which provide spatially continuous elevation measurements within the boundaries of the spacecrafts' orbits. The elevation accuracy of the DEM data, however, is low, which leads to errors when deriving WSS for short reach lengths and narrow rivers[7,8]. In addition, also the temporal resolution of DEM data is low, if the models are time-dependent at all. Just recently (December 2022), the "Surface Water and Ocean Topography" (SWOT) satellite was launched, targeting a WSS accuracy of 17 mm/km[9]. It was demonstrated that 90% of the sensor's slope errors are in the desired range[10], but SWOT observations are not yet available. In contrast, the unique measurement geometry of the "Ice, Cloud, and Land Elevation Satellite 2" (ICESat-2) with six parallel laser beams enables instantaneous and highly accurate WSS observations since its launch in September 2018. Due to its dense ground track pattern, ICESat-2 is well

Deutsches Geodätisches Forschungsinstitut der Technischen Universität München (DGFI-TUM), TUM School of Engineering and Design, Department of Aerospace and Geodesy, Munich, Germany. ✉e-mail: daniel.scherer@tum.de

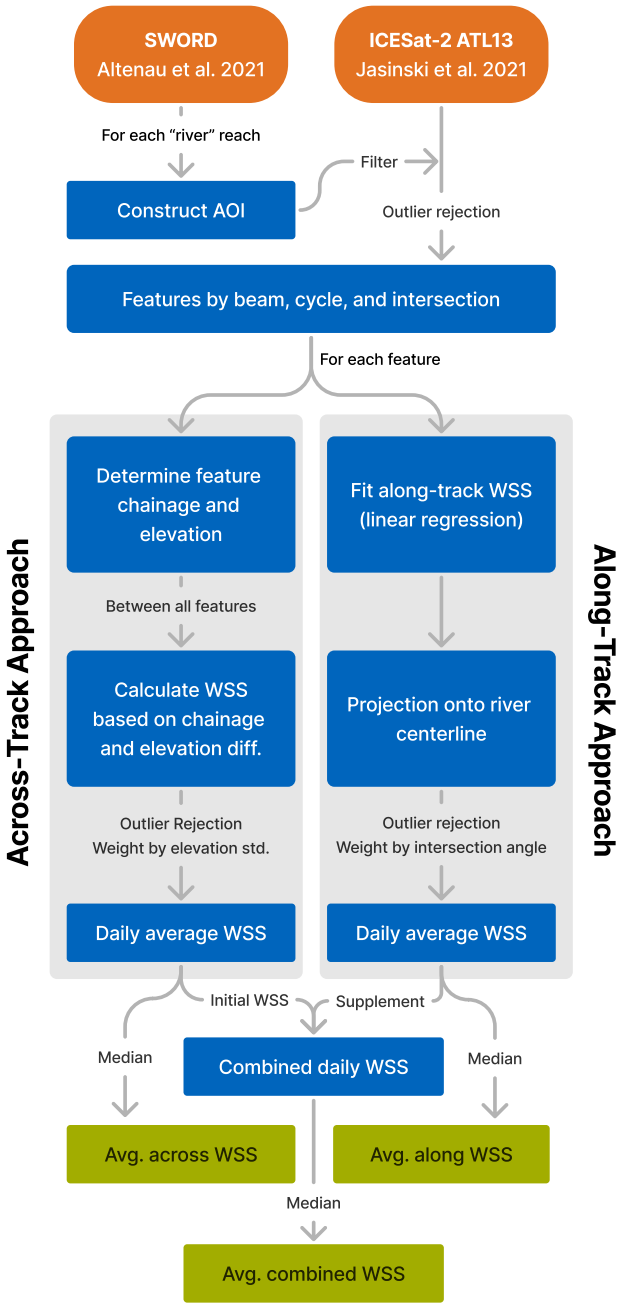

Fig. 1 Processing strategy for the computation of the IRIS water surface slope (WSS) data.

suited for global studies of the Earth's hydrosphere[11]. ICESat-2 WSE observations have already been used to derive WSS in small study areas[2,12], but not at the global scale. WSS datasets at the global scale so far exist only on the basis of DEM data such as the "Global River-Slope" (GloRS[13]) or as part of the "SWOT Mission River Database" (SWORD[14]).

In a previous study[2], we developed an approach to derive reach-scale WSS from ICESat-2 observations. The approach was applied to 815 reaches in Europe and North America where sufficient validation data was available. For 89% of those reaches, the approach could be used to estimate WSS with a median absolute error of 23 mm/km, almost complying with the SWOT requirements of 17 mm/km. For the remaining studied reaches, there were no or not sufficient observations from ICESat-2. In order to create the global "ICESat-2 River Surface Slope" (IRIS[15]) dataset, we applied our approach[2] to all reaches defined within SWORD. By referencing SWORD, IRIS can be easily compared or combined with SWOT mission observations as they become available. IRIS is the first WSS dataset with global coverage based on ICESat-2 observations. In this paper, we briefly review the materials and methods and present the resulting dataset.

Dataset	Variable	Description
SWOT Mission River Database (SWORD[14,18])		
	reach_id	ID of each reach (Used as key and to identify the reach type)
	centerline	Reach centerline shapefile geometry (Used to construct the reach AOI and measure the chainage)
	width	Average reach width (Used to construct the reach AOI)
ATLAS/ICESat-2 L3A Along Track Inland Surface Water Data (ATL13[17])		
	ht_water_surf	Water surface height per short segment with reference to WGS84 ellipsoid
	cloud_flag_asr_atl09	Cloud probability using Apparent Surface Reflectance (ASR).
	snow_ice_atl09	NOAA snow/ice flag.

Table 1. Input data for the IRIS dataset.

Variable Name	Unit	Description
reach_id		The SWORD reach identifier
lon	degrees east	Approx. centroid longitude of the SWORD reach
lat	degrees north	Approx. centroid latitude of the SWORD reach
across_flag		Flags indicating whether ICESat-2 [across/along/combined] slope is available (1) for the reach or not (0)
along_flag		
combined_flag		
avg_across_slope	mm/km	Average (median) ICESat-2 [across/along/combined] slope for the reach
avg_along_slope		
avg_combined_slope		
min_across_slope	mm/km	Minimum ICESat-2 [across/along/combined] slope for the reach
min_along_slope		
min_combined_slope		
max_across_slope	mm/km	Maximum ICESat-2 [across/along/combined] slope for the reach
max_along_slope		
max_combined_slope		
std_across_slope	mm/km	ICESat-2 [across/along/combined] slope standard deviation for the reach
std_along_slope		
std_combined_slope		
n_across_slope	days	Number of days with ICESat-2 [across/along/combined] slope observations for the reach
n_along_slope		
n_combined_slope		
min_date_across_slope	days since 2000-01-01	First date of ICESat-2 [across/along/combined] slope observations for the reach
min_date_along_slope		
min_date_combined_slope		
max_date_across_slope	days since 2000-01-01	Latest date of ICESat-2 [across/along/combined] slope observations for the reach
max_date_along_slope		
max_date_combined_slope		

Table 2. Contents of the resulting IRIS dataset.

Methods

Except for minor differences in preprocessing (more details below), the methodology used to derive the global "ICESat-2 River Surface Slope" (IRIS, Version v1[15]) dataset follows our published approach[2], which has already been applied to derive and validate a regional dataset (Version v0[16]). Figure 1 shows a flowchart of the main steps in the processing of the IRIS dataset. The approach combines two different methods that are applicable depending on the intersection angle between the satellite orbit and the river: If ICESat-2 crosses a river reach nearly perpendicularly, the across-track approach calculates the WSS between the crossings of the sensor's multiple beams. Otherwise, if satellite orbit and river are nearly parallel, the along-track approach calculates the WSS directly from the continuous water level observations along a single intersecting beam. The WSS within IRIS is defined as positive for a decreasing water surface elevation (WSE) in downstream direction. Table 1 lists the required input data. Besides the fundamental ICESat-2 and SWORD data, no auxiliary inputs are required. Version v1 of IRIS comprises ICESat-2 ATL13 version 5[17] data from cycles 1 to 16 (October 2018 to August 2022) and uses SWORD version v2[14,18]. In the following, we briefly describe the materials and relevant processing steps. For a more detailed description, we refer the reader to our previous publication[2].

SWOT mission river database (SWORD). Version v1 of IRIS is designed as a supplement to version v2 of the "SWOT Mission River Database" (SWORD[14,18]), which contains high-resolution (30 m) river centerline

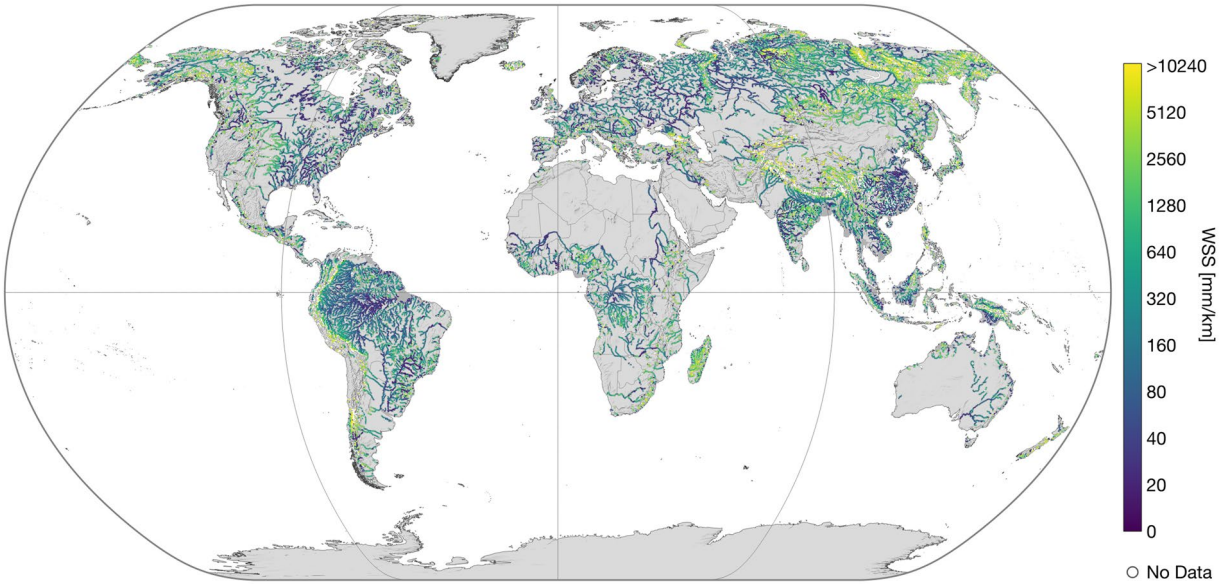

Fig. 2 Averaged combined water surface slope (WSS).

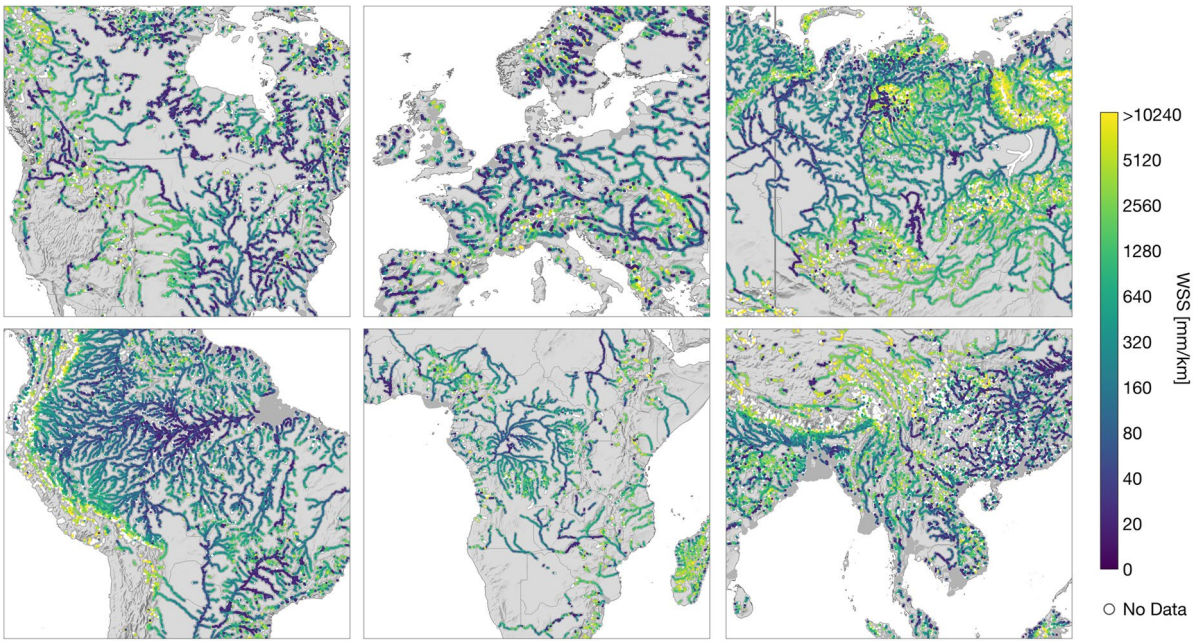

Fig. 3 Detailed views of the averaged combined WSS for North America, Europe, and Siberia (upper f.l.t.r.), South America, Central Africa, and East Asia (lower f.l.t.r.).

geometries and river widths from the "Global River Widths from Landsat" (GRWL[19]) dataset segmented into reaches approximately every 10 km and topologically ordered. The direction of flow can be inferred from the reach identifiers, which increase upstream. The reaches are segmented at natural and artificial river obstructions such as dams and waterfalls, or anomalies like basin boundaries and tributary junctions. Therefore, we assume the WSS within each reach to be reasonably homogeneous. Each SWORD reach has an assigned type, and only reaches of type "*river*" or "*lake on river*" are processed for IRIS. SWORD also contains WSE and WSS data from MERIT Hydro[20] which is derived from the multi-error-removed improved-terrain (MERIT) DEM[21] based on SRTM. We use the SWORD WSS for comparison with IRIS. IRIS uses the SWORD reach identifier as a key so that both datasets can be used together.

In the first step of preprocessing, we buffer each SWORD reach's centerline geometry by its average width to construct a polygon that defines the area of interest (AOI) for further processing. The resulting AOI is thus twice as wide as the average SWORD reach's width to account for any significant temporal and spatial variability (e.g., on braided rivers). Note, that for the creation of the regional dataset (version v0), the AOIs were even wider by

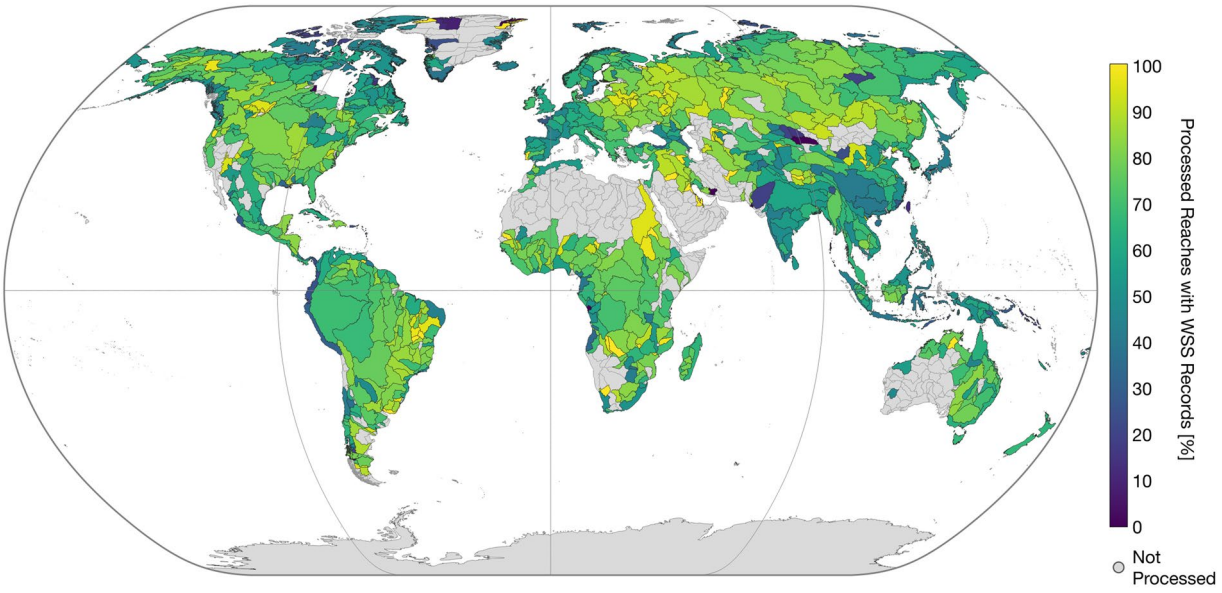

Fig. 4 Percentage of processed reaches with Water Surface Slope (WSS) results per Pfaffstetter level 4 basin.

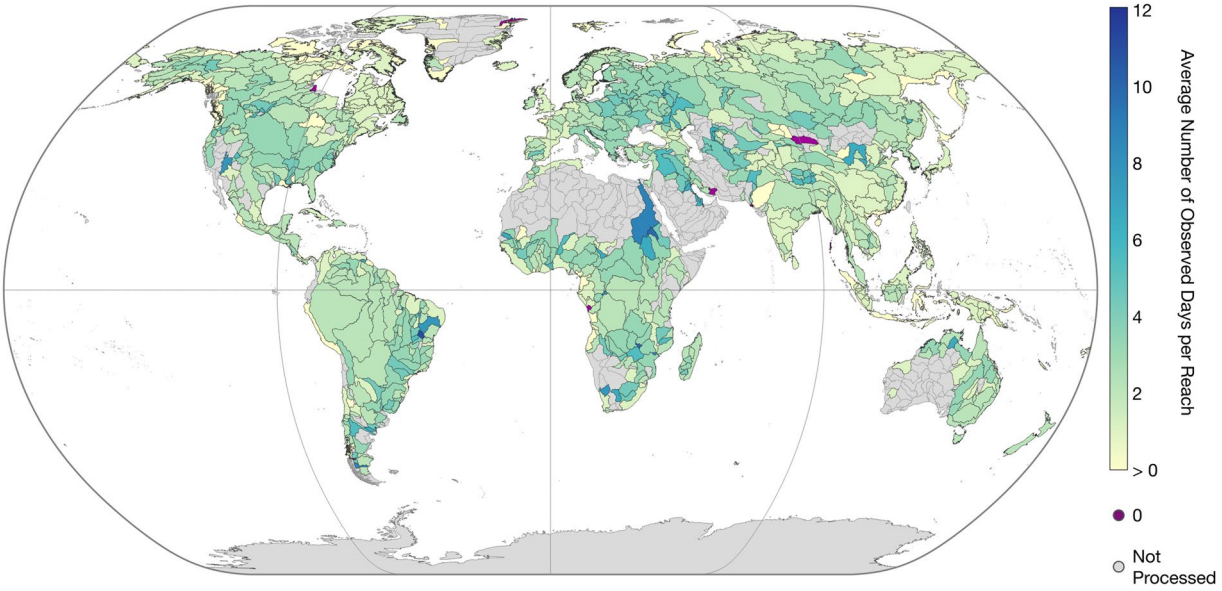

Fig. 5 Average number of days with WSS results per Pfaffstetter Level 4 basin.

four times the width's standard deviation[2]. We reduced the AOI size for version v1 because we observed a significant number of AOIs overlapping with adjacent water bodies on the global scale. In this way, some input data from ICESat-2 (see below) might be lost, but we also reduce the number of outliers.

Ice, cloud, and land elevation satellite 2 (ICESat-2). Each reach AOI is used to spatially filter WSE measurements from the "ATLAS/ICESat-2 L3A Along Track Inland Surface Water Data" (ATL13, Version 5[17]) dataset provided by the "National Snow & ICE Data Center" (NSIDC). These measurements are taken by ICESat-2's photon-counting lidar sensor "Advanced Topographic Laser Altimeter System" (ATLAS) which determines the travel time of an emitted photon to the Earth and back to the sensor along three pairs of beams at a pulse rate of 10 kHz (i.e., one pulse every 0.7 m) and a footprint of approximately 17 m in diameter[22]. However, depending on water and atmospheric conditions, the sensor can detect only a maximum of 2.9 photons per meter over inland waters[23]. Each pair of beams consists of a high energy (175 ± 17 J) and a low energy (45 ± 5 J) beam. The energy of the beams used to estimate the WSS has no significant influence on the WSS accuracy[2]. The spatial resolution is relatively high compared to other repeat-orbit satellite altimetry missions because the 91-day repeat orbit with an inclination of 92 degrees and changing off-nadir pointings over a two-year period results in a track density of 2 km[24]. Version v1 of IRIS is based on ATL13 data from ICESat-2's cycles 1 to 16 (October 2018 to August 2022).

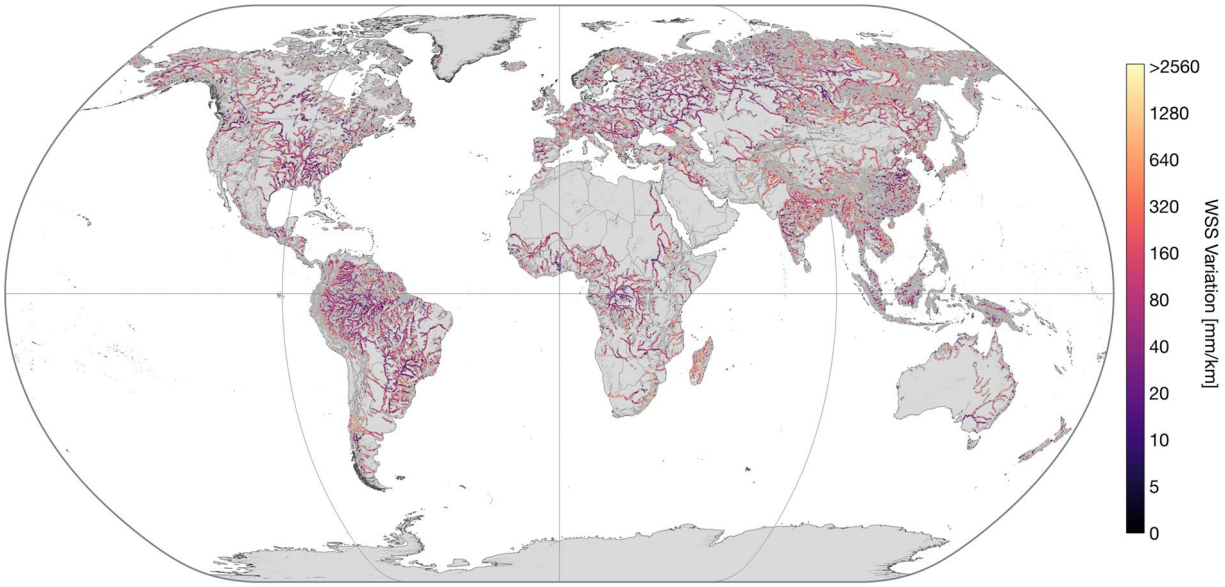

Fig. 6 Combined water surface slope (WSS) variation. Only reaches with more than 3 days of record are shown.

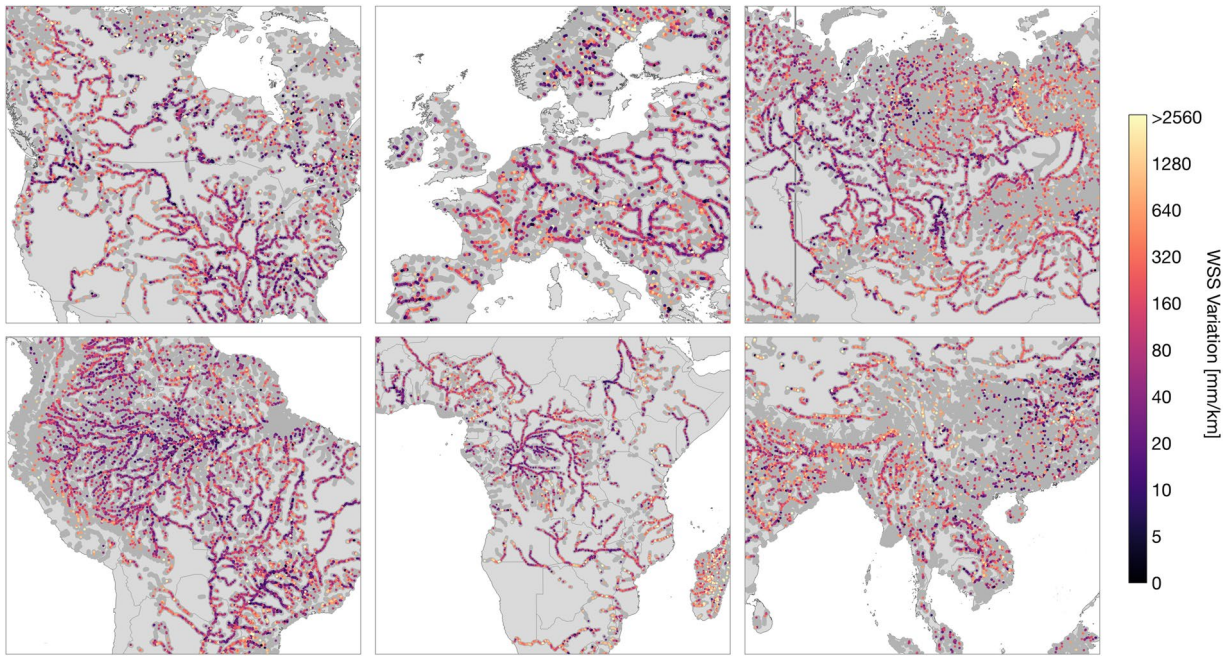

Fig. 7 Combined water surface slope (WSS) variation details. Only reaches with more than 3 days of record are shown.

ATL13 does not contain photon-level observations but representative values over short segments of 75 to 100 consecutive received photons above inland water bodies. These short segments have an along-track length of 30 to several hundred meters, depending on the number of received signal photons per pulse[23]. We use the mean water surface height parameter ("*ht_water_surf*") with reference to the WGS84 ellipsoid and apply the EIGEN-6C4 geoid[25], which, unlike the EGM2008 geoid used for the ATL13 orthometric heights, also includes measurements from the GOCE mission. Additionally, we use the "*cloud_flag_asr_atl09*" and "*snow_ice_atl09*" (new in version v1 compared to v0) parameters to identify and reject outliers caused by clouds and ice coverage. All remaining ATL13 observations within the respective AOI are grouped by beam, cycle, and individual river intersection into so-called features (3D-geometries containing points of common properties). For each feature i, the chainage value x_i of its intersection with the river centerline or otherwise of the nearest point of the centerline is determined. We detect further outliers within each feature by calculating the absolute deviation around the median (ADM) within a rolling window and a linear support vector regression (SVR), similar to the approach applied in DGFI-TUM's

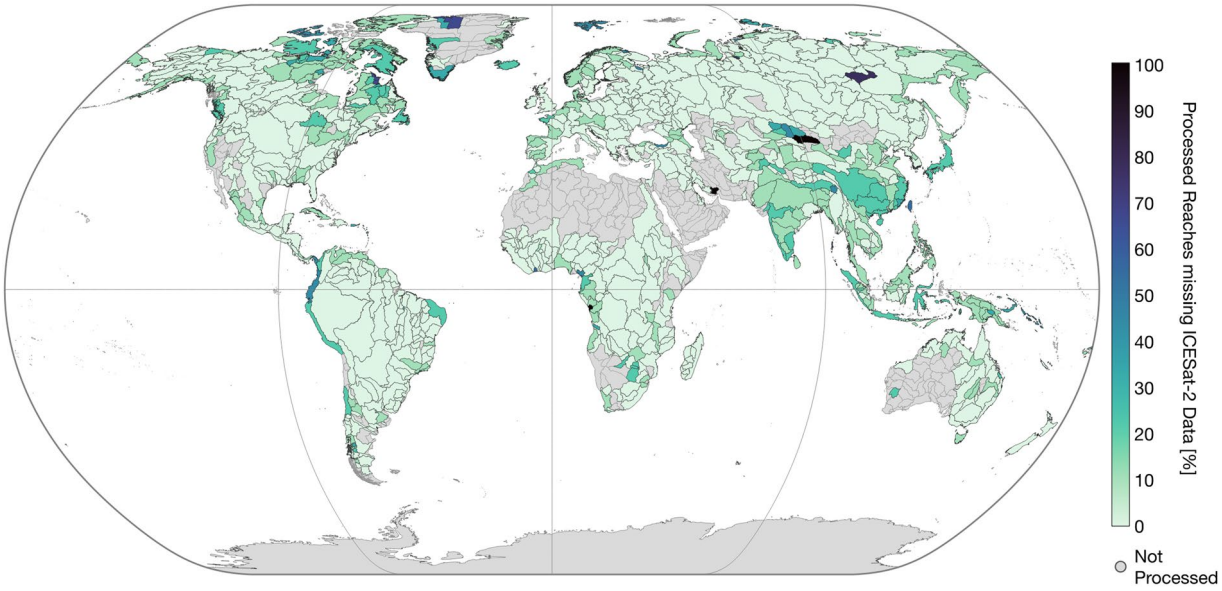

Fig. 8 Percentage of processed reaches with missing ICESat-2 ATL13 data per Pfaffstetter level 4 basin.

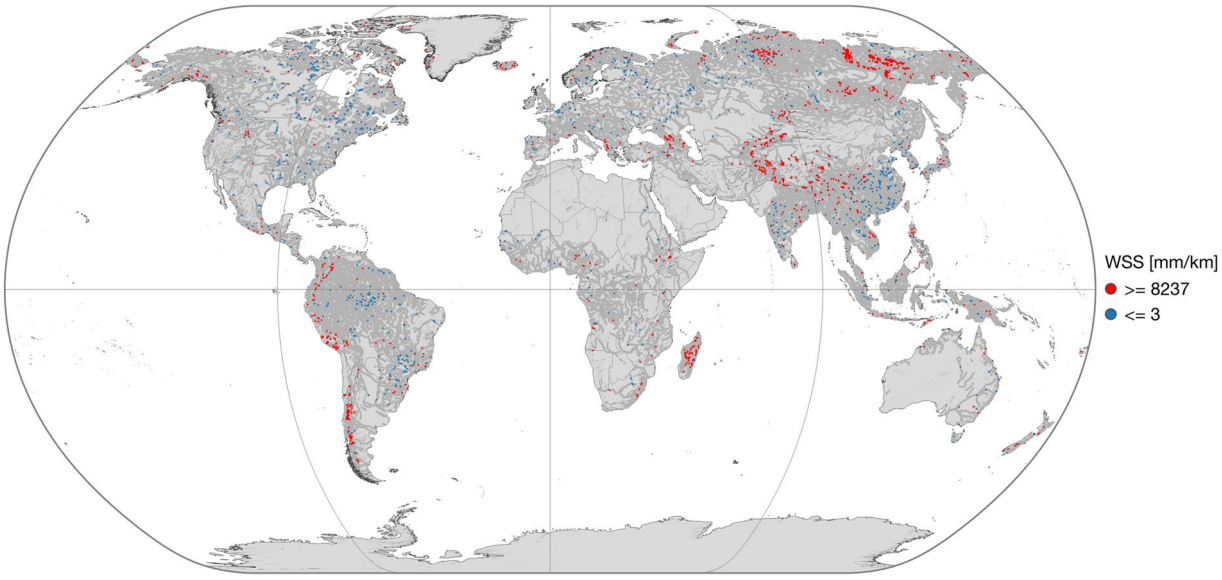

Fig. 9 Averaged combined water surface slope (WSS) extremes. Reaches with an average WSS above the 99th percentile (8,237 mm/km, red) and below the 1st percentile (3 mm/km, blue).

"Database for Hydrological Time Series over Inland Waters" (DAHITI[26]). Observations deviating more than 5 cm from the SVR or the respective median are rejected. If a feature contains a gap larger than 500 m, it is split at this gap, and only the largest cluster is processed further.

Estimation of across-track WSS. For each feature i, we calculate the average elevation h_i of all valid ATL13 observations, weighted by their inverse distance to the river centerline. Then, the instantaneous WSS between i and every other feature j observed at the same date and within the same reach can be calculated as follows:

$$WSS(i, j) = \frac{h_i - h_j}{x_i - x_j}$$

Pairs of features with $|x_i - x_j| < 1$ km are not considered, and negative WSS estimates are viewed as outliers and rejected. Multiple instantaneous WSS observations of identical dates are averaged, weighted by the inverse

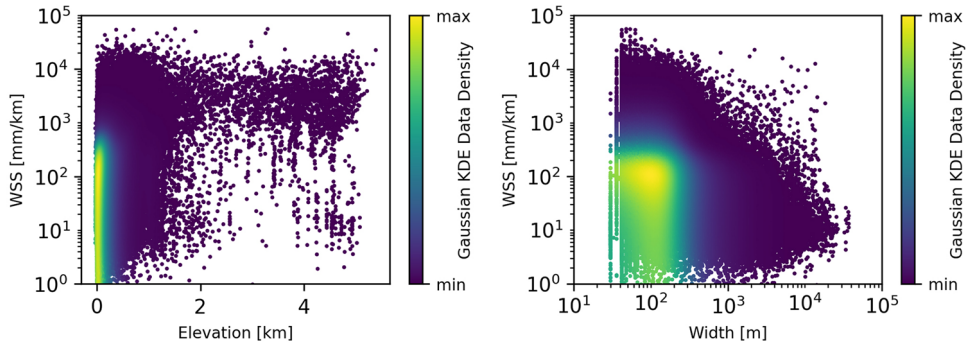

Fig. 10 Averaged combined water surface slope (WSS) by reach elevation (left) and reach width (right).

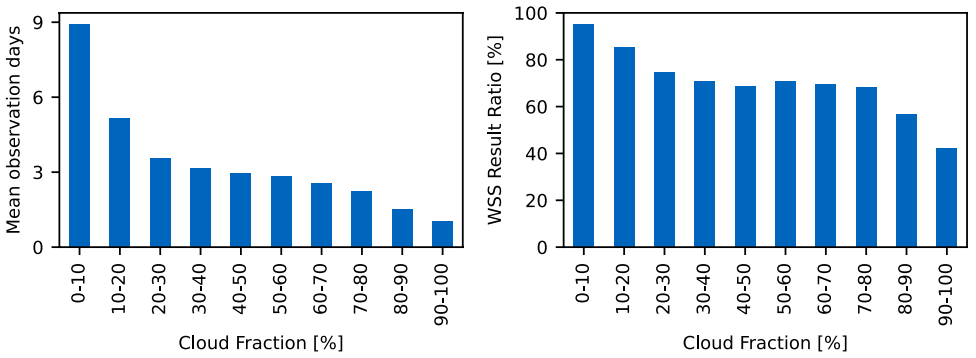

Fig. 11 Mean number of observation days (left) and processed reaches with Water Surface Slope (WSS) results (right) by mean cloud fraction.

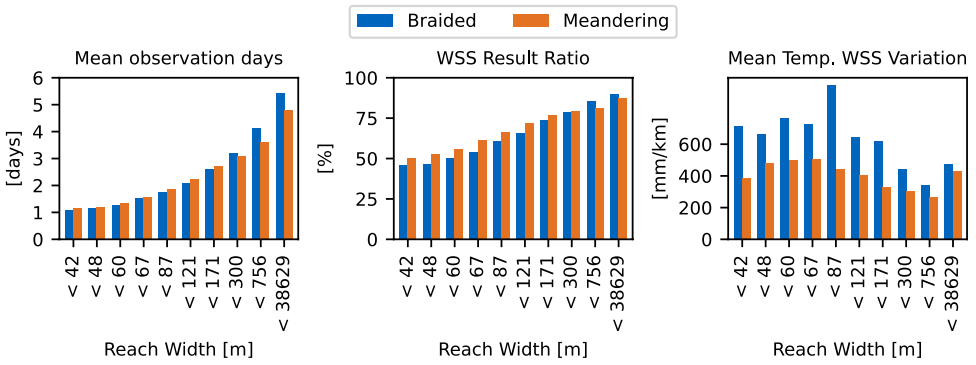

Fig. 12 Mean number of observation days, WSS result ratio, and mean WSS variation per reach width grouped by 10% percentiles and river morphology.

sum of WSE standard deviations in both respective features, to get a reach-scale across-track WSS time series with daily temporal resolution.

Estimation of along-track WSS. Taking advantage of the high spatial resolution, precision, and accuracy of ATLAS, the along-track WSS (tan β) can be estimated by fitting a linear regression to the ATL13 WSE observations and their position along the track within a single feature. However, tan β only represents the WSS along the beam ground track which is not fully parallel to the river centerline. This results in an erroneous WSS. Therefore, tan β is projected onto the river centerline tangent vector $\vec{c}$ to obtain an undistorted WSS along the river:

$$WSS = \frac{\|\vec{b}\|tan\beta}{\|\vec{b}'\|}\text{sgn}(\vec{b}\cdot\vec{c}) \quad \text{with} \quad \vec{b}' = \frac{\vec{b}\cdot\vec{c}}{\|\vec{c}\|^2}\vec{c},$$

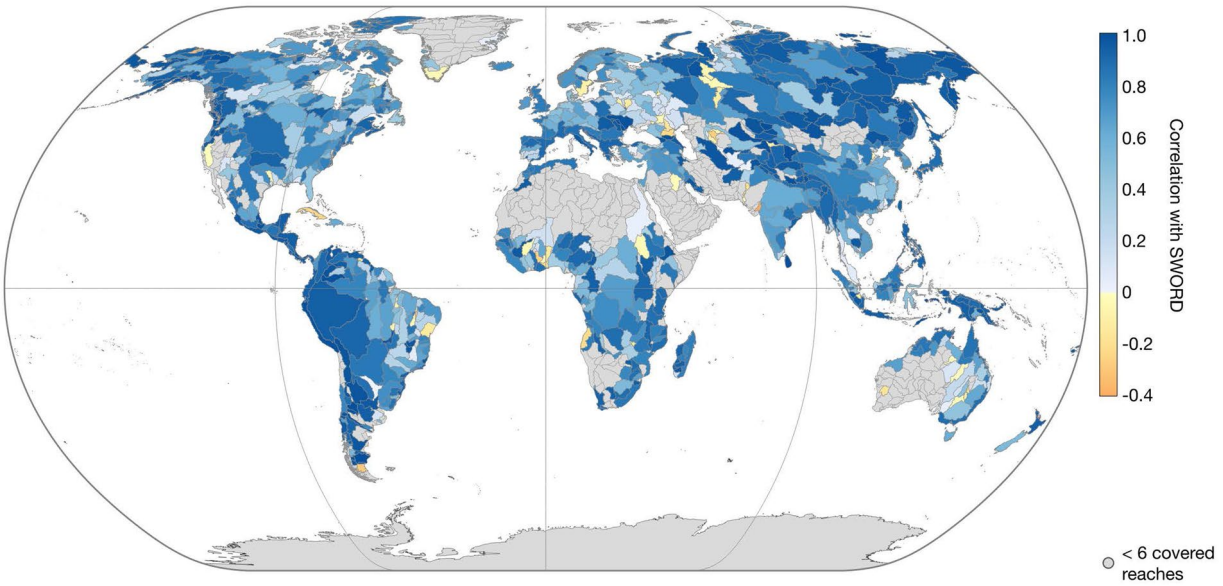

Fig. 13 Correlation coefficient between IRIS average combined WSS and SWORD WSS from MERIT Hydro per Pfaffstetter level 4 basin enclosing more than 5 reaches covered with WSS results.

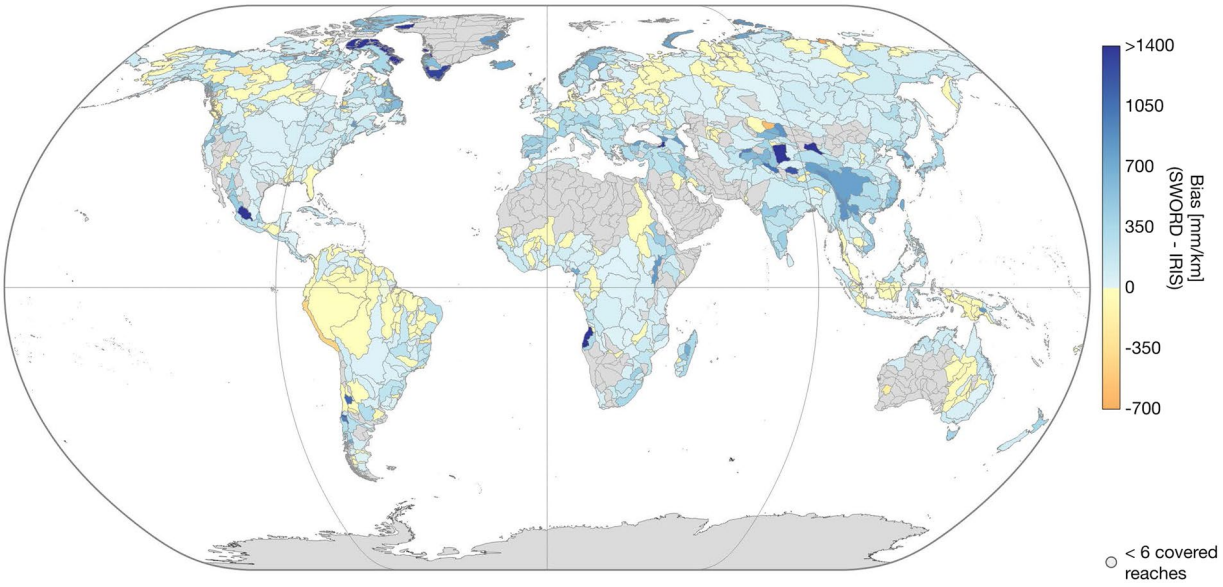

Fig. 14 Bias (SWORD - IRIS) between IRIS average combined WSS and SWORD WSS from MERIT Hydro per Pfaffstetter level 4 basin enclosing more than 5 reaches covered with WSS results.

where $\overrightarrow{b}$ is the vector of the feature's beam ground track segment. As above, negative WSS are rejected. In addition, an angle-dependent outlier threshold is applied to the confidence interval (CI) of tan β. The smaller the angle between $\overrightarrow{c}$ and $\overrightarrow{b}$, the higher the allowed CI, with a maximum angle of 65° and a maximum CI of 300 mm/km. These constraints were determined empirically by comparison with *in-situ* data[2]. We obtain a reach-scale along-track WSS time series by averaging the instantaneous results from identical dates weighted by the inverse of the angle between $\overrightarrow{c}$ and $\overrightarrow{b}$.

Combined estimation of WSS. To increase the overall spatial and temporal coverage, we combine both methods. Depending on the intersection angle, only one of them may provide a WSS result. Thus, in the combination the reach-scale daily averaged across- and along-track WSS time series are merged, with the across-track results being preferred in the case of overlapping dates as this is the more accurate and robust approach[2].

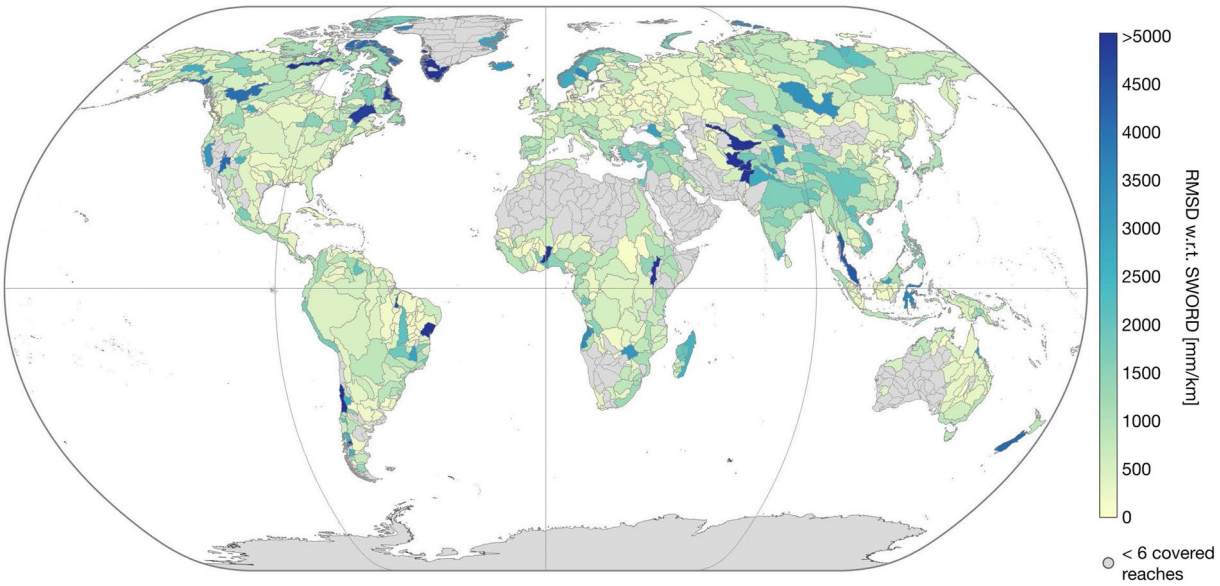

Fig. 15 Root mean square deviation (RMSD) between IRIS average combined WSS and SWORD WSS from MERIT Hydro per Pfaffstetter level 4 basin enclosing more than 5 reaches covered with WSS results.

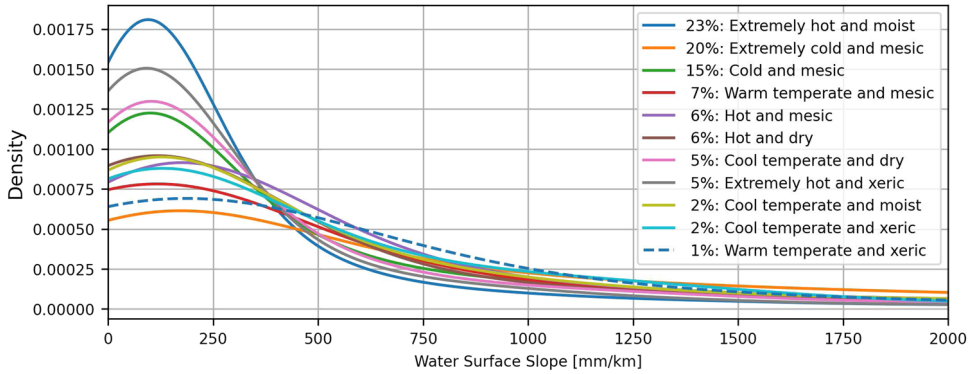

Fig. 16 Probability density of the IRIS average combined WSS per climate zone.

Data Records

The global "ICESat-2 River Surface Slope" (IRIS[15]) dataset is available at Zenodo. IRIS is stored in a single NetCDF4 file, which is structured in a single group containing the variables listed in Table 2. IRIS can be used as a supplement to SWORD by joining the datasets via the "*reach_id*" key. Otherwise, the "*lon*" and "*lat*" variables give the approximate centroid of the reach. All other variables are provided separately for each method. The "*[across/along/combined]_flag*" variable indicates the availability of data from the respective method.

The main content of IRIS is the reach-scale median WSS from the combined approach ("*avg_combined_slope*") shown in Fig. 2. More detailed views on specific regions are presented in Fig. 3. In dark grey, both figures display reaches that were not processed due to the SWORD type flag filter, such as ghost reaches or reaches with unreliable topography. Reaches that have been processed but do not contain valid results are shown in white. Overall, 178,659 (74.1%) of the total 241,107 reaches in the SWORD dataset pass the type flag filter (types "*river*" or "*lake on river*") and are further processed. The approach yields results for 121,583 reaches which corresponds to a coverage of 68.1% of the processed SWORD reaches. Figure 4 shows the ratio of processed reaches with WSS results per river basin (Pfaffstetter level 4[27]).

IRIS provides the number of days with WSS observations per reach by the parameter "*n_[across/along/combined]_slope*". Figure 5 shows the average number of days with combined observations per basin. The detection of WSS changes over time is possible through the continuous addition of ICESat-2 observations. IRIS contains the minimum ("*min_[across/along/combined]_slope*") and maximum ("*max_[across/along/combined]_slope*") WSS obtained with the respective method per reach. The amplitude of WSS variations ("*max_combined_slope*" - "*min_combined_slope*") for reaches with more than 3 days of WSS observations can be seen in Fig. 6. More detailed views of specific regions are provided in Fig. 7. The parameters "*min_date_[across/along/combined]_slope*" and "*max_date_[across/along/combined]_slope*" give the first and latest observation of the respective

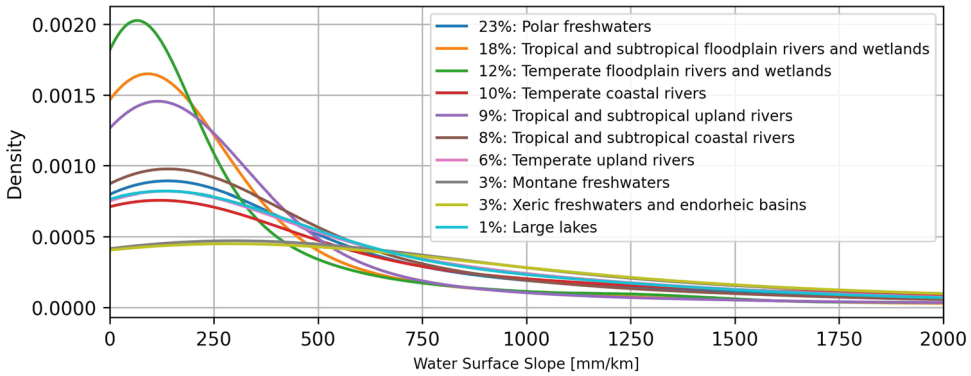

Fig. 17 Probability density of the IRIS average combined WSS per freshwater habitat.

method per reach, and "*std_[across/along/combined]_slope*" provides the standard deviation of all respective WSS observations per reach.

Technical Validation

The approach was validated at 815 reaches in a regional study[2] with a median absolute error (MAE) of 23 mm/km for the "*avg_combined_slope*" compared to gauge data. The MAE for the "*avg_across_slope*" and "*avg_along_slope*" were 19 and 47 mm/km, respectively[2]. Although a global validation is not feasible, the overall robustness of the results can be inferred from Figs. 2, 3. Especially at the free-flowing Amazon and Congo Rivers, the WSS increases gradually in upstream direction. Discontinuities can be observed primarily in basins influenced by human intervention. For example, reservoirs in the western Mississippi River basin are apparent as single discontinuities with low WSS (cf. Fig. 3). In Figs. 6, 7, low variations of WSS can be observed along river main stems and regulated rivers. Large fluctuations, on the other hand, occur mainly at upstream reaches.

Among others, high coverage can be achieved for Eastern Europe, Brazil, and the Nile River. Below-average coverage is apparent for parts of the Lena and Indus Rivers, Western Europe, East Asia, and the Pacific coast of South America. This is caused, among other factors, by missing ATL13 input data (cf. Figure 8). Overall, 16,754 (9.4%) of the processed reaches are not covered by ATL13 data.

Figure 9 displays extremely high (99th percentile: 8,237 mm/km) and low (1st percentile: 3 mm/km) "*avg_combined_slope*" WSS values. Except for some plateaus, low WSS values are located in low-lying regions. On the other hand, high WSS values are not limited to regions of high elevation as shown in Fig. 10 on the left. Figure 10 also provides the averaged combined WSS by reach width. With increasing width, the WSS tends towards 10 mm/km. Extremely high WSS are limited to narrow reaches. The data density in Fig. 10 indicates that the majority of the studied reaches are less than 300 m wide and situated lower than 200 m.

In Fig. 11 the number of observed days and and the coverage with WSS results is compared with cloud coverage data from MODIS[28] during the ICESat-2 period. Both values, especially the number of observed days, depend strongly on cloud coverage since the ATLAS lidar sensor cannot penetrate clouds. Additionally, Fig. 12 shows the number of observed days, the coverage with WSS results, and mean temporal WSS variation ("*max_combined_slope*" - "*min_combined_slope*") per 10% reach width percentiles for meandering ($n = 96{,}900$) and braided ($n = 24{,}683$) rivers. For the morphological classification, the "Global River Morphology" (GRM) raster from the "Global Channel Belt" (GCB[29,30]) dataset is sampled along each reaches' centerline, assigning the class with the highest summed probability. Figure 12 shows that with increasing width, more observations can be provided. The mean temporal WSS variation is significantly larger for braided rivers than for meandering rivers, especially at widths below 171 m.

DEM data cannot be used to validate the accuracy of the results. However, for further analysis of the statistical soundness of the IRIS WSS, we compare the "*avg_combined_slope*" to the SWORD WSS derived from the MERIT Hydro DEM. Figures 13–15 show the correlation coefficient r, the bias (SWORD - IRIS), and the root mean square deviation (RMSD) between the two datasets per Pfaffstetter level 4 basin. Basins with less than six reaches covered by IRIS are not included because there is not enough data to make a meaningful comparison. On basin scale, r is greater than 0.50 for 580 (72%) out of the 808 basins with more than 5 covered reaches. Of the major river basins, only the Nile has a low correlation (0.03, cf. Figure 13). Over all IRIS and SWORD WSS, r is 0.73.

The bias ranges from −657 to 4,774 mm/km at the basin scale (with more than 5 reaches covered) with a mean of 149 mm/km. Thus, SWORD tends to have greater WSS than IRIS, especially in East Asia, while for almost the entire Amazon basin, the WSS results are greater in the IRIS dataset (cf. Figure 14). The overall RMSD after subtracting the bias between SWORD and IRIS is 1,514 mm/km, ranging from 12 to 19,994 mm/km at the basin scale (with more than 5 reaches covered) with a mean RMSD of 942 mm/km.

One reason for low correlations or large biases at the basin scale could be the gap between the acquisition time of the SWORD and IRIS input data, which spans 18 years in the case of SRTM and ICESat-2. During this time, significant hydraulic structures affecting the WSS may have been constructed and the river morphology may have changed. In addition, the bias between the two datasets is expected due to the better vertical accuracy

of ICESat-2 compared to the MERIT DEM[31] used to derive the SWORD WSS. The MERIT DEM shows significant elevation errors[21] compared to the first ICESat mission in basins where large biases occur between IRIS and SWORD (e.g., in East Asia).

For an additional analysis of the statistical soundness, we classify the "*avg_combined_slope*" by different hydro-environmental classifications provided by HydroATLAS[32] at the basin scale (BasinATLAS). Figures 16, 17 show the WSS probability density by different climate zones[33] and freshwater habitats[34], respectively. The legends listing the classes also show the relative contribution of each class to the total number of basins. Classes with a percentage of less than 1% are not shown.

Usage Notes

Although IRIS contains separate values for each of the three approaches, the "*avg_combined_slope*" is likely to be appropriate for most use cases because it has the highest spatial and temporal coverage. Users should consider the number of days with WSS observations ("*n_[across/along/combined]_slope*") when using the aggregated "*max_[across/along/combined]_slope*", "*min_[across/along/combined]_slope*", and "*std_[across/along/combined]_slope*" parameters. With fewer samples, these aggregated parameters get less significant or not meaningful at all. In this paper, only reaches with more than 3 days of WSS observations were used when plotting the parameters (i.e., Figs. 6, 7). IRIS will be updated progressively by adding future ICESat-2 cycles. This will provide increasing insight into the temporal variability of WSS. IRIS will also be updated with new versions of SWORD. Additionally, for future versions it is planned to include WSS uncertainty values derived from the confidence of fit or the WSE uncertainties for the along- and across-track method, respectively. Note, that the IRIS dataset is generated fully automatically and depends on the availability and quality of the ATL13 observations and flags, as well as the accuracy of the SWORD centerline, topology, and type parameters. Therefore, isolated outliers cannot be excluded, e.g., caused by missing dams in SWORD.

Code availability

A code example of IRIS is available at Zenodo[35]. The methodology is described in detail in our regional study[2].

Received: 3 February 2023; Accepted: 5 May 2023;
Published online: 06 June 2023

References

1. Global Climate Observing System. *The 2022 GCOS Implementation Plan (GCOS-244)* (World Meteorological Organization, Geneva, 2022).
2. Scherer, D., Schwatke, C., Dettmering, D. & Seitz, F. ICESat-2 based river surface slope and its impact on water level time series from satellite altimetry. *Water Resources Research* **58**, e2022WR032842, https://doi.org/10.1029/2022WR032842 (2022).
3. Halicki, M., Schwatke, C. & Niedzielski, T. The impact of the satellite ground track shift on the accuracy of altimetric measurements on rivers: A case study of the Sentinel-3 altimetry on the Odra/Oder River. *Journal of Hydrology* **617**, 128761, https://doi.org/10.1016/j.jhydrol.2022.128761 (2023).
4. Julien, P. Y. River dynamics. In *River Mechanics*, chap. 11, https://doi.org/10.1017/9781316107072.012, 2 edn (Cambridge University Press, Cambridge, 2018).
5. Grill, G. *et al*. Mapping the world's free-flowing rivers. *Nature* **569**, 215–221, https://doi.org/10.1038/s41586-019-1111-9 (2019).
6. Dettmering, D., Ellenbeck, L., Scherer, D., Schwatke, C. & Niemann, C. Potential and limitations of satellite altimetry constellations for monitoring surface water storage changes–a case study in the Mississippi basin. *Remote Sensing* **12**, https://doi.org/10.3390/rs12203320 (2020).
7. LeFavour, G. & Alsdorf, D. Water slope and discharge in the Amazon River estimated using the shuttle radar topography mission digital elevation model. *Geophysical Research Letters* **32**, 1–5, https://doi.org/10.1029/2005GL023836 (2005).
8. Rodríguez, E., Morris, C. S. & Belz, J. E. A global assessment of the SRTM performance. *Photogrammetric Engineering and Remote Sensing* **72**, 249–260, https://doi.org/10.14358/PERS.72.3.249 (2006).
9. Biancamaria, S., Lettenmaier, D. P. & Pavelsky, T. M. The SWOT mission and its capabilities for land hydrology. *Surveys in Geophysics* **37**, 307–337, https://doi.org/10.1007/s10712-015-9346-y (2016).
10. Altenau, E. H. *et al*. Temporal variations in river water surface elevation and slope captured by AirSWOT. *Remote Sensing of Environment* **224**, 304–316, https://doi.org/10.1016/j.rse.2019.02.002 (2019).
11. Cooley, S. W., Ryan, J. C. & Smith, L. C. Human alteration of global surface water storage variability. *Nature* **591**, 78–81, https://doi.org/10.1038/s41586-021-03262-3 (2021).
12. Wang, S., Cui, D. & Xu, J. Monitoring and analysis of water surface slope of the Yarlung Zangbo River based on remote sensing. *Water* **14**, 3304, https://doi.org/10.3390/w14203304 (2022).
13. Cohen, S., Wan, T., Islam, M. T. & Syvitski, J. P. Global river slope: a new geospatial dataset and global-scale analysis. *Journal of Hydrology* **563**, 1057–1067, https://doi.org/10.1016/j.jhydrol.2018.06.066 (2018).
14. Altenau, E. H. *et al*. The surface water and ocean topography (SWOT) mission river database (SWORD): a global river network for satellite data products. *Water Resources Research* **57**, https://doi.org/10.1029/2021WR030054 (2021).
15. Scherer, D., Schwatke, C., Dettmering, D. & Seitz, F. IRIS: ICESat-2 river surface slope, version v1. *Zenodo* https://doi.org/10.5281/zenodo.7516381 (2023).
16. Scherer, D., Schwatke, C., Dettmering, D. & Seitz, F. IRIS: ICESat-2 river surface slope, version v0. *Zenodo* https://doi.org/10.5281/zenodo.7098114 (2022).
17. Jasinski, M. *et al*. ATLAS/ICESat-2 L3A along track inland water surface water data, release 5. *NASA National Snow and Ice Data Center Distributed Active Archive Center* https://doi.org/10.5067/ATLAS/ATL13.005 (2021).
18. Altenau, E. H. *et al*. SWOT river database (SWORD), version v2. *Zenodo* https://doi.org/10.5281/zenodo.5643392 (2021).
19. Allen, G. H. & Pavelsky, T. Global extent of rivers and streams. *Science* **361**, 585–588, https://doi.org/10.1126/science.aat0636 (2018).
20. Yamazaki, D. *et al*. MERIT Hydro: a high-resolution global hydrography map based on latest topography dataset. *Water Resources Research* **55**, 5053–5073, https://doi.org/10.1029/2019WR024873 (2019).
21. Yamazaki, D. *et al*. A high-accuracy map of global terrain elevations. *Geophysical Research Letters* **44**, 5844–5853, https://doi.org/10.1002/2017GL072874 (2017).
22. Neumann, T. A. *et al*. The ice, cloud, and land elevation satellite - 2 mission: A global geolocated photon product derived from the advanced topographic laser altimeter system. *Remote Sensing of Environment* **233**, 111325, https://doi.org/10.1016/j.rse.2019.111325 (2019).

23. Jasinski, M. *et al. Algorithm Theoretical Basis Document (ATBD) for Along Track Inland Surface Water Data, ATL13, Release 5*, https://doi.org/10.5067/RI5QTGTSVHRZ (NASA Goddard Space Flight Center, Greenbelt, MD, 2021).
24. Markus, T. *et al.* The ice, cloud, and land elevation satellite-2 (ICESat-2): science requirements, concept, and implementation. *Remote Sensing of Environment* **190**, 260–273, https://doi.org/10.1016/j.rse.2016.12.029 (2017).
25. Foerste, C. *et al. EIGEN-6C4 the latest combined global gravity field model including GOCE data up to degree and order 2190 of GFZ Potsdam and GRGS Toulouse* https://doi.org/10.5880/icgem.2015.1 (2014).
26. Schwatke, C., Dettmering, D., Bosch, W. & Seitz, F. DAHITI - an innovative approach for estimating water level time series over inland waters using multi-mission satellite altimetry. *Hydrology and Earth System Sciences* **19**, 4345–4364, https://doi.org/10.5194/hess-19-4345-2015 (2015).
27. Lehner, B. & Grill, G. Global river hydrography and network routing: baseline data and new approaches to study the world's large river systems. *Hydrological Processes* **27**, 2171–2186, https://doi.org/10.1002/hyp.9740 (2013).
28. Pincus, R. *et al.* Updated observations of clouds by MODIS for global model assessment. *Earth System Science Data Discussions* **2022**, 1–20, https://doi.org/10.5194/essd-2022-282 (2022).
29. Nyberg, B. Global channel belt (GCB). *Zenodo* https://doi.org/10.5281/zenodo.7680163 (2022).
30. Nyberg, B., Henstra, G., Gawthorpe, R. L., Ravnås, R. & Ahokas, J. Global scale analysis on the extent of river channel belts. *Nature Communications* **14**, 2163, https://doi.org/10.1038/s41467-023-37852-8 (2023).
31. Chen, W. *et al.* Towards ice-thickness inversion: an evaluation of global digital elevation models (dems) in the glacierized tibetan plateau. *The Cryosphere* **16**, 197–218, https://doi.org/10.5194/tc-16-197-2022 (2022).
32. Linke, S. *et al.* Global hydro-environmental sub-basin and river reach characteristics at high spatial resolution. *Scientific Data* **6**, 1–15, https://doi.org/10.1038/s41597-019-0300-6 (2019).
33. Metzger, M. J. *et al.* A high-resolution bioclimate map of the world: a unifying framework for global biodiversity research and monitoring. *Global Ecology and Biogeography* **22**, 630–638, https://doi.org/10.1111/geb.12022 (2013).
34. Abell, R. *et al.* Freshwater ecoregions of the world: a new map of biogeographic units for freshwater biodiversity conservation. *BioScience* **58**, 403–414, https://doi.org/10.1641/B580507 (2008).
35. Scherer, D. Minimum working example of IRIS global river slope processing. *Zenodo* https://doi.org/10.5281/zenodo.7761212 (2023).

Acknowledgements

This work was funded by the Deutsche Forschungsgemeinschaft (DFG, German Research Foundation)-Project number 324641997, Grant DE 2174/10-2. Open access funding enabled and organized by Projekt DEAL. We thank the NSIDC and the authors of SWORD for openly sharing the input data required for IRIS.

Author contributions

D.S. developed the methodology and wrote the manuscript. C.S. curated the data. D.D. and F.S. supervised the study and contributed to the discussion of the results. All authors reviewed the manuscript.

Funding

Open Access funding enabled and organized by Projekt DEAL.

Competing interests

The authors declare no competing interests.

Additional information

Correspondence and requests for materials should be addressed to D.S.

P4 Monitoring river discharge from space: An optimization approach with uncertainty quantification for small ungauged rivers

Scherer, D., Schwatke, C., Dettmering, D., & Seitz, F. (2024). **Monitoring river discharge from space: An optimization approach with uncertainty quantification for small ungauged rivers**. *Remote Sensing of Environment*, *315*, 114434. https://doi.org/10.1016/j.rse.2024.114434

Date of Publication: 21 September 2024

Abstract

The number of in-situ stations measuring river discharge, one of the Essential Climate Variables (ECV), is declining steadily, and numerous basins have never been gauged. With the aim of improving data availability worldwide, we propose an easily applicable and transferable approach to estimate reach-scale discharge solely using remote sensing data that is suitable for filling gaps in the in-situ network. We combine 20 years of satellite altimetry observations with high-resolution satellite imagery via a hypsometric function to observe large portions of the reach-scale bathymetry. The high-resolution satellite images, which are classified using deep learning image segmentation, allow for detecting small rivers (narrower than 100 m) and can capture small width variations. The unobserved part of the bathymetry is estimated using an empirical width-to-depth function. Combined with precise satellite-derived slope measurements, river discharge is calculated at multiple consecutive cross-sections within the reach. The unknown roughness coefficient is optimized by minimizing the discharge differences between the cross-sections. The approach requires minimal input and approximate boundary conditions based on expert knowledge but is not dependent on calibration. We provide realistic uncertainties, which are crucial for data assimilation, by accounting for errors and uncertainties in the different input quantities. The approach is applied globally to 27 river sections with a median normalized root mean square error of 12% and a Nash-Sutcliffe model efficiency of 0.560. On average, the 90% uncertainty range includes 91% of the in-situ measurements.

Contribution

D.S. developed the methodology, gathered the data, validated the results, and wrote the manuscript. C.S. curated the data and contributed to the discussion of the results. D.D. and F.S. supervised the study and contributed to the discussion of the results. All authors reviewed the manuscript.

Criteria	Own Contribution
Idea and conceptual design	90%
Data acquisition and preparation	80%
Implementation and realisation	90%
Analysis and discussion	90%
Figure compilation	95%
Manuscript structure and writing	80%
Overall contribution	88%

Remote Sensing of Environment 315 (2024) 114434

Contents lists available at ScienceDirect

Remote Sensing of Environment

journal homepage: www.elsevier.com/locate/rse

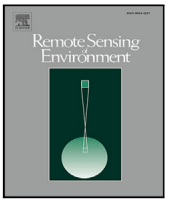

Monitoring river discharge from space: An optimization approach with uncertainty quantification for small ungauged rivers

Daniel Scherer *, Christian Schwatke, Denise Dettmering, Florian Seitz

Deutsches Geodätisches Forschungsinstitut der Technischen Universität München (DGFI-TUM), Arcisstraße 21, Munich, 80333, Germany

ARTICLE INFO

Edited by Menghua Wang

Dataset link: https://doi.org/10.5281/zenodo.10611165

Keywords:
Discharge
Streamflow
Ungauged rivers
ICESat-2
Satellite altimetry
PlanetScope

ABSTRACT

The number of in-situ stations measuring river discharge, one of the Essential Climate Variables (ECV), is declining steadily, and numerous basins have never been gauged. With the aim of improving data availability worldwide, we propose an easily applicable and transferable approach to estimate reach-scale discharge solely using remote sensing data that is suitable for filling gaps in the in-situ network. We combine 20 years of satellite altimetry observations with high-resolution satellite imagery via a hypsometric function to observe large portions of the reach-scale bathymetry. The high-resolution satellite images, which are classified using deep learning image segmentation, allow for detecting small rivers (narrower than 100 m) and can capture small width variations. The unobserved part of the bathymetry is estimated using an empirical width-to-depth function. Combined with precise satellite-derived slope measurements, river discharge is calculated at multiple consecutive cross-sections within the reach. The unknown roughness coefficient is optimized by minimizing the discharge differences between the cross-sections. The approach requires minimal input and approximate boundary conditions based on expert knowledge but is not dependent on calibration. We provide realistic uncertainties, which are crucial for data assimilation, by accounting for errors and uncertainties in the different input quantities. The approach is applied globally to 27 river sections with a median normalized root mean square error of 12% and a Nash–Sutcliffe model efficiency of 0.560. On average, the 90% uncertainty range includes 91% of the in-situ measurements.

1. Introduction

River discharge is one of the "Essential Climate Variables" (ECV) defined by the "Global Climate Observing System" (GCOS) (World Meteorological Organization, 2022). Knowledge of this parameter is required for various tasks related to water management and civil protection. Furthermore, river discharge is an important quantity in studies of the hydrological cycle and climate change impacts. Despite this relevance, the number of publicly accessible in-situ discharge stations in databases like the GRDC (Global Runoff Data Centre, 2023) is steadily declining, especially in remote places (Hannah et al., 2011; Riggs et al., 2023). Therefore, multiple studies aim at extending previously active in-situ discharge stations using remote sensing observables such as water level, river width, or reflectance ratios and a calibrated functional relationship to the river discharge, often referred to as rating curve (e.g., Tarpanelli et al., 2019; Elmi et al., 2021; Gleason and Durand, 2020; Riggs et al., 2023). To establish the functional relationship, the periods of remote sensing and in-situ data do not necessarily have to overlap (Tourian et al., 2013). Still the river must have been gauged at some point in time. However, many river basins have never been gauged due to their remoteness or security concerns. In some places, political factors prohibit or restrict data sharing (Gleason and Durand, 2020).

For ungauged rivers, shallow water equations like the Gauckler–Manning–Strickler equation (Manning, 1891) are regularly used with a combination of different remote sensing data. These equations require the channel geometry, water surface slope, and a roughness coefficient. Bjerklie et al. (2018), Zakharova et al. (2020), and Scherer et al. (2020) derive the channel geometry from river widths observed by the Landsat mission and water levels observed by satellite altimetry. However, the geometry can only be partially reconstructed this way, and the river depth is either estimated from empirical relationships or literature values. Water surface slope is also derived from satellite altimetry data, and roughness coefficients are determined based on literature or empirical relationships (Bjerklie et al., 2018; Zakharova et al., 2020; Scherer et al., 2020). The approach by (Lamine et al., 2021) is similar but uses higher resolution PlanetScope data at an ephemeral section of the Niger River where the full bathymetry can be

* Corresponding author.
E-mail address: daniel.scherer@tum.de (D. Scherer).

https://doi.org/10.1016/j.rse.2024.114434
Received 26 January 2024; Received in revised form 4 September 2024; Accepted 16 September 2024
Available online 21 September 2024

observed. These approaches demand extensive user input and judgment to estimate discharge at even a single cross-section.

To reduce the number of assumptions, many studies (e.g., Durand et al., 2014; Garambois and Monnier, 2015; Gleason and Hamdan, 2017; Hagemann et al., 2017) use the principle of mass conservation or "Mass-Conserved Flow Law Inversion" (McFLI) (Durand et al., 2023), considering the discharge to be constant in space within a short reach of steady (in time, constant river stage during the satellite observation), and uniform or gradually varied (in space, with the river shape the same throughout the studied reach) flow (Rhoads, 2020). Using this constraint, the unknown parameters such as roughness and depth can be better approximated, but the problem remains ill-posed. There is no exact solution, and boundary constraints are required (Roux and Dartus, 2005; Gleason and Durand, 2020). Most of these approaches are designed specifically for and tested with simulated data from the new "Surface Water and Ocean Topography" (SWOT) mission, which measures river width, height, and slope simultaneously. The unconstrained SWOT methods for ungauged rivers still require model data as prior information (Durand et al., 2023). Due to the current lack of SWOT observations, the McFLI "Bayesian At-Many-Stations Hydraulic Geometry-Manning Algorithm" (BAM) (Hagemann et al., 2017) is primarily used with river widths from satellite imagery. Feng et al. (2019) use BAM with river widths extracted from Landsat 8, Sentinel-2, and PlanetScope satellite imagery. However, without slope and height data, BAM requires a priori data from global runoff reanalysis datasets. Lin et al. (2023) apply the BAM and the updated geoBAM (Brinkerhoff et al., 2020) algorithms to more than 3000 globally distributed river reaches using Landsat imagery. With the standard configuration, up to 39% of sites show good model performance, and with more sophisticated a priori data, this number increases to 65%. The operational SWOT discharge product will provide uncertainty estimates based on random and systematic errors of the SWOT sensor, the flow law approximation employed, and parameter estimation (Durand et al., 2023). A total uncertainty of 30% is expected for SWOT estimates at ungauged rivers (Durand et al., 2023).

In this study, we leverage and fuse the large amount of diverse remotely sensed data on water level, slope, and width to derive a discrete river discharge time series. The approach does not depend on SWOT data. Instead, we use over 20 years of water level observations from satellite altimetry, beginning with the Jason-1 and Envisat missions in 2001. Using the unique measurement geometry of the ICESat-2 mission with six parallel observations, we obtain global reach-scale average measurements of river slopes. We observe small rivers (< 100 m), as categorized by Nielsen et al. (2022), and small variations in river width using 3 m resolution PlanetScope satellite imagery. However, the approach can also be applied to larger rivers. A hypsometric curve is fitted to simultaneous water level and surface area observations to reconstruct the river bathymetry. An empirical width-to-depth relationship is used to obtain a first estimate of the unobserved part of the river bathymetry, which is further optimized by reducing the difference between adjacent cross-sections. Based on the principle of mass conservation, we optimize the roughness coefficient to minimize the discharge difference between multiple consecutive cross-sections. Observation errors and uncertainties from all measurement techniques involved are included in the estimation of uncertainty. Our approach is specifically designed for ungauged rivers, where no calibration data is available and SWOT would only cover the most recent years. The new method works with minimal user input such as label points for the image classification and requires only approximate boundary conditions for the optimization. However, expert judgment is still needed to assess the results and adjust the boundary conditions. We provide uncertainty ranges to facilitate the assimilation of our results into hydrological models. The amount and variety of satellite data employed are unprecedented, and yet the approach is transferable to other river reaches with steady uniform or gradually varied flow. The approach is expected to be extremely valuable for hydrological modeling by providing discharge time series with uncertainty estimates in remote ungauged basins without requiring any calibration data.

2. Materials and methods

We estimate discharge time series for m consecutive cross-sections within a river reach of steady uniform or gradually varied flow and aim to minimize the differences in discharge based on the principle of mass conservation. To calculate the river discharge $Q(t,x)$ at a given cross-section at chainage x and time t, we first divide the cross-section into $n = 30$ vertical segments as recommended by Boyer (1964), which is also common practice for field measurements (Turnipseed and Sauer, 2010; Rhoads, 2020). For each segment i, the partial discharge is calculated by multiplying the depth-averaged flow velocity $\bar{v}_i(t,x)$ calculated for the segment and its cross-sectional wetted area $A_i(t,x)$. Both parameters vary over time depending on the water level at the cross-section $h(t,x)$. The final discharge at the cross-section is the sum over all the vertical segments:

$$Q(t,x) = \sum_{i=1}^{n} \bar{v}_i(t,x) \cdot A_i(t,x) \tag{1}$$

We calculate the depth-averaged river flow velocity within a segment using the Gauckler–Manning–Strickler equation (Manning, 1891):

$$\bar{v}_i(t,x) = k_i(t,x) \cdot R_i(t,x)^{\frac{2}{3}} \cdot I(t,x)^{\frac{1}{2}} \quad \text{with} \quad R_i(t,x) = A_i(t,x)/P_i(t,x) \tag{2}$$

where $k_i(t,x)$ is the Strickler roughness coefficient (the inverse of Manning's n), whose larger magnitude leads to a more stable optimization compared to the small values of Manning's n. $I(t,x)$ is the water surface slope, and $P_i(t,x)$ is the wetted perimeter of the segment. Note that $P_i(t,x)$ only includes the riverbed of the vertical segment and not the boundaries to the adjacent segments. For the nearly rectangular segments in the center of the cross-section, this is identical to replacing the hydraulic radius $R_i(t,x)$ with the depth of the vertical segment, as studied by Song et al. (2017). However, using the hydraulic radius improves the generality of the approach because it is recommended for channels with small width-depth ratios or complex geometry such as vertical segments close to the river bank (Julien, 2018; Song et al., 2017; Wei et al., 2023). Fig. 1 depicts two schematic cross-sections and the cross-sectional parameters per vertical segment. Except for $k_i(t,x)$, and the depth and shape of the cross-section below the minimum observed water level, all parameters can be derived from remote sensing data.

We calculate $k_i(t,x)$ using a base Strickler value $k_B(x)$ and the reach sinuosity $s(x)$ at the cross-section:

$$k_i(t,x) = \frac{k_B(x)}{d \cdot s(x)} \quad \text{with} \quad d = \begin{cases} \left(d_i(t,x)/d_0\right)^{-\epsilon} & \text{if } d_i(t,x) > d_0 \\ 1, & \text{otherwise} \end{cases} \tag{3}$$

where d is a parameter to adjust the roughness for the flow depth so we can account for different surface types across the cross-section, and $s(x)$ is the sinuosity, which accounts for the increased resistance caused by meandering (Chow, 1959). Variations in $s(x)$ along the studied reach introduce additional constraints to the problem, which aids in finding an optimal solution. The concept of a roughness coefficient depending on depth and sinuosity has been successfully demonstrated in previous studies that have estimated discharge from remote sensing data (Bjerklie et al., 2018; Bjerklie, 2007). To calculate d, we apply a method proposed by Jain et al. (2004), which requires the section's depth $d_i(t)$ and the parameters d_0 and ϵ. d_0 is the minimum depth below which the roughness is assumed to be constant, and ϵ is the drag coefficient. In contrast to the fixed relationship used by Bjerklie et al. (2018), the parameters of Eq. (3) are adjusted during optimization. Fig. 2 shows the depth-dependent Strickler roughness coefficient as calculated with Eq. (3) for example values of the $d_0, \epsilon, k_B(x)$, and $s(x)$ parameters. In summary, we calculate the roughness coefficient $k_i(t,x)$ from the parameters $k_B(x), s(x), d_i(t,x), d_0$, and ϵ from which only $s(x)$ can be derived from remote sensing data and the remaining parameters must be inferred from the optimization.

In the following sections, we derive the observable parameters for Eq. (2) ($I(t,x)$ and partially $R_i(t,x)$) from satellite altimetry and

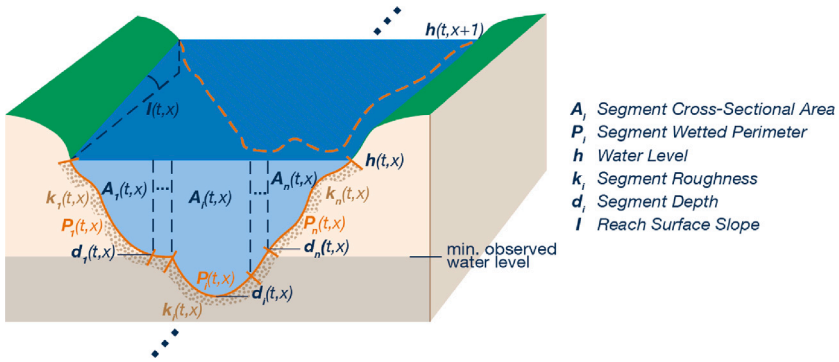

Fig. 1. Schematic cross-sections with required parameters per vertical segment. Note that the width of the segments is exaggerated in relation to the depth.

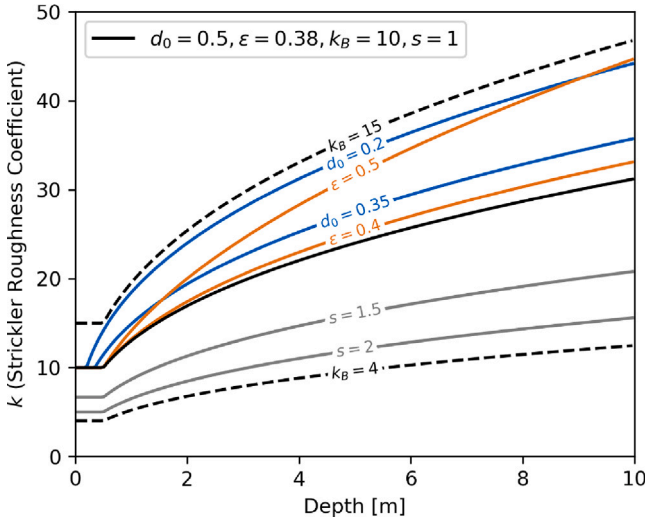

Fig. 2. Depth-dependent Strickler roughness coefficient for a set of example parameters (solid black) at the bounds of s, d_0, and ϵ, and variations in the base value k_B (dashed black), sinuosity s (gray), d_0 (blue), and ϵ (orange). (For interpretation of the references to color in this figure legend, the reader is referred to the web version of this article.)

remote sensing observations for multiple consecutive cross-sections. Fig. 3 shows a flowchart of these first steps. In Section 2.3, we obtain the water level time series which is used in Section 2.4 to find representative satellite images for high and low flows and the range between. Section 2.4 also describes the water classification. The resulting binary water masks are combined with the water level time series using a fitted hypsometric function to construct the observed river bathymetry raster.

Two optimization steps follow the construction of the observable river bathymetry. In Section 2.6, we optimize the shape of the cross-sections below the baseflow (minimum observed water level) to get $d_i(t,x)$ and the entire $R_i(t,x)$. Then, in Section 2.7, we optimize the roughness parameters $k_B(x)$, d_0, and ϵ to obtain a set of roughness coefficients $k_i(t,x)$ that minimize the difference in discharge between all cross-sections. Fig. 4 shows a flowchart of these two sections.

2.1. Framework: SWOT mission river database

The basic framework for our approach is the "SWOT Mission River Database" (SWORD) (Altenau et al., 2021a,b) version 15. SWORD provides vectorized river centerlines divided into ~10 km long reaches and nodes with a spacing of ~200 m along the centerlines. The vectors are derived from the 30 m resolution "Global River Widths from Landsat" (GRWL) data set (Allen and Pavelsky, 2018). In our study, we use the SWORD nodes within a given "Area Of Interest" (AOI) to define the locations x of the m cross-sections. The number of cross-sections (m) depends on the size of the AOI. We manually remove irregular cross-sections (e.g., cutoff at the edge or not aligned with the neighboring cross-sections). The AOI should comprise a uniform or gradually varied river section without significant lateral inflows so the discharge can be assumed constant. Choosing a straight river section increases the probability of a uniform or gradually varied channel shape, which is required for the flow law inversion and is easier to reconstruct from remote sensing data than a strongly curved section, where a river can naturally and severely erode its own bed (Scherer et al., 2020). SWORD reaches are designed to not incorporate major tributaries, and we set up the AOI to be smaller than a typical SWORD reach (i.e., < 10 km chainage) at which McFLI approaches are commonly applied (Durand et al., 2023). Hence, we consider the assumption of mass conservation within the AOI to be valid. SWORD includes many hydrological and morphological attributes, such as the node-scale river sinuosity, which we use as $s(x)$ in Eq. (3). Based on the location of the consecutive up- and downstream nodes, we calculate each node's normal along which we extract the cross-sectional geometry (see Section 2.6). The normal width is derived from the SWORD nodes' river width attribute.

2.2. Slope: ICESat-2 river surface slope

We use the "ICESat-2 River Surface Slope" (IRIS) (Scherer et al., 2023) dataset version 2 as input for $I(t,x)$ in Eq. (2). IRIS contains average and extreme water surface slopes for each SWORD reach. The water surface slope is derived from water level measurements by the photon-counting "Advanced Topographic Laser Altimeter System" (ATLAS) lidar sensor onboard the "Ice, Cloud, and Land Elevation Satellite 2" (ICESat-2). ATLAS measures along six parallel lidar beams, which, in combination with ICESat-2's 91-day repeat orbit at an inclination of 92°, results in thorough spatial coverage, such that 89% of all SWORD reaches flagged as "*river*" or "*lake_on_river*" are covered by IRIS. However, due to the orbit configuration and clouds that ATLAS cannot penetrate, the temporal resolution is relatively low. Therefore, IRIS cannot be used as a time-variable slope input, and we assume $I(t,x)$ to be constant in time due to the lack of suitable data. The IRIS water surface slope is determined across pairs of beams or along individual beams, depending on the intersection angle of spacecraft orbit and river centerline (Scherer et al., 2022). We use the "*avg_combined_slope*" value, which combines the result of both approaches as an average over all observations. Additionally, we use extreme values "*min_combined_slope*" and "*max_combined_slope*" observed over time when calculating the confidence interval.

2.3. Water level: Database for hydrological time series of inland waters

The resulting discharge is based on water level time series from DGFI-TUM's "Database for Hydrological Time Series of Inland Waters" (DAHITI) (Schwatke et al., 2015). Water levels of DAHITI are derived

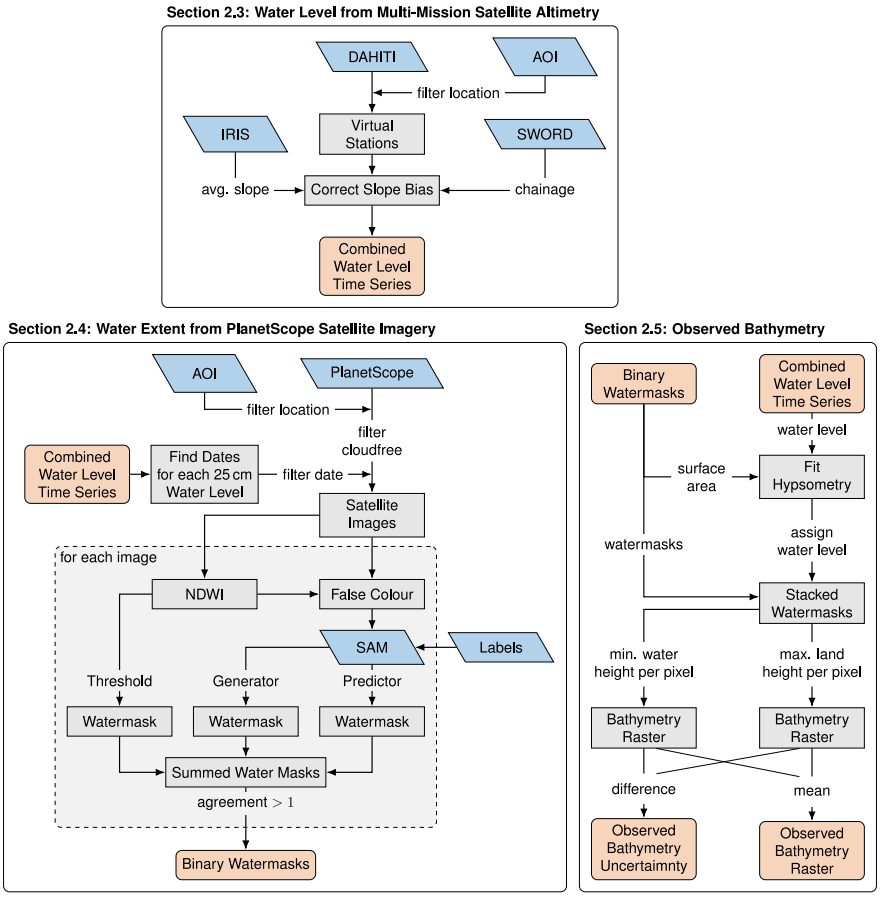

Fig. 3. Flowchart of Section 2.3 to 2.5 summarizing the steps to obtain the observable part of the river bathymetry.

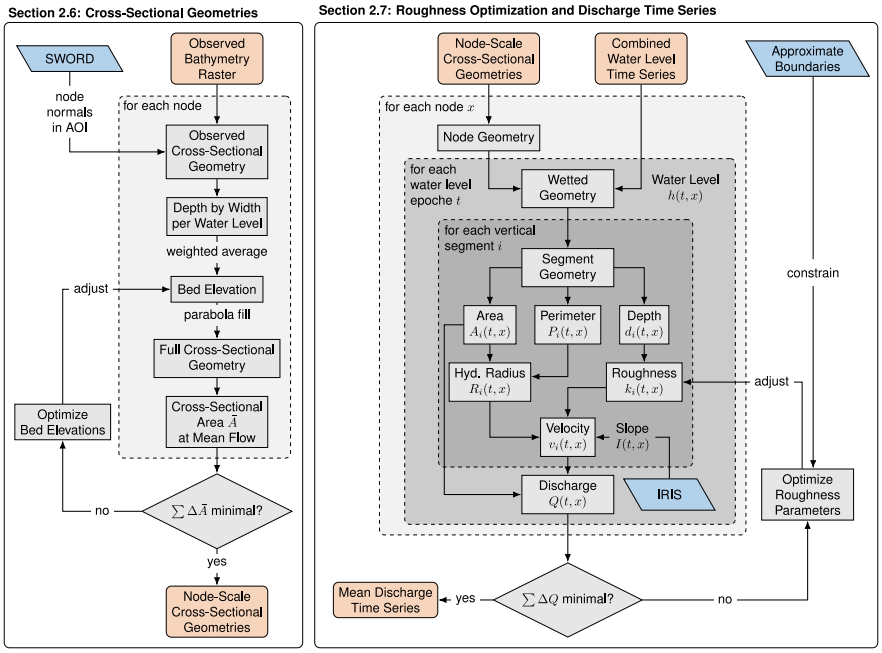

Fig. 4. Flowchart of Sections 2.6 and 2.7 summarizing the optimization of the cross-sectional geometries and the roughness parameters.

from numerous satellite altimetry missions at so-called virtual stations where the satellite's ground track intersects a lake or river. Data from virtual stations are available worldwide but are limited by the orbit configuration of the satellites and the measurement geometry of the sensors, which only measure in the nadir direction (Dettmering et al., 2020). The orbit configuration also affects the temporal resolution of the water level time series, which are between 10 days (Jason-1/2/3, Sentinel-6A) and 35 days (Envisat) for the missions used in

this study. Pulse-limited or low-resolution mode (LRM) radar altimeter sensors are most suitable for rivers wider than 200 m. For smaller rivers, measurement errors, mainly caused by topography contamination of the large radar footprint, often exceed decimeters (Calmant et al., 2016; Schwatke et al., 2015; Sulistioadi et al., 2015). For narrower rivers, missions equipped with synthetic aperture radar (SAR), interferometric SAR (SARIn), or light detection and ranging (lidar) sensors are capable of measuring the water level with high accuracy (Halicki and Niedzielski, 2022; Cooley et al., 2021; Lao et al., 2022). In this study, we use virtual stations from the Envisat (LRM), Jason-1/2/3 (LRM), Sentinel-3A/B (SAR), and Sentinel-6A (LRM) missions, depending on the river width. The quality of the water level time series at virtual stations strongly depends on the surrounding topography and the intersection angle (Schwatke et al., 2015).

The satellite altimetry data processed in DAHITI are extracted from the "Open Altimeter Database" (OpenADB) (Schwatke et al., 2023). DAHITI applies extensive automatic outlier detection and Kalman filtering. DAHITI water level time series are corrected for the wet and dry atmosphere, ionosphere, solid Earth and pole tides, and inter-mission biases from a multi-mission cross-over analysis (Bosch et al., 2014; Schwatke et al., 2015). In addition to the standard corrections applied in DAHITI, we correct the water levels for the slope bias caused by the satellites' slightly shifting ground tracks over the sloped river (Scherer et al., 2022; Halicki et al., 2023). To calculate the slope bias, the distance along the SWORD centerline between each orbit's intersection to a defined reference point is multiplied by the average water surface slope from IRIS. In this way, we can also bin observations from multiple virtual stations within an AOI to a combined reach-scale time series $h(t, x)$. Note that $h(t, x)$ is thus constant in space across the cross-sections x. This affects only the bathymetry and cross-sectional geometry but not the slope, which is based on the reach-scale IRIS data. Possible uncertainties of this bias correction caused by ambiguous crossings (i.e., a bending river reach is crossed multiple times by one satellite track) are added to the uncertainties provided by DAHITI. We use the combined uncertainties to calculate the confidence interval in Section 2.8.

2.4. Water extent: PlanetScope satellite imagery

In previous studies, we used multispectral satellite imagery from the Landsat and Sentinel-2 missions to determine the time-variable water surface extents of rivers and lakes as well as the water bodies' bathymetry (Schwatke et al., 2019; Scherer et al., 2020; Schwatke et al., 2020). However, the ground sample resolutions of these missions are limited to 30 m (Landsat) and 10 m (Sentinel-2). Here, we apply 3 m resolution PlanetScope scene tiles (Planet Labs PBC, 2022). Besides the significantly improved spatial resolution, which allows us to detect smaller changes and narrower rivers, the near-daily temporal resolution (Roy et al., 2021) of the current PlanetScope constellation of approximately 130 CubeSats increases the probability of monitoring the surface water extent at water level extremes and acquiring cloud-free images with a minimum time interval to the altimetry observations. However, in contrast to Landsat and Sentinel-2, PlanetScope data are not freely available, and with a basic research license, only a limited quota is available for download per month. Therefore, we download only the minimum number of images required to observe approximately each 25 cm step between the minimum and maximum water level. Because of the small number of obtained images, gap-filling approaches based on a large number of long-term surface water observations (Schwatke et al., 2019) cannot be applied. Furthermore, the water classification used by Schwatke et al. (2019) cannot be applied to the PlanetScope scenes as the classification is designed for multispectral images that include two shortwave infrared bands. However, the PlanetScope scenes used here do not include shortwave infrared bands.

To classify water, we first calculate the "Normalized Difference Water Index" (NDWI) (McFeeters, 1996) in each PlanetScope scene based on the green and near-infrared bands. Then, we apply three different approaches to obtain three binary land–water masks. The first approach is based on a simple NDWI threshold and the two other approaches use the "Segment Anything Model" (SAM) (Kirillov et al., 2023) software, an artificial intelligence model trained with over 1 billion masks on 11 million images. Although SAM was most probably not trained on water masks and satellite imagery, its zero-shot transfer capabilities based on minimal user inputs are sufficient for our study (Osco et al., 2023), and SAM is also already used in the segment-geospatial package (Wu and Osco, 2023). All approaches require the user to define one or more label points to specify the water body of interest. Additionally, the "SAM Predictor" approach can be improved by user-defined label points inside and outside the water body of interest. SAM does not work with multispectral images and instead requires a 3-band image. However, we do not apply a typical red, green, and blue combination. Instead, we use the infrared, the previously calculated NDWI, and the red band for both SAM approaches because this combination shows high contrast between water and non-water areas. The three classification approaches are:

NDWI Thresholding: Using the PeakUtils software (Negri and Vestri, 2017), we determine the pixel values of the land and water peaks in the NDWI histogram. We use the mean pixel value between both peaks as the threshold to distinguish between land (<threshold) and water (>threshold), similar to Schwatke et al. (2019). A connected-component labeling algorithm (Weaver, 1985) is applied to label each water body in the binary water mask. The label of the water body of interest is defined by the first user-defined label point so that an isolated water mask of the river can be created.

SAM Predictor: The "SamPredictor" class of SAM automatically creates a binary water mask showing only the river of interest using the user-defined label points within and outside the river surface. In contrast to the NDWI thresholding approach, no further labeling algorithm is required to identify connected-components. However, the classification can be refined by additional user-defined label points.

SAM Generator: The "SamAutomaticMaskGenerator" does not require label points for classification but automatically generates masks for every detected feature. However, one label point is still required to determine the feature containing the river surface after classification. We define a minimum feature size of 10% of the AOI area.

After applying the three approaches, we sum up the three binary water masks of the river. This results in an image with four classes: 0 (land), 1 and 2 (mixed result), and 3 (river). To ensure the robustness of our method, we require that at least two of the classification approaches match. Hence, we accept every pixel with a value of 2 or 3 to create our final river water mask for each PlanetScope scene.

2.5. River bathymetry

Following Schwatke et al. (2020) and Scherer et al. (2020), we fit a modified hypsometric Strahler function (Strahler, 1952) to the DAHITI water level (h) and synchronous surface area (a) from the classified PlanetScope scenes within the AOI:

$$h(a) = \left[\frac{a_{min} - a}{a_{min} - a_{ip}} \cdot \frac{a_{max} - a_{ip}}{a_{max} - a}\right]^{z} \cdot h_{scale} + h_{min} \quad (4)$$

where a_{min} and a_{max} define the minimum and maximum surface area, h_{min} the minimum water level, and h_{scale} the water level variation. z and a_{ip} describe the shape of the curve and the abscissa of its inflection

point, respectively. h_{min} must be selected by the user, whereby the fitting quality must be assessed. h_{min} does not represent the final river bed elevation of the cross-sectional geometry but is only used for fitting the hypsometry. In contrast to previous studies (Scherer et al., 2020; Schwatke et al., 2020) using Landsat and Sentinel-2 data with a time lag of several days, the time lag between water level and the frequent surface area observations from PlanetScope is much smaller and often shorter than one day. However, fitting the hypsometric function is still useful to reduce the influence of water level errors, interpolate the water level in case there is a time lag of a few days caused by cloud cover, and detect surface area outliers caused by rare errors (i.e., over- or underestimation of the water surface extent) of the water classification (Section 2.4). Such outliers are removed manually.

Each water mask is assigned a water level based on the hypsometry, and the masks are sorted accordingly. The pixels in all masks are aligned, and a bathymetry raster is constructed by using the water level of the lowest water classification that occurs for each pixel column. Additionally, a second bathymetry raster is derived from the elevation of the maximum land classification per pixel column. Usually, the two rasters disagree due to changes in the river bed or classification errors. We use the mean of both rasters to derive the main cross-sectional geometry, and the difference between the minimum and maximum is used in the uncertainty estimation (Section 2.8). This process and the difference between the bathymetry rasters is depicted in Fig. A.1 in the appendix. Note that the resulting raster contains only the bathymetry above the minimum observed water level. The part underneath is constructed in Section 2.6.

2.6. Depth optimization and cross-sectional geometry

Our approach requires multiple cross-sectional geometries at the location of m consecutive SWORD nodes (x). We extract the geometries along each node's normal from the previously constructed mean river bathymetry raster. However, these geometries are incomplete below the minimum observed water level, and the geometry below the baseflow is estimated as follows. We calculate the cross-sectional width $w(h,x)$ for each water level h from the geometry at the cross-section x and then estimate the depth $d(h,x)$ following Scherer et al. (2020) using an empirical width-to-depth relationship derived from observations by Moody and Troutman (2002):

$$d(h,x) = 0.27\left(\frac{w(h,x)^2}{7.2^2}\right)^{0.39} \tag{5}$$

By subtracting $d(h,x)$ from h, we get multiple estimates for the river bed elevation $h_0(h,x)$. To obtain an average river bed elevation per cross-section $h_0(x)$, we weight these results by

$$\text{weight} = \frac{h_{max} - h}{h_{max} - h_{min}} \tag{6}$$

with h_{max} and h_{min} being the maximum and minimum observed water level. In this way, the estimates based on low flows have the greatest weight. This reduces the possibility of overestimation caused by large widths at high flows when the river could exceed its banks during a flood. However, the estimated river bed elevations may vary significantly and unrealistically between consecutive cross-sections. Therefore, we optimize the bed elevations bounded by the minimum and maximum estimates to minimize the differences between the cross-sectional areas at the mean water level. For this optimization, we use a parallel version (Gerber and Furrer, 2019; Gerber et al., 2023) of the "limited-memory Broyden–Fletcher–Goldfarb–Shanno algorithm with box constraints" (L-BFGS-B) (Byrd et al., 1996; Broyden, 1970; Fletcher, 1970; Goldfarb, 1970; Shanno, 1970) because it is particularly suitable for solving large optimization problems (in this study we need to solve up to 31 unknowns) and can handle boundary constraints which we require (Byrd et al., 1996). BFGS is a quasi-Newton method that considers gradient changes of the objective function, with the distinctive feature that it efficiently approximates the Hessian matrix instead of calculating the true Hessian matrix (Nocedal and Wright, 2006). The efficient and parallel L-BFGS-B approach allows us to use very approximate boundary conditions and calculate many iterations within a reasonable time.

Finally, the gap in the geometry below the minimum observed elevation and the optimized river bed elevation $h_0(x)$ is filled by a parabola (Bjerklie et al., 2018; Scherer et al., 2020). The minimum and maximum of all optimized river bed elevations are used in the uncertainty estimation (Section 2.8). As recommended by Boyer (1964), we divide the geometry at each cross-section x into $n = 30$ segments. For each segment i, we obtain the cross-sectional geometry parameters $A_i(t,x)$, $P_i(t,x)$, and $d_i(t,x)$ based on the water level $h(t,x)$ from satellite altimetry.

2.7. Roughness optimization and discharge time series

The discharge time series is based on the timestamps and heights of the water level time series, which is used to obtain the time variable cross-sectional geometric parameters at each node x. In contrast to the slope $I(t,x)$ and the cross-sectional geometry parameters $A_i(t,x)$ and $P_i(t,x)$, the roughness coefficient $k_i(t,x)$ and its parameters $k_B(x)$, d_0, and ϵ (cf. Eq. (3)) cannot be derived from remote sensing data. However, based on the principle of mass conservation and assuming steady flow conditions, we can assume that the reach-scale discharge at each timestamp t is constant across all cross-sections x within the selected AOI. Therefore, a set of roughness parameters must be found that minimizes the square sum of discharge differences between the cross-sections over the entire time series. This constraint is formulated by the following objective function, which we minimize using the parallel L-BFGS-B optimization algorithm (cf. Section 2.6) to obtain the optimal set of values for $k_B(x)$, d_0, and ϵ:

$$\min_{\dot{\mathbf{k}}} \frac{max(k_B)}{min(k_B)} \sum_{a=1}^{m} \sum_{b=1,a\neq b}^{m} \left(\frac{1}{\bar{Q}(a)} \sqrt{\frac{1}{l} \sum_{t=1}^{l} (Q(t,a) - Q(t,b))^2} \right)^2 \tag{7}$$

where l is the number of all timestamps t in the water level time series, m is the number of cross-sections at which the discharge Q is estimated, and a and b are pairs of cross-sections between which the root mean square difference is calculated and normalized by the mean discharge $\bar{Q}$ at cross-section a. The function is minimized with respect to the parameter vector $\dot{\mathbf{k}}$, which contains the roughness parameters $k_B(x)$ for each of the m cross-sections as well as d_0 and ϵ:

$$\dot{\mathbf{k}} = (k_B(a), \ldots, k_B(m), d_0, \epsilon) \tag{8}$$

The score of the optimization function is the summed squared normalized root mean squared discharge deviation between all cross sections. Without normalization, the optimization would lead to solutions with the lowest average discharge. The objective function score is scaled by the ratio of the maximum ($max(k_B)$) and minimum ($min(k_B)$) occurring base roughness parameter per run to avoid unrealistic rapid changes of the roughness within the reach. Note that there might be multiple local minima in the objective function. Therefore, the user can define the bounds for $\dot{\mathbf{k}}$ to improve the optimization. Following Jain et al. (2004), the bounds of d_0 and ϵ are $0.2 <= d_0 <= 0.5$ and $0.38 <= \epsilon <= 0.5$ by default. Approximate bounds must be given for k_B, which can be taken from published empirical values like Lecher et al. (2021). Typical values for natural rivers range from 10 (high friction) to 50 (low friction). However, because of the resource-efficient and parallel L-BFGS-B algorithm, the optimization works with a large range between the k_B bounds, so these can be given loosely. We obtain the final reach-scale discharge time series by taking the daily mean discharge of all cross-sections' results of the optimal solution.

For the uncertainty estimation, we calculate the Hessian matrix, which describes the curvature of the optimization function at the location of the optimum parameters. In contrast to the L-BFGS-B, we obtain

the Hessian matrix using finite difference, which is computationally more expensive but provides a more accurate representation of the Hessian matrix. We derive the covariance matrix as the inverse of the Hessian and obtain the standard deviation of each base roughness value $k_B(x)$ from the squared diagonal values of the covariance matrix. These standard deviations and the minimum and maximum bounds of d_0 and ϵ are considered for the uncertainty estimation in Section 2.8.

2.8. Uncertainty estimation

We use the uncertainties of each previously estimated parameter to derive the total discharge uncertainty range and assess the influence of each individual parameter. We run the optimal solution (standard run) from Section 2.7 and vary the following parameters individually:

Water Surface Slope: In contrast to the standard run, where we apply the IRIS "*avg_combined_slope*", we use the "*min_combined_slope*" and "*max_combined_slope*" values to estimate the uncertainties resulting from the time-variable water surface slope.

Water Level: The DAHITI water level time series contain processing uncertainties, e.g., from Kalman filtering. Additionally, the crossing position of the satellite ground track with the river centerline can be ambiguous when there are multiple intersections with a bending river. In this case, we add an error based on the distance between the possible crossing position and the IRIS water surface slope. For the uncertainty estimation, we add and subtract these water level uncertainties to the DAHITI water levels before rerunning the optimal solution.

Bathymetry: In Section 2.5, we obtain three different bathymetry rasters, which represent the minimum water, maximum land, and mean occurring hypsometric water level per pixel. Differences between these rasters can occur because of water misclassifications by SAM. The mean raster is used in the standard run, and the minimum water and maximum land rasters are used to estimate the uncertainty resulting from the water classification, hypsometry fitting, and the time-varying river bed.

Cross-Sectional Geometry: We optimize the river bed elevation $h_0(x)$ for each cross-section x (Section 2.6). Depending on the uniformity of the studied river reach, $h_0(x)$ varies between the cross-sections. We conduct two runs, one with all $h_0(x)$ set to the minimum estimated river bed elevation and the other one with them set to the maximum estimated value across all cross-sections.

Roughness Parameters: As described in Section 2.7, the standard deviations of $k_B(x)$ and the minimum and maximum boundaries of d_0 and ϵ are propagated to the uncertainty estimation. We conduct two runs using the respective minimum and maximum values (for $k_B(x)$ with subtracted and added standard deviations) to estimate the discharge uncertainty introduced by the roughness optimization.

Total Uncertainty Range: In addition to the individual runs with single parameters varied, we conduct two runs using the minimum and maximum values across all parameters listed above. This represents the worst cases of over- or underestimated discharge.

The uncertainty range is not equivalent to a statistical error propagation but is computed using an ensemble of multiple computations with different parameter configurations based on the maximum observed uncertainty of these parameters. For each timestamp t, we take the 5th and 95th percentile of all the listed runs to estimate the 90% uncertainty range $Q_\epsilon(t)$. This 90% percentile range is selected based on the empirical analysis discussed in Section 3.5.

2.9. Validation

To validate the resulting discharge time series, we compare them to daily discharge data obtained from the GRDC, the ADO (Alpine Drought Observatory, 2023), and the "National Water Dashboard" by the U.S. Geological Survey (2023). We calculate the "Root Mean Squared Error" (RMSE), the RMSE normalized by the range between the minimum and maximum true data (NRMSE), the squared "Pearson Correlation Coefficient" (R^2), and the "Nash–Sutcliffe Model Efficiency Coefficient" (NSE). Furthermore, we calculate the confidence coverage probability (CP) of the results, i.e., the percentage of true data points within the 90% uncertainty range.

In addition to the validation against in-situ measurements, we calculate a "Coefficient of Variation" (CV), which shows the average proportion of the uncertainty range from the maximum range of the discharge signal. The CV is defined as follows:

$$\mathrm{CV} = \frac{1}{l}\sum_{t=1}^{l}\frac{Q_\epsilon(t)}{Q_{max} - Q_{min}} \tag{9}$$

where l is the number of observations, $Q_\epsilon(t)$ is the 90% uncertainty range (cf. Section 2.8), and Q_{min} and Q_{max} are the minimum and maximum values of the resulting discharge time series. High CV values represent lower reliability of the time series signal and a more volatile result. In contrast, low CV values are desirable as they suggest that the signal exceeds the uncertainty range.

3. Results and discussion

We apply our approach to 27 globally distributed study sites to examine its accuracy and applicability for estimating river discharge from remote sensing data without calibration. The locations of the study sites are shown in Fig. 5. Fig. A.2 in the appendix shows the studied sites in more detail. They are chosen according to the availability of in-situ discharge stations (for validation) and their temporal overlap with remote sensing data. Water level observations from satellite altimetry are only available at the intersections of the satellite ground track with a river. Depending on the mission and river geometry, these intersections can be hundreds of kilometers apart or unsuitable for a virtual station. For meaningful validation, the in-situ station must be connected to a virtual station without obstructions or significant confluences in between. Additionally, the number of study sites is limited by our PlanetScope download quota. We select the sites to represent rivers of different mean annual discharge and width. Rivers surrounded by dense forests cannot be observed, and we do not investigate arctic rivers due to cloud, ice, and snow coverage. Most of the rivers are located in temperate, tropical, or arid climate zones. All studied reaches are non-braided meandering, as classified by Nyberg et al. (2023). Braided rivers can change dramatically over time, causing significant errors in the derived river bathymetry. Additionally, the empirical width-to-depth relationship used in Section 2.6 tends to significantly overestimate the river depth of braided rivers.

Table 1 lists all studied reaches by river name and includes the error metrics, the number of validation samples, the coverage probability (CP) and coefficient of variation (CV), the optimal d_0 and ϵ parameters of the roughness coefficient, the mean discharge during the studied period ($\bar{Q}$, from GRDC or USGS), the reach width and chainage (from SWORD), the available satellite altimetry missions, the SWORD reach ID, the chainage distance (Length) between the most up- and downstream cross-sections, the number m of cross-sections, and the k_B bounds given to the optimization algorithm. The mean in-situ discharge of the studied reaches is between 37 and 1648 m^3/s. The studied reaches are between 63 and 349 m wide and between 0.8 and 15.4 km long. The median RMSE, NRMSE, NSE, and R^2 are 132 m^3/s, 12%, 0.560, and 0.77, respectively. The NRMSE aligns with the expected uncertainty of SWOT discharge of less than 30% in ungauged basins (Durand et al., 2023). However, the requirement of

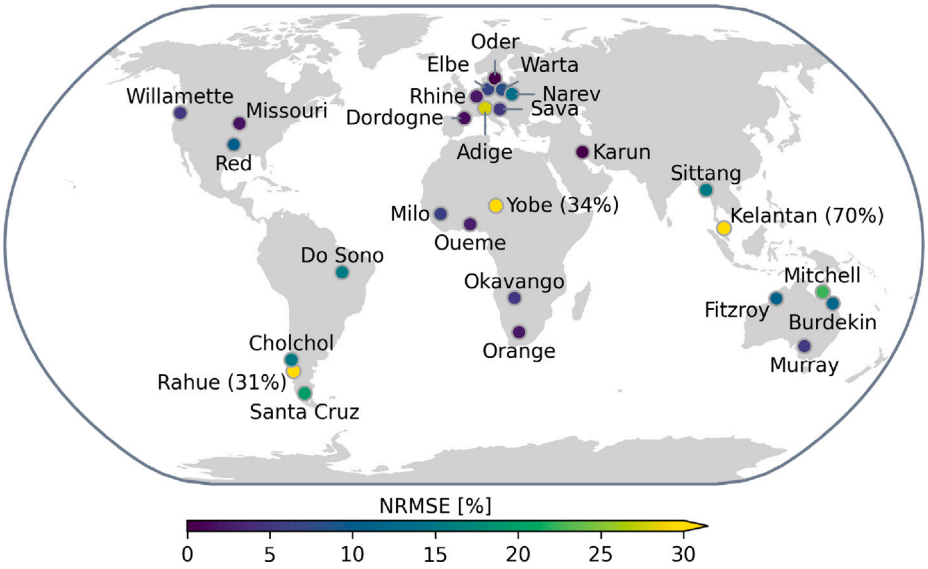

Fig. 5. Location and NRMSE of the studied reaches. Values exceeding 30% are shown in brackets.

Table 1
Studied river reaches with error metrics, number of validated samples (n Val.), coverage probability (CP), coefficient of variation (CV), reach-scale roughness parameters (ϵ and d_0), mean discharge ($\bar{Q}$), used satellite altimetry missions (ENV: Envisat, J1/2/3: Jason-1/2/3, S3A/B: Sentinel-3A/B, S6A: Sentinel-6A), number of cross-sections (m), base roughness parameter bounds (k_B), width, length, and chainage.

River	RMSE [m^3/s]	NRMSE [%]	NSE	R^2	n Val.[a]	CP [%]	CV [%]	ϵ	d_0	$\bar{Q}$ [m^3/s]	Width [m]	Chainage [km]	Missions[b]	SWORD Reach ID	Length [km]	m	k_B Bounds
Adige	162	28	−1.088	0.49	43	14	30	0.40	0.40	159	63	289	S3B	21404000301	1.0	6	25 – 40
Burdekin	132	16	0.266	0.50	92	78	25	0.40	0.40	288	263	60	S3A	56321000075	10.1	11	10 – 40
Cholchol	70	18	0.420	0.95	42	100	62	0.40	0.40	120	100	91	S3A	66210800101	3.4	18	20 – 40
Do Sono	194	18	−0.460	0.73	110	80	13	0.40	0.40	660	154	1359	J2/3, S6A	62444300121	4.0	19	15 – 40
Dordogne	74	7	0.851	0.83	217	99	43	0.40	0.40	231	104	123	J3, S6A	23216000411	4.0	21	10 – 40
Elbe	218	11	0.560	0.96	281	99	68	0.40	0.40	611	270	213	J2/3, S6A	23281000271	4.6	6	5 – 25
Fitzroy	211	15	−0.036	0.55	145	4	9	0.50	0.40	246	80	448	J2/3, S6A	56220300181	5.8	29	5 – 30
Karun	74	6	0.703	0.68	146	100	76	0.40	0.40	478	236	596	J2/3, S6A	29420300251	2.0	10	10 – 40
Kelantan	1032	70	−9.387	0.71	69	0	128	0.40	0.40	485	260	90	J2/3, S6A	44403800091	0.8	5	15 – 50
Milo	72	11	0.871	0.75	47	45	27	0.50	0.40	136	102	4198	S3A	14298200091	2.8	13	5 – 40
Missouri	280	7	0.855	0.88	152	100	59	0.40	0.40	1273	210	2967	ENV, S3A	74293900061	1.4	8	25 – 55
Mitchell	240	24	−1.412	0.81	419	3	41	0.40	0.40	211	94	106	J1/2/3, S6A	56298300081	4.0	10	20 – 50
Murray	173	10	0.361	0.52	523	92	69	0.40	0.40	146	123	717	J2/3, S6A	56410700021	1.0	6	5 – 30
Narev	41	17	0.483	0.76	52	87	44	0.40	0.40	89	87	540	S3A	24248000081	1.2	7	15 – 50
Oder	101	6	0.799	0.87	637	100	119	0.41	0.40	469	245	187	J2/3, S3A/B, S6A	24221000161	3.4	18	5 – 40
Okavango	73	10	0.813	0.80	455	89	66	0.40	0.40	190	101	709	J2/3, S6A	12991004741	1.2	7	15 – 40
Orange	340	8	0.709	0.39	327	87	22	0.40	0.40	178	190	1007	J2/3, S3A, S6A	12770100821	5.8	17	5 – 30
Oueme	76	8	0.928	0.84	44	91	26	0.50	0.40	213	68	132	ENV, J2/3, S6A	14306500081	2.0	5	5 – 30
Rahue	101	31	0.243	0.75	10	50	23	0.40	0.40	241	88	94	S3A	66210200231	1.0	14	10 – 40
Red	204	14	0.639	0.90	298	99	55	0.40	0.40	285	188	1481	J3, S3B, S6A	74225000191	2.8	12	5 – 30
Rhine	247	8	0.851	0.77	78	97	39	0.40	0.40	1648	349	452	S3B	23263000051	5.0	25	10 – 40
Santa Cruz	267	22	0.465	0.98	39	100	67	0.43	0.40	748	175	319	S3A	65380000231	5.0	18	15 – 50
Sava	56	10	0.820	0.78	61	100	83	0.40	0.40	262	83	2072	S3A	22740900101	1.6	9	10 – 50
Sittang	135	18	0.547	0.66	71	85	65	0.40	0.40	309	177	281	ENV, S3A	44560100411	4.2	15	5 – 40
Warta	47	12	0.611	0.96	96	99	37	0.42	0.40	190	90	279	S3A/B	24223000061	2.8	15	15 – 40
Willamette	98	10	0.779	0.94	99	96	27	0.40	0.40	349	98	400	S3A	78220000231	15.3	16	20 – 40
Yobe	25	34	0.164	0.58	18	22	32	0.50	0.40	37	65	218	S3A	16245000141	1.2	6	5 – 35
Mean	176	17	0.050	0.75		75	50			380	151	720			3.6		
Median	132	12	0.560	0.77		91	43			246	104	319			2.8		

[a] Number of validated samples.
[b] ENV: Envisat, J1/2/3: Jason-1/2/3, S3A/B: Sentinel-3A/B, S6A: Sentinel-6A.

10% measurement uncertainty, which marks a breakthrough according to GCOS (World Meteorological Organization, 2022), can only be met for 7 out of the 27 studied rivers. The errors are comparable with the results of Bjerklie et al. (2018), who achieved an NRMSE of 4 and 8% and an NSE of 0.94 and 0.62 using the Manning equation at two sections of the Yukon River. Lamine et al. (2021) obtained an NRMSE of 19.7% and an NSE of 0.93 at an ephemeral of the Niger River. Both approaches use similar input data as this study but have not been transferred to other rivers and do not provide uncertainty estimates.

We use between 5 and 29 cross-sections per site. There is no correlation between the number of cross-sections and NRMSE and no clear spatial pattern in the NRMSE of the results, except for higher values for the Australian rivers (cf. Fig. 17), which are dominated by high interannual variability and highly variable flood behavior (Finlayson, 2010). The CP of true data points within the 90% confidence interval is at or above 80% for 19 out of the 27 studied reaches, with a mean coverage of 75%. Therefore, although the errors compared to in-situ data are relatively high, the uncertainty ranges are reliable to estimate the range of the true discharge. The mean and median CV values

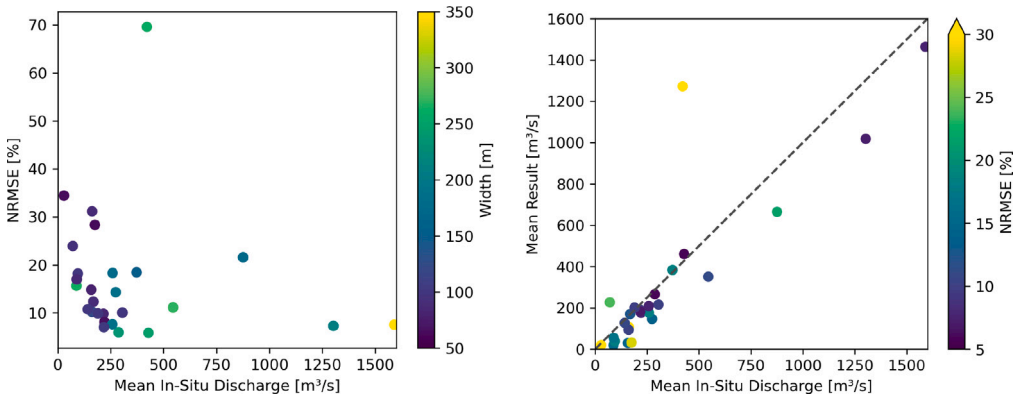

Fig. 6. Left: NRMSE by mean in-situ discharge and river width. Right: Mean discharge by mean in-situ discharge and NRMSE.

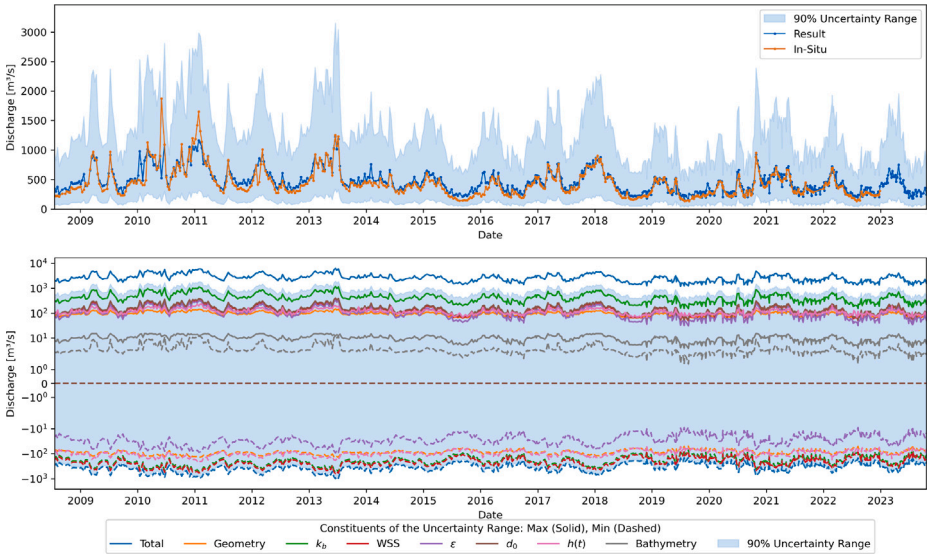

Fig. 7. Top: Discharge time series for the Oder River from this study (blue) and GRDC (orange). The 90% uncertainty range from this study is shown as a blue area. Bottom: Components of the uncertainty range. (For interpretation of the references to color in this figure legend, the reader is referred to the web version of this article.)

are about 50%, which suggests that the 90% uncertainty range is, on average, half the maximum observed amplitude.

The left panel of Fig. 6 shows the NRMSE by the mean in-situ discharge during the studied period $\bar{Q}$ and river width. There is no clear correlation between the NRMSE and $\bar{Q}$ or width. However, an NRMSE of 10% cannot be achieved below a $\bar{Q}$ of 150 m^3/s, and below 50 m^3/s, the best result is 35%. This behavior might be related to a dominant section control caused by the pooling of water, as described by Bjerklie et al. (2023), or by rapid changes in the flow parameters during flood events. In both cases, the assumptions of uniform flow and mass conservation would not be valid for the river section. The river width is not a limiting factor for the approach, as an NRMSE of 8% was achieved for the 68 m wide Oueme, one of the narrowest rivers studied. The right panel shows the mean result of this study by $\bar{Q}$ and NRMSE. The correlation between our results and $\bar{Q}$ is 0.82. Our results tend to underestimate $\bar{Q}$ for most of the studied reaches.

In the following sections, we present and discuss the results of three example rivers (Sections 3.1 to 3.3), all remaining discharge time series (Section 3.4), the uncertainty range (Section 3.5), the slope (Section 3.6), the image classification using SAM (Section 3.7), the roughness optimization (Section 3.8), and the unobserved cross-sectional geometry (Section 3.9).

3.1. Oder River

The approach yields the best results in terms of NRMSE for the 3.4 km long studied reach of the Oder River with a value of 6%, corresponding to an RMSE of 101 m^3/s. This reach also has the most available validation data, with 637 matching samples. Almost the complete water level time series from satellite altimetry data of Jason-2/3, Sentinel-6A, and Sentinel-3A/B is covered by the GRDC discharge time series that we used for validation. The 0.87 correlation of our results with the in-situ data and the NSE of 0.799 are only exceeded at a few other studied reaches.

Fig. 7 shows the resulting discharge time series for the Oder River, the validation data, and the 90% uncertainty range. The result matches the validation data well but misses isolated extreme flood events between 2010 and 2012 when PlanetScope satellite imagery was not yet available. Because similar flood events are unrepresented in the period covered by PlanetScope, the surface areas for respective extreme water levels are missing in the hypsometry. Thus, the approach is not limited to bankfull discharge but is prone to errors for water levels that did not occur during the period used to generate the bathymetry. From 2019, the noise in the resulting discharge time series increases (cf. Fig. 7). This period coincides with the beginning of the Sentinel-3B mission so that three different missions (Sentinel-3A/B and Sentinel-6A) are

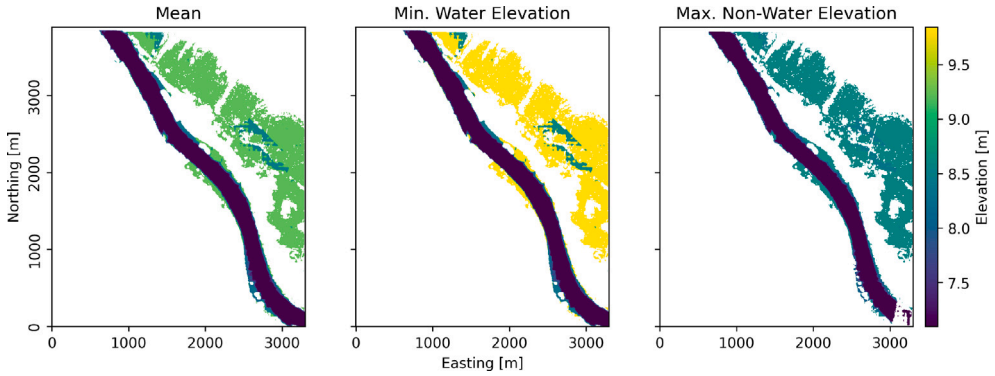

Fig. 8. The different bathymetric rasters for the Oder River are based on the maximum non-water elevation per pixel (right), the minimum water level per pixel (center), and the mean of both rasters (left), which is used for the standard run.

used. As described in Section 2.3, the water level time series from the different missions at multiple virtual stations are combined using multi-mission crossover analysis and the IRIS water surface slope. However, judging from the noise, some height bias still remains.

With a CV of 119%, the uncertainty range is, on average, larger than the maximum discharge variation. Below the time series, Fig. 7 shows the components of the uncertainty range as calculated in Section 2.8. The input uncertainties of most components are not symmetrical in the negative and positive domains. Additionally, parameters varying $A_i(t, x)$ (i.e., $h(t)$, geometry, and bathymetry) affect Eqs. (1) and (2), which leads to an exponential behavior of the uncertainties. The standard deviations of the base roughness parameters k_B have the largest influence on the confidence interval. The water surface slope (WSS) with extreme values of 31 and 219 mm/km and an average value of 129 mm/km used in the standard run has a similar effect on the confidence interval as the uncertainties of the geometry varied by the river bed elevation h_0, the roughness parameters d_0 and ϵ, and the water levels $h(t)$. The effects on the total confidence range from the different observed bathymetry rasters is less than 10 m^3/s.

Fig. 8 shows the different bathymetry rasters as computed in Section 2.5. Fine structures along the shore are visible, but the bathymetry is generally uniform, and there are also only minor differences between the three bathymetric rasters. Hence, the contribution of using different bathymetric rasters to the uncertainty range shown in Fig. 7 is insignificant. The biggest difference is the elevation of the floodplain, which is of minor importance for most dates of the discharge time series. The large adjacent floodplain is not covered by the cross-sections anyway (cf. Fig. 9).

Fig. 9 shows the location of all used cross-sections at the studied reach of the Oder River. On the right, the figure shows the cross-sectional geometries. The optimized river bed elevation $h_0(x)$ varies by ~ 1 m. Overall, the cross-sections are uniform or gradually varied, and more than half of the depth is covered by the parabola below the minimum observed water level. Isolated outliers can be identified to the left of the cross-sections at the SWORD nodes 029 and 031.

Fig. 10 shows the result for $k_B(x)$ for each cross-section x. Each iteration during the roughness optimization is shown as an individual line colored by the objective function's score, with the optimal result used in the standard run in red. The maximum and minimum k_B values from the 189 results represented by solid lines are considered in the uncertainty estimation. The variability of these results is low, with a minimum of 5 and a maximum of 10 for k_B, which leads to a small contribution to the uncertainty range, as shown in Fig. 7. Across the nodes defining the cross-sections, the variability is also low within each run, caused by the uniform cross-sections. The right labels of Fig. 10 show the roughness values converted with Eq. (3) at the maximum occurred depth of 7.35 m and a river sinuosity of 1. The figure demonstrates the loose bounds given to the optimization process. The converted values for the maximum bound exceed any literature value as it depends on the optimized values for ϵ and d_0.

3.2. Oueme River

For rivers like the Oueme, our approach is particularly beneficial. There are many similar remote and ungauged rivers with comparable characteristics. Because of the discontinuation of the in-situ time series in 2008, only 44 samples could be validated against GRDC data with an NRMSE of 8%, corresponding to an RMSE of 76 m^3/s, a correlation of 0.84, and an almost optimal NSE of 0.928. At the Oueme River, we look at two AOIs (cf. Fig. A.2) that are still close enough to assume mass conservation, with a distance between the most up- and downstream cross-section of 2 km. For the area between the AOIs, we could not obtain enough cloud-free satellite imagery. Fig. 11 shows the mean bathymetry and cross-sectional geometries for both AOIs. The bathymetry and the geometries are much less uniform compared to the Oder River (cf. Fig. 8) and instead more gradually varied. A much larger portion of the cross-sectional geometry can be constructed from satellite altimetry observations due to the large seasonality and nearly ephemeral characteristics of the Oueme River, as indicated by our results and the validation data shown in Fig. 12. The uncertainty range of our results for the Oueme River is much smaller than for the Oder River, with a CV of 26%. Again, the water surface slope contributes significantly to the uncertainty range, especially in the negative domain. The water surface slope varies from 27 to 219 mm/km, with an average value of 168 mm/km used in the standard run. The satellite altimetry errors have a similar effect on the discharge uncertainty. The variations of $k_B(x)$ between 5.0 and 7.6 and d_0 are especially significant in the positive domain of the uncertainty range. The effect of the different bathymetric rasters shows more variations throughout the different approaches compared to the Oder River, as shown in Fig. 13. Although there is no cross-section at the specific location, an island is visible in the bathymetry based on the maximum non-water elevation, which is missing in the bathymetry based on the minimum water elevation. Fig. 13 reveals further detailed differences between the two approaches and the mean bathymetric raster used in the standard run.

3.3. Willamette River

In the example of the Willamette River, we demonstrate how the user can judge the results and adjust the boundary conditions when necessary. Using the default loose bounds for $k_B(x)$ of 5 and 40, the optimization tends to yield the lowest possible values, as shown on the top of Fig. 14. However, these values lead to an almost constant low discharge, as shown on the bottom of Fig. 14. An expert user could judge this time series as wrong without in-situ data based on the expected typical seasonal variability and mean discharge of comparable rivers in similar climate regimes. Fig. 14 shows a second local minimum of the objective function and, hence, a possible optimal solution above $k_B(x)$ values of 25. Adjusting the minimum bounds to a value of 25 leads to the results shown in Fig. 15 and listed in Table 1 with an

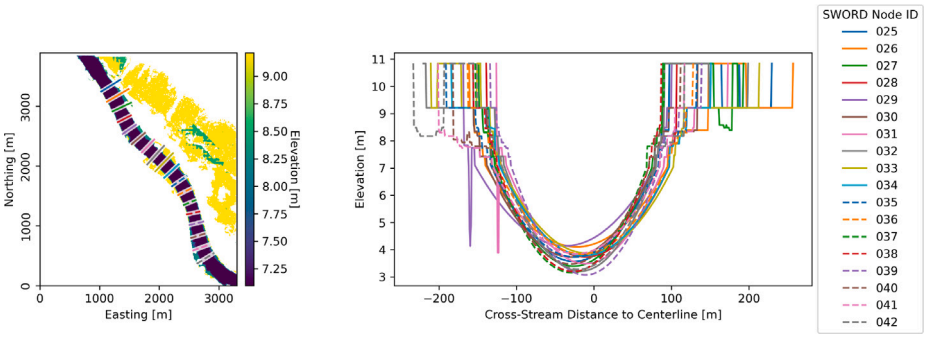

Fig. 9. Left: Location of cross sections at SWORD nodes over the mean bathymetry of the studied reach of the Oder River. Right: Geometry at each cross-section.

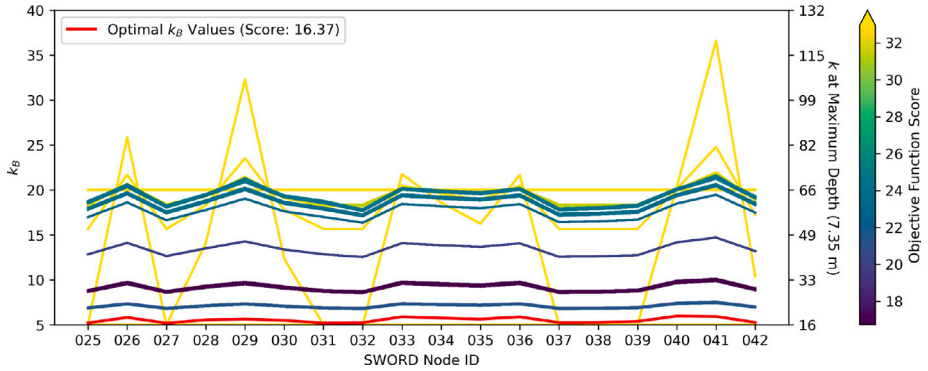

Fig. 10. k_B results of the roughness optimization by the nodes defining the cross-sections of the studied reach of the Oder River. Each line represents the result of one iteration, colored by the score of the objective function. The red line shows the optimal result. Note that many runs differ only slightly and appear as one stacked line. The labels on the right show the result of Eq. (3) at the maximum occurred depth.

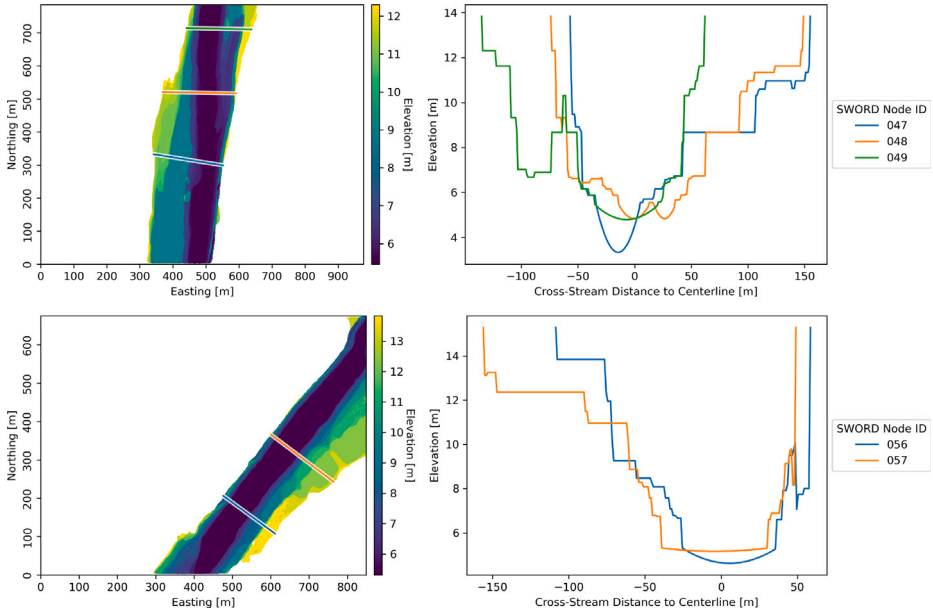

Fig. 11. Left: Location of cross-sections at SWORD nodes over the mean bathymetry of the AOIs at the studied reach of the Oueme River. Right: Geometry at each cross-section.

NRMSE of 10% and an NSE of 0.941. However, the converted roughness values at maximum depth based on Eq. (3) exceed the maximum literature values for natural channels. Therefore, the river bed elevation might be overestimated, which results in an underestimated cross-sectional area of the geometries shown in Fig. 16. As the roughness values exceed the literature values, confidence in the result would be low without validation data. A framework such as Durand et al. (2023), which integrates the results of multiple reaches, branches, and reservoirs at the basin level, would be beneficial to further improve the confidence. With 15.3 km, this reach of the Willamette River has the longest distance between the most up- and downstream cross-section of all studied reaches and is slightly longer than the average SWORD reach. However, a large section in between the two AOIs is not used because of the strong meandering (cf. Fig. A.2). Despite the length, the resulting errors are comparable to the shorter studied reaches, implying that the principle of mass is applicable to such a long reach without

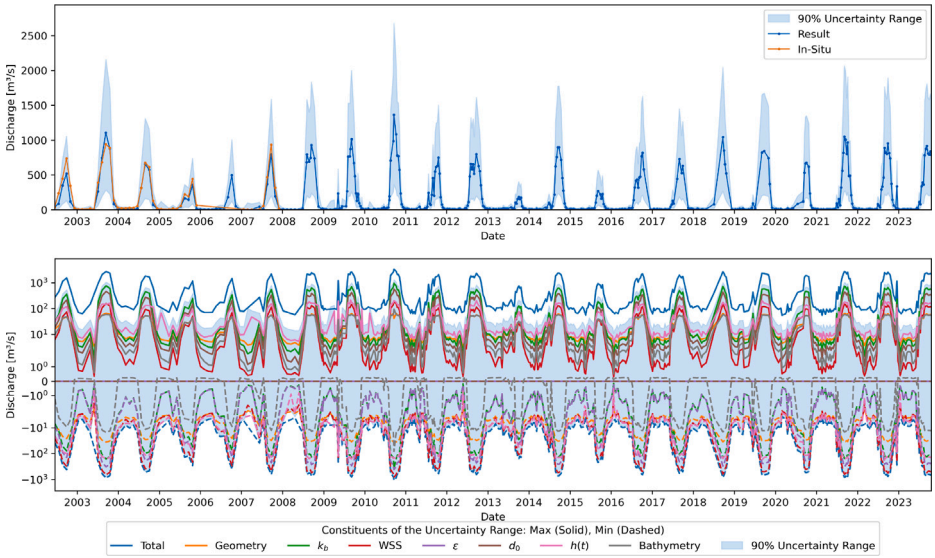

Fig. 12. Top: Discharge time series for the Oueme River from this study (blue) and GRDC (orange). The 90% uncertainty range from this study is shown as a blue area. Bottom: Components of the uncertainty range. (For interpretation of the references to color in this figure legend, the reader is referred to the web version of this article.)

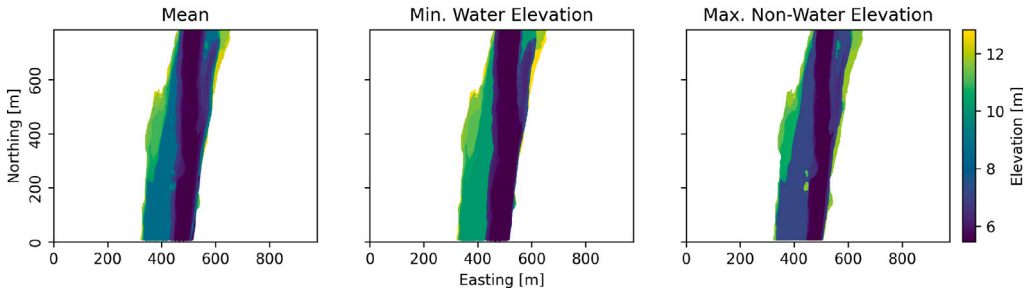

Fig. 13. The different bathymetric rasters for the Oueme River are based on the maximum non-water elevation per pixel (right), the minimum water level per pixel (center), and the mean of both rasters (left), which is used for the standard run.

major lateral inflows. The section spans across two SWORD reaches, so different IRIS slopes are applied for the cross-sections in the respective reaches.

3.4. Time series characteristics

Fig. 17 shows the time series of all other studied reaches sorted by the maximum derived discharge. The longest time series span 21 years, starting in 2002 with the launch of Envisat. The number of results and their temporal resolution depend on the duration of the altimetry missions and their revisit cycle. There is a significant gap within the time series of the Sittang and Missouri Rivers from 2010, when the Envisat mission ended, until 2016 when the Sentinel-3A mission started. In between, the reach was not covered by any satellite altimetry observations. The results of many reaches begin with the launch of Sentinel-3A. Either because the ground tracks of previous missions did not intersect with these reaches or because LRM altimeters, in contrast to the newer SAR sensors, could not deliver useful measurements. The time series for the Do Sono River lacks data from 2016 to 2020 during the period of the Jason-3 mission. There are no altimetry observations during that time, most probably caused by an incorrect reception window used in the onboard processing caused by erroneous a priori elevation information (Gac et al., 2021). The quality of the results is independent of the seasonal variability. For example, the noisy and nearly constant time series of the Karun River without annual variation matches our result well with an NRMSE of 6%. However, the approach cannot capture the short-term extreme events at the Burdekin and Fitzroy Rivers with an NRMSE of up to 18%. The results for the Adige and Kelantan show a significant bias that strongly affects the NSE of these time series.

3.5. Uncertainty range

On average, the cross-sectional geometry and base roughness parameters $k_B(x)$ contribute most to the total uncertainty range with 20% each. This large contribution is expected and reasonable as both parameters cannot be observed from remote sensing data. They rely on empirical assumptions and depend on the number of degrees of freedom in the optimization problem. The contribution of water level and water surface slope errors is similar at 20% and 16%, respectively. Both parameters are expected to be measured with improved accuracy and resolution using future missions like SWOT and have the potential to significantly lower the uncertainty range. The contributions of d_0 and ϵ are at 11% each. The lower contributions of d_0 and ϵ are caused by the low variability of these parameters throughout the solutions. Changes to d_0 and ϵ affect all cross-sections equally and do not appear to change the result of the objective function significantly, so they remain at or close to the initial value during the optimization process. Errors within the observed part of the bathymetry are considerably lower, at 3%.

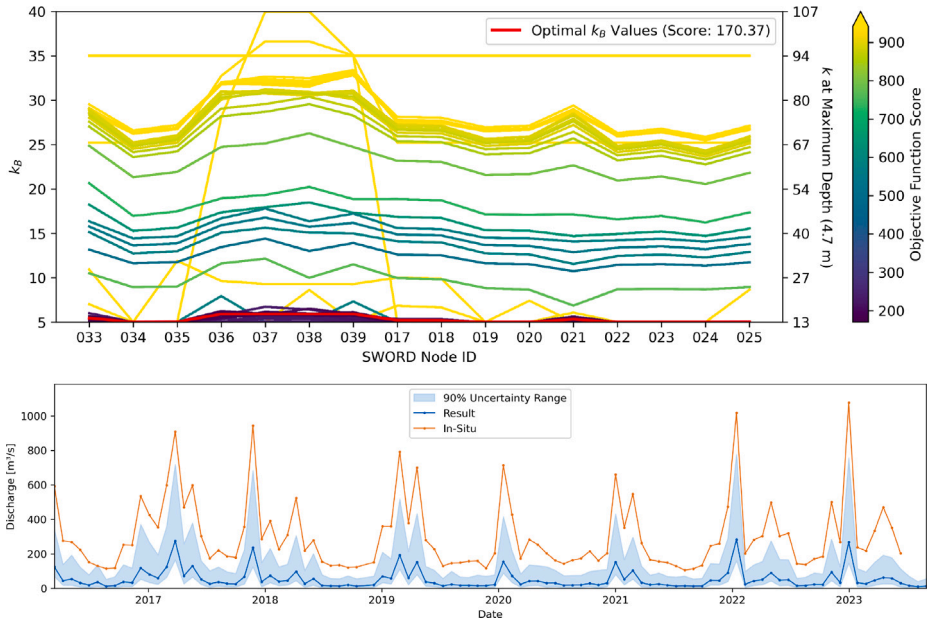

Fig. 14. Top: Roughness optimization at the Willamette River with default bounds. Bottom: Resulting discharge time series at the Willamette River with default bounds.

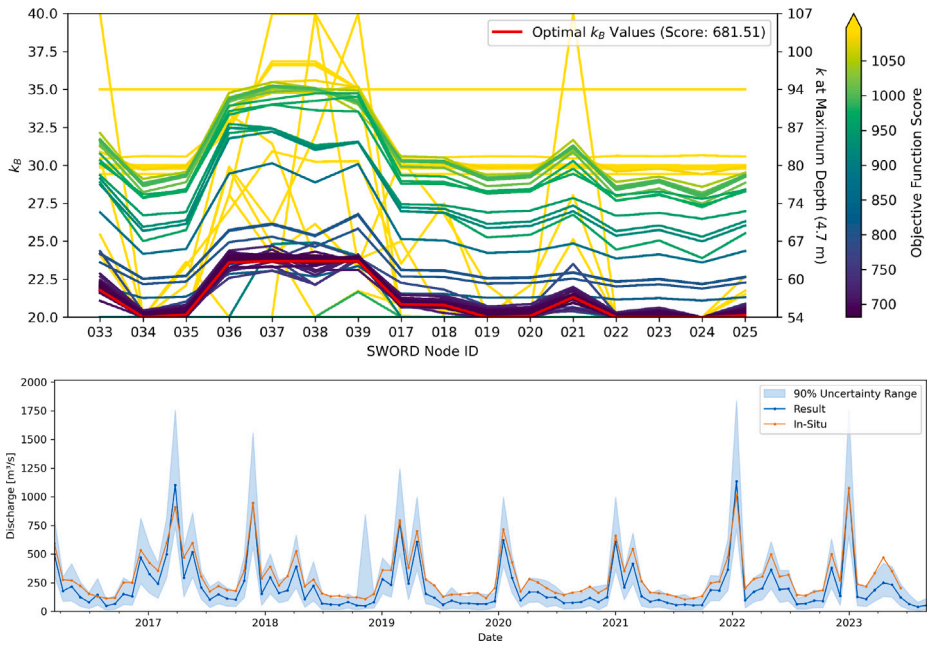

Fig. 15. Top: Roughness Optimization at the Willamette River with adjusted bounds. Bottom: Resulting discharge time series at the Willamette River with adjusted bounds.

These errors are basically propagated misclassifications of SAM, and the low value underlines the good quality of the SAM classification.

The total uncertainty range with all inputs set to their respective minimum or maximum values is very pessimistic. The resulting large total uncertainty values are not useful for data assimilation. However, we assume an uncertainty range greater than the most uncertain component to be realistic because the river depth and roughness can neither be measured nor estimated accurately. Therefore, we study the effect of different inter-percentile ranges on the CP to compute a reduced uncertainty range based on the total uncertainty range and its components.

Table 2 shows the median CP and CV of all studied sites for the different inter-percentile ranges. The 100% range is equivalent to the most pessimistic total uncertainty, while the 90% range is used in this study. With the 90% range, the CP is just 9% less than the 100% range, but the CV drops significantly from 97% to 43%. However, when choosing a lower range of 85%, the CP drops significantly, which suggests that this range would be too optimistic. Therefore, judging by this empirical test, we used the 90% range from the 5th to the 95th percentile for our uncertainty estimation.

Table 2
Median Coverage Probability (CP) and Coefficient of Variation (CV) of different inter-percentile ranges for the computation of the uncertainty range.

Range [%]	CP [%]	CV [%]
100	100	97
95	98	69
90	91	43
85	56	24

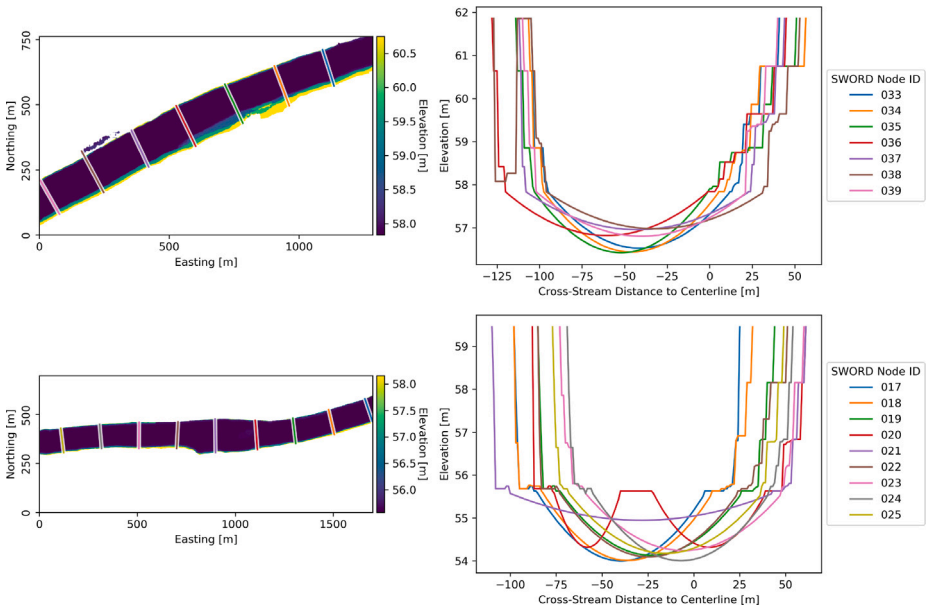

Fig. 16. Left: Location of cross-sections at SWORD nodes over the mean bathymetry of the AOIs at the studied reach of the Willamette River. Right: Geometry at each cross-section.

3.6. Water surface slope

As explained in Section 2.2, we cannot use a time-variable slope $I(t,x)$ but must assume a constant slope over time due to the lack of suitable data. Here, we use the average reach-scale water surface slope from the IRIS dataset and the minimum and maximum observed measurements for the uncertainty estimation. The range between the minimum and maximum slope contributes 16% of the total uncertainty range (cf. Section 3.5). Accurate time-variable slope data could significantly reduce this uncertainty.

As discussed by Scherer et al. (2022), it is not feasible yet to obtain a reliable water surface slope time series from ICESat-2 with a sufficient number of samples to study the temporal water surface slope characteristics. This may change as more ICESat-2 cycles become available over time, and most likely with the availability of continuous SWOT data. SWOT improves the accuracy of remotely sensed water surface slopes, meeting its science requirement of 17 mm/km. Additionally, it increases the temporal resolution due to its repeat orbit of 21 days (ICESat-2: 92 days) in connection with its 120 km wide swath, which enables it to revisit the same location on up to ten passes during one cycle (Fu et al., 2012, 2024). As the approach of this study refers to reaches from SWORD, which is the same framework used for the SWOT mission, implementing time-variable slopes from SWOT can be achieved without major modifications. When using SWOT in conjunction with other satellite altimetry missions, it will still be necessary to generate a stage-slope relationship that considers hysteresis effects to transfer the slope variability to observations outside the SWOT period.

3.7. Water classification using SAM

The authors of SAM state that their model can miss fine structures when masking image features (Kirillov et al., 2023). However, the quality of the automatically generated masks is sufficient to map the variability in river width as small as the PlanetScope pixel size of 3 m. The number of false-positive and false-negative classified water areas is marginal and easy to improve with the definition of additional label points. The use of two different SAM-based methods and a classical NDWI thresholding for masking makes our approach robust. If wrongly classified areas remain, they appear as outliers in the hypsometric curve fitted to the water level and surface area observations and can be manually removed. The source of errors can be clouds, mountain or cloud shadows, boats, or water with high sediment content.

In contrast to the classification by Schwatke et al. (2019), this approach is much more versatile in terms of the spectral characteristics of the input image. However, the SAM-based approach has a lower level of automation because it requires more user-defined label points than Schwatke et al. (2019).

3.8. Roughness optimization

The unknown roughness parameters are optimized using the L-BFGS-B algorithm by minimizing the difference in discharge between adjacent cross-sections. The approach requires only approximate boundary conditions that can be derived from literature values. However, as demonstrated in Section 3.3, expert judgment is still necessary to slightly adjust these boundaries since erroneous geometries can cause unrealistic roughness values. We modify the base roughness value $k_B(x)$ depending on the depth of the cross-section segment $d_i(t,x)$ to account for different surface types within the cross-section (e.g., floodplain, bank, bar, and thalweg). The functional relationship between depth and final roughness is defined by the unknown parameters ϵ and d_0. However, the optimization algorithm rarely deviates from the initial values of ϵ and d_0. Fig. 18 shows the depth-dependent roughness coefficient calculated with Eq. (3) using the average optimized parameters $k_B(x)$, ϵ, and d_0 and the average sinuosity $s(x)$ per studied river reach by occurring depth range and the mean discharge.

Applying the depth-dependent roughness coefficient improves the accuracy of our results, as demonstrated in Fig. 19 for the Okavango River. Without applying the depth-dependent roughness adjustment (i.e., setting $d = 1$ in Eq. (3) and running a new optimization), the NRMSE rises from 10% to 19%. Fig. 20 shows this behavior throughout all studied sites except for the Kelantan and Mitchell Rivers, where the effect is the opposite, and the method without depth-depended roughness adjustment yields better results. Overall, the median NRMSE rises from 12% to 27% without applying the depth-dependent roughness adjustment.

3.9. Unobserved cross-sectional geometry

In addition to the roughness coefficient, the full cross-sectional geometry (i.e., the permanently submerged bathymetry) cannot be observed from remote sensing data, and both unknowns are estimated in an optimization approach. Both unknowns contribute equally to

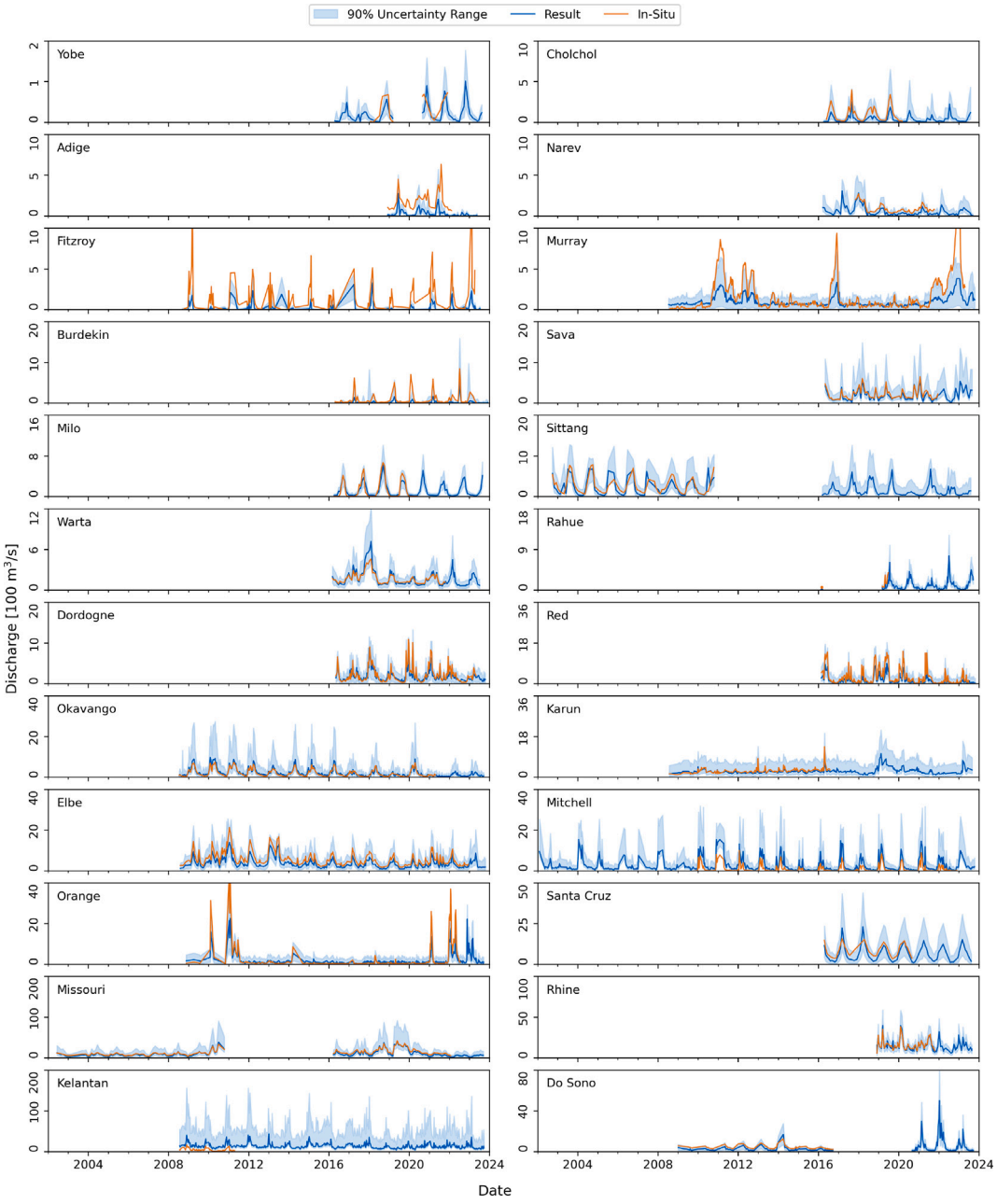

Fig. 17. Discharge results of the remaining sites with uncertainty (blue) and in-situ data (orange). The time series are discontinued at data gaps larger one year. (For interpretation of the references to color in this figure legend, the reader is referred to the web version of this article.)

the uncertainty range (cf. Section 3.5). There is no data across all studied sites to validate either of the parameters. Therefore, we cannot distinguish between errors introduced by these parameters. Scherer et al. (2020) used a similar approach to obtain the cross-sectional geometry and estimate the discharge of the Lower Mississippi River. In contrast to this study, in-situ bathymetry and slope were available for the Mississippi. Thus, a closed-loop test could be conducted in which the estimated parameters were substituted individually by in-situ measurements. This test identified the roughness coefficient as a more significant source of error compared to the cross-sectional geometry.

The optimization of both parameters runs over the number of cross-sections within the AOI. The AOI size depends on the length of the reach, which is bounded to a section where the flow can be assumed to be steady uniform or gradually varied judging from satellite imagery. Additionally, the AOI location and size can be constrained by the availability of a sufficient number of cloud-free satellite images to observe the water extent at high and low water levels. Therefore, the approach is limited to short sections for some rivers. For example, the studied section of the Kelantan River comprises only five cross-sections because clouds obscured the surrounding sections during water level extremes. Still, multiple studied sections comprise only six or seven cross-sections and yield good results below 10% NRMSE. Fig. 17 shows that the discharge for the Kelantan is overestimated. The optimization yielded the largest depth and an average roughness coefficient for the Kelantan compared to the other rivers (cf. Fig. 18). One possible reason is that the river sections lacks sufficient variability in the observables, such as width and sinuosity, so that the optimization of the cross-sectional area and roughness coefficients are not properly constraint. Additionally, Fig. A.2 shows that the observable AOI contains a section just before a sharp river bend, potentially affected by backwater effects not accounted for by the employed sinuosity value. These effects

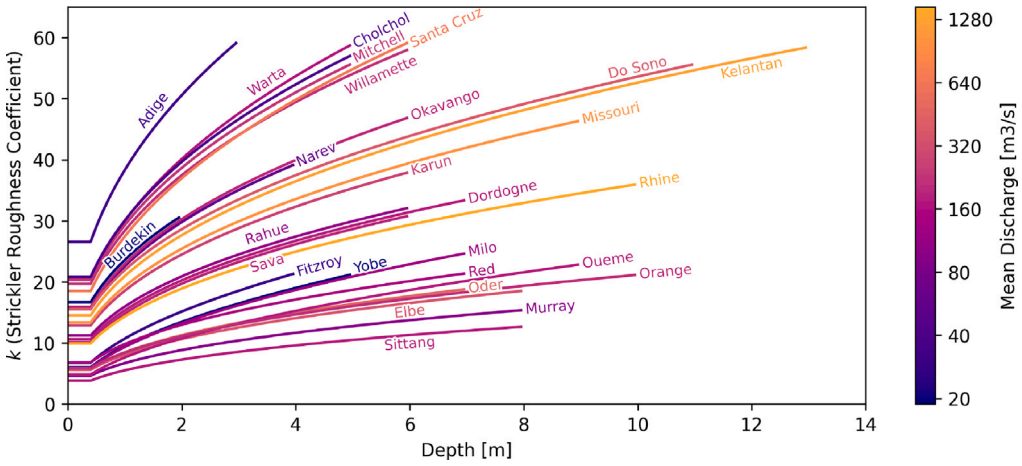

Fig. 18. Depth-dependent Strickler roughness coefficient with the average optimized parameters per studied river reach by mean discharge.

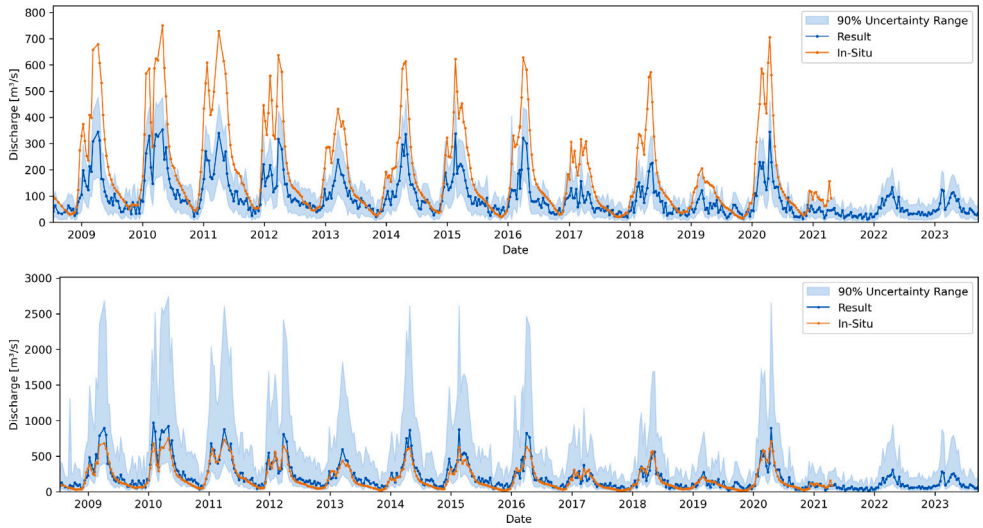

Fig. 19. Results for the Okavango River without (upper) and with (lower) applying the depth-dependent roughness adjustment.

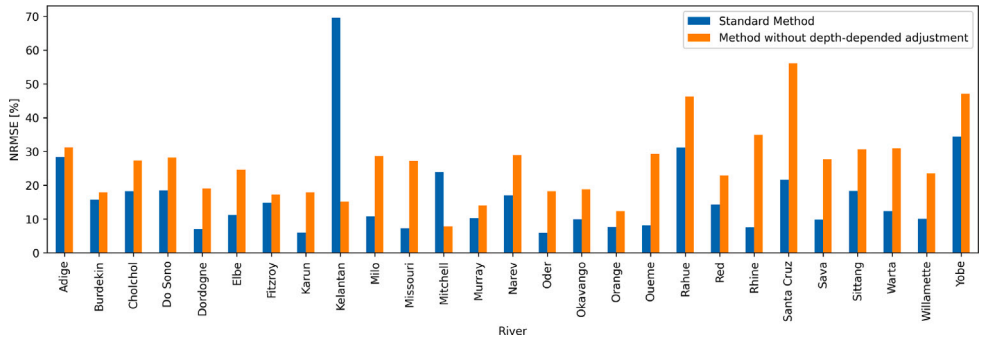

Fig. 20. NRMSE with (blue) and without (orange) applying the depth-dependent roughness adjustment. (For interpretation of the references to color in this figure legend, the reader is referred to the web version of this article.)

may result in an increased width, deviating from the used width-to-depth relationship. Therefore, we assume the cross-sectional area to be overestimated in this case of an unfavorable study site.

4. Conclusion and outlook

We present an approach specifically designed to estimate satellite-based river discharge time series for narrow, ungauged rivers. The approach leverages the variety of remote sensing data available over the past 20 years. We calculate the river discharge using the Gauckler–Manning–Strickler equation, which requires information about the river's slope, cross-sectional geometry, and roughness coefficient. While we derive the slope from the global reach-scale "ICESat-2 River Surface Slope" (IRIS) dataset, we determine the water surface area and even minor river width variations from 3 m resolution PlanetScope satellite images. The images are classified into water and land pixels utilizing the "Segment Anything Model" (SAM), which we considered

suitable for the purpose of this study. The classification requires minimal user input, and by applying three different methods, water can be detected robustly. To reconstruct the river bathymetry, a hypsometric curve is fitted to the surface area and DAHITI water level time series. We extract the cross-sectional geometries from the bathymetry and approximate the submerged part below the baseflow using an empirical width-to-depth relationship. Under the assumption of mass conservation, we optimize the parameters of the depth-dependent roughness coefficient at multiple consecutive cross-sections within a pre-defined AOI by minimizing the difference between the estimated discharges at individual cross-sections. By taking into account all uncertainties of the input parameters, we estimate the uncertainty of the resulting discharge time series. In contrast to other approaches, the method does not require a model of the river or data outside the respective AOI.

We applied our approach to 27 globally distributed reaches of different widths and mean discharge under various climate conditions. The number of studied examples and their locations are limited by the availability of in-situ validation data and our PlanetScope download quota. The ground track pattern of the altimeter missions further limits the application. In this respect, however, the new SWOT mission can be expected to provide a huge improvement.

To apply the approach based on the concept of mass conservation and uniform or gradually varied flow, the user must ensure that there are no significant tributaries or flow obstructions within the studied section or the downstream reach. Otherwise, significant errors can occur, as demonstrated in the case of the Kelantan River, where backwater effects from a narrow and sharply bending downstream section likely caused an overestimation of discharge. The river must not be braided, and sufficient cloud-free satellite imagery must be available covering the entire range from low to high flows to reduce the uncertainty and errors caused by the unobserved part of the river bathymetry. River sections with gradual variations in width, slope, or sinuosity are beneficial for the optimization, as they introduce additional constraints. The approximate boundaries of the base Strickler roughness coefficient should be set based on literature values for natural channels, typically within the range between 5 and 50. In cases where the optimization shows multiple possible solutions at different local minima, such as the Willamette River example presented in this study, expert judgment is required to adjust the boundary conditions and prevent unrealistic low or high discharge patterns.

The median RMSE, NRMSE, NSE, and R^2 are 132 m^3/s, 12%, 0.560, and 0.77, respectively. Large errors occur at rivers where depth appears overestimated or the concept of mass-conservation is not applicable. Insights from further studies on identifying suitable river sections from satellite imagery could help to mitigate these errors. On average, the 90% uncertainty range covers 91% of the in-situ data and measures 43% of the observed amplitude. Besides the standard deviation of the unknown roughness parameters, the uncertainty of the cross-sectional geometry, influenced mainly by the unknown river bed elevation, contributes most to the total discharge uncertainty range. Improved techniques for satellite-derived bathymetry, either through lidar measurements or more sophisticated empirical relationships, would significantly enhance this approach.

The approach depends strongly on the frequency of water level observations and thus would benefit from techniques that interpolate water level observations along the river and over time, such as using spatiotemporal kriging (Boergens et al., 2017), to enhance the temporal resolution of the derived discharge time series. No discharge can be derived for extreme water levels that have never occurred during the period of simultaneous water level and surface area observations required for the reconstruction of the bathymetry. The approach would also benefit from sub-reach-scale or time-variable water surface slopes since $I(t, x)$ currently only varies if the AOI comprises multiple SWORD reaches. If this variability could be better resolved spatially and temporally, we expect the optimization problem to be better constrained and result in a more distinct solution with lower uncertainties. Again, concerning sub-reach-scale and time-varying slope measurements, we can expect significant improvement in errors and uncertainty as soon as continuous SWOT measurements become available. Our approach is not fully automated, but it requires only minimal user input, such as label points for the water classification and approximate boundaries for the optimization, and can be transferred to other locations with fairly minimal effort. However, it cannot be easily transferred to braided rivers, which require a different depth estimation. Some label points must be defined, and expert judgment is required to set up and adjust the boundary conditions for the optimization process. The amount of expert input and judgment might be reduced by integrating the results of multiple reaches, branches, and reservoirs at the basin level, which must yield coherent and rational results (e.g., increasing discharge in the downstream direction).

The key advantage of the presented method is that in-situ data are not needed for calibration and that no data is required beyond the studied reach (like in extensive hydrological models). These attributes make the approach especially valuable for applications in ungauged or poorly gauged basins. The propagated uncertainties facilitate the assimilation with models. Furthermore, the approach is based on readily available global satellite data spanning up to 20 years, whereas methods specifically designed for the new SWOT mission cover only the period since 2023.

CRediT authorship contribution statement

Daniel Scherer: Writing – original draft, Visualization, Validation, Software, Methodology, Investigation, Conceptualization. **Christian Schwatke:** Writing – review & editing, Data curation. **Denise Dettmering:** Writing – review & editing, Supervision, Project administration, Funding acquisition. **Florian Seitz:** Writing – review & editing, Supervision, Project administration, Funding acquisition.

Declaration of competing interest

The authors declare that they have no known competing financial interests or personal relationships that could have appeared to influence the work reported in this paper.

Data availability

The discharge data resulting from this study are available at Zenodo (https://doi.org/10.5281/zenodo.10611165). Part of the code is available upon request from the main author.

Acknowledgments

This work was funded by the Deutsche Forschungsgemeinschaft (DFG, German Research Foundation)—Project number 324641997, Grant DE 2174/10-2. Open access funding enabled and organized by Projekt DEAL. We thank the U.S. Geological Survey (USGS), Alpine Drought Observatory (ADO), and Global Runoff Data Centre (GRDC) for providing the in-situ data.

Appendix

Fig. A.1 shows a schematic of the method used in Section 2.5 for creating the different observed bathymetry rasters from the stacked watermasks with an example for two pixel columns.

Fig. A.2 shows detailed maps of each studied river section with the selected AOIs within which the approach is applied, the SWORD reaches, the locations of the DAHITI virtual stations where the water level is measured from satellite altimetry and the ground tracks of the respective satellite missions.

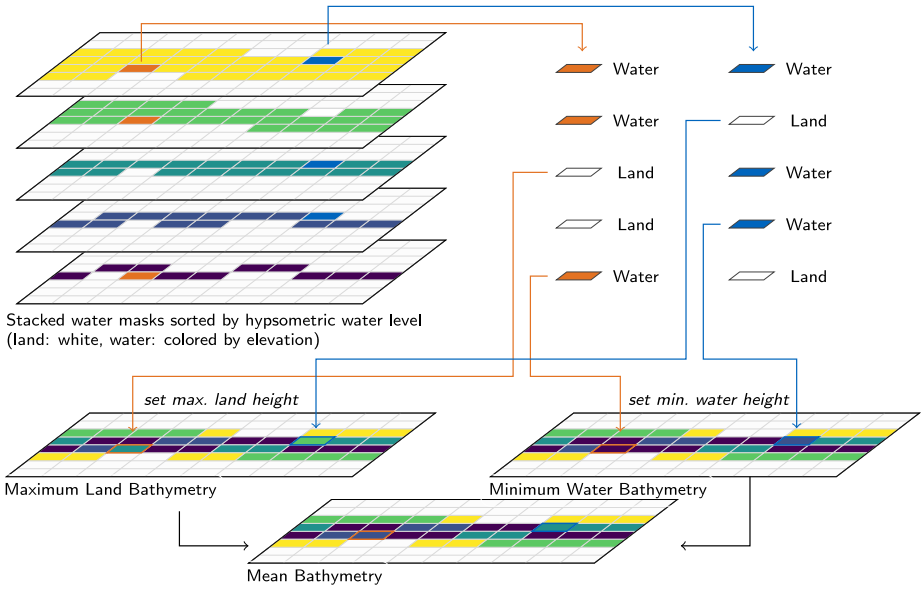

Fig. A.1. Schematic creation of the maximum land, minimum water, and mean bathymetry mask from the stacked water masks with an example for two pixel columns.

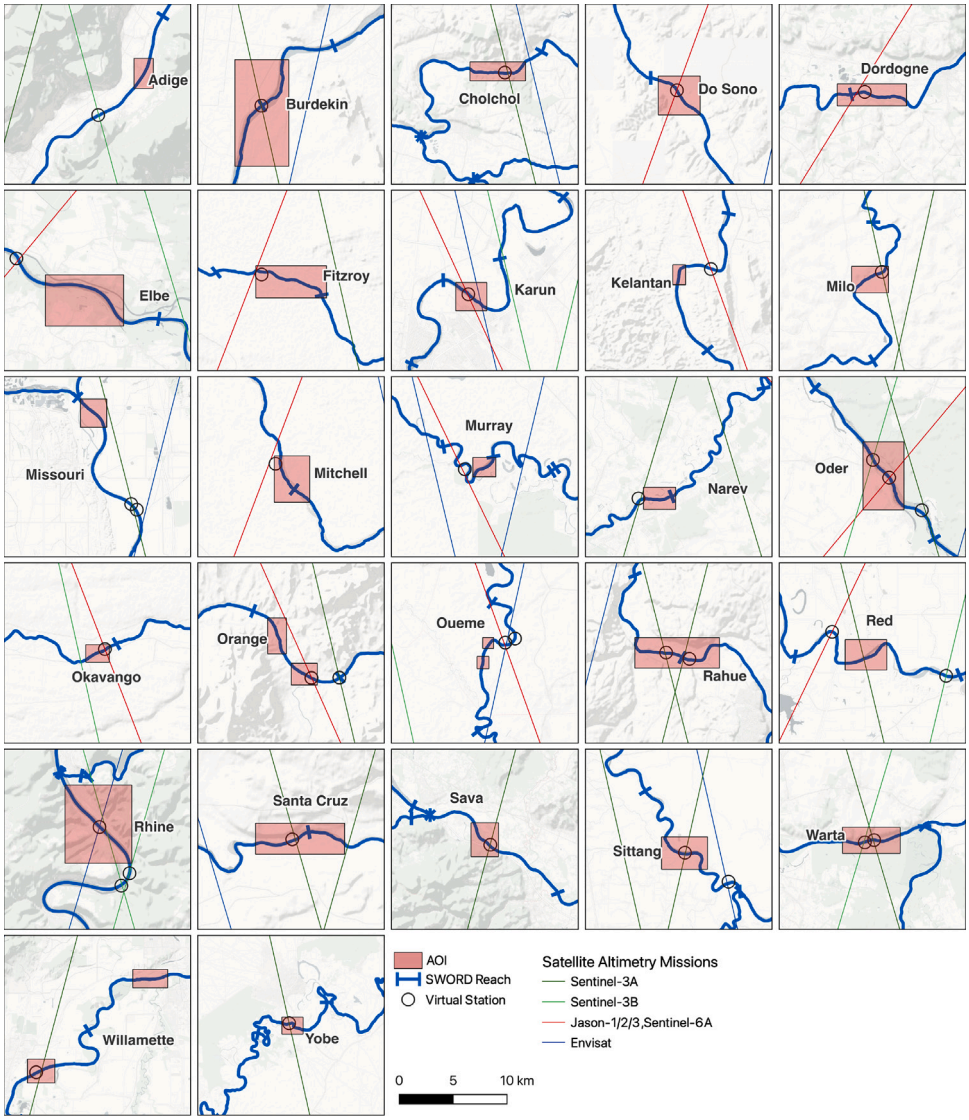

Fig. A.2. Detailed maps of the AOIs with SWORD reaches, virtual stations, and tracks of the satellite altimetry missions.

References

Allen, G.H., Pavelsky, T., 2018. Global extent of rivers and streams. Science 361 (6402), 585–588. http://dx.doi.org/10.1126/science.aat0636.

Alpine Drought Observatory, 2023. Alpine drought observatory: Hydrological database. URL: https://ado.eurac.edu/. (Accessed: 31 October 2023).

Altenau, E.H., Pavelsky, T.M., Durand, M.T., Yang, X., Frasson, R.P.d.M., Bendezu, L., 2021a. SWOT River Database (SWORD). http://dx.doi.org/10.5281/zenodo.5643392, Zenodo.

Altenau, E.H., Pavelsky, T.M., Durand, M.T., Yang, X., Frasson, R.P.d., Bendezu, L., 2021b. The Surface Water and Ocean Topography (SWOT) Mission River Database (SWORD): A Global River Network for Satellite Data Products. Water Resour. Res. 57 (7), http://dx.doi.org/10.1029/2021WR030054.

Bjerklie, D.M., 2007. Estimating the bankfull velocity and discharge for rivers using remotely sensed river morphology information. J. Hydrol. 341, 144–155. http://dx.doi.org/10.1016/j.jhydrol.2007.04.011.

Bjerklie, D.M., Birkett, C.M., Jones, J.W., Carabajal, C., Rover, J.A., Fulton, J.W., Garambois, P.-A., 2018. Satellite remote sensing estimation of river discharge: Application to the Yukon River Alaska. J. Hydrol. 561, 1000–1018. http://dx.doi.org/10.1016/j.jhydrol.2018.04.005.

Bjerklie, D., Durand, M., Lenoir, J., Dudley, R.W., Birkett, C., Jones, J.W., Harlan, M., 2023. Satellite remote sensing of river discharge: A framework for assessing the accuracy of discharge estimates made from satellite remote sensing observations. J. Appl. Remote Sens. 17, http://dx.doi.org/10.1117/1.jrs.17.014520.

Boergens, E., Buhl, S., Dettmering, D., Klüppelberg, C., Seitz, F., 2017. Combination of multi-mission altimetry data along the Mekong River with spatio-temporal kriging. J. Geod. 91, 519–534. http://dx.doi.org/10.1007/s00190-016-0980-z.

Bosch, W., Dettmering, D., Schwatke, C., 2014. Multi-Mission Cross-Calibration of Satellite Altimeters: Constructing a Long-Term Data Record for Global and Regional Sea Level Change Studies. Remote Sens. 6 (3), 2255–2281. http://dx.doi.org/10.3390/rs6032255.

Boyer, M.C., 1964. Streamflow measurement. In: Chow, V.T. (Ed.), Handbook of Applied Hydrology. McGraw-Hill, New York, chapter 15.

Brinkerhoff, C.B., Gleason, C.J., Feng, D., Lin, P., 2020. Constraining Remote River Discharge Estimation Using Reach-Scale Geomorphology. Water Resour. Res. 56, http://dx.doi.org/10.1029/2020WR027949.

Broyden, C.G., 1970. The Convergence of a Class of Double-rank Minimization Algorithms 1. General Considerations. IMA J. Appl. Math. 6 (1), 76–90. http://dx.doi.org/10.1093/imamat/6.1.76.

Byrd, R.H., Peihuang, L., Nocedal, J., Argonne National Lab., I., 1996. A limited-memory algorithm for bound-constrained optimization. http://dx.doi.org/10.2172/204262.

Calmant, S., Crétaux, J.F., Rémy, F., 2016. Principles of Radar Satellite Altimetry for Application on Inland Waters. In: Microwave Remote Sensing of Land Surfaces: Techniques and Methods. pp. 175–218. http://dx.doi.org/10.1016/B978-1-78548-159-8.50004-9.

Chow, V.T., 1959. Open Channel Hydraulics. Mcgraw-Hill Civil Engineering Series, McGraw-Hill, http://dx.doi.org/10.1016/B978-0-7506-6857-6.X5000-0.

Cooley, S.W., Ryan, J.C., Smith, L.C., 2021. Human alteration of global surface water storage variability. Nature 591 (7848), 78–81. http://dx.doi.org/10.1038/s41586-021-03262-3.

Dettmering, D., Ellenbeck, L., Scherer, D., Schwatke, C., Niemann, C., 2020. Potential and Limitations of Satellite Altimetry Constellations for Monitoring Surface Water Storage Changes—A Case Study in the Mississippi Basin. Remote Sens. 12 (20), http://dx.doi.org/10.3390/rs12203320.

Durand, M., Gleason, C.J., Pavelsky, T.M., Frasson, R.P.d., Turmon, M., David, C.H., Altenau, E.H., Tebaldi, N., Larnier, K., Monnier, J., Malaterre, P.O., Oubanas, H., Allen, G.H., Astifan, B., Brinkerhoff, C., Bates, P.D., Bjerklie, D., Coss, S., Dudley, R., Fenoglio, L., Garambois, P.A., Getirana, A., Lin, P., Margulis, S.A., Matte, P., Minear, J.T., Muhebwa, A., Pan, M., Peters, D., Riggs, R., Sikder, M.S., Simmons, T., Stuurman, C., Taneja, J., Tarpanelli, A., Schulze, K., Tourian, M.J., Wang, J., 2023. A Framework for Estimating Global River Discharge From the Surface Water and Ocean Topography Satellite Mission. Water Resour. Res. 59, http://dx.doi.org/10.1029/2021WR031614.

Durand, M., Neal, J., Rodríguez, E., Andreadis, K.M., Smith, L.C., Yoon, Y., 2014. Estimating reach-averaged discharge for the River Severn from measurements of river water surface elevation and slope. J. Hydrol. 511, 92–104. http://dx.doi.org/10.1016/j.jhydrol.2013.12.050.

Elmi, O., Tourian, M.J., Bárdossy, A., Sneeuw, N., 2021. Spaceborne River Discharge From a Nonparametric Stochastic Quantile Mapping Function. Water Resour. Res. 57, http://dx.doi.org/10.1029/2021WR030277.

Feng, D., Gleason, C.J., Yang, X., Pavelsky, T.M., 2019. Comparing Discharge Estimates Made via the BAM Algorithm in High-Order Arctic Rivers Derived Solely From Optical CubeSat, Landsat, and Sentinel-2 Data. Water Resour. Res. 55, 7753–7771. http://dx.doi.org/10.1029/2019WR025599.

Finlayson, B., 2010. Rivers in Australia. Front. Earth Sci. China 4, 375–385. http://dx.doi.org/10.1007/s11707-010-0129-y.

Fletcher, R., 1970. A new approach to variable metric algorithms. Comput. J. 13 (3), 317–322. http://dx.doi.org/10.1093/comjnl/13.3.317.

Fu, L.-L., Alsdorf, D., Morrow, R., Rodriguez, E., Mognard, N., 2012. SWOT: The Surface Water and Ocean Topography Mission: Wide-Swath Altimetric Measurement of Water Elevation on Earth. Jet Propulsion Laboratory, Pasadena, California, URL: https://hdl.handle.net/2014/41996.

Fu, L.-L., Pavelsky, T., Cretaux, J.-F., Morrow, R., Farrar, J.T., Vaze, P., Sengenes, P., Vinogradova-Shiffer, N., Sylvestre-Baron, A., Picot, N., Dibarboure, G., 2024. The Surface Water and Ocean Topography Mission: A Breakthrough in Radar Remote Sensing of the Ocean and Land Surface Water. Geophys. Res. Lett. 51, http://dx.doi.org/10.1029/2023GL107652.

Gac, S.L., Boy, F., Blumstein, D., Lasson, L., Picot, N., 2021. Benefits of the Open-Loop Tracking Command (OLTC): Extending conventional nadir altimetry to inland waters monitoring. Adv. Space Res. 68, 843–852. http://dx.doi.org/10.1016/j.asr.2019.10.031.

Garambois, P.-A., Monnier, J., 2015. Inference of effective river properties from remotely sensed observations of water surface. Adv. Water Resour. 79, 103–120. http://dx.doi.org/10.1016/j.advwatres.2015.02.007.

Gerber, F., Blake, L., Savola, N., 2023. optimParallel-python: Type hints. http://dx.doi.org/10.5281/zenodo.10426043.

Gerber, F., Furrer, R., 2019. optimParallel: An R package providing a parallel version of the L-BFGS-B optimization method. R J. 11 (1), 352–358. http://dx.doi.org/10.32614/RJ-2019-030.

Gleason, C.J., Durand, M.T., 2020. Remote Sensing of River Discharge: A Review and a Framing for the Discipline. Remote Sens. 12, 1–28. http://dx.doi.org/10.3390/rs12071107.

Gleason, C.J., Hamdan, A.N., 2017. Crossing the (watershed) divide: Satellite data and the changing politics of international river basins. Geogr. J. 183, 2–15. http://dx.doi.org/10.1111/geoj.12155.

Global Runoff Data Centre, 2023. GRDC Data Download portal. 56068 Koblenz, Germany, URL: https://portal.grdc.bafg.de. (Accessed: 31 October 2023).

Goldfarb, D., 1970. A family of variable-metric methods derived by variational means. Math. Comp. 24 (109), 23–26. http://dx.doi.org/10.1090/s0025-5718-1970-0258249-6.

Hagemann, M.W., Gleason, C.J., Durand, M.T., 2017. BAM: Bayesian AMHG-manning inference of discharge using remotely sensed stream width, slope, and height. Water Resour. Res. 53, 9692–9707. http://dx.doi.org/10.1002/2017WR021626.

Halicki, M., Niedzielski, T., 2022. The accuracy of the Sentinel-3A altimetry over Polish rivers. J. Hydrol. 606, 127355. http://dx.doi.org/10.1016/j.jhydrol.2021.127355.

Halicki, M., Schwatke, C., Niedzielski, T., 2023. The impact of the satellite ground track shift on the accuracy of altimetric measurements on rivers: A case study of the Sentinel-3 altimetry on the Odra/Oder River. J. Hydrol. 617, 128761. http://dx.doi.org/10.1016/j.jhydrol.2022.128761.

Hannah, D.M., Demuth, S., van Lanen, H.A.J., Looser, U., Prudhomme, C., Rees, G., Stahl, K., Tallaksen, L.M., 2011. Large-scale river flow archives: importance, current status and future needs. Hydrol. Process. 25, 1191–1200. http://dx.doi.org/10.1002/hyp.7794.

Jain, M.K., Kothyari, U.C., Raju, K.G.R., 2004. A GIS based distributed rainfall-runoff model. J. Hydrol. 299, 107–135. http://dx.doi.org/10.1016/j.jhydrol.2004.04.024.

Julien, P.Y., 2018. Steady flow in rivers. In: River Mechanics. Cambridge University Press, Cambridge, http://dx.doi.org/10.1017/9781316107072.006.

Kirillov, A., Mintun, E., Ravi, N., Mao, H., Rolland, C., Gustafson, L., Xiao, T., Whitehead, S., Berg, A.C., Lo, W.-Y., Dollár, P., Girshick, R., 2023. Segment Anything. arXiv:2304.02643.

Lamine, B.O., Ferreira, V.G., Yang, Y., Ndehedehe, C.E., He, X., 2021. Estimation of the Niger River cross-section and discharge from remotely-sensed products. J. Hydrol.: Reg. Stud. 36, http://dx.doi.org/10.1016/j.ejrh.2021.100862.

Lao, J., Wang, C., Nie, S., Xi, X., Wang, J., 2022. Monitoring and analysis of water level changes in Mekong River from ICESat-2 spaceborne laser altimetry. Water 14 (10), 1613. http://dx.doi.org/10.3390/w14101613.

Lecher, K., Lühr, H.-P., Zanke, U.C.E. (Eds.), 2021. Taschenbuch der Wasserwirtschaft, 10t ed. Springer Vieweg, Wiesbaden, Germany.

Lin, P., Feng, D., Gleason, C.J., Pan, M., Brinkerhoff, C.B., Yang, X., Beck, H.E., de Moraes Frasson, R.P., 2023. Inversion of river discharge from remotely sensed river widths: A critical assessment at three-thousand global river gauges. Remote Sens. Environ. 287, 113489. http://dx.doi.org/10.1016/j.rse.2023.113489.

Manning, R., 1891. On the flow of water in open channels and pipes. Trans. Inst. Civ. Eng. Ireland 20, 161–207.

McFeeters, S.K., 1996. The use of the Normalized Difference Water Index (NDWI) in the delineation of open water features. Int. J. Remote Sens. 17 (7), 1425–1432. http://dx.doi.org/10.1080/01431169608948714.

Moody, J.A., Troutman, B.M., 2002. Characterization of the spatial variability of channel morphology. Earth Surf. Process. Landf. 27, 1251–1266. http://dx.doi.org/10.1002/esp.403.

Negri, L.H., Vestri, C., 2017. PeakUtils: v1.1.0. http://dx.doi.org/10.5281/zenodo.887917, Zenodo.

Nielsen, K., Zakharova, E., Tarpanelli, A., Andersen, O.B., Benveniste, J., 2022. River levels from multi mission altimetry, a statistical approach. Remote Sens. Environ. 270, 112876. http://dx.doi.org/10.1016/j.rse.2021.112876.

Nocedal, J., Wright, S.J., 2006. Quasi-Newton methods. In: Numerical Optimization. Springer New York, New York, NY, pp. 135–163. http://dx.doi.org/10.1007/978-0-387-40065-5.

Nyberg, B., Henstra, G., Gawthorpe, R.L., Ravnås, R., Ahokas, J., 2023. Global scale analysis on the extent of river channel belts. Nature Commun. 14, http://dx.doi.org/10.1038/s41467-023-37852-8.

Osco, L.P., Wu, Q., de Lemos, E.L., Gonçalves, W.N., Ramos, A.P.M., Li, J., Marcato, J., 2023. The Segment Anything Model (SAM) for remote sensing applications: From zero to one shot. Int. J. Appl. Earth Obs. Geoinf. 124, 103540. http://dx.doi.org/10.1016/j.jag.2023.103540.

Planet Labs PBC, 2022. Planet Application Program Interface: In Space for Life on Earth. Planet, URL: https://api.planet.com.

Rhoads, B.L., 2020. River Dynamics: Geomorphology to Support Management. Cambridge University Press, http://dx.doi.org/10.1017/9781108164108.

Riggs, R.M., Allen, G.H., Wang, J., Pavelsky, T.M., Gleason, C.J., David, C.H., Durand, M., 2023. Extending global river gauge records using satellite observations. Environ. Res. Lett. 18, http://dx.doi.org/10.1088/1748-9326/acd407.

Roux, H., Dartus, D., 2005. Parameter identification using optimization techniques in open-channel inverse problems. J. Hydraul. Res. 43, 311–320. http://dx.doi.org/10.1080/00221680509500125.

Roy, D.P., Huang, H., Houborg, R., Martins, V.S., 2021. A global analysis of the temporal availability of PlanetScope high spatial resolution multi-spectral imagery. Remote Sens. Environ. 264, http://dx.doi.org/10.1016/j.rse.2021.112586.

Scherer, D., Schwatke, C., Dettmering, D., Seitz, F., 2020. Long-Term Discharge Estimation for the Lower Mississippi River Using Satellite Altimetry and Remote Sensing Images. Remote Sens. 12 (17), http://dx.doi.org/10.3390/rs12172693.

Scherer, D., Schwatke, C., Dettmering, D., Seitz, F., 2022. ICESat-2 Based River Surface Slope and Its Impact on Water Level Time Series From Satellite Altimetry. Water Resour. Res. 58 (11), http://dx.doi.org/10.1029/2022WR032842, e2022WR032842.

Scherer, D., Schwatke, C., Dettmering, D., Seitz, F., 2023. ICESat-2 river surface slope (IRIS): A global reach-scale water surface slope dataset. Sci. Data 10 (1), 359. http://dx.doi.org/10.1038/s41597-023-02215-x.

Schwatke, C., Dettmering, D., Bosch, W., Seitz, F., 2015. DAHITI – An innovative approach for estimating water level time series over inland waters using multi-mission satellite altimetry. Hydrol. Earth Syst. Sci. 19 (10), 4345–4364. http://dx.doi.org/10.5194/hess-19-4345-2015.

Schwatke, C., Dettmering, D., Passaro, M., Hart-Davis, M., Scherer, D., Müller, F.L., Bosch, W., Seitz, F., 2023. OpenADB: DGFI-TUM's Open Altimeter Database. Geosci. Data J. http://dx.doi.org/10.1002/gdj3.233.

Schwatke, C., Dettmering, D., Seitz, F., 2020. Volume Variations of Small Inland Water Bodies from a Combination of Satellite Altimetry and Optical Imagery. Remote Sens. 12 (10), http://dx.doi.org/10.3390/rs12101606.

Schwatke, C., Scherer, D., Dettmering, D., 2019. Automated Extraction of Consistent Time-Variable Water Surfaces of Lakes and Reservoirs Based on Landsat and Sentinel-2. Remote Sens. 11 (9), 1010. http://dx.doi.org/10.3390/rs11091010.

Shanno, D., 1970. Conditioning of quasi-Newton methods for function minimization. Math. Comp. 24 (111), 647–656. http://dx.doi.org/10.1090/s0025-5718-1970-0274029-x.

Song, S., Schmalz, B., Zhang, J.X., Li, G., Fohrer, N., 2017. Application of modified Manning formula in the determination of vertical profile velocity in natural rivers. Hydrol. Res. 48, 133–146. http://dx.doi.org/10.2166/nh.2016.131.

Strahler, A.N., 1952. Hypsometric (area-altitude) analysis of erosional topography. GSA Bull. 63 (11), 1117–1142. http://dx.doi.org/10.1130/0016-7606(1952)63[1117:HAAOET]2.0.CO;2.

Sulistioadi, Y.B., Tseng, K.H., Shum, C.K., Hidayat, H., Sumaryono, M., Suhardiman, A., Setiawan, F., Sunarso, S., 2015. Satellite radar altimetry for monitoring small rivers and lakes in Indonesia. Hydrol. Earth Syst. Sci. 19 (1), 341–359. http://dx.doi.org/10.5194/hess-19-341-2015.

Tarpanelli, A., Santi, E., Tourian, M.J., Filippucci, P., Amarnath, G., Brocca, L., 2019. Daily River Discharge Estimates by Merging Satellite Optical Sensors and Radar Altimetry Through Artificial Neural Network. IEEE Trans. Geosci. Remote Sens. 57, 329–341. http://dx.doi.org/10.1109/TGRS.2018.2854625.

Tourian, M.J., Sneeuw, N., Bárdossy, A., 2013. A quantile function approach to discharge estimation from satellite altimetry (ENVISAT). Water Resour. Res. 49, 4174–4186. http://dx.doi.org/10.1002/wrcr.20348.

Turnipseed, D.P., Sauer, V.B., 2010. Discharge Measurements at Gaging Stations. In: Techniques and Methods, U.S. Geological Survey, Reston, VA, http://dx.doi.org/10.3133/tm3A8.

U.S. Geological Survey, 2023. U.S. Geological Survey National Water Dashboard. URL: https://dashboard.waterdata.usgs.gov. (Accessed: 31 October 2023).

Weaver, J.R., 1985. Centrosymmetric (cross-symmetric) matrices, their basic properties, eigenvalues, and eigenvectors. Amer. Math. Monthly 92 (10), 711–717, URL: http://www.jstor.org/stable/2323222.

Wei, M., Cheng, N.-S., Lu, Y., 2023. Revisiting the concept of hydraulic radius. J. Hydrol. 625, 130134. http://dx.doi.org/10.1016/j.jhydrol.2023.130134.

World Meteorological Organization, 2022. The 2022 GCOS ECVs Requirements. Geneva, URL: https://library.wmo.int/idurl/4/58111.

Wu, Q., Osco, L.P., 2023. samgeo: A Python package for segmenting geospatial data with the Segment Anything Model (SAM). J. Open Source Softw. 8 (89), 5663. http://dx.doi.org/10.21105/joss.05663.

Zakharova, E., Nielsen, K., Kamenev, G., Kouraev, A., 2020. River discharge estimation from radar altimetry: Assessment of satellite performance, river scales and methods. J. Hydrol. 583, 124561. http://dx.doi.org/10.1016/j.jhydrol.2020.124561.